

DTIC FILE COPY



AGARD-CP-482

AGARD-CP-482

AGARD

ADVISORY GROUP FOR AEROSPACE RESEARCH & DEVELOPMENT

7 RUE ANCELLE 92200 NEUILLY SUR SEINE FRANCE

AD-A229 641

AGARD CONFERENCE PROCEEDINGS No.482

Advances in Components for Active and Passive Airborne Sensors

(Progrès des Composants pour les Systèmes
de Détection Active et Passive Aéroportes)

DTIC
ELECTE
DEC 11 1990
S E D

NORTH ATLANTIC TREATY ORGANIZATION



DISTRIBUTION AND AVAILABILITY
ON BACK COVER

DISTRIBUTION STATEMENT A

Approved for public release;
Distribution Unlimited

90 12 10 157

NORTH ATLANTIC TREATY ORGANIZATION
ADVISORY GROUP FOR AEROSPACE RESEARCH AND DEVELOPMENT
(ORGANISATION DU TRAITE DE L'ATLANTIQUE NORD)

AGARD Conference Proceedings No.482

**Advances in Components for
Active and Passive Airborne Sensors**

(Progrès des Composants pour les Systèmes
des Détection Active et Passive Aéroportes)

Accession For	
NTIS GRA&I	<input checked="" type="checkbox"/>
DTIC TAB	<input type="checkbox"/>
Unannounced	<input type="checkbox"/>
Justification	
<i>PC/ME 23.00 NTIS</i>	
By _____	
Distribution/	
Availability Codes	
Dist	Avail and/or Special
<i>A-121</i>	



Papers presented at the Avionics Panel Specialists' Meeting held in Bath, England, 9-10 May 1990.

The Mission of AGARD

According to its Charter, the mission of AGARD is to bring together the leading personalities of the NATO nations in the fields of science and technology relating to aerospace for the following purposes:

- Recommending effective ways for the member nations to use their research and development capabilities for the common benefit of the NATO community;
- Providing scientific and technical advice and assistance to the Military Committee in the field of aerospace research and development (with particular regard to its military application);
- Continuously stimulating advances in the aerospace sciences relevant to strengthening the common defence posture;
- Improving the co-operation among member nations in aerospace research and development;
- Exchange of scientific and technical information;
- Providing assistance to member nations for the purpose of increasing their scientific and technical potential;
- Rendering scientific and technical assistance, as requested, to other NATO bodies and to member nations in connection with research and development problems in the aerospace field.

The highest authority within AGARD is the National Delegates Board consisting of officially appointed senior representatives from each member nation. The mission of AGARD is carried out through the Panels which are composed of experts appointed by the National Delegates, the Consultant and Exchange Programme and the Aerospace Applications Studies Programme. The results of AGARD work are reported to the member nations and the NATO Authorities through the AGARD series of publications of which this is one.

Participation in AGARD activities is by invitation only and is normally limited to citizens of the NATO nations.

The content of this publication has been reproduced directly from material supplied by AGARD or the authors.

Published September 1990

Copyright © AGARD 1990
All Rights Reserved

ISBN 92-835-0584-0



Printed by *Specialised Printing Services Limited*
40 Chigwell Lane, Loughton, Essex IG10 3TZ

Theme

The survivability of aircraft and their capability of carrying out different missions rely on numerous sensor systems such as radars, altimeters, radionavigation, measure and countermeasure equipments. It is very important that the most advanced semiconductor technologies be used in those systems as early as possible because it is appearing that avionic equipment performance is limited by the available components.

Therefore, this specialist meeting is aimed at focusing on emerging semiconductor component and sensor technologies.

Thème

La survie et la capacité de conduire différentes missions des aéronefs dépendent de nombreux systèmes de détection tels que radars, altimètres, équipements de radionavigation, de mesures et de contremesures. Il est très important que les technologies de composants électroniques les plus récentes soient introduites dans les systèmes le plus tôt possible car il arrive que des performances d'équipements avioniques soient limitées par les composants.

Cette réunion de spécialistes a pour but de faire le point des technologies et composants émergents et de voir comment elles peuvent repousser les limitations constatées.

Avionics Panel

Chairman: Dr Richard Klemm
FFM—FGAN
Neuenahrer Str.20
D-5307 Wachtberg 7
Germany

Deputy Chairman: Eng. Jose M.B.G.Mascarenhas
C-924
c/o Cinciberlant Hq
2780 Oeiras
Portugal

TECHNICAL PROGRAMME COMMITTEE

Chairman: Mr Jean M.Brice
Directeur Technique
Thomson BCS-TMS
B.P. 123
38521 Saint Egreve
Cedex
France

Mr John J.Bart
Technical Director
Directorate of Reliability & Compatibility
Rome Air Development Center (AFSC)
Griffiss AFB, N.Y. 13441
United States

Mr Paul B.Homer
Naval Weapons Center, Code 35
China Lake, CA 93555-6001
United States

Dr L.Hoivik
A/S Informasjonskontroll
P.O.Box 265
N-1371 Asker
Norway

Mr M.Jacobsen
Manager, Airborne EW Systems Dept.
AEK Aktiengesellschaft
Sedanstrasse 10
7900 Ulm Donau
Germany

Dr Wolfgang Keydel
Director
D.F.V.L.R. e.V.
Institut für Hochfrequenztechnik
D-8031 Wessling/Oberpfaffenhofen
Germany

Dr Richard Klemm
Forschungsinstitut für Funk und
Mathematik FFM
Neuenahrer Strasse 20
D-5307 Wachtberg 7
Germany

Eng. Jose M.B.G.Mascarenhas
Data General Portugal
Estrada Lisboa-Sintra
2700 Amadora
Portugal

Prof. Dr Tim V.Pampoucas
22, Politcias Avenue
GR-14563 Kifissia, Athens
Greece

AVIONICS PANEL EXECUTIVE

Lt Colonel James E.Clay

Mail from Europe:
AGARD—OTAN
Attn: AVP Executive
7, rue Ancelle
92260 Neuilly sur Seine
France

Mail from US and Canada:
AGARD—NATO
Attn: AVP Executive
APO New York 09777

Tel: 33(1) 47 38 57 65
Telex: 610176 (France)
Telefax: 33(1) 47 38 57 99

Contents

	Page
Theme/Thème	iii
Avionics Panel Officers and Technical Program Committee	iv
Rapport d'Evaluation Technique/Technical Evaluation Report par T.Weil	TER
	Reference
SESSION I – INTRODUCTION	
Specific Aspects of Advanced Components for Airborne Applications by J-M.Brice	1
Microwave and Millimeter Wave Components, Performances, Perspectives and Applications to Avionics by P.Briere and D.Pons	2
SESSION II – NEW MATERIALS/COMPONENTS	
Multiple Quantum Well NIR Optical Modulators - A Review of the Optical Signal Processing using III-V Semiconductors by D.R.P.Guy, D.D.Besgrove and N.Apsley	3
Quantum Well Infra-Red Detectors: An Introduction by M.J.Kane, M.T.Emeny, N.Apsley and C.R.Whitehouse	4
Paper 5 withdrawn	
Low-Noise Oscillators for Airborne Radar Applications by R.L.Filler and J.R.Vig	6
SESSION III – MICROWAVE MONOLITHIC ICS	
Paper 7 withdrawn	
GaAs MMICs in Selfaligned Gate Technology for Phased Array Radar Application by E.Pettenpaul and U.Freyer	8
Performances of MMIC X-Band Power Amplifiers Obtained in Foundry by G.Apercé	9
Millimeter-Wave Monolithic Integrated Receiver Circuits by L-P.Schmidt, B.Adelseck, A.Colquhoun and H.Dambkes	10
Broadband Coupling Structures for Microwave Arithmetic Circuits and Phased Arrays by J.A.Mosko	11
Logarithmic Amplification for Passive Airborne Direction Finding in the 1990's by R.Smith Hughes	12

SESSION IV – ACTIVE PHASED ARRAY

Paper 13 withdrawn

- T/R Modules for Phased-Array Antennas** 14
by C.Peignet, Y.Mancuso and J.C.Resneau
- MMIC Impact on Airborne Avionic Systems** 15
by E.J.Jones and W.J.Bocchi, Jr

SESSION V – OPTIC APPLICATIONS TO AVIONICS

- Fibres Optiques Spéciales et Capteurs pour l'Aéronautique** 16
(Special Optical Fibers and Sensors for Aeronautics)
par J-P.Le Pesant et M.Turpin
- The Use of Optical Methods for Microwave Signal Distribution and Control** 17
by W.I.McMillan
- Paper 18 withdrawn
- Laser Obstacle and Cable Update Sensor** 19
by C.K.Bullock, R.T.Hintz and W.Tanaka
- Infra-Red Laser Radar Systems** 20
by A.V.Jelalian and D.R.Bates

RAPPORT D'EVALUATION TECHNIQUE

Les Progrès des Composants pour Capteurs Actifs et Passifs Aéroportés
Conférence de spécialistes de l'AGARD, Bath-upon-Avon, UK, 9-10 mai 1990

Thierry Weil
Technologies Conseils
Thomson, Château de Corbeville,
BP 10, 91404 Orsay Cedex, France

1. INTRODUCTION

Les performances des systèmes électroniques embarqués dépendent crucialement de celles des composants électroniques qu'ils contiennent. Or, la technologie des composants connaît un bouleversement majeur tous les deux ans et demi, qui vient repousser les limites des performances et de la miniaturisation des circuits intégrés.

Pour pouvoir remplir la mission qui lui est assignée, l'AGARD doit donc faire le point régulièrement sur l'état de l'art et les perspectives dans le domaine des composants susceptibles d'être incorporés dans les systèmes électroniques embarqués, et tout particulièrement au niveau des capteurs, qui constituent souvent le maillon critique du système.

Tel était l'objectif de ce "specialist meeting". Après deux jours consacrés à l'évaluation des possibilités des supraconducteurs à haute température critique, la deuxième session de cette réunion était consacrée aux technologies dont la disponibilité est plus immédiate.

Après un rappel des caractéristiques spécifiques qui distinguent les composants susceptibles d'être incorporés dans des systèmes électroniques embarqués, les communications présentées faisaient le point des progrès dans deux domaines :

- les microondes, notamment les ondes millimétriques, avec la présentation de résultats récents sur les circuits pour radars à formation de faisceau en bandes C et X,
- les applications optiques (composants, fibres et capteurs).

(*) Les numéros entre [] renvoient à la communication portant ce numéro

A l'intérieur de chaque domaine, les résultats couvraient toute la filière technique :

- les possibilités offertes par les nouveaux matériaux, notamment l'utilisation des III-V épitaxiés à mailles adaptées ou non,
- les progrès en matière de CAO, notamment au niveau des méthodes de modélisation et des outils de simulation,
- la construction de bibliothèques de cellules, dans le domaine des composants microondes,
- et bien sûr la présentation de résultats récents en matière de réalisation de composants et de circuits.

Nous laisserons le lecteur se reporter au texte des communications présentées pour le détail des résultats exposés, et concentrerons ce rapport d'évaluation sur les thèmes suivants :

- la spécificité des composants embarqués [1] (*)
- les progrès des circuits intégrés monolithiques à microonde (MMIC) [2, 6, 11] et leur application à la réalisation d'antenne radar à formation de faisceau [8, 9, 10, 12, 14, 15]
- les progrès des composants optiques (circuits et fibres) [3, 4, 16, 17, 19, 20]

et nous conclurons sur les autres thèmes qui doivent être étudiés pour tirer parti du progrès du capteur.

2. LA SPECIFICITE DES COMPOSANTS EMBARQUES [1]

Les composants embarqués doivent respecter des contraintes d'environnement beaucoup plus astreignantes que les circuits civils équivalents :

- faible encombrement et poids,
- faible consommation d'énergie,
- résistance à des conditions d'environnement très agressives (températures, radiations ionisantes, accélérations et vibrations).

Leurs performances, leur complexité et leur fiabilité, comme pour d'autres composants militaires, doivent cependant être souvent très supérieures aux composants civils équivalents (souvent dix fois plus de portes logiques pour les ASIC par exemple).

Ces contraintes et ce niveau d'exigence des spécifications conduisent souvent à recourir à des solutions techniquement très avancées qui seraient inabordable pour des composants civils. Par exemple, en utilisant des technologies permettant de superposer trois ou quatre niveaux de métal, ou en trouvant des solutions d'encapsulation de très haute densité (TAB, boîtiers à cavités multiples, connexion sur silicium, "wafer scale integration" ...).

A ces contraintes sur les performances et la robustesse, s'ajoutent la durée de vie de vingt ans des équipements et un temps de conception qui atteint parfois dix ans, alors qu'une nouvelle technologie apparaît tous les deux ou trois ans et que la durée de vie industrielle totale d'une filière technologique ne dépasse pas dix ans. Comme l'explique Jean-Michel Brice, président de cette conférence, les composants doivent être définis dans une technologie qui n'existe pas encore et devront un jour être produits dans une technologie qui n'existera plus.

Si l'on considère également que les quantités produites sont souvent d'une centaine d'unités (contre des séries de 100 000 à 10 000 000 pour les composants civils), on voit que malgré la volonté d'utiliser autant que faire se peut des composants et des technologies civils, le marché des composants aéroportés restera en grande partie spécifique et ne pourra être approvisionné que par des producteurs capables d'offrir les technologies les plus élaborées et une qualité de service exceptionnelle.

Les composants devront donc rester l'objet d'une vigilance considérable pour l'OTAN et en particulier pour l'AGARD.

Après ce rappel des spécificités des composants embarqués, les présentations de la conférence étaient consacrées aux capteurs (et à une partie de l'électronique qui leur est directement liée). Nous rendrons compte successivement des résultats présentés dans le domaine des microondes puis dans celui des signaux optiques.

3. LES COMPOSANTS A MICROONDES

Les résultats présentés portaient sur trois domaines :

- les nouveaux matériaux et dispositifs [2], les techniques et résultats en matière d'intégration de circuits intégrés MMIC à base de transistors MESFETS [8, 9, 10, 14, 15],
- quelques sujets importants pour les performances des systèmes à microondes, mais ne portant pas directement sur les circuits de capteurs ou le traitement de premier niveau [2, 6, 11, 12].

3.1 Les nouveaux matériaux et dispositifs

L'utilisation de technologie d'épitaxie permet de produire des composants à hétérojonction(s), bipolaires (HBT) ou à effet de champ (HFET ou HEMT) qui permettent d'atteindre des performances très supérieures aux meilleurs MESFET.

Le tableau suivant, extrait de la présentation [2] résume quelques résultats récents.

Ft and Fmax - state of the art - 2 Q 1990

device type	substrate	Lg (um)	Ft (GHz)	Fmax (GHz)	Company
MESFET	GaAs	0.2	75	130	SEVERAL
HEMT	GaAs	0.25	90	230	G.E
PM-HEMT	GaAs	0.15	150	350	G.E., HUGHES, ...
LM-HEMT	InP	0.15	185	405	G.E., HUGHES, VARIAN
HBT	GaAs	1.2 (LE)	105	210	NTT, ROCKWELL

Les tendances actuelles sont :

- l'utilisation de canaux InGaAs dans les HEMT, soit sous forme contrainte (pseudomorphique) sur un substrat de GaAs, soit sur des substrats d'InP. Ceci permet de disposer d'une plus grande densité de charges, d'une meilleure mobilité et d'un meilleur confinement de celles-ci. Un facteur de bruit de 1,4 dB à 94 GHz a ainsi pu être obtenu avec le système GaInAs/InP, et des fréquences de coupure de 185 GHz. Avec des doubles hétérojonctions, ces dispositifs allient un très faible niveau de bruit et un bon niveau de puissance,
- les techniques d'attaque ionique sélective (R.I.E.) et de dopage planar permettent d'intégrer les HEMT et de fabriquer des MMIC ayant d'excellentes performances,
- le HBT conserve l'avantage pour les applications de puissance, notamment les amplificateurs et les émetteurs.

Les HBT peuvent servir à fabriquer des sources de puissance à haut rendement, des oscillateurs locaux à faible bruit de phase, des convertisseurs ADC rapides, tandis que les HEMT peuvent être utilisés pour des récepteurs à faible bruit et large bande et pour les dispositifs à ondes millimétriques (communication, radars, autodirecteurs).

3.2 Circuits intégrés à base de transistors MESFET GaAs pour les microondes

Un tiers des papiers présentés à la conférence portaient sur la réalisation de circuits de modules d'antenne radar en bandes C et X et sur les premiers étages d'amplification qui leur sont associés, nous renvoyons le lecteur à ces papiers pour les détails des performances atteintes. Quelques traits saillants nous paraissent dignes d'être soulignés:

◇ L'émergence d'un bon environnement de conception pour les MMIC.

- en CAO, le projet européen ESPRIT 255 a permis d'élaborer un outil "MMIC CAD" très fiable jusqu'à 20 GHz
- l'utilisation de modèles de simulation ne dépendant pas de paramètres empiriques du process mais seulement de facteurs géométriques a permis à Electronique Serge Dassault de réaliser des conceptions "tolérantes aux variations

de process" et d'avoir des circuits corrects dès la première passe de fonderie

- certains industriels comme SIEMENS et THOMSON commencent à disposer de bonnes bibliothèques de cellules analogiques pour des circuits microonde.

◇ Des process ayant de bons rendements commencent à être au point.

◇ Enfin le programme COBRA (Counter Battery Radar) de radar de champ de bataille contre l'artillerie stimule considérablement les recherches en offrant la perspective de séries de fabrication importantes.

Il semble que les circuits à faible bruit dans la gamme 10 GHz soient entrés dans une phase industrielle et que la prochaine étape clé soit la réalisation de circuits à 94 GHz qui deviennent envisageables.

3.3 Circuits périphériques

Trois articles portaient respectivement sur les amplificateurs logarithmiques (12), sur les oscillateurs à faible bruit (6) et sur la distribution du signal aux différents modules de transmission d'un radar à balayage électronique (17).

Le problème du bruit de phase des oscillateurs est particulièrement crucial pour les radars embarqués qui subissent des accélérations et des vibrations importantes, modifiant les fréquences de résonance des quartz qui régulent l'oscillateur. En l'absence de correction, cet effet empêche un radar d'hélicoptère de détecter des cibles lentes (quelques km/h).

Le papier présenté par le laboratoire militaire de Fort Monmouth faisait le point sur les différentes solutions pratiquées, montrant que la plupart ne fonctionnent que dans des domaines de fréquence assez restreints. D'après ces auteurs, les solutions les plus prometteuses utilisent la distribution des amplitudes de vibration entre les différents points d'un résonateur.

La distribution des signaux de commande et de synchronisation aux différents modules d'antenne d'un radar à formation de faisceau est un problème délicat pour lequel les fibres optiques semblent une solution adaptée. Outre des avantages évidents de poids, de bande passante, de faibles pertes et d'immunité aux contre-mesures, les fibres peuvent être pliées pour les antennes

de satellites qui doivent être déployées dans l'espace.

Des systèmes ont été dessinés dans les laboratoires de MARCONI pour alimenter 512 modules avec des signaux de 5 GHz. Une fibre suffit pour commander 32 modules. Le système est tolérant à une panne d'un module.

3.4 Modélisation

Signalons enfin deux contributions aux thèmes plus exotiques portant sur la modélisation des systèmes.

◊ Une contribution du Centre d'Armenant Naval de China Lake (11) était consacrée au couplage entre les circuits. L'auteur présentait plusieurs structures de couplages originales et efficaces et montrait :

- qu'une résolution des équations de couplage était possible et permettait d'optimiser les systèmes
- que l'approche consistant à optimiser séparément le module d'antenne radiative et le circuit d'alimentation et à les coupler au mieux, était très sous-optimale et qu'à l'avenir il faudrait optimiser le système globalement en prenant explicitement en compte le couplage entre les éléments.

◊ Par ailleurs, il semble que les pannes des composants MMIC soient souvent dues aux contraintes induites dans le matériau. Une équipe du centre de développement de Rome (New-York) a donc utilisé des méthodes d'éléments finis pour modéliser numériquement les contraintes thermiques, électriques et mécaniques induites dans un composant. Ceci permet par exemple de prédire l'existence de points d'échauffement anormaux et de modifier la conception de ceux-ci.

4. LES COMPOSANTS OPTIQUES

Outre l'utilisation des fibres optiques pour transmettre les signaux de commande et de synchronisation des radars à formation de faisceaux que nous avons mentionnés plus haut, trois aspects de l'optique ont été évoqués lors de la conférence :

- les possibilités offertes pour l'optronique par les nouveaux matériaux [3,4]
- les radars à lasers infra-rouge [19, 20]

- les autres capteurs utilisant des méthodes optiques [16].

4.1 Les nouveaux matériaux

Quelques utilisations des propriétés électriques des systèmes à puits quantiques multiples obtenus par épitaxie d' $\text{Al}_x\text{Ga}_{1-x}\text{As}$ sur GaAs ou de InGaAs sur InP ont été présentées.

◊ Les réseaux de modulateurs électro-optiques fabriqués au RSRE (Royal Signal & Radar Establishment) permettent de moduler une lumière à $1.6 \mu\text{m}$ à des fréquences atteignant 20 GHz (les pics d'absorption, assez aigus, sont déplacés par le champ électrique).

◊ Les multipuits quantiques peuvent aussi servir à réaliser des guides d'ondes parallèles à la surface des circuits avec des déphasages modulables électriquement.

◊ Enfin, dans l'infra-rouge moyen (8-10 μm), on peut utiliser non plus les transitions interbandes, mais les transitions entre niveaux électroniques confinés entre deux puits quantiques voisins, l'écartement des niveaux étant proportionnel au champ électrique dans les régions des puits, donc aisément modulable. Le bruit de fond de ces dispositifs reste cependant important à température ambiante.

4.2 Les radars à laser infra-rouge

Les radars à lumière infra-rouge, parfois appelés lidars ou ladars (laser detection and ranging) fonctionnent suivant le même principe que les radars utilisant les ondes radio. Leur longueur d'onde différente (9 à 11,5 μm pour les systèmes utilisant un laser à gaz carbonique) a les conséquences suivantes :

- meilleures précision et résolution
- déplacements en fréquence beaucoup plus sensibles permettant de mesurer l'effet Doppler sans avoir à échantillonner et à faire des traitements complexes
- possibilité d'utiliser des faisceaux très directs pour avoir des détectivités en d^{-2} au lieu de d^{-4}
- malheureusement une grande sensibilité aux conditions atmosphériques qui limite beaucoup leur portée en dehors de quelques fenêtres en longueur d'onde.

Une application de ces radars est de rendre possible des vols rapides et à basse altitude, de nuit ou dans de mauvaises conditions de visibilité. Le système LOCUS (Laser Obstacle and Cable Update Sensor) de GEC vient ainsi compléter les FLIR (Forward Looking Infrared Radars) et compenser la faible profondeur de champ de ceux-ci.

4.3 Capteurs à base de fibres optiques

Les applications habituelles des fibres optiques à l'avionique utilisent le faible poids de celles-ci, leur immunité électromagnétique et leur large bande passante pour des liaisons à haut débit.

L'existence récemment démontrée de cellules photovoltaïques à haut rendement de conversion (> 55%) permet même d'utiliser des fibres pour l'alimentation en énergie des systèmes électroniques.

Une autre application courante des fibres à l'avionique est le gyroscope à effet Sagnac.

En revanche, la possibilité d'utiliser des fibres optiques à structures particulières comme capteurs de pression ou de température est moins connue. Dans ces fibres biréfringentes, une variation de température ou de pression sur un tronçon de fibre provoque une variation de la différence des vitesses de propagation entre les deux polarisations orthogonales et donc une augmentation du déphasage entre celles-ci. Au point d'entrée de chaque tronçon de fibre constituant un capteur, on couple une partie de l'énergie lumineuse d'une polarisation dans l'autre. Les deux polarisations se propageant à des vitesses de phase différentes, un interféromètre situé à l'extrémité de la fibre permet de savoir à quel endroit la variation de température ou de pression observée a lieu. La fibre joue à la fois le rôle de plusieurs capteurs en série, de multiplexeur et de canal de transmission des signaux de ces capteurs.

Dans les parties de la structure de l'avion faites en matériau composite, une fibre incluse dans le matériau peut servir à détecter les contraintes que subit celui-ci (échauffements, compressions, contraintes, déformation) et de surveiller in situ, en continu, le vieillissement et la fatigue du matériau. Les fibres peuvent être un composant essentiel des "peaux intelligentes" des avions.

5. RECOMMANDATIONS POUR LES ACTIONS FUTURES

La conférence, parfaitement organisée sur le plan logistique, a atteint son objectif de stimuler la discussion sur l'évolution des composants. Tout au plus peut-on déplorer que la simultanéité d'une importante conférence sur les circuits microondes qui se tenait à Dallas ait provoqué l'absence de nombreux spécialistes du domaine.

Par ailleurs, les cinq contributions sur les circuits MIMIC abordaient des thèmes très proches et une présentation synthétique du sujet aurait peut être été opportune.

Compte tenu de la rapidité des évolutions dans ce domaine, il serait opportun de programmer une nouvelle session de mise à jour dans trois ans. D'ici là deux thèmes pourraient faire l'objet d'une rencontre analogue :

- Les circuits de traitement du signal et de l'information :

En effet, les performances nouvelles des capteurs ne pourront être pleinement exploitées que si les signaux détectés peuvent être traités de manière adéquate. Par ailleurs, l'architecture générale des systèmes du traitement et la frontière entre traitement du signal et traitement de l'information pourraient être mises en cause pour tirer pleinement parti des possibilités des nouvelles technologies.

- La fusion des données :

Les limitations différentes des capteurs de différents types (infrarouge proche, infrarouge moyen, radars) et la nécessité de résister aux contre-mesures pousseront les avioneurs à utiliser plusieurs capteurs simultanément. Compte tenu de la rapidité avec laquelle les ambiguïtés d'interprétation doivent être levées et des faibles délais de réaction qu'imposent les contraintes des missions, le traitement des différents signaux devra être automatisé et le pilote d'avion disposera d'une information synthétique cohérente et ergonomique.

Les techniques de fusion de données et la qualité des interfaces homme-machine constitueront donc un élément critique pour l'efficacité des avions de combats.

6. CONCLUSION

En conclusion, l'impression générale qui se dégage est que l'avionique militaire est très dépendante de la disponibilité de composants adaptés à ses besoins. Quatre des vingt technologies critiques répertoriées par le DOD étaient fondamentalement présentes dans les sujets évoqués. Cela montre que les avionneurs ne peuvent attendre de trouver sur le marché les composants dont ils ont besoin sans mettre en péril la supériorité des systèmes de défense de l'OTAN et que la vigilance qu'exerce l'AGARD à travers des rencontres comme celle de Bath est indispensable.

TECHNICAL EVALUATION REPORT

Advances on components for active and passive airborne sensors
AGARD specialist meeting, Bath-upon-Avon, UK, 9-10 may 1990

Thierry Weil
Technologies Conseils
Thomson, Château de Corbeville,
B.P. 10, 91404 Orsay Cedex, France

1. INTRODUCTION

Performances of airborne electronic systems crucially depend upon the characteristics of their electronic components. However, semiconductor technology experiences major improvements every two and a half years, which pushes further the limits of performance and miniaturization of integrated circuits.

In order to fulfill its mission, the AGARD needs to periodically assess the state of the art and the trends of the components which may be involved in airborne electronic systems, especially of the sensors which are often the critical link of the system.

This assessment of the state of the art was the purpose of this meeting of specialists. After two days spent in assessing the perspectives of high temperature superconductors, the second session of this meeting was dedicated to more immediately available technologies.

After having stressed the specificity of airborne components, the speakers presented recent advances in two main areas :

- microwaves, especially millimeter waves, with recent results on circuit for phased array radars in the C and X band,
- the use of optics (components, fibers and sensors).

Inside each domain, results covering the whole process were discussed :

- possible applications of new materials, especially the III-V semiconductor grown by epitaxy with or without matching lattice,

- advances in CAD, especially modelization and simulation tools,
- the building of cell libraries for microwave circuits,
- and, of course, recent results on components and circuits.

Details about the results can be found in the text of the following papers, while this technical evaluation report will focus on :

- the specificity of airborne circuits,
- advances in monolithic microwave integrated circuits (MMIC) [2, 6, 11] and their applications to phased array radar antennas,
- new optical components and sensors (both circuits and fibers) [3, 4, 16, 17, 19, 20].

We shall conclude this report discussing other topics which should be studied by AGARD in order to take better advantage of the progress made on sensors.

2. WHY ARE AIRBORNE COMPONENTS SPECIFIC ?

Airborne circuits have to experience much more stringent environmental conditions than their civil equivalents :

- small volume and weight,
- low power consumption,
- aggressive environmental conditions (temperatures, radiations, accelerations and vibrations).

Furthermore, their performances, complexity and reliability, as in other military applications, are much higher than those of similar civil components (e.g. often ten times the number of gates for a military ASIC).

Due to these numerous constraints, one has often to rely on very advanced techniques which would be unaffordable for civil applications, e.g. processes with 3 or 4 layers of metal or very high density packaging (TAB, multiple cavity carrier, connection or silicon, wafer scale integration, and so on).

Last but not least, airborne equipments should work at least 20 years while their total design time lasts sometimes 10 years and while a new generation of technology appears every 2 or 3 years.

So, according to Jean-Michel Brice, the chairman of this meeting, airborne components have to be designed in a technology which is not yet available and will one day have to be manufactured in a technology which will no longer exist.

Furthermore, the manufactured quantities are generally about 100 pieces, while the size of civil production series ranges from 100 000 to 10 000 000 pieces. So even if one should choose to use civil products and technology whenever possible, a large share of the airborne circuit will still remain specific and rely on dedicated manufacturers, able to supply access to the most sophisticated technologies and to provide outstanding service.

Therefore, components should remain a topic of active awareness for NATO and especially for AGARD.

After these general considerations on the specificity of airborne circuits, the meeting was devoted to the sensors and to the electronics directly linked to them. We shall now present results concerning microwave and optical signals.

3. MICROWAVE COMPONENTS

The speeches covered three main topics :

- new materials and devices [2],
- new techniques and circuits for MESFET, MMICs [8, 9, 10, 14, 15],
- some important issues for system performances which did not directly concern the sensor and its first stage electronics [2, 6, 11, 12].

3.1 New materials and devices

Epitaxially grown heterojunction bipolar transistor (HBT) or field effect transistors (HFET or HEMT) clearly outperform clearly the best MESFETs. The following table, presented in paper 2, shows some measurements of best recent devices :

Ft and Fmax - state of the art - 2 Q 1990

device type	substrate	Lg (um)	Ft (GHz)	Fmax (GHz)	Company
MESFET	GaAs	0.2	75	130	SEVERAL
HEMT	GaAs	0.25	90	230	G.E
PM-HEMT	GaAs	0.15	150	350	G.E, HUGHES, ...
LM-HEMT	InP	0.15	185	405	G.E, HUGHES, VARIAN
HBT	GaAs	1.2 (LE)	105	210	NTT, ROCKWELL

Current trends are :

- the use of In GaAs channels in HEMT, either with strained layers (pseudomorphic) on a GaAs bulk material or on InP. This provides a higher density of carriers, and these carriers show higher mobility and better confinement. A noise factor as good as 1, 4 dB at 94 GHz was measured with GaInAs/InP, with cut off frequencies as high as 185 GHz. Double heterojunction devices may provide both high power and a low noise level.
- Reactive Ion Etching and Planar Doping make it possible to integrate HEMTs and to produce high performances MMICs.
- HBTs remain the best solution for power devices, especially amplifiers and transmitters. HBT are very well suited to produce efficient power supplies, low noise local oscillators and fast analog-digital convertors, while HEMTs may be efficiently used for low noise wide-band receivers and for millimeter wave devices (for communications, radars and tracking).

3.2 Integrated circuits with GaAs MESFET for microwave application

About a third of all the contributions to the meeting were focussed on circuits for C and X band phased array radar antennas and on their first amplification stages. Some interesting trends appear :

* A good design environment for MMICs

- concerning CAD, the european ESPRIT program 255 resulted in "MMIC CAD", a very reliable tool up to 20 GHz,
- using simulation models based on geometrical parameters which did not depend upon semi-empirical fits, Electronique Serge Dassault has achieved some "process tolerant designs" which allowed them to obtain working circuits after the first foundry pass
- some manufacturers as Siemens and Thomson have built good analog cell libraries for microwave circuits.

* High yield processes are available

Note that the COBRA program (Counter Battery Radar) has considerably fostered research by providing the perspective of large scale fabrication.

Low noise circuits at 10 GHz seem to have entered the industrial stage. The next key step will be the production of 94 GHz circuits.

3.3 Other circuits and techniques

Three papers were dedicated to logarithmic amplifiers [12], low noise oscillators [6], and signal distribution to the modules of an array [17].

Phase noise of oscillators is a key issue for airborne radars experiencing huge accelerations and vibrations which shift the resonator frequencies of the quartz. If uncorrected, this can make a helicopter radar unable to detect low targets (a few km/h).

A paper by the military laboratory of Fort Monmouth presented the state of the art of different devices, showing that most of them could only work well in narrow frequency windows.

According to the authors, the most promising solution uses the distribution of vibration amplitudes among different location of the resonator.

The distribution of control and synchronization signals to the different cells of a phased array radar is a tough problem for which optic fibers look well suited. Fibers are light, have a large bandwidth, few losses and might be wound up for satellite antennas.

Marconi has designed systems to feed 512 modules with signals at 5 GHz. A single fiber can control 32 modules. The system can tolerate a faulty module.

3.4 Modelization

Two contributions were dedicated to somewhat exotic modelization problems.

* A paper of the Naval Weapon Center of China Lake [11] was dedicated to the coupling between circuits. Several original and efficient coupling structures were discussed and it was shown that :

- solving the exact coupling equation was possible and allowed optimization of the systems.
- the traditional way of optimizing separately the radiator and the power circuit and then of coupling them as best as possible leads to very underoptimal designs. Therefore, taking explicitly into account the coupling between the components when designing the system is possible and strongly recommended.

* Failures of MMIC seem to be often due to mechanical stresses of the device. Scientists of the Rome Air Development Center (New-York) used finite element analysis to achieve numerical modelization of thermal, electrical and mechanical stresses in components. They were able to predict abnormal heating in some locations and to modify the design to avoid it.

4. OPTICAL DEVICES

Apart from the use of optic fibers for carrying synchronization signals to phased array radars which we already mentioned above, three topics on optical devices were discussed

- Optronic applications of new materials [3,4]
- Infra-red laser radars [19, 20]
- Other optical sensors [16].

4.1 New materials

Some applications of the electrical properties of multiple quantum wells systems grown by epitaxy of $Al_x Ga_{1-x}$ As on GaAs or of InGaAs on InP were discussed :

* At the RSRE, electro-optical modulator arrays allow modulation of 1.6 μm light at frequencies up to 20 GHz (the sharp absorption peaks are shifted by the electrical field).

* Multiple quantum wells can also be used to build waveguides parallel to the sample surface where phaseshifts can be electrically tuned.

* Finally in the Intermediary Infra-Red range (8 to 10 μm) intraband transition between the confined level in two neighbor wells are used instead of intraband absorption. The distance between final and initial states is proportional to the field induced in the wells area, so it can easily be tuned. However, at room temperature these devices are limited by the band thermal noise.

4.2 Infra-red laser radars

Infra-red radars, also called lidars or ladars (laser detection and ranging) rely on the same principles as radars using radio waves. However the different frequency range (9 to 11,5 μm for systems using CO_2 laser) has some consequences :

- better accuracy,
- larger Doppler shift allowing direct measurements without complex sampling and processing,
- opportunity to use very narrow beams, yielding detectivity in d^{-2} instead of d^{-4} ,
- unfortunately, these sensors are very sensitive to bad atmospheric conditions and then have a rather short range (a few km).

These radars are useful for night attacks at low altitude or other missions whenever the pilot must fly at low altitude with poor visibility. GEC developed a Laser Obstacle and Cable Warning Sensor system (LOCUS) which can be used together with a FLIR (forward looking infra-red radar) and compensate for the poor field depth of this radar.

4.3 Sensors using optical fibers

Most use of fiber optics for avionic relies on their light weight, their immunity to electromagnetic interferences and their very large bandwidth.

Due to the recent availability of high efficiency photovoltaic cells (> 55 % conversion), fibers

can even be used to supply power to electronic systems.

Another well-known application of fiber optics is the gyroscope using the Sagnac effect.

However, the use of fibers as pressure or temperature sensors is not well known enough. In birefringent fibers, a variation of the temperatures or of the pressure on a segment of fiber induces some additional difference between the speeds of the two polarizations.

At the beginning of each sensor section, the polarizations are slightly coupled. A variation of pressure or temperature in the sensor will then result in an additional phase shift. Since both polarized waves propagate at different speeds, one may use an interferometer together with an analyser to detect where this coupling has occurred. The fiber then works as a serie of several sensors, with a multiplexer and a transmission channel (the single fiber performing all these tasks).

When composite material is used in the plane structure, an optical fiber included in the material can monitor in situ the local stresses (heating, compression, stress, strain) and the aging of structure. Fibers can then be an essential component of the "smart skins" of the planes.

5. RECOMMENDATIONS FOR FUTURE TIONS

The meeting was perfectly organized and did achieve its goal of encouraging an informed discussion on the evolution of airborne components. The only draw back was a problem of agenda : a world leading conference on microwaves took place at the same time in Dallas causing the absence of many good specialists. Furthermore, five papers on MMIC were dealing with very similar topics and a more synthetical presentation might have been useful.

Because of the fast pace of evolutions in that field; it would be a good idea to schedule an update meeting in about 3 years. Meanwhile, two topics could deserve such a meeting :

- Signal and data processing circuits

Better sensors will only yield interesting improvement if their signals are suitably processed. Furthermore, the general architecture of systems, especially the boundary between signal and data processing could experience major

changes in order to make better use of the advances of new technologies.

- Data fusion

In order to take advantage of the various limitations of different kinds of sensors (near infra-red, intermediate infra-red, radars) as well as to resist electronic counter-measures, airplane manufacturers will tend to use several sensors simultaneously. Ambiguities in data interpretation should be rapidly reduced and most of the processing will have to be performed automatically. The pilots should be directly provided with consistent synthetic and easy-to-use information.

Thus the techniques of data fusion and of friendly man-machine interface will be critical for the efficiency of fighting aircrafts.

6. CONCLUSION

The general feeling after this meeting is that military avionics strongly depends on the availability of suitable components. Four of the twenty critical technologies listed by the DoD were at the core of the papers discussed at the meeting. It shows that airplane manufacturers cannot expect to find their critical components off the shelf without putting at risk the superiority of the defense means of NATO. Therefore, the awareness of AGARD, through meeting as the Bath specialist meeting, is absolutely necessary.

**SPECIFIC ASPECTS OF ADVANCED COMPONENTS
FOR AIRBORNE APPLICATIONS**

Jean-Michel BRICE
THOMSON COMPOSANTS MILITAIRES ET SPATIAUX
BP 123 - 38521 SAINT EGREVE CEDEX - FRANCE

This presentation deals with some important specific aspects of electronic components, mainly high speed, high performance integrated circuits used for airborne applications. It is shown that the requirements such as complexity, performance, power consumption, are more stringent for airborne components than for the other components, civil ones in particular. In addition the long lifetime of airborne equipments, typically 25 to 30 years, requires specific arrangement to assure the long term availability of the strategic components, as the semiconductor technologies don't survive more than 10 years. The antinomy, use of standard and mature technologies for low cost and large product base but necessity to get access to specific or advanced technologies for specific performance requirements, can be solved by the add on military concept, where civil technologies are used whenever possible, but specific developments are undertaken to fulfil the military airborne specifications.

When considering electronic components for airborne applications, there are two very simple ideas which can explain their specific situation. One is that they have to fit to the very specific airborne environment or, in other words, they have to fly ! The other is that they are military components, and as such, have to comply with a number of severe requirements going from the temperature range to the respect of military norms.

In addition, the performance needed for modern combat aircraft avionics, in a more and more hostile counter-measure environment, as well as the numerous functionalities required to achieve the best operational efficiency, lead to the use of a very broad range of electronic components, in almost all technologies available, as summarized in table 1. Then, it is easy to determine the particular features of advanced airborne components from the two considerations above mentioned.

COMPONENTS FOR AIRBORNE APPLICATIONS
<p>Airborne applications require a very broad range of components :</p> <ul style="list-style-type: none"> - Microwave components and sensors - Image sensors <p>and also :</p> <ul style="list-style-type: none"> - memories - microprocessors - bus interface circuits - ASICs - high voltage, high power IC's - linear circuits - discrete components <p>with various technologies :</p> <ul style="list-style-type: none"> - III-IV compounds : GaAs, InP, ... - Silicon CMOS, bipolar, CCD - optica - Packaging and hybrids

TABLE 1

It is well known that there is no room in an aircraft and that the equipments must be as light as possible and consume the lowest achievable power, whilst giving the best performance to the avionics. Table 2 summarizes the main qualities and characteristics necessary for airborne components.

As far as the performances are concerned, figures 1 and 2 show the evolution of representative features of new generation radars. It is clear that the advances of the sensors (phase array antennas for instance) require a huge computation power to process the enormous data flow coming from them, in a continuously decreasing volume. This means that airborne systems not only need high performance sensors but also very complex and high speed integrated circuits for data processing.

COMPONENTS FOR AIRBORNE APPLICATIONS

For electronic components, Airborne applications mean :

- low weight
- low volume
- low power consumption

but :

- high performance
- high complexity
- high reliability
- high resistance to severe environmental conditions

In addition, Airborne equipments need a very long development time (typically 10 years) and have to be produced and maintained for an even longer period (15 to 20 years)

Finally, the product quantities are generally small, which makes it difficult to get competitive prices

TABLE 2

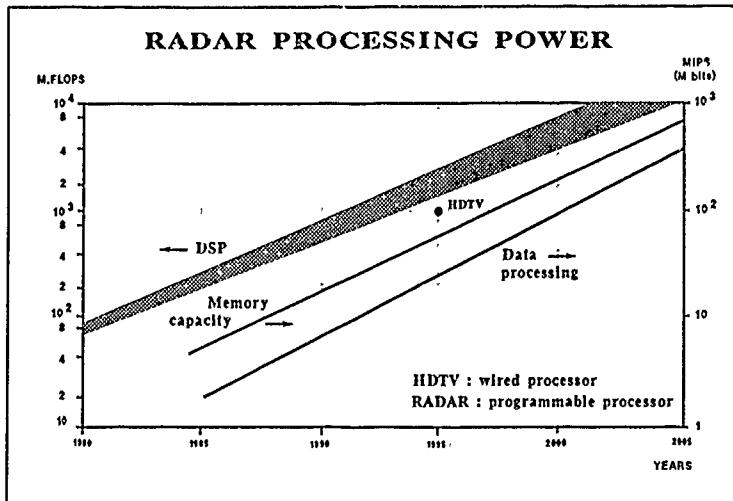


FIGURE 1

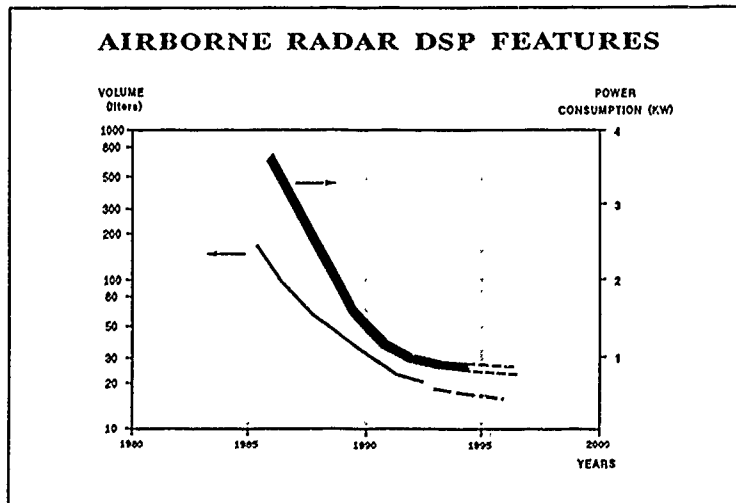


FIGURE 2

Among all components needed for avionics, two examples are interesting to investigate because they suggest another important establishment. The military needs are far from being fully covered by the standard products available on the semiconductor market.

The first example is the fast A to D converter family. Figure 3 shows that the field of very high speed, medium resolution A to D converters is badly addressed by commercial offering. To fulfil the requirements of radars, scramblers and, to a lesser extent, of image processing, it is necessary to develop fast A to D converters not easily available on the market and sold by only few semiconductor companies.

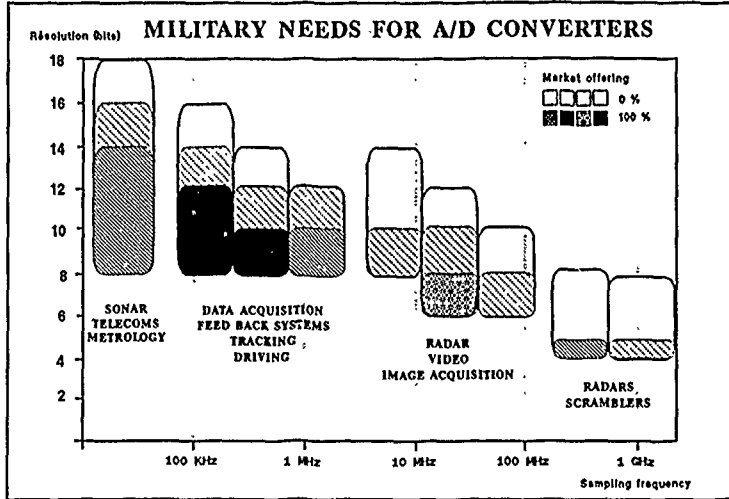


FIGURE 3

The second example is related to digital ASICs. Figures 4 and 5 show the evolution of the digital ASIC complexity, compared to civil components. Once again, it can be seen that the performances of military, and in particular airborne, ASICs are far ahead of the mainstream of commercial products, which implies advanced technologies and circuit development to fill the military requirements.

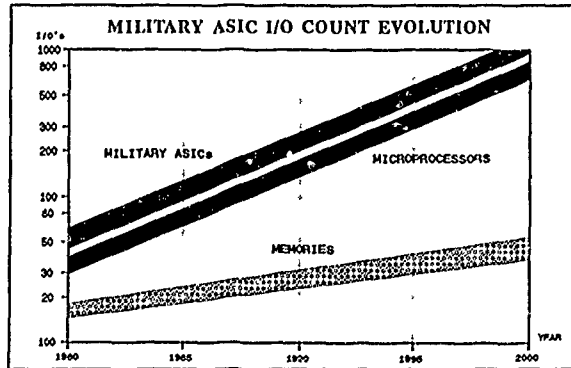


FIGURE 4

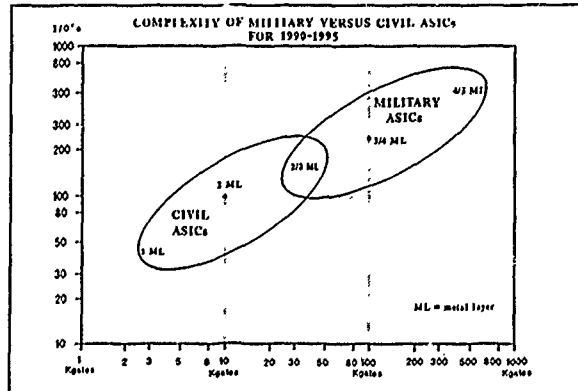


FIGURE 5

Another important issue, for military airborne components, is the life time of the equipments. As shown in figure 6, 25 to 30 years can elapse from the development starting point to the end of use of the equipment. This is roughly twice to three times the life time of semiconductor technologies. This means that adequate solutions have to be found to guaranty the long term availability of strategic products.

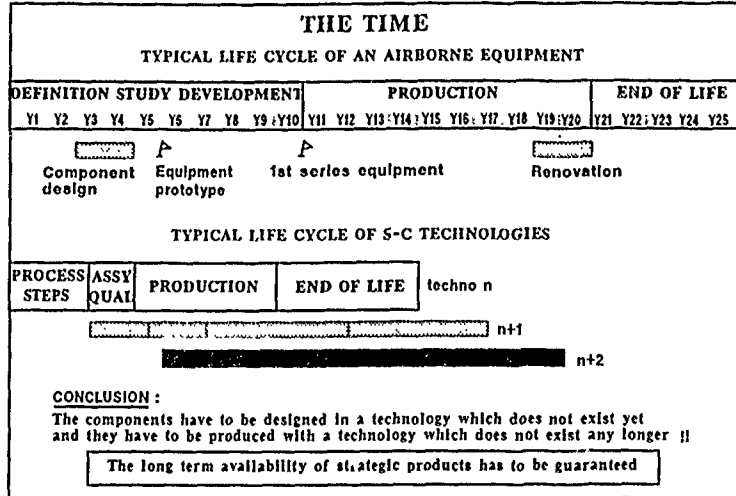


FIGURE 6

Another view of this problem is shown in figure 7 where military and civil products are situated in a life time-quantity diagram. One can see that there is no overlap between civil and military components. What is more, airborne components, together with space ones, are in the upper left corner of the diagram because the product quantities are among the smallest and the life time can exceed thirty years.

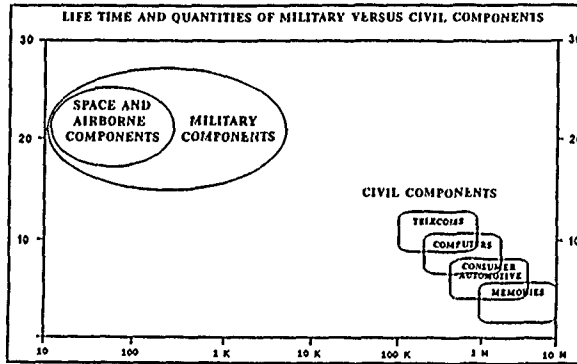


FIGURE 7

Another specific aspect of airborne components is their environmental conditions, given in figure 8. The most demanding characteristic is the radiation hardening required for high altitude operation, which leads to specific technologies, as Silicon On Sapphire or silicon On Insulator, not used for commercial products.

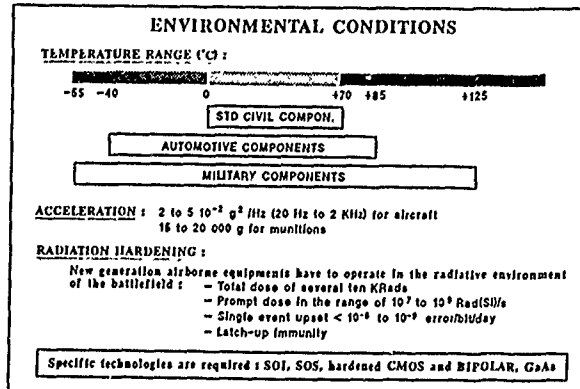


FIGURE 8

Finally it should be pointed out that airborne systems call for fast advances in packaging well more than the other applications do. It is well known that the active semiconductor volume of a radar, for example, represents less than one thousandth of the total electronic equipment volume. This means that very high density packaging (VHDP) techniques are mandatory for future airborne equipments, as it is finally those packaging and interconnection technologies which determine the final weight, volume and also the final performance of the systems. Among the currently investigated techniques, the following are promising :

- Interconnections on silicon substrate to benefit from the reduced pitches enabled by semiconductor technologies (less than 10 μm , over few cm length).
- Wafer scale integration technique, enabling a complete system to be integrated on a silicon wafer.
- Solder bumps and TAB for high pin count above 300.
- Multicavity packages for memory arrays or complex analog functions.
- Optical interconnections.
- Macrohybrids.

The tables 3 and 4 summarize the critical technologies for the future airborne components. It can be seen that they are numerous and that some of them are still in the development stage, as GaAs on silicon or photonics. But it is also clear that silicon is necessary almost everywhere. This is not surprising if one considers the maturity of all silicon processes and the huge R and D resources devoted to those technologies. The question is to know whether the non-silicon processes can benefit from this mainstream or not. The answer is surely yes but this does not mean that they will catch up with silicon. So, there will always be a trade-off to find between top level performance and production feasibility and cost.

CRITICAL TECHNOLOGIES FOR THE FUTURE OF AIRBORNE COMPONENTS

1. MICROWAVE COMPONENTS

- III-V technologies : GaAs, InP
For : Schottky, PIN, IMPATT, GUNN diodes
laser diodes
POWER FET transistors
HEMT, HBT transistors
Microstrip lines
- Silicon
For PIN, IMPATT diodes, microstrip lines
- III-V on silicon heteroepitaxy
For high density MMIC's

TABLE 3

CRITICAL TECHNOLOGIES FOR THE FUTURE OF AIRBORNE COMPONENTS

2. SIGNAL AND DATA PROCESSING

- SILICON
 - . For high speed, highly parallel applications using microprocessors, memories, ASICs...
 - . For analog functions using ADC, high voltage interfaces...
 - . For Rad Hard circuits (SOI)
 - . For opto-electronic components
 - . For high density, high speed interconnections
- GaAs
For very high speed digital circuits and SRAMs
- GaAs ON SILICON
For very high speed ADC's and logic circuits
- Optics and photonics
 - . For high density optical interconnections
 - . For high-performance parallel knowledge processors

TABLE 4

As a conclusion, it appears that, more than the other military components, the components for airborne applications are faced with an antinomy : on one hand, the search for low cost, secure and fast development components leads to the use of mature, state of the art, high volume technologies, but on the other hand, the specific requirements and the outstanding performances necessary to airborne applications impose the development of specific technologies or the early availability of advanced processes and circuits. Moreover, certain technologies never will be available on the civil market, due to their specific features and high cost. In short, the military needs are ahead of the civil needs.

In addition, the long term availability plus the compliance to severe military norms require an adequate service to the equipment manufacturers, a service which is incompatible with a low cost, high volume semiconductor organisation.

In front of this problem, one possible solution consists of using the ADD-ON MILITARY concept :

- to use the mainstream technologies and components whenever it is possible but,
- to develop a strong know-how for specific technologies or products not available on the civil market to fulfil in real time the strategic needs of military applications,
- and finally to offer a dedicated service to military equipment manufacturers through specialized semiconductor organizations, only oriented towards civil markets.

Discussion

Paper n° 1

Question : Professor D. BOSMAN (University of Twente, Panel Member)

I was intrigued by your remark that, wherever possible, civil developed chips should be adapted to military needs. But, when CAD models and reliability optimisation of complex circuits are well-developed in the near future, the civil products are already stressed to their limits ; precluding adaptation to wider military requirements without complete redesign. Would you comment on that ?

Answer : J.M. BRICE

This is an excellent question.

Civil products will not be designed at the very limit of available technology in every field because of the prohibitive cost and of the lack of sufficient market.

For example :

- . radiation hardening : no needs for the civil market
- . complexity : limited at what is absolutely necessary on civil products, because of the cost of the mm² of Si in large quantities and of the packaging.

However, if military specifications are abandoned or relaxed, some civil components could match the needs without major changes. The user is eventually the one who takes the decision, but airborne system manufacturers do not seem to be ready to give up their specifications.

Question : Dr. G.H. HUNT (Royal Aerospace Est., Panel Member)

You have omitted any reference to superconductors in your review of the materials and technologies for components. How do you assess their suitability for avionics applications ?

Answer : J.M. BRICE

I have forgotten on purpose, since I think that everything on that topic has been said in the former session.

However I do not think that high T_c superconductors will have any significant practical impact in the coming 5 or even 10 years, except maybe for high frequency interconnections with low densities of current.

MICROWAVE AND MILLIMETER WAVE COMPONENTS
PERFORMANCES, PERSPECTIVES AND APPLICATIONS TO AVIONICS

by
Pierre BRIERE, THOMSON COMPOSANTS MICROONDES
Dominique PONS, THOMSON-CSF LCR
Domaine de Corbeville - 91401 ORSAY Cedex
France

1. Summary

Significant advances in microwave and millimeter-wave three-terminal devices have been obtained in the last few years, leading to impressive performance improvements in noise figure, power gain, and power output up to 100 GHz.

Significant improvements in materials growth, heterojunction device structures and processing technology have resulted in noise figure as low as 1.4 dB and power output in excess of 50 mw, both at 94 GHz.

In addition, the emergence of HBT based MMIC's opens new possibilities for high power and high efficiency circuits, low phase noise VCO and others.

In this paper we review the different types of these advanced devices and focus on their performance characteristics in low noise and power applications.

Potential applications of such devices with their specific advantages in electronic airborne equipment will also be tentatively covered.

2. Introduction

In the last five years, two major trends have been observed in the field of compound semiconductors. One is the intensification of efforts towards better Gallium Arsenide device and manufacturability and industrialization (in most cases under financment from government agencies). The second trend can readily be observed by the quantity of published papers on III-V semiconductor. Development on what can be called "Advanced Devices" (as opposed to standard MESFET based MMIC) has really been impressive in the last two years since published values of the two usual frequency merit factors, Ft and Fmax have more than doubled.

The basic requirements of system people concerning performance of three-terminal solid state components are the following :

. In general : They ask for an increase in the maximum frequency operation of the device since, in that case, it will work better even at a lower frequency, with higher performance and possibly higher reliability.

. For receivers : A decrease of the noise figure and an increase of the associated gain at the specified frequency is required.

. For transmitters : It is important to increase the power output, the power gain and the power added efficiency.

How such performance improvements are made possible is illustrated on the diagram of Figure 1.

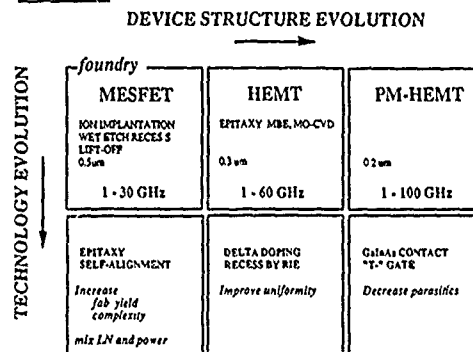


Figure 1

Today, commercial or even captive foundries are offering performances only up to 20 GHz. They are mostly using GaAs MESFET technology with implanted active layers, and a 0.5 µm gate length process. Most of them are using wet etch techniques for the recess step. Some technological evolutions are however under way : use of epitaxial material leads to improved performance, possibly going up to 30 GHz. Self alignment techniques under development will increase the circuit yield on wafer and bring some additional advantages of device performance. Technological processes able to combine power circuits with small-signal and even logic circuits are under development. However it is not expected that pure MESFET based MMIC's will have significant impact of frequencies above 30/40 GHz (i.e. in the millimeter wave range) since the gate length reduction under 0.3 µm which is necessary to go higher in frequency cause detrimental "short channel effects" with a rapid increase of the parasitic elements, which in turn will result in lower than expected Maximum Available Gain (MAG).

Reduced "short channel effect" is one of the key advantages of heterostructure FETs commonly called HEMT or MODFET or TEGFET (Figure 2).

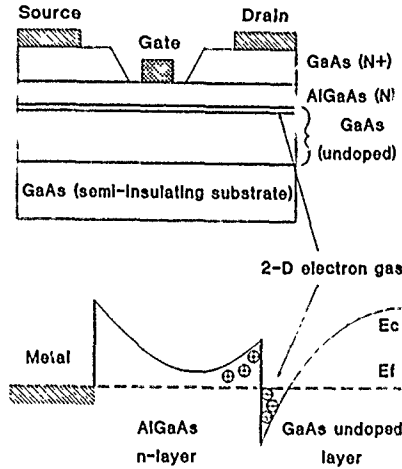


Figure 2

With these devices, the combined technological and device structure evolution have resulted in useful operation up to 100 GHz. These improvements (as mentioned in Figure 1) concern those which have a primary effect on device-to-device and wafer-to-wafer uniformity :

- i) dry etching using low damage reactive ion etching,
- ii) planar doping which gives better threshold voltage uniformity and reduces the so-called "DX center" density.

Another type of technological improvements have permitted an impressive progression of the F_{max} value on these HEMT structures. Lower source contact and access resistance, R_s , has been obtained through the use of an epitaxial GaInAs doped contact layer. Similarly, the T gate (or mushroom gate) technology has maintained the resistance of gate fingers, R_g , at reasonable values though the reduced gate length.

All these improvements are explicitly shown on Table 1 which summarizes the state of the art values of the two commonly used factors of merit of three-terminal devices : F_t and F_{max} (*).

F_t and F_{max} - state of the art - 2 Q 1990

device type	substrate	L_g (um)	F_t (GHz)	F_{max} (GHz)	Company
MESFET	GaAs	0.2	75	130	SEVERAL
HEMT	GaAs	0.25	90	230	GE
PM-HEMT	GaAs	0.15	150	350	G.E., HUGHES, ...
LM HEMT	InP	0.15	185	405	G.E., HUGHES, VARIAN
HBT	GaAs	12 (LE)	105	210	NTT, ROCKWELL

Table 1

(*) F_t is the cut-off frequency of current gain $|h_{21}| = 1$
 F_{max} is the frequency where the power gain falls to unity.

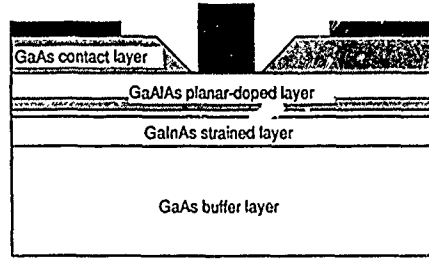
3. HFET devices

Under the generic name of HFET, for Heterostructure Field Effect Transistors (including HEMT, MODFET, TEGFET), we can find a rather large variety of devices which can be classified according to :

- . the substrate material which is either GaAs or InP,
- . the active channel material which can be doped or undoped and which can be made either of a material system where lattice is matched to the substrate (same lattice constant) or with a material system having a different lattice constant which, in this case, is strained with respect to the lattice substrate. Such a structure is called "Pseudomorphic".

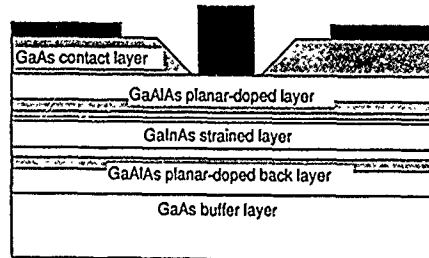
. Additionally there could be devices with more than one very closely spaced heterojunction leading to devices having a M.Q.W. (Multiple Quantum Well) structure.

Some Basic HFET structures are shown on Figures 3 to 6.



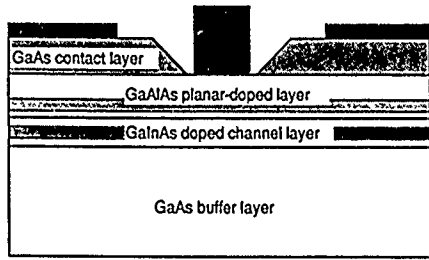
Planar-doped PM-HEMT

Figure 3



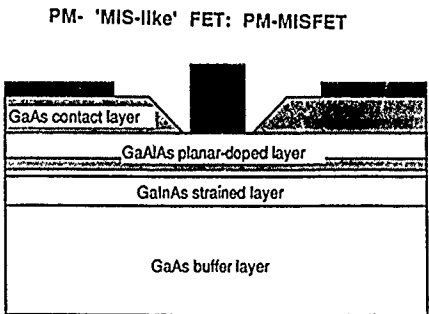
Double heterojunction (DH-) PM-HEMT

Figure 4



Doped channel (DC-) PM-HFET

Figure 5



PM- 'MIS-like' FET: PM-MISFET

Figure 6

With the growing experience in pseudomorphic epitaxial material technology, work on conventional GaAs HEMT has been reduced and emphasis has been put on the GaInAs channel material system.

The main advantages of this material as compared to GaAs are the following :

- . Higher low-field mobility,
- . Higher saturated velocity,
- . Higher charge transfer density (Ns),
- . Better electron confinement in the active channel giving rise to reduced short channel effects.

The higher the Indium fraction, the more pronounced these properties are. On InP substrate the indium fraction, for a lattice-matched growth, is 53% for the best achievable transport properties, and today, the lowest noise figures are obtained with this material system. With a GaAs substrate the growth of GaInAs is pseudomorphic and there is a maximum Indium fraction that can be incorporated without deleterious material defect densities. This limit is in the 25% - 35% range.

4. Low noise devices : state of the art
Noise figure of discrete devices

Using the well known FUKUI formula

$$F = 1 + Kf/ft \cdot (Gm Rs + Rg)^{1/2}$$

we can see that there is a linear relationship between the noise figure F and the frequency f, for a given device. We have drawn, on Figure 7, using a linear scale, the dependence of noise figure versus frequency for the different types of devices. The advantage of using GaInAs material on an InP substrate is clearly shown. Impressive noise figures of 1.4 dB at 93 GHz and 0.8 dB at 60 GHz have been obtained. Use of pseudomorphic GaInAs on a GaAs substrate results in something like 0.5 to 1 dB noise figure degradation compared to the previous results.

NOISE PERFORMANCES OF MM-WAVE FETs

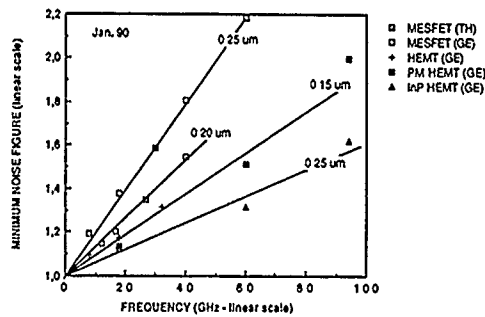


Figure 7

In Table 2 are given the most significant results of noise figure together with associated gain for the different device structures. The results shown in Table 2, obtained on discrete, hybrid matched devices, have constituted the basis for an emerging new generation of millimeter wave monolithic integrated circuits (MWMIC).

Low noise HEMT devices - state of the art - 2 Q 1990

device structure	In %	Substrate	Freq (GHz)	NF (dB)	G _{max} (dB)	L _g (um)	Company
MESFET	0	GaAs	40	1.9	6.5	0.2	THOMSON MA 89
HEMT	0	GaAs	18	0.7	13.8	0.25	GE JUN 88
			60	1.6	6.4		
PM-HEMT	35	GaAs	18	1.65	15	0.15	GE JAN 90
			60	1.8	7.6		
LM-HEMT	63	InP	60	0.8	8.7	0.1	HUGHES JUN 89
			93	1.4	6.65	0.15	GE JAN 90
			95	-	12.6		

Table 2

Table 3 gives a survey of the more interesting circuits realized up to now.

HEMT-based MMIC state of the art - 2 Q 1990

device type	substrate	circuit	F (GHz)	Gain (dB)	Notes (dB)	L _g (μm)	Company
HEMT	GaAs	distributed	0.5-60	6.6	-	0.32	HP, Oct 89
HEMT	GaAs	LNA 1st	50-60	6	-	0.30	TH, Dec 89
HEMT	GaAs	LNA 1st	55-65	6.1	4.0	0.25	TRW, Oct
PM-HEMT	GaAs	LNA 4st	57-60	20.7	3.7	0.25	COMSAT JAN 90
PM-HEMT	GaAs	LNA 1st	43	6.7	1.32	0.10	VARIAN JUN 90
PM-HEMT	InP	distributed	5-100	5	-	0.10	VARIAN JAN 90
			94	6.4	-		

Table 3

5. Advanced millimeter wave power devices

The fabrication of power devices is probably the most challenging work for device engineers. Today much effort is still devoted to MESFET circuits using discrete in order to increase both the power*frequency product and improve the manufacturability.

In this paper we will examine some results obtained with FET and HEMT devices above 20 GHz.

When designing a power device, it is desirable to obtain the best trade-off between maximum current capability and maximum operating voltage. When first introduced, HEMT devices were not intended to be able to compete with MESFET for power applications. Breakdown voltages of HEMT could not exceed 5 - 7 volts since the AlGaAs doping levels had to be high for a good charge transfer, and maximum current density was in the 100 to 200 mA per millimeter of gate length as compared to 400 to 500 mA/mm for GaAs MESFET. The situation has changed with pseudomorphic devices and values as high as 750 mA/mm have been reported for both PM-HEMT on GaAs and 1000 mA/mm for InP HEMT. On the other hand with the technological advances made using planar doping and/or MIS-like FET structures shown on Figure 6, higher breakdown voltages are likely to be obtained.

The most significant results concerning the state of the art power devices are presented in Table 4. At present, results on MESFET devices are obtained using monolithic integration with one or several amplification stages, while results on HFET's are obtained on hybrid matched discrete devices. It can be speculated that, before long, power HEMT MMIC will appreciably advance the state of the art in output power in the millimeter wave region.

Discrete and MMIC power devices - state of the art - 2 Q 1990

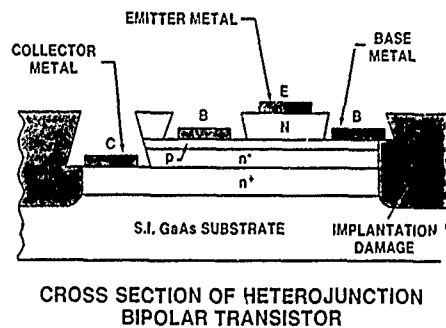
device type	F (GHz)	Power (W)	Gain (dB)	P.A.E (%)	L _g (μm)	W/mm	Company
MMIC 2st	28	0.68	6.2	15	0.6	-	TOSHIBA JUN 89
MMIC 1st	35	0.17	6	21	0.25	0.42	TEXAS SEP 89
MMIC 2st	42.5	0.175	6	22	0.35	-	COMSAT JUN 89
MMIC 1st	50	0.22	6	25	0.20	0.44	AVANTEK OCT 89
PM-HEMT	35	0.42	6	20	0.25	0.47	GE JUN 91
Discrete	44	0.78ed	5.1	41	0.25	0.79	
DM-PM-HEMT	60	0.125	6.6	32	0.15	0.83	GE DEC 91
Discrete	84	0.087	3	16	0.15	0.38	

Table 4

6. Heterojunction Bipolar Transistors (HBT)

Although the principles of operation of HBT have been known for years and the experimental work was started early in the seventies, usable microwave devices have only been realized in the last few years.

When looking at the cross section of an HBT and at its materials structure, (Figures 8 and 9), it can be seen that the successive constitutive layers can only be grown using a very high quality epitaxial deposition process (MBE or MOCVD), able to ensure precise thickness and doping control of each layer, and sharp interface between layers, with high uniformity. Similarly, a sophisticated processing technology is required in order to realize the connections of the three electrodes of the transistor as well as those of on-chip passive matching circuits.



CROSS SECTION OF HETEROJUNCTION BIPOLAR TRANSISTOR

Figure 8

	COMPOSITION	THICKNESS (Å)	DOPING (cm ⁻³)
CAP	n ⁺ GaAs	750	1 × 10 ¹⁹
EMITTER	n ⁺ GaAs	1250	5 × 10 ¹⁷
BASE	n ⁺ Ga _{0.7} Al _{0.3} As	2500	5 × 10 ¹⁷
COLLECTOR	p ⁺ GaAs OR InGaAs	500-1000	5 × 10 ¹⁶ - 1 × 10 ¹⁷
BURIED n ⁺	n ⁺ GaAs	5000	3 × 10 ¹⁸
SUBSTRATE	n ⁺ GaAs	4000	4 × 10 ¹⁸
	EMULATOR GaAs		

Figure 9

Much work in the experimental field has now improved the control of HBT technology, and full exploitation of the advantages of these devices is now possible.

Compared to the MESFET, the major advantage of the HBT is that it allows a much higher power density (expressed in terms of watt per mm of emitter periphery to be compared with watt per mm of gate width in MESFET case : the figures are 4 W/mm and 1W/mm.

This is due to the fact that, owing to vertical transport of the electrons, the current density is higher, and that the P-N collector-base junction can sustain higher breakdown voltage than the Schottky drain gate junction of MESFET. A very important requirement of high power amplifiers, especially in the case of airborne equipment, concerns the power added efficiency (PAE). This PAE being limited to less than 50% in class A operation, it is important to have devices able to work properly in class AB or B (especially in pulsed conditions). The major advantages of HBT will probably be found in such an application. This is supported by the fact that silicon bipolar at 3 GHz is able to deliver 100 Watts under 10% duty cycle with efficiencies of 50-70% while the GaAs PET is limited, even at 4 GHz, to the 20W/30W level with efficiencies of 30 - 40%. The higher frequency capability of GaAs HBT versus Si Bipolar, in conjunction with its high power capability, should be expected to lead to new devices able to deliver power output from C to Ku band above the MESFET state of art, with high power added efficiency.

Today major results on X band power HBT are summarized in Table 5.

X-band HBT CW Power Performance

Mode	Number of Emitter Fingers	Power (W)	Gain (dB)	W/mm	PAE
Common Base	5	0.3	6.1	3.0	36
	10	0.75	6.2	3.8	31
	20	1.42	6	3.6	31
	41	2.9	5.2	3.5	31
Common Emitter	10	0.6	5.9	3.0	41
	20	1.2	5.9	3.0	40
Monolithic (CE)	20	1	5.8	2.5	40
	60	2.5	6.1	2.1	39
	100	4.3	4.3	2.15	32
	120	5.3	4.3	2.2	33

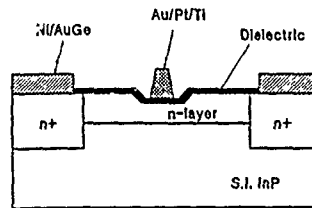
B. BAYRAKTAROGLU TEXAS EMCS SEPT 83

Table 5

7. Other Miscellaneous Power Devices

A review of power three-terminal solid state devices should make a short mention of two outsiders which could eventually have an impact in power applications.

There are the Indium Phosphide MISFET (Figure 10) and the Gallium Arsenide Permeable Base Transistor = PBT (Figure 11).



High power InP MISFET structure

Figure 10 PERMEABLE BASE TRANSISTOR

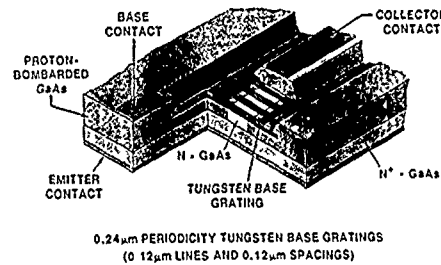


Figure 11

Both devices are still in their stage of feasibility experiments. Although both have relatively simple structures compared to the HBT or PM HEMT, they suffer however from a critical step in their process which still must be mastered. That challenge of PBT is to grow a high quality epitaxial layer on a metal grating. That one of MISFET is to grow a reproducible and a stable dielectric insulator, with a well-controlled low density of surface states between the gate metal and the semiconductor surface.

The InP MISFET is a potential candidate for high power sources from C band to Ka band and would take advantage of the better thermal conductivity of InP (compared to GaAs).

On the other hand the potential interest of the PBT is primarily for power and, may be, low noise amplification in millimeter wave frequency range.

Discussion

Paper n°2

Question : Mr. AL JELALIAN (Raytheon, Author)

Many system applications need power levels from 1 to 10 watts in the 35 GHz to 94 GHz region. What is the potential to achieve this in the future ?

Answer : Mr. P. BRIERE

There is a theoretical $P \times f^2$ (power x frequency square) limit on the power that can be delivered by a single device (at a given impedance level). From that limit, it can be deduced that about 1,5 watt at 35 GHz and 200 mW at 94 GHz are achievable on a single device.

With monolithic integration, it should be possible to build prototype of solid state amplifier able to deliver power levels of several watts at 35 GHz and maybe 1 watt at 94 GHz within the next 5 to 10 years.

Question : D.V. MERCY (THORNEMI, U.K.)

With regard to the low noise devices, do you have any information on performance degradations, due to pulse overloads, that could occur in the receiver of a T/R system of a radar.

Answer : Mr. P. BRIERE

What has been reported, to my knowledge, is a delay time or a low response of the front end device in response to pulse overloaded signals, making the receiving function degraded during hundred of ns to few μ s. This effect may be related to surface trapping effects in the device, induced by the overload and are probably related to non-mature technology. There is a controversy whether HEMT are more sensitive than low noise MESFET.

In general case, overload surge capability is a potential problem for low noise microwave FET if non especially designed devices, with unadequate gate process technology, are used in radar receiver applications. Overload capability should be taken into account when designing the device, according to the precise requirements.

Multiple Quantum Well NIR Optical Modulators
 - A Review of the Potential for Optical Signal Processing using III-V Semiconductors

by

David R P Guy, Dan D Besgrove & Norman Apsley
 DPI Division
 Royal Signals & Radar Establishment
 St. Andrews Road
 Malvern
 Worcs.
 WR14 3PS
 UK

SUMMARY

The potential for the use of optical and electro-optical techniques in information processing has been recognised for some time, but the field is only now reaching the stage of maturity when demonstration systems can be assembled. This paper reviews the potential for electro-optic modulators in III-V compound semiconductors to form the basic components within optical signal processing systems, particularly small fast electrically-driven spatial light modulator arrays operating in the near infrared for optical interconnect applications. Emphasis is on the use of artificially-layered "Low Dimensional Structures"; GaAs-Al_xGa_{1-x}As, in which modulation in excess of 20dB has been reported at 850nm, and In_{0.53}Ga_{0.47}As-InP, in which devices which should produce similar modulation at the optical fibre wavelengths of 1.3 and 1.55μm are proposed and the performance of a 5 × 5 spatial light modulator operating at 1.6μm is described.

PREFACE

There are potentially enormous speed advantages to be gained in replacing conventional electronics with optical or electro-optical parallel processing in a variety of information processing systems. The advantages, which come from the parallelism offered by optical systems, are achieved at the expense of greater complexity.

The ultimate aim of optical processing technology, a fully optical digital computer perhaps using a neural network approach, is some years away, but simple electro-optic processors and optical logic gates have been constructed from III-V semiconductors. AT&T Bell Laboratories has recently demonstrated the first digital optical processor of any real complexity, comprising four 32-pixel arrays interconnected via free space¹. The initial applications of optical and electro-optic processing are likely to be in optical interconnect, for example in chip-to-chip communications within a computer, in the distribution of signals around a local area network (e.g. within an aircraft) or in the transmission of information down an optical fibre link from a remote sensing system. It is

in these latter applications that the effective immunity from electro-magnetic interference or eavesdropping provided by the optical fibre may be an important consideration.

A key component of optical information processing systems is the spatial light modulator (SLM). This is a two-dimensional array of individually addressed pixels by means of which information can be impressed on optical "carriers". Light beams incident on each pixel may be independently intensity (or phase) modulated by the application of appropriate electrical biases to the individual pixels. In this way information may be transmitted in a massively-parallel configuration, either through free-space or an optical fibre link, to be detected and interpreted by a 'remote' receive station. Each pixel within the SLM is therefore an intensity or phase modulator, operating in transmission or, in certain intensity modulation configurations, in reflection. The pixels (or mesas) are sometimes referred to as light valves. When formed from III-V semiconductors, they operate over a finite wavelength range in the near infrared (NIR) using either the electro-optic effect itself or the mathematically-related band-edge electro-absorption.

This paper reviews the current status of both individual electro-optic modulator pixels formed from III-V compound semiconductors and the 2-D SLM arrays which have been fabricated in this materials system, with particular emphasis on the aims and achievements of the RSRE programme. Much of the recent impetus for the continued development of such components has come from the improvements in performance gained by using 'Low Dimensional Structures'. These structures are introduced, then devices employing them are described. First single pass transmission modulators, including the RSRE InGaAs-InP 5×5 SLM² are considered, then methods of modulation enhancement using resonant structures are outlined^{3,4}, including that which is possible by exploitation of the zero-reflection condition of an asymmetric Fabry-Perot etalon⁵. The scope for extension to other wavelengths is briefly discussed.

Spatial light modulator technology is better developed in liquid crystals than in the III-V semiconductors which are being considered here, but the potential for III-V devices to operate in the NIR at room temperature at high speeds - microwave frequencies of at least 20GHz and probably over 100GHz - with low switching power makes them of considerable interest. Liquid crystal SLM's of 128×128 pixels on a $1.65 \mu\text{m}$ pitch have been produced with 23dB of contrast, an extinction which III-V modulators will be hard-pressed to match over such an array.

OUTLINE

The paper is organised as follows:-

1. III-V Semiconductors and the Electro-Optic Effect
 - a) Low Dimensional Structures
- "Bandgap Engineered" Materials
 - b) Quantum Well Absorption
 - c) Electro-Absorption in Quantum Wells:
The "Quantum-Confined Stark Effect"
2. Electro-Optic & Electro-Absorptive III-V Semiconductor Modulators
 - a) Transmission Modulators
 - b) Modulation Enhancement Techniques
 - c) Fabry-Perot Reflection Modulators
 - d) SLM Technology
 - e) Performance Considerations
3. Conclusions

1. III-V Semiconductors and the Electro-Optic Effect

Unlike the elemental semiconductor silicon, the III-V semiconductors with which this paper is concerned are compounds, formed between a metallic element from Group III of the periodic table (Al, Ga or In) and a Group VB element (P, As or Sb). The compound thus formed is isoelectronic with silicon and is semiconducting, that is it possesses a forbidden energy range or 'gap' between the highest occupied electronic states and the lowest unoccupied states. The energy gap (at room temperature) varies with materials system from 170meV in InSb through the 1.42eV of GaAs to 2.26eV in GaP, giving cut-off wavelengths of $7 \mu\text{m}$, 873nm and 550nm respectively. This gap effectively prevents electrical conduction from occurring in "pure" material (strictly only true at absolute zero of temperature) and prevents light of wavelength longer than the cut-off from being absorbed, leading to an absorption edge (or onset) at the cut-off wavelength. It is the effect of an electric field on this edge which forms the basis of the devices under consideration in this paper.

Certain of these III-V semiconductors, GaAs and InP for example, may be produced in large cylindrical single crystals, some inches in diameter. The active layers under consideration in this paper are normally less than $10 \mu\text{m}$ thick and are grown by an epitaxial technique upon a slice cut from such a single crystal, 2" or greater in diameter and ~ 0.3 - 0.4mm in thickness.

The electro-optic effect is a change in the real part of the refractive index of a material in an applied electric field. It is always accompanied by electro-absorption, a change in the absorption coefficient and the imaginary part of the refractive index (the Franz-Keldysh effect). The mathematical relation between the two effects is described by the Kramers-Kronig relations. Most of this paper is concerned with electro-absorption modulators, but in certain geometries the electro-optic effect has been used to good effect.

GaAs has a non-centrosymmetric crystal structure and possesses relatively large electro-optic coefficients⁶, both linear and quadratic, and strong associated electro-absorption⁷. The coefficients are large enough to be used at room temperature in any optical signal processing application in which a 1-D array is sufficient. The electro-optic effect can then be used in waveguide (horizontal)

geometry with interaction lengths from $100\mu\text{m}$ to over 2mm to give substantial phase modulation at relatively low voltage. RSRE has recently demonstrated 'PHAROS'⁸ (phased array optical switch), a GaAs beam-steering device which works on this principle at $1.06\mu\text{m}$ wavelength. Alternatively the change in absorption coefficient of order 2000cm^{-1} may be employed in similar geometry to give high-contrast intensity modulation ($>20\text{dB}$) with less than 0.3dB insertion loss over a narrower wavelength range ($\Delta\lambda\sim 25\text{nm}$) on the long wavelength side of the fundamental band-gap of 870nm ⁷. In perpendicular (surface-normal) configuration, modulation approaching 3dB has been achieved in a $2\mu\text{m}$ active thickness bulk GaAs device⁹.

In the perpendicular geometry which is required for 2-D arrays for SLM applications, the shortened interaction lengths mean that the enhanced absorption and electro-absorption properties of 'low dimensional' III-V semiconductor structures such as multiple quantum wells (MQW's)¹⁰ are required to give low voltage switching with viable modulation contrast ratios.

a) Low Dimensional Structures - "Bandgap Engineered" Materials

Modern epitaxial growth techniques enable III-V semiconductors to be deposited on a suitable substrate essentially one atomic monolayer at a time¹¹, introducing the ability to change composition abruptly between one layer and the next; thus precise artificially-structured materials may be constructed with length scales in the growth direction ranging from one atomic monolayer (2.63\AA in GaAs) upwards, and typically of order 100\AA (around 40 monolayers). Such materials have a two-dimensional character due to the compositional modulation in the growth direction.

The growth of these "Low Dimensional Structures" is on a semiconductor substrate with the same lattice spacing as the materials being deposited, a typical substrate being of 2" diameter. Typical III-V semiconductor systems are $\text{In}_{0.53}\text{Ga}_{0.47}\text{As}$ with its lattice-match InP (grown on InP) and the $\text{Al}_x\text{Ga}_{1-x}\text{As}$ system (grown on GaAs) in which there is less than 0.05% mismatch between the extremes AlAs and GaAs. If the grown layers differ in lattice spacing from each other and/or from the substrate a "strained layer" results. This in itself leads to interesting new properties¹², but these must remain outside the scope of this paper.

If two semiconductors of different band-gaps are deposited in this way on the scale of about 40 atomic layers (100\AA) of each composition, conduction band electron and valence band hole states become confined within the 2-D planes of the narrower gap material, the "Quantum Well", by the potential barrier presented by the wider gap material. The carriers are free to move within the planes. The confinement, on the spatial scale of the electron wavefunction, leads to quantum effects, in particular discrete energy sub-bands in the narrower-gap material with respect to transport perpendicular to the layers. This is essentially a realisation of the quantum mechanical particle-in-a-box model.

RSRE possesses state of the art growth capability in both the III-V semiconductor systems described above, although the modulator work has focussed on $\text{In}_{0.53}\text{Ga}_{0.47}\text{As-InP}$. GaAs- $\text{Al}_x\text{Ga}_{1-x}\text{As}$ is grown by the UHV technique of molecular beam epitaxy (MBE)¹³ and InGaAs-InP is grown by the technique of metal-organic chemical vapour deposition (MOCVD)¹⁴, also called metal-organic vapour phase epitaxy (MOVPE). The two materials systems are hereafter referred to as GaAs-AlGaAs and InGaAs-InP for simplicity.

The quantum well is illustrated schematically in Figure 1, which also shows the versatility of the structure in having the potential to operate in a number of different wavebands. The particular energies of each of the transitions may be further tailored to suit specific device requirements in a number of ways, in particular the NIR 'interband' transition moves strongly to higher energy as the width of the well is decreased. In the InGaAs-InP system the interband transition may be tailored from $1.6\mu\text{m}$ in InGaAs to less than $1.3\mu\text{m}$ in wells of the lattice-matched quaternary system $\text{In}_{1-x}\text{Ga}_x\text{As}_y\text{P}_{1-y}$ (where $y=2.197x$)¹⁵. It is this ability to determine the bandgap at the time of crystal growth that is sometimes termed 'bandgap engineering', and is a particular feature of MQW systems.

The modulators described here are configured as PIN diodes (Figure 2), with the active MQW structure within the undoped (intrinsic) region. An applied reverse bias will then generate a high static field within the intrinsic region (up to $4.5\times 10^5\text{Vcm}^{-1}$ before breakdown in the best RSRE samples). A typical sample has a $1\mu\text{m}$ intrinsic region and would thus require 10V bias to generate a typical operational field of 10^5Vcm^{-1} . Where resonant Fabry-Perot structures are required,

the high-reflectors (and anti-reflectors) can be grown into the structures using quarter-wavelength stacks of suitable semiconductors^{16,17} and the dopants may be incorporated in these regions.

b) Quantum Well Absorption

Here we are particularly concerned with the NIR transitions in the two materials systems mentioned above; GaAs-AlGaAs which has particularly strong MQW absorption¹⁸, and is in many ways the ideal system for demonstration of quantum well effects, and with InGaAs-InP¹⁹⁻²¹. Typical MQW absorption spectra of these systems are shown in Figure 3. These spectra, in common with all others in this paper, were taken at room temperature using a lamp and monochromator system. Particular features of the MQW absorption are that the confined states provide high, well-defined excitonic absorption peaks at the NIR energies of the transitions between the confined electron and hole sub-bands, and that these peaks persist to room temperature. (There are two closely-spaced peaks because there are two valence band hole states with differing effective masses at slightly different energies.) It is the lowering in the transition energies (the red-shift) of these peaks in an electric field which produces the large changes in absorption coefficient at band-edge energies which make the MQW structure attractive for electro-optic modulation.

There are three differences to note between the spectra from the two materials systems. 1) The inter-band absorption edges at which the electro-absorption effects occur are at quite different NIR wavelengths in the two systems, namely around 850nm in GaAs-AlGaAs and 1.55-1.6 μ m in InGaAs-InP. InGaAs-InP is therefore compatible with the low-loss point of fibre-optic systems and, if the quaternary alloy InGaAsP is used, compatibility with the zero-dispersion point at 1.3 μ m is possible¹⁵. 2) In GaAs-AlGaAs the GaAs substrate material is the narrow band-gap component and thus the substrate is opaque at the wavelengths of modulation and must be etched off in any transmission device, a non-trivial process, whereas InGaAs-InP is grown on InP, the wide-gap constituent, which is effectively transparent. 3) The GaAs exciton provides a very high absorption coefficient, up to 12000cm⁻¹ (averaged over equal thicknesses of well and barrier material), whereas the maximum coefficient at the excitonic absorption in InGaAs is of order 4000cm⁻¹, not much enhanced over the bulk absorption edge. The InGaAs-InP system, therefore, does not exhibit

the same strength of electro-absorption as GaAs-AlGaAs.

c) Electro-Absorption in Quantum Wells: The "Quantum-Confined Stark Effect"

The electro-optic effect in QW's is quantitatively different from the Franz-Keldysh effect in bulk semiconductors since it is primarily the effect of the electric field on the confined excitonic state. It has been termed the 'Quantum-Confined Stark Effect' (QCSE)¹⁸. As can be seen in absorption in Figure 4, it is characterised by a shift of the excitonic absorption to lower energy with some loss of absorption peak height. Changes in absorption coefficient of 3000cm⁻¹ have been obtained in RSRE's InGaAs wells²¹ and in GaAs changes of 6000cm⁻¹ have been reported^{18,22}. The electro-absorption is accompanied by an electro-optic change in the real part of the refractive index. This is illustrated in the RSRE model of GaAs refractive index³ in Figure 5. The electro-optic properties of QW's have not been extensively studied and are given only this briefest of mentions here, although they are potentially of considerable device importance.

2. Electro-Optic and Electro-Absorptive III-V Semiconductor Modulators

a) Transmission Modulators

In their simplest form the modulators are operated as non-resonant (single-pass) transmission devices. Here we consider modulators in which no attempt has been made either to enhance or suppress the weak Fabry-Perot resonant cavity which is naturally formed between the front and rear surfaces of the epitaxial material.

i) GaAs-AlGaAs Modulators:

The large absorption coefficient changes in GaAs have enabled 10dB modulation with 11dB insertion loss, i.e. modulation between 0.8% and 8% transmission (0-20V bias), to be obtained with a 4 μ m-thick 200-repeat QW structure²² (this is to be contrasted with a typical MQW sample of 32 or 50 repeats).

Additionally the sharpening and consequent increase in maximum absorption coefficient of the excitonic feature in GaAs at low temperatures have enabled 30dB modulation with only 1.5dB insertion loss to be obtained from a 100 repeat structure at 4K²³. The same structure also gives almost complete

switching, between 95% and 0.17% transmission.

All the above modulation was obtained over fairly narrow bands (e.g. 2nm width), centred around 850nm (room temperature) and 803nm (4K).

ii) InGaAs-InP Modulators:

The transmission modulation of 4.1dB (4.9dB insertion loss) achieved in a $3\mu\text{m}$, 150-well RSRE sample is illustrated in Figure 6. This remains both the thickest InGaAs-InP MQW structure and the greatest modulation reported²⁴. However, the fact that 150 wells are required together with 40V to produce modulation which is very modest by GaAs standards illustrates very strongly the effect of the lower absorption coefficients in this materials system and points to the need for enhancement of the modulation using resonant structures.

Figure 6 also illustrates well the general form of the modulation obtained in single pass MQW QCSE modulators, namely that the strongest modulation (at the $n=1$ exciton) occurs in two distinct regimes. In the shorter wavelength regime the transmission increases with bias as the strong zero-field absorption at the peak of the exciton weakens - this regime generally gives the greater modulation in terms of contrast ratio. The longer wavelength regime exhibits a reduced transmission in the applied field as the excitonic absorption shifts into this normally low absorption regime. In general the percentage change in transmission is greater at these longer wavelengths.

It is also worth noting that the QW absorption coefficients in InGaAs-InP are not very much higher than those of bulk InGaAs and that the direct benefits of going to MQW structures are not as pronounced as in GaAs.

b) Modulation Enhancement Techniques

A variety of methods of enhancing the modulation obtainable from perpendicular geometry transmission and reflection modulators have been proposed based on the tuning of the reflection coefficients of front and back surfaces in order to either enhance or offset the weak Fabry-Perot resonant cavity naturally formed by the MQW region. A cavity is illustrated schematically in Figure 7.

The cavity-enhancement techniques involve the use of optical folding, i.e. double or multiple passes of light through the structure in a resonant configuration. This necessitates the use of at least a rear reflector (with or without a front anti-reflector) in the simplest

optically-folded device, and ultimately becomes a full high finesse Fabry-Perot etalon. The symmetric Fabry-Perot etalon has the potential to operate simultaneously in both transmission and reflection, but other resonant devices operate in reflection.

In order to offset the effects of the natural cavity, front and rear anti-reflection coatings are required²³. The transmission modulator thus produced should have lowered insertion loss but the contrast ratio of the modulation is not always increased²².

c) Fabry-Perot Reflection Modulators

i) Symmetric Cavity

A symmetric Fabry-Perot cavity, that is one in which the front and rear reflection coefficients are equal ($R_f=R_b$), exhibits a zero in reflection on resonance only if there is precisely zero absorption within the cavity. In the case of a semiconductor cavity with the substrate present (as is usually the case), the $R_f=R_b$ condition is satisfied with a lower number of repeats in the front quarter-wave stack than in the rear because the front air-semiconductor interface has higher reflectance than the interface between the rear stack and the semiconductor substrate.

The cavity may be operated in two modes: electro-optic mode, in which the wavelength of the resonance is altered on the application of the electric field, and electro-absorptive mode, in which the cavity absorption is switched on by the application of the field, leading to an increase in the reflectance at the resonant wavelength through a partial destruction of the cavity resonance. RSRE modelling has predicted substantial modulation in both modes^{3,4} using relatively few wells and low voltage, and the potential for switching transmitted and reflected signals simultaneously (Figure 8). Transmit/reflect devices should have an important role to play in optical signal processing systems. A disadvantage of resonant structures is that as the structure becomes increasingly resonant the band of wavelengths over which the modulation occurs becomes narrower: the advantages of modulation enhancement must be balanced against this disadvantage in any potential application.

The fact that the cavity absorption is not precisely zero even some distance from the onset of the MQW absorption means that full high-contrast modulation (i.e. modulation with a zero in reflection in one of states) cannot be achieved in a symmetric MQW cavity. High contrast modulation can, however, be obtained

in an asymmetric cavity which, because of its complexity and potential importance, is dealt with in detail in the next section.

ii) Asymmetric Cavity

Under certain conditions a zero in reflectance may be obtained from an absorptive, asymmetric Fabry-Perot cavity. This entirely general result has recently been applied to GaAs-AlGaAs MQW modulators^{5,25}. A low front reflection coefficient is used in conjunction with a high rear reflection coefficient to form the asymmetric cavity. The zero in overall reflectance may then be obtained by balancing the front and rear reflection coefficients of the cavity through the introduction of a controlled amount of cavity absorption. The QCSE in an MQW structure is a convenient method of introducing such absorption: operating at a wavelength slightly greater than that of the onset of the zero-field $n=1$ excitonic absorption, the application of an electric field lifts the absorption coefficient from a low value through that required for the $R=0$ condition, providing high reflectance in zero-field and $R=0$ at high field. In excess of 20dB contrast has been obtained in a GaAs-AlGaAs MQW asymmetric reflection modulator²⁵.

The general result for the reflectance of an absorptive cavity on resonance²⁶ is

$$R = R_f \left[\frac{1 - (R_\alpha/R_f)}{1 - R_\alpha} \right]^2 \quad (1)$$

$$\text{where } R_\alpha = \sqrt{R_f R_b} e^{-\alpha d} \quad (2)$$

It may be seen from (1) that the cavity exhibits a zero in reflectance when $R_\alpha = R_f$, i.e. when the effective reflection coefficient of the rear reflector, when viewed from the front reflector through the absorber, is equal to R_f . Thus the cavity is made effectively symmetric by the presence of the absorber. Setting $R_\alpha = R_f$ reveals the condition required for zero reflectance:

$$\alpha d (R=0) = 0.5 \ln(R_b/R_f) \quad (3)$$

The analysis of the asymmetric cavity is begun by choosing a high (but easily attainable) value of rear reflection coefficient, $R_b=0.95$. A high R_b is required to give acceptably low insertion loss. We now examine the modulation performance of the cavity for a range of front reflection coefficients, R_f , to determine the most suitable for use with the particular absorption characteristics of different materials.

Figure 9 shows the calculated reflectance of the cavity as a function of cavity loss (αd) for structures of varying asymmetry. At the two extremes are curves (a) and (e), for R_f of 0.005 and 0.95 respectively. The former is essentially an anti-reflection coated cavity which gives a reflectance which falls slowly with increasing cavity loss and, if the AR coating is perfect, no $R=0$ condition. The latter is the high finesse symmetric etalon which has been discussed earlier.

iii) Variations on Asymmetric Cavities

Curve (b) of Figure 9 shows the case for $R_f=0.3$ as initially proposed⁵ and used experimentally^{25,27}. The precise zero of reflectance occurs at $\alpha d=0.58$, but the reflectance remains below 1% from $\alpha d = 0.46$ to 0.72. Thus the $R_f=0.3$ structure will tend to be relatively insensitive to growth irregularities and to small variations in electric field across the active region, but at the same time the $R=0$ condition occurs at an αd value attainable in MQW GaAs-AlGaAs. These are the peculiar strengths of this strikingly simple modulator design in which the front reflectance is provided by the natural $R \sim 30\%$ of the front air-semiconductor interface. It has limitations, however, and these become severe when using active materials with relatively low absorption coefficients. For example in InGaAs-InP some 145 quantum wells of $\alpha_{\max}=2000\text{cm}^{-1}$ would be required to give high-contrast modulation.

Curve (c) illustrates a slightly less asymmetric case where $R_f=0.52$. The required value of αd for $R=0$ has reduced to 0.30 at the expense of higher insertion loss when $\alpha d=0$. The great advantage of this intermediate asymmetry structure is that it brings the high-field $R=0$ condition within the range of lower loss cavities, for example 75 InGaAs-InP wells would suffice: this has recently been proposed by RSRE as a useful variation on the $R_f=0.3$ cavity²⁸.

iv) Variations on Symmetric Cavities

Consider now the symmetric case where $R_f=R_b=0.95$, curve (e). As mentioned above, in order for $R=0$ to be achieved there must be absolutely no residual absorption within the cavity at zero-field. It appears that this will prove to be a serious problem in fully-symmetric cavities.

It is possible to achieve high-contrast reflection modulation, with $R=0$ attained at low values of αd (and therefore low drive voltage), despite having residual absorption in zero-field. This is accomplished by making the cavity slightly asymmetric ($R_f < R_b$), as shown in

curve (d) in Figure 9 where $R_f=0.82$. Now the $R=0$ condition is satisfied at a low, non-zero value of cavity loss ($\alpha d=0.07$) and the reflectance increases with voltage from the zero. The $R=0$ condition may occur either at zero or very low field, and it may be necessary for a small voltage to be applied to attain $R=0$, possibly forward bias to offset a part of the built-in field of the *pin* diode. The insertion loss in this mode is determined by the high-field value of the reflectance. In curve (d), 10dB insertion loss is achieved at $\alpha d=0.16$, 5dB at $\alpha d=0.32$ and 3dB at $\alpha d=0.55$.

The slightly asymmetric cavity is therefore able to fully accommodate some residual cavity absorption in the $R=0$ state, and the insertion loss is determined by the high-field cavity absorption. This has been proposed by RSRE as a method of overcoming residual absorption problems in high-finesse symmetric etalons²⁸.

v) Reflectance Spectra of InGaAs-InP Asymmetric MQW Modulators

The results of the foregoing analysis are now demonstrated in modelled spectra of InGaAs-InP MQW modulators. Figure 10 shows the results of modelling InGaAs-InP 75 repeat MQW structures. (a) shows the variation on the asymmetric cavity with $R_f=0.52$ and $R_b=0.95$, i.e. adjusted to suit InGaAs-InP MQW's, and so gives $R=0$ in the applied field. The modulation at 1650nm is between 33.3% and 0.05% - being the closest to zero achieved in this simulation. The contrast is >28dB and the insertion loss is 4.8dB, achieved at a predicted drive voltage of 14V. In (b) a variant on the symmetric cavity is shown. $R=0$ is attained in zero-field under the influence of the residual absorption with $R_f=0.82$ and $R_b=0.95$. Here modulation of >28dB contrast is predicted with 36.0% reflectance in the applied field; insertion loss 4.4dB. Note that the higher finesse in (b) narrows both the resonance and bandwidth of modulation.

A similar variation on the asymmetric cavity with MQW GaAs-AlGaAs should require only 39 wells and less than 5V since the αd requirement has been reduced from 0.58 to 0.30.

As the asymmetric cavities switch between reflecting and resonantly-enhanced absorbing states, they have considerable potential to operate as sensitive detectors, but equally when operating as modulators there is the possibility of unwanted heating within the device due to the optical power being absorbed.

d) SLM Technology: InGaAs-InP 5x5 SLM Array

RSRE material from the same growth run as that which produced the 4.1dB modulation described above has been processed by STC Technology Ltd., Harlow, UK, into the first monolithic SLM array in InGaAs-InP². Using a silicon oxynitride passivation technique, a 5×5 array of square pixels of 200 μ m linear dimension has been produced on a 400 μ m pitch. The substrate doping on this particular sample has limited the maximum transmission possible, and some of the pixels lost their electrical integrity during handling, but the electro-absorption characteristics of the eight pixels from across the array which it was possible to measure show good uniformity (Figure 11) and demonstrate the establishment of an SLM technology in this system.

GaAs-AlGaAs array technology includes a 6×6 array²⁹ and a 16×16 array comprising 8×16 transmission and 8×16 reflection elements³⁰.

e) Performance Considerations

Speed and Power Considerations

Since the QCSE is an electronic effect, it occurs on a very short timescale and consequently QCSE devices should operate at high frequencies. Measurement of operation at 5.5GHz in GaAs-AlGaAs using a 50 μ m diameter mesa³¹ and 5.3GHz in InGaAs-InP (40 μ m diameter mesa)³² have been reported. The 3dB roll-off point is determined by RC time constant rather than by the fundamental electro-absorption process which has been estimated to have a response time as low as 0.2psec³³.

The electrical drive power requirements of the device may be crudely estimated as $\frac{1}{2}CV^2$. The capacitance of a typical small device of say 25 μ m diameter with an intrinsic region of 1 μ m is less than 0.1pF and with switching at perhaps 2V applied bias, this implies an electrical switching energy of less than 1pJ.

The actual optical power handling capabilities are much less clear, certainly the absorption of MQW structures does saturate³⁴, but for practical purposes the limit may be set by the power absorption within the device and consequent temperature changes.

QCSE Modulators as Detectors

In the wavelength ranges in which the materials discussed here are absorbing, they are also good photodetectors. The photodetection

properties of the strong absorption in GaAs MQW's and its potential tunability have not been extensively studied, but an RSRE measurement of the response time of the photocurrent³⁵ suggests that MQW PIN detectors should operate well into GHz frequencies. The use of the same structure for detection and modulation opens possibilities of bidirectional data transmission using MQW structures, some of which have been demonstrated in GaAs³⁶.

All-Optical Switching in Quantum Wells

MQW's exhibit strong intrinsic optical bistability when placed in a suitable resonant environment³⁷, and hybrid optical switching devices involving electrical feedback - the co-called 'Self Electro-Optic Effect Devices' (SEED's) have been demonstrated in a variety of configurations³⁸. All-optical switching with pJ switching energy has been reported in both GaAs-AlGaAs³⁹ and InGaAs-InP⁴⁰.

GaAs on Silicon

The technology of growing GaAs devices directly onto silicon substrates is now being developed in order to exploit the obvious advantage of interfacing GaAs circuit elements directly onto silicon electronics. The best GaAs modulators thus grown have shown performance equal to those on normal GaAs substrates⁴¹. GaAs on Si technology will no doubt feature prominently in future generations of devices.

Extensions To Other Wavelengths

Materials systems which might provide electro-optic switching at other wavelengths are at a much earlier stage of development and many are strained layer systems. InAs coupled with the correct wide-gap partner might operate out towards 5 μ m, and there is scope for antimonide systems to operate at even longer wavelengths. There is an immense materials science effort directed at developing these and other systems. It will be interesting to see just what can be achieved in the medium infrared.

3. Conclusions

In this paper it has been shown that optical modulators and detectors based on MQW systems are likely to make a major impact in optical signal processing systems. In addition to their speed and low power requirements, one of their main strengths lies in the ability to determine the wavelength of operation at the time of growth by

specification of layer compositions and thicknesses. MQW modulators could therefore be individually matched to semiconductor lasers for example. Furthermore it is possible to integrate a laser and MQW waveguide modulator on the same wafer, separating the two using the ability of selective disordering of the MQW to define lateral structures in the wafer after growth.

Additionally MQW modulators will operate at high speed (this is also true of their bulk counterparts), at microwave frequencies certainly in excess of 20GHz, as they have low switching energies. Their switching voltages can be made compatible with semiconductor electronics voltages.

It is the potential for wavelength tunability of the modulation which gives MQW modulators distinct advantages over bulk semiconductor modulators, even in cases where the MQW electro-absorption is comparable with that in the bulk material.

References

1. see Photonics Spectra (February 1990) 16
2. Henshall GD, Greene PD, Bourne WO, Guy DRP, Besgrove DD, Taylor LL, Apsley N & Bass SJ; *Semicond. Sci. Tech.* 5 (1990) in press
3. Guy DRP & Apsley N; *SPIE Proc.* 861 (1987) 27-32
4. Guy DRP, Apsley N, Taylor LL, Bass SJ & Klipstein PC; *SPIE Proc* 792 (1987) 189-196
5. Whitehead M & Parry G; *Electron. Lett.* 25 (1989) 566-568
6. Kaminow IP; *An Introduction to Electrooptic Devices*, Holt, Rinehart & Winston (1976)
7. Wight DR, Heaton JM, Kier AM, Norcross RJ, Pryce GJ, Wright PJ & Birbeck JCH; *IEE Proc. Part J* 135 (1988) 39-44
8. Wight DR & Heaton JM; To be published. See also Bennion I & Walker R; *Physics World* 3 (Part 3, March 1990) 47-50
9. Wight DR, Allen PC, Trussler JWA, Cooper DP, Esdale DJ & Oliver PE; *Institute of Physics Conf. Ser.* 79 (1985) 667-672
10. Miller DAB; *Optical Engineering* 26 (1987) 368-372
11. Tsang WT, in *Semiconductors & Semimetals*, edited by WT Tsang (Academic Press, New York, 1985) Vol.22 Part A
12. Kothiyal GP, Hong S, Debar N, Bhattacharya PK & Singh J; *Appl. Phys. Lett.* 51 (1987) 1091-1093

13. Anderson DA & Whitehouse CR; RSRE Research Review 1985, pp136-141
14. Bass SJ, Barnett SJ, Brown GT, Chew NG, Cullis AG, Skolnick MS & Taylor LL; NATO ASI Ser. B:Physics 163 pp.137-150
15. Zucker JE, Bar-Joseph I, Miller BI, Koren U & Chemla DS; Appl. Phys. Lett. 54 (1989) 10-12
16. Guy DRP, Taylor LL, Bass SJ & Apsley N; Semicond. Sci. Tech. 2 (1987) 466-467
17. Simes RJ, Yan RH, Geels RS, Coldren LA, English JH, Gossard AC & Lishan DG; Appl. Phys. Lett. 53 (1988) 637-639
18. Miller DAB, Chemla DS, Damen TC, Gossard AC, Wiegmann W, Wood TH & Burrus CA; Phys. Rev. B, 32 (1985) 1043-1060
19. Bar-Joseph I, Klingshirn C, Miller DAB, Chemla DS, Koren U & Miller BI; Appl. Phys. Lett. 50 (1987) 1010-1012
20. Guy DRP, Besgrove DD, Taylor LL, Apsley N & Bass SJ; IEE Proc. Part J: Optoelectronics 136 (1989) 46-51
21. Guy DRP, Besgrove DD, Taylor LL, Apsley N & Bass SJ; Opt. Soc. Am. Technical Digest Series 10 (1989) 202-205
22. Hsu TY, Wu WY & Efron U; Electron. Lett. 24 (1988) 603-605
23. Bailey RB, Sahai R, Lastufka C & Vural K; Opt. Soc. Am. Technical Digest Series 10 (1989) 210-213
24. Guy DRP, Taylor LL, Besgrove DD, Apsley N & Bass SJ; Electron. Lett. 24 (1988) 1253-1255
25. Whitehead M, Rivers A, Parry G, Roberts JS & Button C; Electron. Lett. 25 (1989) 984-985
26. Miller A & Parry G; Optical & Quantum Electronics 16 (1984) 339-348
27. Yan RH, Simes RJ & Coldren LA; Appl. Phys. Lett. 55 (1989) 1946-1948
28. Guy DRP & Apsley N; IEE Colloquium Digest No: 1990/030 7/1-7/4
29. Livescu G, Miller DAB, Henry JE, Gossard AC & English JH; Optics Letters 13 (1988) 297-299
30. Bailey RB, Sahai R & Lastufka C; Opt. Soc. Am. Technical Digest Series 10 (1989) PD1-1 to PD1-4
31. Boyd GD, Bowers JE, Soccolich CE, Miller DAB, Chemla DS, Chirovsky LMF, Gossard AC & English JH; Electron. Lett. 25 (1989) 558-560
32. Koren U, Miller BI, Tucker RS, Eisenstein G, Bar-Joseph I, Miller DAB & Chemla DS; Electron. Lett. 23 (1987) 621-622
33. Wood TH, Burrus CA, Miller DAB, Chemla DS, Damen TC, Gossard AC & Wiegmann W; Appl. Phys. Lett. 44 (1984) 16-18
34. Miller DAB, Chemla DS, Eilenberger DJ, Smith PW, Gossard AC & Tsang WT; Appl. Phys. Lett. 41 (1982) 679-681
35. Manning RJ, Bradley PJ, Miller A, Roberts JS, Mistry P & Pate M; Electron. Lett. 25 (1989) 269-270
36. Wood TH, Carr EC, Kasper BL, Linke RA, Burrus CA & Walker KL; Electron. Lett. 22 (1986) 528-529
37. Miller A, Steward G, Blood P & Woodbridge K; Optica Acta 33 (1986) 387-396
38. Miller DAB; Surf. Sci. 174 (1986) 221-232
39. Jewell JL, Lee YH, Warren M, Gibbs HM, Peyghambarian N, Gossard AC & Wiegmann W; Appl. Phys. Lett. 46 (1985) 918-920
40. Tai K, Jewell JL, Tsang WT, Temkin H, Panish M & Twu Y; Appl. Phys. Lett. 50 (1987) 795-797
41. Barnes P, Zouganeli P, Rivers A, Whitehead M, Parry G, Woodbridge K & Roberts C; Electron. Lett. 25 (1989) 984-985

Acknowledgements

The InGaAs-InP samples used in this work were grown at RSRE by LL Taylor and SJ Bass. The GaAs-AlGaAs sample was grown at RSRE by MT Emeny and CR Whitehouse. The 5 x 5 InGaAs-InP array was fabricated at STC Technology Ltd., Harlow, UK by GD Henshall, PD Greene and WO Bourne. We gratefully acknowledge the contributions of these colleagues.

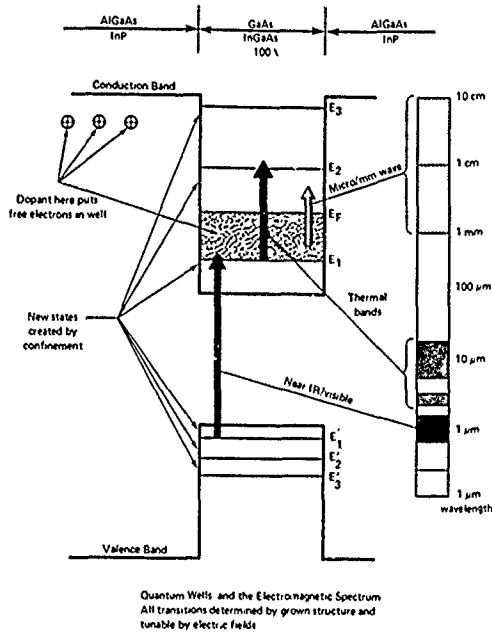


Figure 1 (left). Quantum Wells and the Electromagnetic Spectrum. A quantum well is shown schematically with the lowest energy point of each sub-band marked, and transitions in three different wavelength bands indicated. It is the NIR inter-band transition which is of interest in this work.

Figure 2 (right). Schematic of a Contacted MQW Modulator Mesa. An early structure with undoped InP spacer regions is indicated on the left, on the right is the 150-repeat structure reported here. The mesas used were circular, of 400 μm diameter and were formed by a wet-etch process. The contacts are ohmic. The n-type is offset on the top of the mesa and the p-type is around the base.

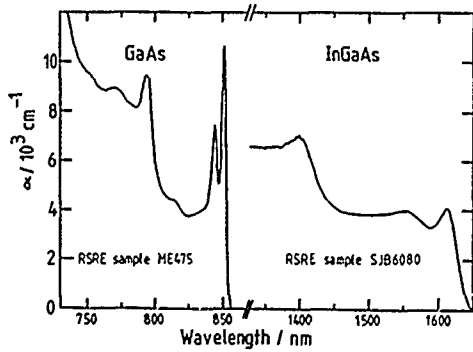
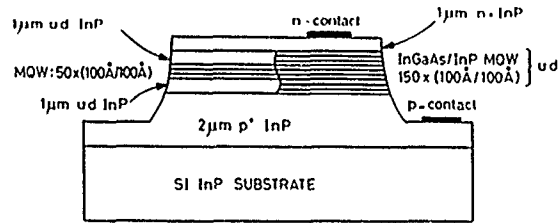


Figure 3 (left). MQW Absorption at 300K. The absorption coefficients have been averaged over well and barrier material, assuming equal thicknesses of each: the absorption within the well itself is twice the indicated value.

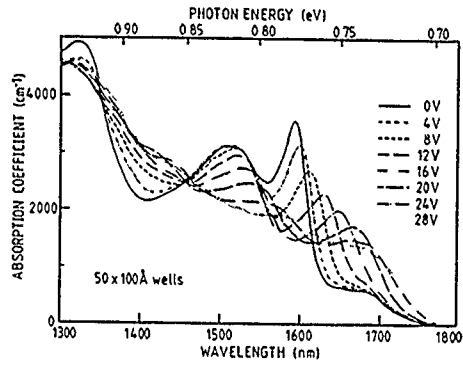


Figure 4 (left). The Quantum-Confined Stark Effect illustrated in a 50-repeat structure of InGaAs-InP. The red-shift and broadening of the exciton can be clearly seen. 28V bias gives $\sim 2.8 \times 10^5 \text{Vcm}^{-1}$ in this sample with a $1 \mu\text{m}$ undoped region.

Figure 5 (right). GaAs Refractive Index. Upper traces: real part, n , with 3.5 subtracted. Lower traces: imaginary (absorptive) part. In both cases the full line represents the zero-field values and the dotted line a field of 10^5Vcm^{-1} .

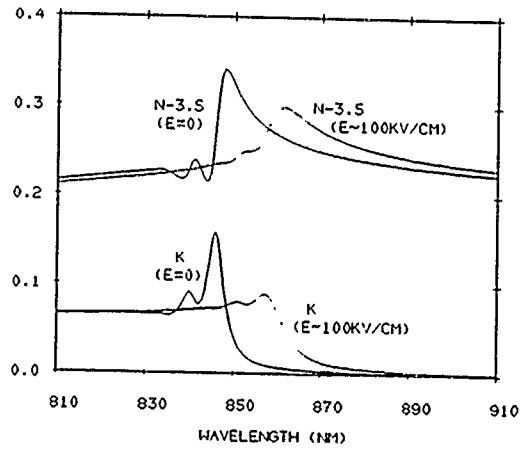
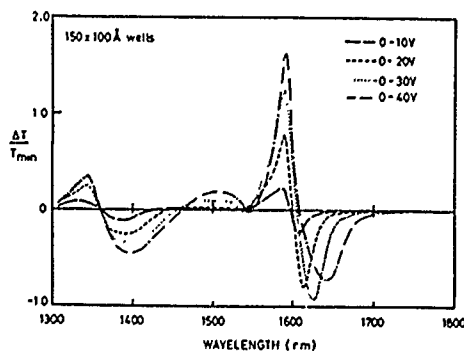
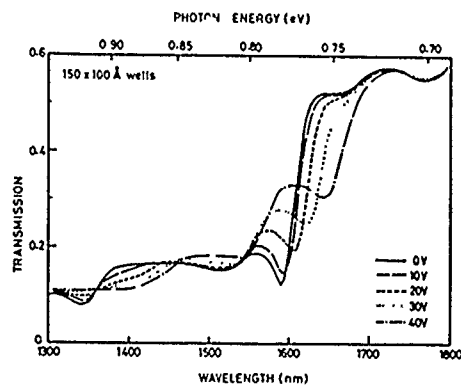


Figure 6 (left). The Modulation Properties of MQW InGaAs-InP. The 150 repeat MQW sample gives 4.1dB modulation at $1.58 \mu\text{m}$. Upper plot: transmission. Lower plot: modulation.

Figure 7 (right). Schematic Diagram of a Fabry-Perot Etalon. R and T are respectively the reflected and transmitted intensities.

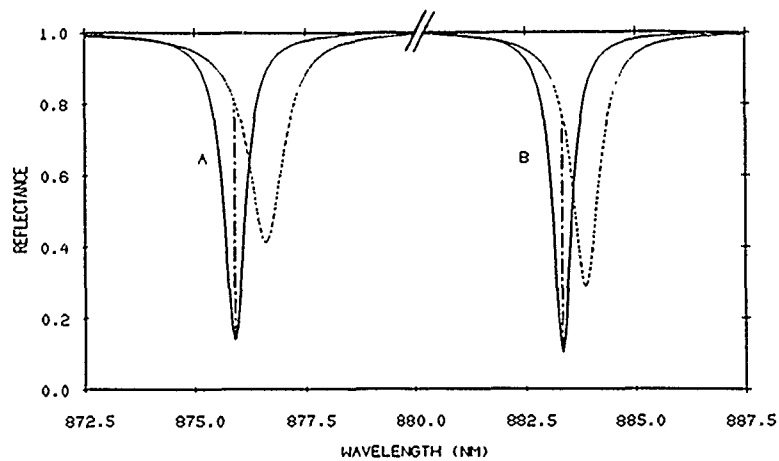
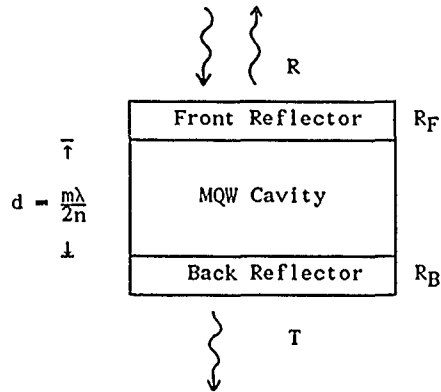


Figure 8 (a - above). The modelled electro-optic modulation from a symmetric GaAs MQW etalon. The modulator has 32 wells each of 100Å in the optical cavity separated by barriers of (A) 125Å and (B) 130Å. The thicker barriers give a greater optical depth to the cavity and hence the transmission resonance occurs at a longer wavelength. In both (A) and (B) the solid line represents the zero-field case, and the dotted line a field of $\sim 10^5 \text{Vcm}^{-1}$. Maximum modulation is indicated by a broken vertical line in each case. Note that in (A) the wavelength of the modulation is relatively close to the excitonic absorption whereas in (B) it is further away. The consequently weaker electro-optic effect in (B) results in a smaller wavelength-shift of the resonance, but the weaker electro-absorption gives a lower minimum reflectance.

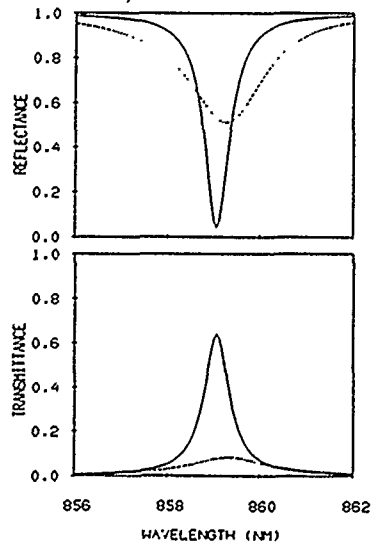


Figure 8 (b - left). Modelled transmit/reflect modulation from a symmetric MQW etalon operating by electro-absorption. Full line: zero-field. Dotted line: 10^5Vcm^{-1} , which in this 4-well GaAs model should require 2V bias. The contrast in both transmission and reflection is approx 10dB with just over 2dB insertion loss.

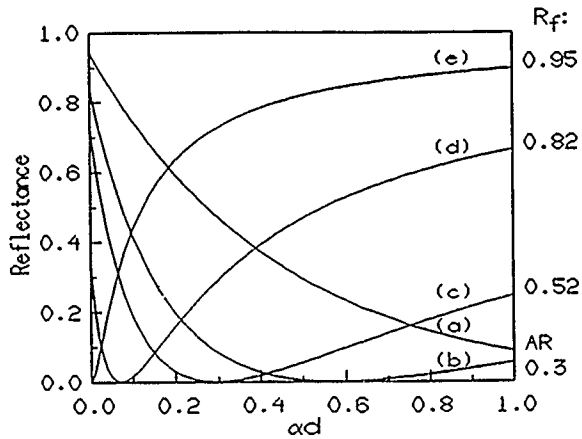


Figure 9 (left). The reflectance of an absorptive Fabry-Perot cavity as a function of cavity loss. Rear reflection coefficient, R_b , is 0.95. The front reflection coefficient values are listed. AR indicates 0.5% R_f , effectively an anti-reflection coating.

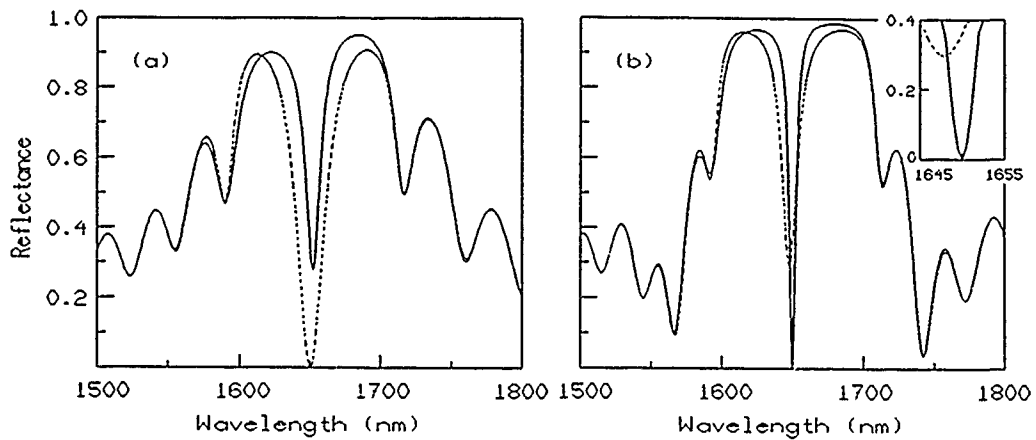


Figure 10 (above). The reflectance of 75-well InGaAs-InP MQW asymmetric cavities with $R_b=0.95$. Full line:- zero field; Dashed line:- field $\sim 10^5 \text{Vcm}^{-1}$. (a) Variation on the asymmetric cavity: $R_f=0.52$, $R=0$ is attained in the applied field. (b) Variation on the symmetric cavity: $R_f=0.82$, $R=0$ is attained in zero field.

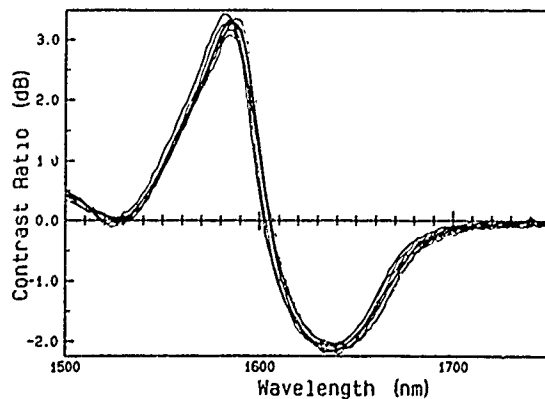


Figure 11 (left). The 0-40V traces of eight pixels from the InGaAs-InP SLM show good uniformity of modulation. The contrast ratio is defined to be $10 \log_{10}(T(E)/T_0)$, where T_0 is zero-bias transmission and $T(E)$ is transmission in field E .

Discussion

Paper n° 3

Question : Dr. R. KLEMM, GE (Forschungsinstitut für Funk und Mathematik, Wachtbert, Germany, Panel Chairman

What is the electrical bandwidth of these devices ? Could you also comment on linearity and dynamic range ?

Answer : Dr. GUY

Electrical bandwidth of 20 GHz have already been measured, but as the device is based on an

electronic effect with a response time of the order of 0.2 ps, there is considerable scope for extending the bandwidth to 100 GHz and beyond.

Linearity has not been addressed to date, but I expect that alterations to the design will be required to make it acceptably linear. The device should operate at very low incident powers, the device will saturate at higher powers - just how high will depend on the configuration of the particular device.

Quantum Well Infra-red Detectors: an introduction

by

M J Kane, M T Emeny, N Apsley and C R Whitehouse

Royal Signals and Radar Establishment

St. Andrews Road

Worcs. WR14 3PS

U.K.

Summary

The bandstructure of gallium arsenide – aluminium gallium arsenide quantum wells can be made such that the spacing of the confined energy levels corresponds to the energy of photons in the mid infra-red. This allows infra-red electro-optic devices to be made from this versatile general purpose electronic materials system which was not previously thought of as an infrared detector materials system. This potentially enables the whole of the well developed technology of gallium arsenide to be employed in this region. This paper will describe the performance of quantum well infrared photoconductive detectors fabricated using molecular beam epitaxy. The link between the detector parameters such as operating wavelength, quantum efficiency, dark current and noise and the structure parameters is discussed. Background limited performance is demonstrated and the dominant source of detector noise is shown to be shot noise.

1 An introduction to the quantum well infrared detector

The quantum well infrared detector is a new kind of infra-red photon detector. The detector is fabricated from multilayer structures of compound semiconductors, typically GaAs and $\text{Al}_x\text{Ga}_{1-x}\text{As}$ and works by the photoexcitation of an electron from a quantum well of finite depth. The photoresponse, therefore, has a well defined low energy threshold which can be set anywhere in the energy range 75 to 200 meV, corresponding to a wavelength range of about 6 to 17 microns, when made from GaAs/AlGaAs. Detectors for use in this wavelength region are usually made from highly specialized materials systems such as $\text{Hg}_x\text{Cd}_{1-x}\text{Te}$ and are therefore difficult to integrate with other forms of electronics. The quantum well detectors are fabricated from GaAs/AlGaAs epitaxial structures which are normally grown on large wafers (>2 inch diameter). The fabrication process always produces large arrays of detectors whose properties are uniform across the wafer. The processing methods used to make the quantum well infra red detector are similar to those used to make other GaAs devices and it is therefore possible to conceive of monolithically integrating signal processing and control electronics with the detectors. It should also be possible to grow quantum well infrared

detectors on GaAs layers grown on silicon and thereby allow integration with silicon devices.

Photoconductive quantum well detectors have been the subject of the most detailed study. These detectors show high detectivity and high operating speeds. The first detectivity measurement, made in 1988, reported a peak detectivity of $10^{10} \text{ cm}^2/\text{HzW}^{-1}$ for a detector with a peak response at 8 microns wavelength working at a temperature of 77K¹. Subsequently, similar detectivities were obtained in a detector with a peak responsivity at 10 microns albeit at a relatively low working temperature of 50K². This detectivity was measured with a 180° field of view of room temperature black body radiation and is background limited. Response time faster than 300 pS have been measured³. The most recently published results⁴ give a detectivity of $10^{10} \text{ cm}^2/\text{HzW}^{-1}$ in response to 300K black body radiation at an operating temperature of 68K in a detector with a cut off wavelength of 10.7 μm . Photovoltaic detectors have also been demonstrated^{5,6} but their performance has not been the subject of such detailed study.

The purpose of this paper is to provide an overview of the physical principles underlying the operation of these detectors and to illustrate this with results obtained recently in our laboratory.

2 Principles of operations of the quantum well infra-red detector.

Quantum well devices originated from the development of crystal growth techniques such as molecular beam epitaxy (MBE) which allow the fabrication of multilayer semiconductor structures on atomic length scales. The most developed materials system in this respect consists of layers of GaAs and $\text{Al}_x\text{Ga}_{1-x}\text{As}$ where the near identical atomic radii of Ga and Al allow the composition of the alloy component of the system to be varied continuously without disrupting the crystal lattice. This flexibility is particularly important when one wishes to tailor the operation of a quantum well infra-red detector to a particular wavelength. Almost all of the work reported on quantum well infra-red detectors has used this materials system and this is the only material that will be considered here. The AlGaAs/GaAs material system is particularly well suited to use in detectors working in the 8 to 12 μm band.

A layer of GaAs sandwiched between two layers of $\text{Al}_x\text{Ga}_{1-x}\text{As}$ acts as a finite potential well for an electron in the conduction band. (The quantum well infra-red detector is a pure conduction band device the valence band will not be considered in any discussion that follows.) The depth of this potential well increases with the mole fraction of aluminium in the $\text{Al}_x\text{Ga}_{1-x}\text{As}$. Reducing the thickness of the GaAs to less than a few hundred angstroms means that the Heisenberg uncertainty relation comes in to play as the energy uncertainty due to the spatial localisation of the electron becomes resolvable above any energy smearing due to disorder or thermal effects. A detailed treatment of the system shows that the allowed energy levels of the electron form a ladder of discrete states at energies less than the height of the potential barrier between the GaAs and the AlGaAs. The energy levels merge into a continuum once the electron has an energy greater than this potential step. As the width of the quantum well decreases the number of bound states decreases until there is only one bound state in the quantum well. There is, however, always one bound state, no matter how narrow the quantum well.

If the bound states are numbered in order of increasing energy, starting at number one for lowest energy state, dipole selection rules allow electronic transitions between the lowest energy state and all states with an even index. Dipole transitions are also allowed to the continuum of states above the top of the quantum well. There is a general sum rule, known as the Thomas-Reiche-Kuhn sum rule which states that the integral of the absorption from the ground state of the quantum well over all final states, including those in the continuum is a constant irrespective of the well width. In a wide well, where there are two or more strongly bound states, most of the total absorption occurs between the two lowest energy levels. However, when there is only one bound state in the quantum well, all of this absorption must occur between the localised ground state and the delocalised states in the continuum. This is exactly the configuration required for an infra-red detector. An electron in one of the delocalised continuum states will be mobile in a direction perpendicular to the plane of the quantum wells. The localized bound states are essentially immobile in this direction.

When detailed calculations of the possible absorption spectra are performed, it is found that the strongest absorption occurs when the final state is just above the top of the quantum well because this is where there is the largest density of states. (The joint density of states of the transition is quasi-one dimensional and has a near singularity at final state energies just above the top of the

quantum well.)

Figure 1 shows the results of a calculation of the low energy cut off of a quantum well detector as a function of its material parameters. The band structure of the quantum well is assumed to be described by the envelope function model of Nelson et al⁷. The lowest usable energy is set at 75meV by the onset of lattice absorption in the GaAs.

A typical detector for use around 10 μm wavelength will consist of a stack of 50 GaAs quantum wells doped n-type and typically 40 to 50 Å thick separated by undoped AlGaAs typically 300 to 500 Å thick. The stack of quantum wells would then have n-type contact layers of GaAs either side. The quantum well only responds to light polarised parallel to its growth direction and an optical coupler such as a grating is needed to scatter the light into the correct direction of propagation.

A conceptual framework for the optimisation of the quantum well infra-red detector has been provided by the theoretical analysis of Kinch and Yariv⁸. This work gives a good description of the manner in which detector parameters depend on key material parameters but appears to have difficulties in estimating the absolute values of detector performance parameters.

We will present here a variant of the analysis of Kinch and Yariv which proceeds as follows: Firstly we will consider the quantum efficiency. The quantum well infra-red detector works by the photoexcitation of an electron out of a quantum well. The quantum efficiency of such a detector will be directly proportional to the number of electrons present. Secondly we will consider the factors controlling the dark current. The strength of the optical absorption per electron is such that the quantum wells must be heavily doped in order to obtain significant absorption. This causes the electron gas in the quantum well to be degenerate. The Fermi energy can have a magnitude of up to a few tens of milli-electronvolts. (The electron gas in the quantum well is a two dimensional system and the Fermi energy is directly proportional to the electron sheet density.) The Fermi energy represents the kinetic energy of the motion of the electrons in the plane of the quantum well. A photon carries very little momentum so that the absorption of a photon will not change the in-plane motion of an electron. The energy difference between the initial and final states of an optical transition will be essentially the same for electrons excited from the lowest energy and from the Fermi energy. The thermal excitation of electrons out of the quantum well is, however, mediated by phonons which can have sufficient momentum to change the in-plane motion of the electron so that the effective thermal excitation energy is the difference between the

low energy threshold energy and the Fermi energy. The discussion above enables us to write down the following proportionalities;

$$\text{Responsivity} \propto E_F \quad (1)$$

$$\text{Dark current} \propto \exp(-(E_{\text{photon}} - E_F)/kT) \quad (2)$$

where E_F is the Fermi energy, E_{photon} is the low energy photon threshold energy, k is the Boltzman constant and T is the temperature. The dominant noise source will be shot noise on the dark current, which will be proportional to the square root of the dark current. Again a proportionality relation governing the detectivity of a detector containing a fixed number of wells can be written down;

$$\text{Detectivity} \propto E_F \exp((E_{\text{photon}} - E_F)/2kT) \quad (3)$$

(It is assumed that the thermal dark current a greater than the back ground photocurrent.) This relation clearly shows how to maximise the detectivity by varying the Fermi energy. A small Fermi energy will give a low responsivity and a low detectivity. A large Fermi energy will give a large responsivity but also a large dark current. The detectivity will be maximised when $E_F = 2kT$. The latest results reported by Levine and co-workers which are the best detectivities reported so far have nominal Fermi energies very close to the optimum for a temperature of 77K.

Detectivity is not the only performance criterion one may wish to optimise. In some circumstances The temperature required for background limited operation is more important than the detectivity. (This is the temperature at which the major source of noise is the random fluctuations in the background photon flux incident on the detector through the infra-red windows necessary for signal access to the detector.) This temperature can be determined by equating the thermal dark current to the current due to the photon background. This gives the equation;

$$\eta \Phi_b = I_{d0} \exp(-(E_{\text{photon}} - E_F)/kT_{\text{blip}}) \quad (4)$$

where η is the quantum efficiency per well, Φ_b is the background photon flux and I_{d0} is a constant describing the thermal emission rate from a single quantum well. This equation can be recast into the form

$$T_{\text{blip}} = (E_{\text{photon}} - E_F)/(k(C - \log_e E_F)) \quad (5)$$

where C is a constant into which all of the constants η , Φ_b and I_{d0} are absorbed. The maximisation of T_{blip} as a function of the Fermi energy has a logic similar to that employed in the maximisation of the detectivity. Too low a Fermi energy gives a

low thermal current but a low responsivity and a large Fermi energy gives a large responsivity and a large dark current. The optimum Fermi energy depends on the constant C which is the only real unknown in the equation, the Fermi energy and the photon energy being known in well characterised material. A first principles calculations of the parameters determining C is difficult and no such calculation is known to the author of this paper. (The latest results of Levine et al⁴ indicate that the responsivity is strongly dependent on material quality in a way that will be very difficult to model quantitatively.) However the presence of only one unknown in the equation makes it very useful for extrapolating experimental results forward to optimum conditions.

3 Experimental results

The illustrative results will concentrate on a device very similar to that described by Levine et al¹. The structure consists of 50 quantum wells which are 40 Å wide, separated by 300 Å barriers of $\text{Al}_{0.31}\text{Ga}_{0.69}\text{As}$. The sheet carrier density of the electrons in the quantum well is $5.1 \times 10^{11} \text{ cm}^{-2}$, corresponding to a Fermi energy of 17 meV. The responsivity of the detector as a function of photon energy is shown in figure 2. The peak of the response is found at 8 μm wavelength and the half heights are at 8.7 and 6.9 μm. The peak responsivity corresponds to a quantum efficiency of about one percent at a bias of 2V which is the bias at which the photocurrent saturates.

The figure 3 shows the current passed by the detector at a fixed bias of 1 volt as a function of temperature. The current was measured under two different sets of operating conditions; one with the detector in true darkness and the other with the detector illuminated by 300 K black body radiation at a field of view of 36° (full angle). It is clearly seen that at temperatures below 66K the current passed by the device is dominated by the "window photocurrent", i.e. that background limited operation is obtained. The activation energy of the detector current approaches a limiting value of 157 meV as the bias tends to zero. Using equation (2) and a Fermi energy of 17 meV, a photon energy of 174 meV is deduced, which is close to the peak of the photoresponse spectrum.

In section 2 above it was stated that the dominant source of noise would be shot noise on the dark current through the detector. Figure 4 demonstrates that this is indeed the case. This figure shows the noise generated in the detector as a function of bias current. Three different bias voltages are used and the current is set by changing the temperature. All of the the measured noise currents lie close to the value given by the shot noise formula $(2eI)^{1/2}$. The noise depends only on the bias

current and not on how it is set. The measurement frequency is 2kHz which was chosen because the noise spectrum is white at this frequency.

Conclusions

The quantum well infra-red detector is a relatively new infra-red detector which has demonstrated high performance relatively soon after its invention in 1988. The ability to fabricate infra-red detectors in III-V compound semiconductors enables the whole range of well developed III-V technology and growth techniques to be brought to bear on the problem of fabricating large and uniform arrays of detectors for the purposes of thermal imaging. The key problem that needs to be addressed by research in the immediate future is the temperature required for background limited performance.

© Copyright controller HMSO 1990

References

- 1 B F Levine, C G Bethea, G Hasnain, J Walker and R J Malik, *Appl. Phys. Lett.* **53** 296 (1988).
- 2 B F Levine, G Hasnain, C G Bethea and N Chand, *Appl. Phys. Lett.* **54** 2704 (1989).
- 3 C G Bethea, B F Levine, G Hasnain, J Walker and R J Malik, *J. Appl. Phys.* **66** 963 (1989)
- 4 B F Levine, C G Bethea, G Hasnain, V O Shen, E Pelve, R R Abbott and S J Hsieh
- 5 K W Goossen, S A Lyon and K Alavi *Appl. Phys. Lett.* **53** 1027 (1988)
- 6 A Kastasky, T Duffield, S J Allen and S J Harbison *Appl. Phys. Lett.* **52** 1320 (1988)
- 7 D F Nelson, R C Miller, D A Kleinman *Phys. Rev.* **B35** 7770 (1987)
- 8 M A Kinch and A Yariv *Appl. Phys. Lett.* **55** 2093 (1989)

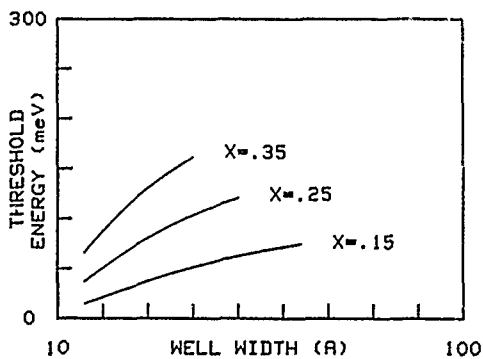


Figure 1 The results of a calculation of the low energy cut off of a quantum well infra-red detector as a function of the quantum well width and the aluminium fraction, x , in the barriers. (The lines end where a second bound state enters the quantum well.)

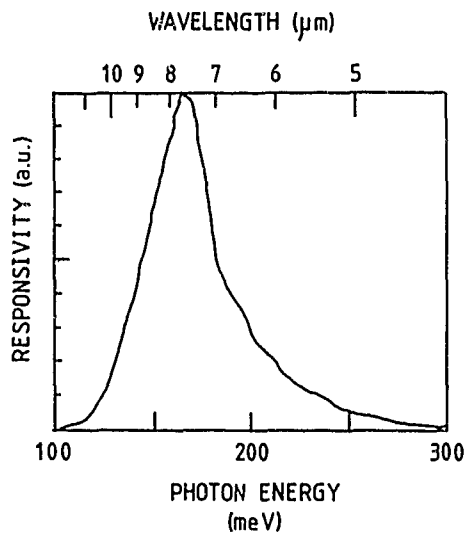


Figure 2 The responsivity of a quantum well infra-red detector as a function of photon energy. The structure consists of 50 wells 40 Å wide and barriers of $\text{Al}_{0.31}\text{Ga}_{0.69}\text{As}$.

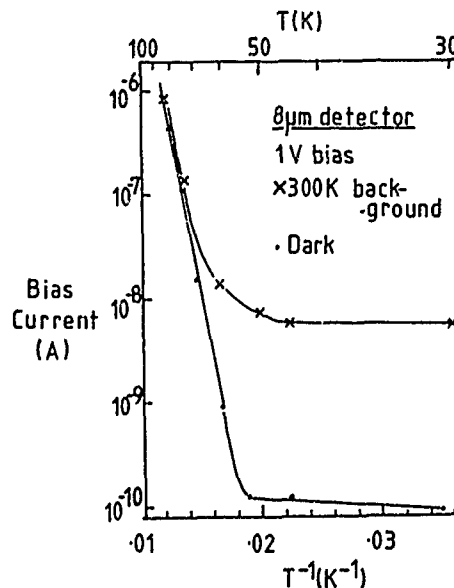


Figure 3 The bias current versus temperature for the quantum well infra-red detector whose response spectrum is shown in figure 2. Below 66K the "window photocurrent", measured here with a field of view of 36° at 300K is greater than the thermal dark current.

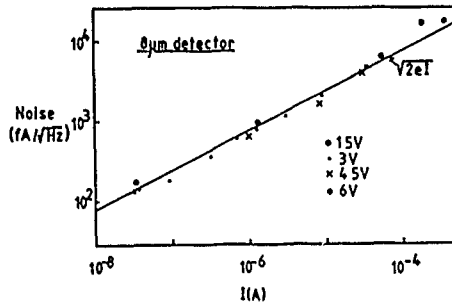


Figure 4 The noise generated by the quantum well infra-red detector. The current is set by varying either the bias voltage or the temperature. The magnitude of the noise generated is given by the shot noise formula, shown as the solid line.

Discussion

Paper n°4

Question : Mr. B. MORBIEU (Sextant Avionique, Observer)

Have you examined the potential of this detector for coherent detection? What is the quantum efficiency in heavily doped material?

Answer : Mr. KANE

Not yet. Our work so far has concentrated on maximising T_{blip} at the expense of quantum efficiency (High Quantum Efficiency is the main requirement for effective coherent detection). The limits to the quantum efficiency of the device are as yet unclear.

Question : JOHN P. HURREL (unregistered)

Why do you think your device is shot noise limited?

Answer : Mr. KANE

The device is operated under bias conditions where all thermally excited electrons are collected in the contacts. The measured noise reflects random fluctuations in the generation rate and is thus given by the shot noise formula. If thermally excited electrons were captured and re-emitted several times before being collected then the shot noise formula would overestimate the noise.

LOW-NOISE OSCILLATORS FOR AIRBORNE RADAR APPLICATIONS

Raymond L. Filler, and John R. Vig
 U.S. Army Electronics Technology and Devices Laboratory
 Fort Monmouth, New Jersey 07703-5000
 U.S.A.

INTRODUCTION

Vibration-induced phase noise can change the probability of detection of moving-target indicator (MTI) radar from near-100 percent to zero. Oscillators that are capable of meeting the requirements of MTI radar systems in a quiet environment are readily available. In the vibrating environments of airborne platforms, however, the phase noise of oscillators will degrade very significantly. For example, a 10 MHz crystal oscillator may have a phase noise of -140 dBc, 100 Hz from the carrier. Assuming a typical 1×10^{-9} per g acceleration sensitivity, and vibration at 100 Hz, this phase noise will degrade to -86 dBc under a 1 g sinusoidal vibration, and to -93 dBc under a 0.1 g^2 per Hz random vibration at 100 Hz away from the carrier. Of course, upon multiplication to 10 GHz, the phase noise increases by at least another 60 dB.

There has been an awareness of acceleration effects in frequency sources at least since the advent of missile and satellite applications,¹⁻⁶ Doppler radars,^{7,8} and other systems requiring extremely low noise.^{9,10} There has not, however, been a general appreciation of the magnitude of the problem. As a case in point, there is little or no mention of acceleration sensitivity in the general texts on quartz crystal oscillators and resonators or of vibration-induced phase noise in radar textbooks.

High-stability frequency sources, including atomic standards, contain quartz crystal resonators. One result of the evolution of electronics, i.e., the transition from tubes to transistors, and from point-to-point wiring to printed circuits, is the establishment of the quartz crystal resonator as the most acceleration-sensitive component in frequency sources. This paper reviews the causes and effects of acceleration sensitivity of bulkwave quartz crystal resonators, and the methods that reduce or compensate for that sensitivity. Most of what is discussed is equally relevant to surface acoustic wave (SAW), shallow bulk acoustic wave (SBAW), and other

microwave oscillators.

THE EFFECT OF ACCELERATION ON A CRYSTAL RESONATOR

A quartz crystal resonator subject to a steady acceleration has a slightly different series resonant frequency than the same resonator experiencing zero acceleration.¹ Furthermore, it has been observed that the magnitude of the frequency shift is proportional to the magnitude of the acceleration, and is also dependent upon the direction of the acceleration relative to a coordinate system fixed to the resonator.¹¹ It has been shown, empirically, that the acceleration sensitivity of a quartz crystal resonator is a vector quantity.¹² Therefore, the frequency during acceleration can be written as a function of the scalar product of two vectors

$$f(\vec{a}) = f_0 (1 + \vec{\Gamma} \cdot \vec{a}) \quad (1)$$

where $f(\vec{a})$ is the resonant frequency of the resonator experiencing acceleration \vec{a} , f_0 is the frequency with no acceleration (referred to as the carrier frequency), and $\vec{\Gamma}$ is the acceleration-sensitivity vector. It can be seen from Eq. (1) that the frequency of an accelerating resonator is a maximum when the acceleration is parallel to the acceleration-sensitivity vector; it is a minimum when the acceleration is antiparallel to the acceleration-sensitivity vector. An important result of Eq. (1) is that the frequency shift, $f(\vec{a}) - f_0$, is zero for any acceleration in the plane normal to the acceleration-sensitivity vector.

The frequency shift described in Eq. (1) is also induced by the acceleration due to gravity (even without motion). This is commonly referred to as "2g-tipover." During "2g-tipover," the magnitude of the acceleration is 1g in the direction towards the center of the earth. (The magnitude of acceleration given in this paper will be in units of g, i.e., the magnitude of the earth's gravitational acceleration at sea level,

980 cm/sec².) When a resonator is rotated 180° about a horizontal axis, the scalar product of the acceleration and the unit vector normal to the initial "top" of the resonator goes from -1g to +1g, which is a difference of 2g. Figure 1 shows actual data of the fractional frequency shift of a resonator (operating in an oscillator) when the oscillator is rotated about three mutually perpendicular axes in the earth's gravitational field.

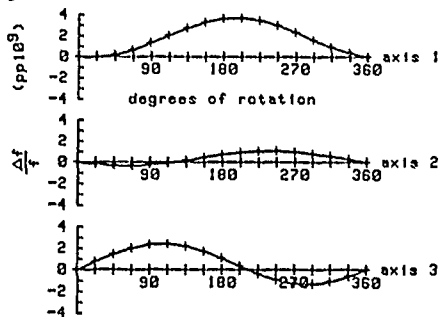


Fig. 1. "2-g tipover," frequency change versus rotation in Earth's gravitational field for three mutually perpendicular axes.

For each curve, the axis of rotation is held horizontal. The sinusoidal shape of each curve is a consequence of the scalar product being proportional to the cosine of the angle between the acceleration-sensitivity vector and the acceleration due to gravity.

THE EFFECT OF VIBRATION ON A CRYSTAL RESONATOR

In most applications, the magnitude of the acceleration is time-dependent. The magnitude of the acceleration-sensitivity vector, for acceleration amplitudes commonly encountered, is independent of acceleration amplitude.¹¹ The time-dependent frequency shift due to a complex vibration can, therefore, be determined from the sum of the individual sinusoidal components, i.e., the system is linear and superposition holds. Simple sinusoidal vibration will be discussed first; the extension will then be made to random vibration.

Simple harmonic motion will be assumed, with an acceleration given by

$$\vec{a} = \vec{A} \cos(2\pi f_v t), \quad (2)$$

where \vec{A} is the peak acceleration vector in units of g, f_v is the frequency of vibration in Hertz, and t is time in seconds. The variation of the frequency with time can be determined by combining Eq. (2) with Eq. (1), resulting in

$$f(\vec{a}) = f_0 (1 + (\vec{\Gamma} \cdot \vec{A}) \cos(2\pi f_v t)). \quad (3)$$

The behavior of the device can be described by defining a rectangular coordinate system fixed to the resonator. The acceleration-sensitivity vector and the acceleration vector can then be described in terms of the three unit vectors defined by that coordinate system. Therefore Eq. (3) can be transformed into a scalar equation containing the three (i, j, and k) components of \vec{A} and $\vec{\Gamma}$, i.e.,

$$f(\vec{a}) = f_0 (1 + \Gamma_i A_i + \Gamma_j A_j + \Gamma_k A_k) \cos(2\pi f_v t). \quad (4)$$

This can be rewritten as

$$f(\vec{a}) = f_0 + \Delta f \cos(2\pi f_v t), \quad (5)$$

where

$$\Delta f = f_0 (\Gamma_i A_i + \Gamma_j A_j + \Gamma_k A_k) \quad (6)$$

is the peak frequency shift due to the acceleration \vec{A} .

There are three quantities with units of frequency to keep in mind: f_0 , f_v , and Δf . It can be seen from Eq. (5) that the output frequency deviates from the center frequency, f_0 , by the amount $\pm \Delta f$, at a rate of f_v . This is shown schematically in Figure 2.

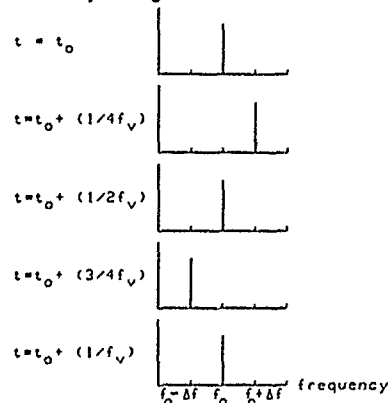


Fig. 2. Instantaneous "carrier" frequency for several instants during one cycle of vibration.

Each plot is the instantaneous output frequency of a crystal oscillator while undergoing a vibration at frequency f_v . Figure 3b is the voltage vs. time at the output of the same crystal oscillator showing, in a much exaggerated way, the variation in the frequency with acceleration amplitude. Figure 3a is the acceleration waveform.

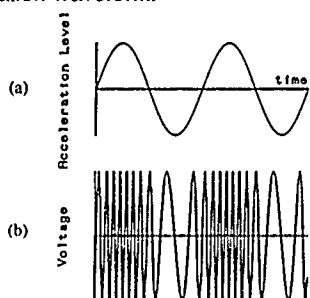


Fig. 3. (a) Acceleration level versus time. (b) Resulting oscillator output showing frequency modulation.

FREQUENCY DOMAIN

It is very useful to transform the effect of vibration into the frequency domain. This will allow the formulation of a convenient measurement scheme and allow comparison of vibration effects to more familiar forms of phase noise.

The voltage appearing at the output of an oscillator is given by

$$V(t) = V_0 \cos(\phi(t)), \quad (7)$$

where the phase $\phi(t)$ is derived from the frequency by

$$\phi(t) = 2\pi \int_{t_0}^t f(t') dt'. \quad (8)$$

When the oscillator frequency is varying due to simple harmonic acceleration modulating the resonant frequency of the resonator, the phase in Eq. (7) becomes, using Eqs. (5) and (8),

$$\phi(t) = 2\pi f_0 t + (\Delta f/f_v) \sin(2\pi f_v t). \quad (9)$$

When Eq. (9) is inserted into Eq. (7), the result is

$$V(t) = V_0 \cos(2\pi f_0 t + (\Delta f/f_v) \sin(2\pi f_v t)). \quad (10)$$

Eq. (10) is the expression for a frequency-modulated signal. It can be expanded in an infinite series of Bessel functions¹³ resulting in¹⁴

$$\begin{aligned} V(t) = V_0 [& J_0(\beta) \cos(2\pi f_0 t) + J_1(\beta) \cos(2\pi(f_0 + f_v)t) \\ & + J_1(\beta) \cos(2\pi(f_0 - f_v)t) + J_2(\beta) \cos(2\pi(f_0 + 2f_v)t) \\ & + J_2(\beta) \cos(2\pi(f_0 - 2f_v)t) + \dots] \end{aligned} \quad (11)$$

where $\beta = \Delta f/f_v = (\bar{r} \cdot \bar{A}) f_0/f_v$ is the modulation index (from standard FM theory.)

The first term in Eq. (11) is a sine wave at the carrier frequency with an amplitude, relative to V_0 , of $J_0(\beta)$. The other terms are vibration-induced sidebands at frequencies $f_0 + f_v$, $f_0 - f_v$, $f_0 + 2f_v$, $f_0 - 2f_v$, etc. The ratio of the power in the n th vibration-induced sideband to the power in the carrier, denoted by $I_n(f_v)$, is given by

$$I_n(f_v) = (J_n(\beta)/J_0(\beta))^2 \quad (12)$$

or, more commonly expressed in decibels as

$$I_n(f_v)(\text{dBc}) = 20 \log(J_n(\beta)/J_0(\beta)), \quad (13)$$

where dBc refers to dB relative to the carrier.

SMALL MODULATION INDEX

Several approximations can be made if the modulation index is less than 0.1. This is the case for most frequency standards in the HF band experiencing "normal" accelerations of 10 g or less at acceleration frequencies above a few hertz. The approximations are

$$\begin{aligned} J_0(\beta) &= 1; & \beta < 0.1 \\ J_1(\beta) &= \beta/2; & \beta < 0.1 \\ J_n(\beta) &= 0; & \beta < 0.1, n > 2. \end{aligned} \quad (14)$$

Therefore, after combining Eqs. (13) and (14):

$$I_1(f_v) \sim 20 + \log((\bar{f} \cdot \bar{A})f_o/(2f_v)) \quad (15)$$

$$I_{n>1}(f_v) \sim 0$$

For small modulation index, therefore, most of the power is in the carrier and a small amount is in the first sideband pair (upper and lower). The amplitudes of the higher sidebands are negligible.

As an example, consider a 5 MHz oscillator with a vibration sensitivity of $2 \times 10^{-9}/g$. If the oscillator experiences an acceleration of 5 g along the direction of the acceleration-sensitivity vector, the value of Δf is $(5 \times 10^6 \text{ Hz}) \cdot (5 \text{ g}) \cdot (2 \times 10^{-9}/g) = 0.05 \text{ Hz}$. The modulation index and $I_1(f_v)$ for several vibration frequencies are shown in Table I.

TABLE I

First sideband level, in dBc, for a 5 MHz oscillator with an acceleration sensitivity of $2 \times 10^{-9}/g$ experiencing an acceleration of 5g peak.

f_v (Hz)	β	$I_1(f_v)$ (dBc)
5	0.01	-46
50	0.002	-60
500	0.001	-66
5000	0.0001	-86

It can be seen that I_1 falls off at 6 dB per octave (20 dB per decade.) A consequence of linearity at low vibration levels is that these sinusoidal accelerations are independent. The amplitude at any frequency is the same if the bright lines are excited separately or in combination. The first three of these vibration-induced sidebands and the carrier are shown in a typical spectrum analyzer output in Figure 4.

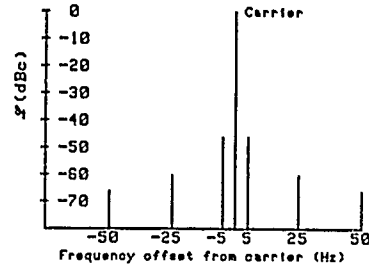


Fig. 4. Vibration-induced sidebands and carrier resulting from sinusoidal acceleration at 5 Hz, 25 Hz, and 50 Hz.

FREQUENCY MULTIPLICATION

Phase noise during vibration is of great concern in systems such as radar, navigation, and satellite communications, where the frequency of the crystal oscillator is multiplied up to the microwave region. Upon frequency multiplication by a factor of N , the vibration frequency f_v is unaffected since it is an external influence. The peak frequency change due to vibration, Δf , however, becomes

$$\Delta f = (\bar{f} \cdot \bar{A})Nf_o \quad (16)$$

The modulation index β is therefore increased by a factor of N . Expressed in decibels, frequency multiplication by a factor N increases the phase noise by $20 \log N$.

The relationship between the vibration-induced phase noise of two oscillators with the same vibration sensitivity and different carrier frequencies is

$$I_B(f_v) = I_A(f_v) + 20 \log(f_B/f_A) \quad (17)$$

Where $I_A(f_v)$ is the sideband level, in dBc, of the oscillator at frequency f_A , and $I_B(f_v)$ is the sideband level of the oscillator at frequency f_B . Frequency multiplication to a higher frequency is indistinguishable from direct frequency generation at the higher frequency. For example, when a $2 \times 10^{-9}/g$ sensitivity 5 MHz

oscillator's frequency is multiplied by a factor of 308 to generate a frequency of 1575 MHz, its output will have identical vibration-induced sidebands to a 1575 MHz SAW oscillator with a sensitivity of $2 \times 10^{-9}/g$. This is identical to the "20 log N" term associated with the increase in phase noise due to frequency multiplication. Again, this relationship holds only if $\beta < 0.1$.

LARGE MODULATION INDEX

If the modulation index β is larger than about 0.1, the approximations made in Eq. (14) are not valid. This often occurs in UHF and higher frequency systems.⁹ At 5 g acceleration, for example, the vibration-induced sidebands produced by the 1575 MHz oscillator and the 5 MHz oscillator multiplied by 308 are shown in Table II.

TABLE II

First sideband level, in dBc, for a 1575 MHz oscillator with an acceleration sensitivity of $2 \times 10^{-9}/g$ experiencing a peak acceleration of 5g.

f_v (Hz)	β	$I_1(f_v)$ (dBc)
5	3.15	+2.3
25	0.63	-9.6
50	0.315	-16.0
500	0.0315	-36.0

It can be seen that the values of $I_1(f_v)$ in Table II are much greater than those in Table I for the same vibration frequency. This is a consequence of the ratio of output frequency to vibration frequency being much larger. It is possible, as can be seen in this example, for the sidebands to be larger than the carrier. Also, there are even conditions where the

carrier disappears and the value of $I_1(f_v)$ goes to infinity, e.g., when β equals 2.4, that is, all of the power is in the sidebands and none is in the carrier.

ALLAN VARIANCE

The effect of sinusoidal phase modulation on the Allan variance of a frequency standard has been shown¹⁵ to be given by

$$\sigma_y = (\Phi/\pi f_0 \tau) \sin^2(\pi f_v \tau) \quad (18)$$

where Φ is the peak phase deviation, f_v is the frequency of the phase modulation, and τ is the measurement time. It can be seen from Eq. (9) that the magnitude of the maximum phase deviation for a single vibration-induced sideband is $\Delta f/f_v$. Therefore, the vibration-induced Allan variance of a frequency standard with an acceleration sensitivity of Γ , subjected to acceleration \bar{A} at a frequency of f_v , is

$$\sigma_y = \{(\Gamma \cdot \bar{A})/(\pi f_v \tau)\} \sin^2(\pi f_v \tau) \quad (19)$$

This effect is shown in Figure 5. The frequency standard is assumed to have an Allan variance of $(1 \times 10^{-12}/\tau)^2$ when not being accelerated.

A plausibility argument for the occurrence of the peaks and valleys in Figure 5 is that the average frequency, as given in Eq. (5), is f_0 for an averaging time equal to an integer multiple of the period of the vibration. Since this is a constant, the variance is zero. The average frequency departure from f_0 is a maximum when the averaging time is an integer multiple of one-half the period of the vibration.

Therefore, the peaks in Figure 5 occur when $\tau = (2n + 1)/(2f_v)$ and the valleys occur when $\tau = (n + 1)/f_v$, where $n = 0, 1, 2, 3, \dots$

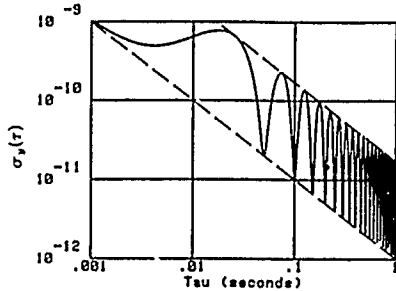


Fig. 5. $\sigma_y(\tau)$ versus τ of oscillator with acceleration-sensitivity of 1 ppb/g during 1-g vibration at 20 Hz.

RANDOM VIBRATIONS

In most situations the acceleration experienced by a frequency standard is not simple harmonic motion; it is random, i.e., the vibratory power is randomly distributed over a range of frequencies, phases, and amplitudes. The acceleration can be described by its power spectral density $G(f)$. The power spectral density of frequency fluctuations, $S_v(f)$, can be obtained by multiplying the power spectral density of acceleration by the square of the acceleration sensitivity in $(\text{Hz/g})^2$. The single-sideband measure of stability, $\mathcal{L}(f)$, is related to $S_v(f)$, if the modulation index is small, by¹⁶

$$\mathcal{L}(f) = S_v(f)/(2f^2). \quad (20)$$

Therefore, $\mathcal{L}(f)$ for random vibration is given by

$$\mathcal{L}(f) = (|\bar{\Gamma}|f_0)^2 G(f)/(2f^2). \quad (21)$$

As an example, consider the random acceleration spectrum given in the upper right of Figure 6. $G(f)$, in units of g^2/Hz , is given by

$$G(f) = 0.04 \quad 5 < f < 220 \text{ Hz}$$

$$G(f) = 0.07 \cdot (f/300)^2 \quad 220 < f < 300 \text{ Hz}$$

$$G(f) = 0.07 \quad 300 < f < 1000 \text{ Hz}$$

$$G(f) = 0.07 \cdot (f/1000)^{-2} \quad 1 < f < 2 \text{ kHz}. \quad (22)$$

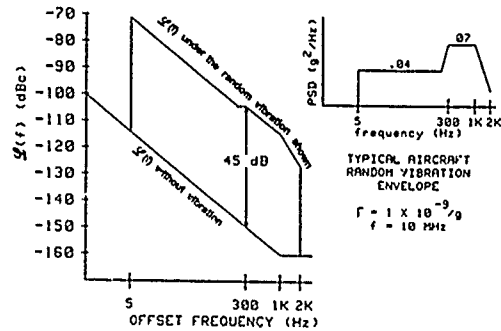


Fig. 6. Random vibration-induced phase noise and random vibration envelope.

If the vibration sensitivity is $1 \times 10^{-9}/\text{g}$ and the oscillator is operating at 10 MHz, the peak frequency deviation is 0.01 Hz. Therefore, $\mathcal{L}(f)$ is

$$\mathcal{L}(f) = (0.04) \cdot (0.01)^2 / (2f^2) \quad 5 < f < 220 \text{ Hz}$$

$$\mathcal{L}(f) = (0.07) \cdot (0.01/100)^2 / 2 \quad 220 < f < 300 \text{ Hz} \quad (23)$$

$$\mathcal{L}(f) = (0.07) \cdot (0.01)^2 / (2f^2) \quad 100 < f < 1000 \text{ Hz}$$

$$\mathcal{L}(f) = (0.07) \cdot (0.01 \cdot 1000)^2 / (2f^4) \quad 1 < f < 2 \text{ kHz},$$

which is shown in Figure 6. Note that outside of the vibration frequency range defined by the given acceleration spectrum, the phase noise is identical to that of a non-accelerated device.

INTEGRATED PHASE NOISE AND PEAK PHASE EXCURSION

Specialists in crystal resonators and oscillators generally characterize phase noise by $S_{\phi}(f)$ or $\mathcal{L}(f)$. Many users of crystal oscillators, however, characterize phase noise in terms of

"phase jitter." Phase jitter is the phase noise integrated over the system bandwidth. Similarly, in phase-lock-loops, it is the magnitude of the phase excursions that determines whether or not the loop will break lock under vibration.

One can use the previous example to investigate the effect of vibration on integrated phase noise. Integrated phase noise is defined, for the band f_1 to f_2 , as

$$\phi_i^2 = \int_{f_1}^{f_2} S_\phi(f) df, \quad (24)$$

where S_ϕ is the spectral density of phase, equal to $2\mathcal{L}$. In the frequency band of 1 Hz to 2 KHz, the phase noise of the nonvibrating oscillator from Figure 6 is given by

$$\begin{aligned} \mathcal{L} &= 1 \times 10^{-10}/f^2 & f \leq 1 \text{ KHz} \\ \mathcal{L} &= 1 \times 10^{-16} & f \geq 1 \text{ KHz} \end{aligned} \quad (25)$$

and the integrated phase noise in the same band is

$$\phi_i^2 \sim 2 \times 10^{-10} \text{ radians}^2. \quad (26)$$

Therefore,

$$\phi_i = 1.4 \times 10^{-5} \text{ radians}. \quad (27)$$

While the oscillator is vibrating, the phase noise is given by Eq. (25) in the band from 1 Hz to 5 Hz, and by Eq. (23) in the band from 5 Hz to 2000 Hz. The integrated phase noise is

$$\begin{aligned} \phi_i^2 &= 2 \left[\int_1^5 (1 \times 10^{-10}/f^2) df + \int_5^{220} (0.04)(0.01/f)^2 df \right] \\ &+ \int_{220}^{300} (0.07)(0.01/300)^2 df \end{aligned}$$

$$\begin{aligned} &+ \int_{300}^{1000} (0.07)(0.01/300)^2 df + \int_{1000}^{2000} (0.07)(0.01 \cdot 1000)^2/f^4 df \\ &= 8 \times 10^{-7} \text{ radians}^2. \end{aligned} \quad (28)$$

Therefore,

$$\phi_i = 9 \times 10^{-4} \text{ radians}. \quad (29)$$

While the oscillator is vibrating, it can be seen that the integrated phase noise is 4000 times that of the noise when it is not vibrating and the rms phase deviation, ϕ_p , is about 60 times larger during vibration.

When the oscillator is subjected to a simple sinusoidal vibration, the peak phase excursion follows from Eq. (9), i.e.,

$$\phi_{\text{peak}} = \Delta t/f_v. \quad (30)$$

For example, if our 10 MHz, $1 \times 10^{-9}/g$ oscillator is subjected to a 10 Hz sinusoidal vibration of amplitude 1 g, the peak vibration-induced phase excursion is 1×10^{-3} radians. If this oscillator is used as the reference oscillator in a 10 GHz radar system, the peak phase excursion at 10 GHz will be 1 radian. Similarly, when an oscillator's frequency is multiplied, the integrated phase noise is increased by the multiplication factor. At 10 GHz, for example, the integrated phase noise in the above example increases from 9×10^{-4} radians to 0.9 radians! Such large phase excursions are detrimental to the performance of many systems, such as those which employ phase lock loops or phase shift keying.

MEASUREMENT

The sidebands generated by vibration can be used to measure the acceleration sensitivity. Eq. (15) can be rearranged to get

$$\Gamma_i = (2f_v/A_i f_0) 10^{1(f_v)/20}, \quad (31)$$

where Γ_i is the component of the acceleration

sensitivity vector in the i direction. Three measurements, along mutually perpendicular axes, are required to characterize $\vec{\Gamma}$, which becomes

$$\vec{\Gamma} = \Gamma_i \hat{i} + \Gamma_j \hat{j} + \Gamma_k \hat{k} \quad (32)$$

with a magnitude of

$$|\vec{\Gamma}| = (\Gamma_i^2 + \Gamma_j^2 + \Gamma_k^2)^{1/2}. \quad (33)$$

One scheme for measuring $\vec{\Gamma}$ is shown in Figure 7.

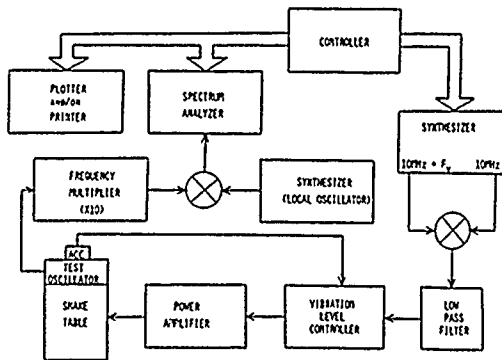


Fig. 7. Typical equipment configuration for measurement of acceleration-sensitivity using sinusoidal acceleration.

The local oscillator is used to mix the carrier frequency down to the range of the spectrum analyzer. If the local oscillator is not modulated, the relative sideband levels are unchanged by mixing. The frequency multiplier is used to overcome dynamic range limitations of the spectrum analyzer, using the "20 log N" enhancement discussed previously. The measured sideband levels must be adjusted for the multiplication factor prior to insertion into Eq. (31). It must be stressed that Eq. (17) is valid only if $\beta < 0.1$. A sample measurement output and calculation is given in Figure 8.

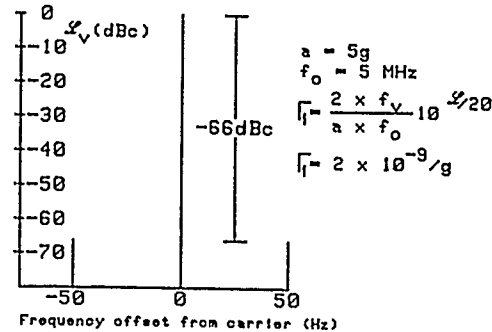


Fig. 8. Sample acceleration-sensitivity measurement using sinusoidal acceleration.

Other measurement schemes include passive excitation¹⁷ of the resonator, the use of random vibration,¹⁸ and the 2-g tipover test. Many oven-controlled oscillators are not suitable for characterization by the 2-g tipover test, however, because rotation of the oscillator results in temperature changes inside the oven that can mask the effects due to the acceleration changes. Vibration tests are also subject to pitfalls since resonances in the oscillator or shake table assembly can produce false results. It is, therefore, important to perform the test at more than one frequency.

THEORY

The theoretical understanding of acceleration sensitivity does not yet enable one to predict the acceleration sensitivity of "real" resonator designs. Theoretical activity started with the study of in-plane forces on simplified resonator models. The first studies were concerned with the closely related force-frequency effect. This effect, first reported by Bottom¹⁹ in 1947, is the change in frequency induced by a pair of opposed forces in the plane of a resonator plate applied at the rim. Those forces distort the quartz plate and, because of the nonlinear elastic behavior, change the acoustic velocity.¹¹

Since the frequency of a resonator is a function of the acoustic velocity and the dimensions of the quartz plate, the forces change the frequency.

The first attempt at an analytical solution to the force-frequency problem was made by Mingins, Barcus, and Perry in 1962.²⁰ They assumed an AT-cut crystal plate of infinite lateral dimension and used a perturbation technique with linear elastic coefficients. In 1963, they discussed nonlinear theory and the need to include the third-order elastic coefficients.²¹ Those coefficients were measured in 1966 by Thurston, McSkimin, and Andreatch.²² The first calculation to use the nonlinear theory was performed by Keyes and Blair in 1967.²³ In 1973, Lee, Wang, and Markenscoff²⁴ published the first of a continuing series of papers (by Lee and his students,) in which they calculated the force-frequency coefficient (as defined by Ratajski²⁵) as a function of azimuth, using the general theory of incremental elastic deformations superimposed on finite initial deformations. The next year, Lee et al., investigated the frequency change due to cantilever bending of the plate.²⁶ In 1977, a variational analysis of the force-frequency effect, including the effect of material anisotropy on initial stress, was given by EerNisse, Ballato, and Lukaszek²⁷ for doubly rotated cuts. In 1978, Janiaud, Nissim, and Gagnepain²⁸ obtained analytic solutions for the biasing stress in singly and doubly rotated plates subject to diametral forces. Those results allowed them to calculate Ratajski's force-frequency coefficient, and also the in-plane acceleration sensitivity. Lee and Wu²⁹ extended the work of reference 24 to treat plates of any cut. In that paper, the solution for an arbitrary number of ribbon supports was obtained.

Under acceleration, body forces in the quartz plate are balanced by reaction forces from the mounting structure. As in the force-frequency

effect, distortion of the crystal lattice causes the resonant frequency to change. For bulkwave resonators, only the in-plane case has been treated. The first analysis was by Valdois, Besson, and Gagnepain¹¹ in 1974, who showed that the effect is linear. Several papers by Lee and Wu²⁹⁻³¹ considered resonators with three- and four-point mounts. Two-point mounts were considered by Janiaud, Nissim, and Gagnepain.²⁸ For SAW resonators, recent work by Shick and Tiersten³² and by Sinha and Locke³³ has treated acceleration both in the plane of the plate and normal to it.

There seems to be a significant dependence of the acceleration sensitivity on small variations in the mounting. Analysis of bulkwave resonators, to-date, have considered only point supports. Real resonators have supports that are distributed over a finite area. In addition, initial stress conditions are difficult to determine and may not be well-reproduced. There is an ongoing effort by Lee and Tang³⁴ to use finite element analysis to more accurately model the mounting structure. It is hoped that this will allow computer simulations that will permit the determination of the optimum design parameters for minimizing acceleration sensitivity.

EXPERIMENTAL RESULTS

Several papers have reported experimental results on the force-frequency effect^{20,25,35} and the effects of bending moments.³⁶ All used point mounts in special fixtures, and results agree fairly well with the theoretical analyses. The reported experimental observations of the actual acceleration sensitivity of real resonators, on the other hand, is remarkable in that it defies simple explanation.

The experimental effort on acceleration-sensitivity started in the 1960's with Smith, Spencer, and Warner.¹⁻⁵ Valdois, Besson, and

Gagnepain¹¹ made measurements on resonators and oscillators to demonstrate that the resonator was the acceleration-sensitive element. Results from 2-g tipover experiments were reported for SC-cut resonators by Kusters, Adams, Yoshida, and Leach³⁷ in 1977. In 1979, Warner, Goldfrank, Meirs, and Rosenfeld³⁸ reported results on SC- and FC-cut devices. In 1981, the first of a series of papers intended to explore a wide range of resonator fabrication parameters was published by Filler and Vig.³⁹ In that same year, Nakazawa, Lukaszek, and Ballato⁴⁰ reported constant-acceleration results that suggested an acceleration sensitivity that is not linear with acceleration level. The only significant parameter for the reduction of acceleration-sensitivity was reported by Filler, Kosinski, and Vig⁴¹ in 1982. As one makes plano-convex and biconvex AT-cut resonators flatter, the acceleration sensitivity decreases. It must be noted, however, that other effects, as yet undetermined, cause large scatter in the data. A survey of a large number of resonator parameters, such as SC-cut contour, thickness, drive level, temperature, and angle of cut, was published in 1983 by Filler, Kosinski, and Vig.⁴² No significant correlations were found.

A paper, by Weglein⁴³ in 1984, reported the acceleration sensitivity of VHF AT- and SC-cut resonators. All of the resonators in that study were disassembled after the acceleration sensitivity measurements to examine fabrication details. That investigation, which seems to summarize the efforts to date, showed "little dependence on any recognizable parameter," except that the lowest average acceleration sensitivity was found in the group of AT units. The large spread in the data, typical of all experimental observations of acceleration-sensitivity, seems to be caused by a combination of sometimes offsetting subtle effects, which are difficult to control during

fabrication.

REDUCTION OF THE ACCELERATION SENSITIVITY OF RESONATORS

The introduction of the stress-compensated cut of quartz, i.e., the SC-cut, was accompanied by the wide-spread expectation that the SC-cut would have significantly lower acceleration sensitivity than other cuts. Unfortunately, that expectation has not been realized. The lowest acceleration sensitivity achieved with AT-cut resonators⁴¹⁻⁴³ equals that achieved with SC-cut resonators; both cuts can have low parts in 10^{10} /g sensitivity.

Efforts to reduce the sensitivity of individual resonators to the effects of acceleration have stressed the support structure. Lukaszek and Ballato⁴⁴ proposed a plate geometry that would assure the proper support configuration to reduce the force-frequency effect. Besson, Gagnepain, Janiaud, and Valdois⁴⁵ proposed a support structure that insured symmetry with the median plane of the resonator plate. Debaisieux, Aubry, and Gros Lambert⁴⁶ and Aubry and Debaisieux⁴⁷ have reported results using QAS resonators, a variation of the BVA,⁴⁸ which insures symmetry of mount as well as accurate mount locations for reducing the force-frequency effect. Their results show a marked reduction in the scatter of the measured acceleration sensitivity.

MODE SHAPE CONTROL

Recent theoretical and experimental evidence by EerNisse, et al.,^{49,50} indicates that the major variable yet to be controlled properly is the shape and location of the mode (active region of vibration) in a "real world" resonator. Theoretically, it can be shown that frequency shift due to a stress on the resonator, such as that caused by acceleration, is given by an

integral of the third-order elastic constant times the mode energy density times the strain pattern set up by the acceleration. Leaving out tensor notation, for simplicity,

$$\Delta f/f = C_3 \int_V G^2(X,Y,Z) E(X,Y,Z) dV \quad (34)$$

where $\Delta f/f$ is fractional frequency shift, G is the normalized strain distribution associated with the mode of vibration (G^2 is proportional to the strain energy density), E is the strain distribution associated with the stress caused by acceleration, C_3 is the third-order elastic constant tensor, V is the volume of the resonator, and $dV = dXdYdZ$.

EerNisse showed that very small changes in the mode shape and location have significant effects on the integral, i.e., on the acceleration sensitivity of resonators. He further argued that, because of material imperfections (such as dislocations), and fabrication imperfections (thickness variations, contouring flaws, electrode mass density and thickness variations), the demands on mode shape control will be impractical to accomplish during manufacturing without some ability to "trim" the mode shape and location for each individual resonator. He was able to produce changes in the acceleration sensitivity of resonators by depositing platinum on selected areas of resonators (in order to change the mode shape and location).

ACCELERATION COMPENSATION OF OSCILLATORS

The lack of progress in reducing the acceleration sensitivity of the resonator below the low parts in $10^{10}/g$ level has spawned several techniques for compensation of the effect. There are two general classes of compensation, passive and active. The first compensation

results were published by Gagnepain and Walls in 1977.⁵¹ They used the passive method of mechanically arranging two resonators such that the components of the acceleration sensitivities normal to the plates were antiparallel. The resonators were electrically connected in series in a single oscillator. Przyjemski¹² and Emmons⁵² used an active technique. They sensed the acceleration magnitude with an accelerometer aligned with the direction of the acceleration sensitivity vector of the resonator. The accelerometer signal was fed into a tuning circuit in the oscillator in order to counter the acceleration-induced frequency changes. A limitation of this technique is the requirement on the linearity of the tuning network at all operating points. Emmons also employed the dual-resonator technique and suggested using an acceleration-sensitive capacitor in the tuning network of the oscillator. The latter technique is available as an option on a commercial cesium-beam frequency standard.

Ballato⁵³ suggested a method for compensation in all directions using a resonator pair made of enantiomorphs. He argued that opposite handedness is the only way to have all three crystallographic axes line up antiparallel. This was extended by a series of patents by Ballato and Vig.⁵⁴⁻⁵⁶ A simplification was patented by Filler,⁵⁷ who showed that, since the acceleration-sensitivity has vector properties, all that is required is that the vectors be aligned antiparallel, independent of the handedness of the quartz. Vig and Walls⁵⁸ extended this work by suggesting a method to accommodate resonators with different acceleration sensitivity magnitudes.

Rosati patented⁵⁹ an active technique of compensation which was further developed by Rosati and Filler.⁶⁰ This method makes use of the polarization effect in doubly rotated resonators, i.e., that the resonant frequency of a doubly rotated resonator is a function of the

voltage applied to the electrodes.⁶¹ If one senses the acceleration using an accelerometer and feeds that signal with appropriate amplification and phase reversal directly to the resonator electrodes, compensation can be achieved. The advantage of feeding the correction signal to the resonator electrodes rather than a varactor is that the polarization effect has superior linearity. When the correction signal is applied to a varactor, the non-linearity of the varactor and of the frequency-capacitance function causes sidebands at harmonics of the vibration frequency. One implementation of this technique was used to compensate a rubidium oscillator.⁶² A refinement was proposed by Frerking.⁶³

CONCLUSION

Vibration effects are a significant problem in modern communication, navigation, and radar systems. Progress has been made in understanding the causes of acceleration sensitivity but a full explanation for real devices has been elusive. A great deal of effort has been expended on compensating for acceleration-sensitivity, but more work is needed to improve the level and bandwidth of the compensation.

REFERENCES

1. A. W. Warner and W. L. Smith, "Quartz Crystal Units and Precision Oscillators for Operation in Severe Mechanical Environments," 14th ASFC, pp 200-216, 1960.
2. W. L. Smith, "An Ultra-Precise Standard of Frequency," Final Report, Contract DA 36-039 sc-73078, US Army, 1960.
3. W. J. Spencer and W. L. Smith, "Precision Crystal Frequency Standards," 15th ASFC, pp 139-155, 1961.
4. W. J. Spencer and W. L. Smith, "Precision Quartz Crystal Controlled Oscillator for Severe Environmental Conditions," 16th ASFC, pp 406-421, 1962.
5. W. L. Smith and W. J. Spencer, "Quartz Crystal Controlled Oscillators," Final Report, Contract DA 36-039 sc-85373, US Army, 1963.
6. D. B. Leeson, "Aerospace Crystal Environmental Requirements," 19th ASFC, pp 49-57, 1965.
7. D. B. Leeson and G. F. Johnson, "Short-Term Stability for a Doppler Radar: Requirements, Measurements, and Techniques," Proc. IEEE, 54, pp 244-248, 1966.
8. G. F. Johnson, "Vibration Characteristics of Crystal Oscillators," 21st ASFC, pp 287-293, 1967.
9. J. Moses, "NAVSTAR Global Positioning System Oscillator Requirements for the GPS Manpack," 30th ASFC, pp 390-400, 1967.
10. J. M. Przyjemski and P. L. Konop, "Limitations on GPS Receiver Performance Imposed by Crystal-Oscillator g-Sensitivity," NAECON '77, 1977.
11. M. Valdois, J. Besson, and J. J. Gagnepain, "Influence of Environment Conditions on a Quartz Resonator," 28th ASFC, pp 19-32, 1974.
12. J. M. Przyjemski, "Improvement in System Performance using a Crystal Oscillator Compensated for Acceleration Sensitivity," 32nd ASFC, pp 426-431, 1978.

13. M. Abramowitz and I. A. Stegun, "National Bureau of Standards, Applied Mathematics Series, No. 55," Government Printing Office, Washington, DC, 1964. Revised by Dover, New York, 1965.
14. R. L. Filler, "The Effect of Vibration on Frequency Standards and Clocks," 35th ASFC, pp 31-39, 1981.
15. S. Stein, private communication, 1986. using eq. 23 from Barnes et. al., "Characterization of Frequency Stability," IEEE Trans. IM, vol. IM-20, 1971.
16. D. Halford, J. S. Shoaf, and A. S. Risley, "Spectral Density Analysis: Frequency Domain Specification and Measurement of Signal Stability," 27th ASFC, pp 421-431, 1973.
17. F. L. Walls and A. E. Wainwright, "Measurement on the Short-term Stability of Quartz Crystal Resonators and the Implication for Crystal Oscillator Design," IEEE Trans. on I&M, IM-24, pp 15-20, 1975.
18. D. J. Healy, III, H. Hahn, and S. Powell, "A Measurement Technique for Determination of Frequency vs. Acceleration Characteristics of Quartz Crystal Units," 37th ASFC, pp 284-289, 1983.
19. V. Bottom, "Note on the Anomalous Thermal Effect in Quartz Oscillator Plates," American Mineralogist, Vol. 32, pp 590-591, Sept - Oct 1947.
20. C. R. Mingins, L. C. Barcus, and R. W. Perry, "Effects of External Forces on the Frequency of Vibrating Crystal Plates," 16th ASFC, pp 47-76, 1962.
21. C. R. Mingins, L. C. Barcus, and R. W. Perry, "Reactions of a Vibrating Piezoelectric Plate to Externally Applied Forces," 17th ASFC, pp 51-87, 1963.
22. R. N. Thurston, H. J. McSkimin, and P. Andreatch, Jr., "Third-Order Elastic Coefficients of Quartz," J. Applied Phys. vol 37, pp 267-275, January 1966.
23. R. W. Keyes and F. W. Blair, "Stress Dependence of the Frequency of Quartz Plates," Proc. IEEE (letters), pp 565-566, 1967.
24. P. C. Y. Lee, Y. S. Wang, and X. Markenscoff, "Elastic Waves and Vibrations in Deformed Crystal Plates," 27th ASFC, pp 1-6, 1973.
25. J. M. Ratajski, "The Force Sensitivity of AT-Cut Quartz Crystals," 20th ASFC, pp 33-48, 1966.
26. P. C. Y. Lee, Y. S. Wang, "Effects of Initial Bending on the Resonance Frequencies of Crystal Plates," 28th ASFC, pp 14-18, 1974.
27. A. Ballato, E. P. EerNisse, and T. Lukaszek, "The Force-Frequency Effect in Doubly Rotated Quartz Plates," 31st ASFC, pp 8-16, 1977 or E. P. EerNisse, T. Lukaszek, and A. Ballato, "Variational Calculation of Force-Frequency Constants of Doubly Rotated Quartz Resonators," IEEE Trans. Sonics Ultrason., Vol. SU-25, No. 3, pp 132-138, May 1978.
28. D. Janiaud, L. Nissim, and J.-J. Gagnepain, "Analytical Calculation of Initial Stress Effects on Anisotropic Crystals Application to Quartz Resonators," 32nd ASFC, pp 169-179, 1978.
29. P. C. Y. Lee and K. M. Wu, "Nonlinear Effect of Initial Stresses in Doubly - Rotated Resonator Plates," 34th ASFC, pp 403-411,

1980.

30. P. C. Y. Lee and K. M. Wu, "Effects of Acceleration on the Resonance Frequencies of Crystal Plates," 30th ASFC, pp 1-7, 1976.

31. P. C. Y. Lee and K. M. Wu, "The Influence of Support Configuration on the Acceleration Sensitivity of Quartz Resonator Plates," 31st ASFC, pp 29-34, 1977.

32. D. V. Shick and H. F. Tiersten, "An Analysis of the Acceleration Sensitivity of ST-Cut Quartz Surface Wave Resonators Supported along the Edges," 40th ASFC, pp 262-268, 1986.

33. B. K. Sinha and S. Locke, "Acceleration and Vibration Sensitivity of SAW Devices," IEEE Trans. on UFFC, vol UFFC-34, 1, pp 29-38, January 1987.

34. P. C. Y. Lee and M. S. H. Tang, "Initial Stress Field and Resonance Frequencies of Incremental Vibrations in Crystal Resonators by Finite Element Method," 40th ASFC, pp 152-160, 1986.

35. A. D. Ballato, "Effects of Initial Stress on Quartz Plates' Vibrating in Thickness Modes," 14th ASFC, pp 89-114, 1960.

36. E. D. Fletcher and A. J. Douglas, "A comparison of the Effects of Bending Moments on the Vibrations of AT and SC (or TTC) Cuts of Quartz," 33rd ASFC, pp 346-350, 1979.

37. J. A. Kusters, C.A. Adams, H. Yoshida, and J. G. Leach, "TTC's - Further Developmental Results," 31st ASFC, pp 3-7, 1977

38. A. Warner, B. Goldfrank, M. Meirs, and M. Rosenfeld, "Low "g" Sensitivity Crystal Units and Their Testing," 33rd ASFC, pp 306-310A,

1979.

39. R. L. Filler and J. R. Vig, "The Acceleration and Warmup Characteristics of Four - Point - Mounted SC and AT-Cut Resonators," 35th ASFC, pp 110-116, 1981.

40. M. Nakazawa, T Lukaszek, and A Ballato, "Force - and Acceleration-Frequency Effects in Grooved and Ring - Supported Resonators," 35th ASFC, pp 71-91, 1981.

41. R. L. Filler, J. A. Kosinski, and J. R. Vig, "The Effect of Blank Geometry on the Acceleration Sensitivity of AT & SC-Cut Quartz Resonators," 36th ASFC, pp 215-219, 1982.

42. R. L. Filler, J. A. Kosinski, and J. R. Vig, "Further Studies on the Acceleration Sensitivity of Quartz Resonators," 37th ASFC, pp 265-271, 1983.

43. R. D. Weglein, "The Vibration Sensitivity of VHF Quartz Crystals for Missile Applications," 38th ASFC, pp 73-79, 1984.

44. T. J. Lukaszek, and A. Ballato, "Resonators for Severe Environments," 33rd ASFC, pp 311-321, 1979.

45. R. Besson, J.-J. Gagnepain, D. Janiaud, and M. Valdois, "Design of a Bulk Wave Quartz Resonator Insensitive to Acceleration," 33rd ASFC, pp 37-345, 1979.

46. A. Debaisieux, J. P. Aubry, and J. Gros Lambert, "Design of SC Cut 10 MHz H.Q. Crystals with g Sensitivity Better than $2 \cdot 10^{-10}/g$," Proc. 15th Prec. Time & Time Int. Conf. (PTTI), pp 635-650, 1983.

47. J. P. Aubry and A. Debaisieux, "Further Results on 5 MHz and 10 MHz Resonators with

BVA and QAS Designs," 38th ASFC*, pp 190-200, 1984.

48. R. J. Besson, "A New Piezoelectric Resonator Design," 30th ASFC*, pp 78-83, 1976.

49. E. P. EerNisse, L. D. Clayton, and M. H. Watts, "Variational Method for Modeling Static and Dynamic Stresses in a Resonator Disc with Mounts," 43rd ASFC*, pp 377-387, 1989.

50. E. P. EerNisse, R. W. Ward, and O. L. Wood, "Acceleration-Induced Frequency Shifts in Quartz Resonators," 43rd ASFC*, pp 388-395, 1989.

51. J.-J. Gagnepain and F. L. Walls, "Quartz Crystal Oscillators with Low Acceleration Sensitivity," NBSIR 77-855, National Bureau of Standards, 1977.

52. D. A. Emmons, "Acceleration Sensitivity Compensation in High Performance Crystal Oscillators," 10th Prec. Time & Time Int. Conf. (PTTI), 1978.

53. A. Ballato, "Crystal Resonators with Increased Immunity to Acceleration Fields," "IEEE Trans S&US, vol SU-27, No. 4, pp 195-201, July 1980; or "Resonators Compensated for Acceleration Fields," 33rd ASFC*, pp 322-336, 1979.

54. A. Ballato and J. R. Vig, "Acceleration Resistant Combination of Opposite - Handed Piezoelectric Crystals," US Patent No. 4,344,010, 1982.

55. A. Ballato and J. R. Vig, "Method of Fabricating Acceleration Resistant Resonators, Resonators so Formed," US Patent No. 4,365,182, 1982.

56. A. Ballato and J. R. Vig, "Method of Fabricating Acceleration Resistant Crystal Resonators," US Patent No. 4,409,711, 1983.

57. R. L. Filler, "Acceleration Resistant Crystal resonators," US Patent No. 4,410,822, 1983.

58. J. R. Vig and F. L. Walls, "Acceleration Insensitive Oscillator," US Patent No. 4,575,690, 1986.

59. V. J. Rosati, "Suppression of Vibration Effects on Piezoelectric Crystal Resonators," US Patent No. 4,453,141, 1984.

60. V. J. Rosati and R. L. Filler, "Reduction of the Effects of Vibration on SC-Cut Quartz Crystal Oscillators," 35th ASFC*, pp 117-121, 1981.

61. J. Kusters, "The Effect of Static Electric Fields on the Elastic Constants of Alpha Quartz," 24th ASFC*, pp 46-54, 1970.

62. C. Colson, "Vibration Compensation of the Seektalk Rubidium Oscillator," 36th ASFC*, pp 197-199, 1982.

63. M. E. Frerking, "Vibration Compensated Crystal Oscillator," U.S. Patent No. 4,891,611, Jan. 2, 1990.

*ASFC - Proceedings of the Annual Symposium on Frequency Control, copies available from

1956 - 1985, National Technical Info. Service
1987 & 1988 5285 Port Royal Rd., Sills Bldg.
Springfield, VA 22161

1986, 1989, Inst. of Electrical & Electronic
1990 Engineers, 445 Hoes Lane
Piscataway, NJ 08854

Discussion

Paper n° 6

Question : Paul A. RYAN (WRDC, OHIO, OBSERVER)

What is your view on the prospects of superconductive resonators for stable oscillators ?

Answer : Dr. John R. VIG

Superconductive resonators are capable of very high Q's, however, high Q is a necessary, but not a sufficient condition for high stability. The frequency of a superconductive resonator will vary with temperature, vibration, etc ..., so it is difficult to see how a superconductive resonator could compete with a high stability crystal oscillator in an avionics environment.

By the way, one can also obtain very high Q's ($\sim 10^9$) by cooling a quartz crystal to low temperature, however, that too cannot be utilized in an avionics environment - for the same reasons, i.e., vibration - sensitivity due to lower heat capacities at low temperature, and lesser temperature stability (even without the vibration problem).

Question : Mr. AL JELALIAN (Raytheon, Author)

Crystal oscillator stability relates to the minimum Doppler shift of a target. If the transmitter frequency is increased, then the minimum Doppler shift capability is improved for the radar.

Answer : Dr. John R. VIG

A high radar frequency does help. For the same target velocity, a higher radar frequency moves the phase noise requirement further out from the carrier. A given phase noise requirement will be easier to meet, e.g. -130 dBc 70Hz from the carrier is a great deal more difficult to achieve than -130dBc 200Hz from the carrier. However, even -130dBc 200 Hz from the carrier (at 10 MHz) is beyond the state-of-the-art in a helicopter environment. Using a higher frequency oscillator, such as SAW or DRO, does not help because such oscillators' vibration sensitivity is as bad, or worse.

GaAs MMICs In Selfaligned Gate Technology
For Phased Array Radar Application

E.Pettenpaul* and U.Freyer**

*Siemens AG, Components Group, Balanstr.73, 8 Munich, FRG

**Siemens AG, Radio and Radar Division, Landshuter Str.26, 8044 Unterschleißheim, FRG

Summary

Design and performance data of GaAs MMICs for C- and X-Band T/R Radar Antenna Modules and broadband ECM application will be described. The devices considered are low noise amplifiers, medium power amplifiers, 3 W high power amplifiers, 4- and 6-bit attenuators, 4- and 6-bit phased shifters, and distributed amplifiers.

The devices are fabricated on a high-volume pilot line with only one standard high-yield process. The process used contains the following main steps: 3"-wafer cassette to cassette airtrack line, selective ion implantation for doping, lithography down to 0.5 um gatelength using I-line stepper, lithography of 0.3 um gatelength using E-beam, and reactive ion etching for dielectrics and substrate vias.

In comparison to other standard MMIC process lines it is specific, that a Self-aligned Gate Technique, the so called DIOM process, is used for production. Thereupon it is another specific aspect that an advanced inhouse CAD package for GaAs MMICs and a very accurate cell library based on on-wafer RF measurements is operational.

Highlights are the very accurate and low-loss 6-bit attenuators and phase shifters and especially a high power amplifier MMIC with 3.6W output power and 31% power added efficiency at C-Band.

1. Introduction

The object of the discussed work is the development of suitable GaAs MMICs for T/R modules in active phased array radar covering C- and X-Band. This includes low noise amplifiers, variable gain amplifiers, medium power amplifiers, high power amplifiers, and phase shifters.

Special emphasis is directed to future performance requirements, increased reliability and especially cost-effective production. To fulfill these requirements, the different MMICs are developed on a high-volume pilot line using the same selfaligned wafer process for all small-signal and high-power devices.

2. Selfaligned DIOM Wafer Process

The wafer technology used for the fabrication of MMICs and discrete MESFETs is established and unchanged in principle since 1984. It comprises a planar process up to the gate deposition with localized ion implantation, selfaligned gate technology, air-bridge crossovers and source substrate vias as low-loss interconnections.

In 1988, a 3"-wafer process was introduced and a new generation of equipment was operational. The wafers are processed now in a semiautomated facility which uses cassette to cassette equipment whenever possible, airtrack lines for the wafer transport in the different modules, I-line wafer stepper lithography down to gatelengths of 0.4 um, e-beam lithography for sub-halfmicron devices, reactive ion etching (RIE) for opening dielectric and substrate vias, and finally a new backside process module.

The most important decision was the promotion of a selfaligned gate technique for MESFETs and MMICs, the so called DIOM process (1,2,3). DIOM is an acronym for double Ge/Si contact implantation, one metallization. This abbreviation explains already the main two modified process steps: the Ohmic contact regions are realized using a combination of germanium (Ge) and silicon (Si) as dopants, allowing a single metallization step for Ohmic contacts and Schottky barriers. The Ohmic contacts consist as usual of the gold-germanium system, the Ge being provided by the implantation process and the gold as part of a suitable deposited metal sandwich (chromium-gold-tungsten-gold).

Compared to the selfaligned techniques for digital ICs, the refractory metal gate technology (4) and the dummy gate technology called SAINT (5), the DIOM process is not selfaligning with respect to the gate/n+-layer but to the gate/Ohmic contacts. Due to the available lithography equipment, the gate to n+-layer definition is on the other hand not a severe problem because the overlay stepper lithography accuracy is 0.1 um in the field by field mode.

The advantages of the DIOM process are improved device performance and reduced fabrication costs. Process simplicity and high yield are mainly a result of the truly planar submicron gate (stepper) lithography, a renunciation of an individual wafer gate recess, and of the simple metallization step. High uniformity of parameters is visible for the same reasons, improved reliability is an additional aspect related to the selfaligned unrecessed process with a tungsten metal barrier.

Using the described DIOM process, currently about 4 million MESFETs and up to 100.000 MMICs are produced the year. In the following, yield figures are presented in Table 1 on the basis of the years production.

<u>Yield of DIOM Devices</u>	
<u>MESFETs</u> : Base 3.0 M P.	
DC	> 70 %
RF	> 85 %
<u>MMIC</u> : Base 80 K P.	
DC	> 60 %
RF	> 85 %

Table 1: Production Yield of DIOM Devices

High uniformity of device dc and rf parameters is documented during 100% dc test of production wafers, wafer mapping, and 100% rf test of packaged devices. Table 2 gives a summary of typical results.

<u>Uniformity of DIOM Devices</u>	
<u>DC-Parameters:</u>	$\Delta R, \Delta G_m \leq 3\%$
	$\Delta V_{th} = 50 \text{ mV}$
<u>RF-Parameters:</u>	$\Delta G, \Delta NF = 3\%$

Table 2: Parameter Statistics of DIOM Devices

Numerous stress tests on a number of DIOM MESFETs and MMICs are routinely run. These life tests include high temperature storage (HTS) and high temperature burn in (HTB). The results summarized in Table 3 reveal 20 times the mean time to failure (MTF) compared to our conventional recess MESFETs with Ti-Pt-Au gates. The DIOM MMIC process is MIL 883 qualified and some thousands of qualified MMICs are delivered the year to US and European customers since several years.

<u>Reliability of DIOM Devices</u>	
<u>HTS:</u>	MTF = $1 \times 10^8 \text{ h}$, $T_C = 150^\circ\text{C}$, $E_A = 1.7 \text{ eV}$
<u>HTB:</u>	MTF = $2 \times 10^6 \text{ h}$, $T_C = 150^\circ\text{C}$, $E_A = 1.2 \text{ eV}$
<u>Proc:</u>	Wafer HTS Pilot Run HTB, C-Test Final Run HTB, C-Test, AQL-Base MIL 883 Qualification

Table 3: Reliability of DIOM Devices

For the realization of the below described T/R module MMICs we used either the standard process DIOM 15, i.e. 0.8 μm -MESFETs with a transit frequency (f_t) of at least 15 GHz, or the enhanced process DIOM 20 (0.5 μm -MESFETs with an f_t of 20 GHz). For the next generation of low noise X-Band devices, the process DIOM 28 (0.3 μm -MESFETs, $f_t=28$ GHz) is already qualified. For all small signal and power devices we apply the same process. Only the channel implantation is modified: flat channel doping profiles with p-buried layers are used for the small signal devices whereas comparable deeper profiles are used for the power devices.

3. CAD Tools and Cell Library

In most cases our MMIC design is carried out with the commercially available microwave program Octopus or a new CAD tool called MMIC CAD. MMIC CAD is the product of an European R&D project ESPRIT 255, started in 1985 and finished in 1989.

Compared to other CAD program, MMIC CAD has the following advanced subprograms:

- Frequency dependent models for passive components (lumped and distributed elements). The models are derived using microstrip theory including losses and line discontinuities (6).
- A broadband MESFET equivalent-circuit model including distributed gate behaviour. The equivalent-circuit elements are derived from measured hot and cold s-parameters (7,8).
- Physical models are available (7,9), which are extremely useful for the technology optimization of FETs and the control of process fluctuations.
- Two specific design kits for frequently used MMICs are available. A fast and user-friendly CAD program for the design of distributed amplifiers (10), and a nonlinear model for Dual Gate MESFET mixer MMICs based on harmonic balance technique are implemented.

An important aspect is that these programs are carefully experimentally verified up to 18 GHz.

In the past year a cell library of low noise MESFETs, switch MESFETs, driver MESFETs, and Dual Gate MESFETs was built up. The specific features of this library are the following:

- All devices show a structure that allow on-wafer RF characterization with a Cascade probe.
- The device structures used are either multifinger or meander line approaches suitable for scaling procedures.
- Scaling rules for different unit finger widths were derived. It should be mentioned that the often used linear scaling of the equivalent-circuit elements with gatewidth is inaccurate for the capacitors. On-wafer measurements of so called passive MESFETs, i.e. MESFETs without doped channel, are helpful to separate parasitic capacitances.
- A systematic follow-up of on-wafer RF measurements of MESFETs at the original substrate (600 μm thickness), thinned substrate (100 μm thickness), and without/with source vias allowed a calculation of substrate effects. As a result, already very early in the MMIC process a wafer qualification is possible. This gives the necessary information to continue or stop the process or even allows options in the following completion of the MMIC via selection and interconnection of suitable passive networks. A cell library of more than 50 devices is already available. This figure excludes the gatelength options ($L = 1.5, 0.8, 0.5, 0.3 \mu\text{m}$). In all cases, the agreement between measurement and simulation is extremely high. In the next months, the extension of the cell library with low noise HEMTs and high power MESFETs is planned.

4. C-Band GaAs T/R Module MMICs

In the following, we report the results of an internal study on C-Band (5-6 GHz) T/R MMICs. First laboratory samples of a low noise amplifier (LNA), a variable gain amplifier/attenuator (VGA), a phase shifter (PHS), a medium power amplifier (MPA) and a high power amplifier (HPA) are available.

These results together with the optimized FET models of the cell library, based on very accurate RF on-wafer measurements, will serve as a basis for the development of a set of T/R MMICs for the C-Band radar COBRA. COBRA (Counter Battery Radar) is a modern multifunction radar with an active antenna. A consortium of Siemens (FRG), Thomson-CSF (F), Thorn EMI (UK), and General Electric (USA) has now signed a development contract for this system. Within the consortium, Siemens has a subtask to develop the GaAs T/R MMICs.

Low Noise Amplifier (LNA)

A family of two-stage amplifiers was designed using in both stages the same 0.8 μm x 600 μm multifinger MESFET. The MMIC contained spiral inductors and MIM capacitors for the matching networks, and additionally bypass and decoupling MIM capacitors.

Different circuit principles were tested to realize broadband frequency response and low noise figure simultaneously. This included resistive parallel feedback and inductive series feedback. Best noise performance was achieved having only inductive feedback in the first stage. Fig. 1a shows a schematic of the circuit. In this case, the noise figure (NF) was 2.8 dB, the gain was 17 dB and VSWR at input and output was better than 2:1 (Fig. 2). A simulation showed that a further reduction of the NF

of about 0.5 dB can be realized by using our 0.5 μm - DIOM MESFET instead of the 0.8 μm - device.

Variable Gain Amplifier/Attenuator (VGA)

A VGA based on segmented Dual Gate MESFETs (SDG FET) was designed as was proposed previously by GE (10-12). By cascading DG FETs of varying gate widths and by independently controlling the second gate of each stage, variable gain operation can be achieved. Compared to analog attenuators, this VGA has the benefit that a single binary command to each control gate gives the desired attenuation. In our case, a VGA with six bits, scaled in a binary fashion was selected, which provides linear gain control in 64 uniform steps. A schematic diagram of the circuit is shown in Fig. 1b.

SDG FETs with gatelength of 0.8 μm and gatewidths of 160, 80, 40, and 20 μm were selected. The two additional bits, normally realized with small DG FETs ($W = 10.5 \mu\text{m}$), are again designed with 20 μm - segments to avoid fringing effects and divided by 2 or 4 via a voltage divider. Specific features of the circuit design are that the control voltages are fed through convenient on-chip resistors and that gate 2 is terminated by capacitors scaled in proportion to the gate width. Broadband matching is possible with a single spiral inductor at the input and output. Finally, special emphasis is directed to realize a compact layout with phase equalization.

The measured performance of the most critical states in the frequency range 3 to 8 GHz is illustrated in Fig. 3. The small signal gain at C-Band was 2.5 dB and the dynamic range was 28 dB (31 dB) realized with an operating current of only 15 mA (25 mA). Input and output return losses at C-Band were 9.5 and 7.0 dB, respectively. Incidental phase variation was $\pm 2^\circ$ for the first 32 states and $\pm 6^\circ$ ($\pm 9^\circ$) for the following 33 - 63 (64) states. Fig. 4 finally shows the gain of the VGA in selected states; precise gain control is achieved.

Phase Shifter (PHS)

A 6-bit PHS has been designed based on complementary phase shift networks to realize wide bandwidth and accurate phase shift. The present design used a combination of different circuit principles as a compromise between performance and chip size. Switched filters were selected for the higher bits (180° , 90°), loaded-line circuits were used for the medium bits (45° , 22.5°), and switched-line circuits for the lowest bits (11.25° , 5.625°). The chip also includes a T/R FET switch.

Accurate characterized lumped element spiral inductors and MIM capacitors were necessary besides transmission lines. The FET periphery was optimized for each bit to assure best VSWR and insertion loss. The two lowest bits were realized twice in a somewhat modified manner to meet the exact phase range. Again a schematic diagram of the circuit is shown in Fig. 1c.

A full analysis of the fabricated circuit included measurements of the complete 6-bit PHS MMIC and the different bits as individual chips. The worst case phase error in C-Band was $\pm 9^\circ$, whereas the RMS phase error was about 3° . The insertion loss of the complete PHS MMIC including the T/R switch was measured to be 10 dB with a maximum loss variation $< 1\text{dB}$ over all phase shift values (Fig. 5). The return loss was 9.5 dB for S 11 and 12 dB for S 22; the isolation of the switch was 16 dB. These results are similar to previous publications of 6-bit C-Band PHS MMICs (13, 14). The problem to be solved is that the two higher bits were about 20° below the target and that the 180° -element showed too much variation across the band.

Medium Power Amplifier (MPA)

An MPA or driver is designed as a 3-stage configuration (Fig. 1d). The circuit is based on a 400 μm gate width FET for the first stage, 800 μm - FET for the second and 1600 μm -FET for the third stage, respectively. The circuit integrated all matching, biasing, bypassing and coupling components. Low-loss transmission lines and MIM capacitors were used for the networks.

Design goal was an output power of about 23 dBm and gain of more than 18 dB with moderate bias conditions ($V_{\text{DS}} = 5\text{V}$, $I < 600\text{mA}$). A comparison between large-signal and small-signal designs showed similar results.

One of the main targets was the realization of the MPA with common DIOM MESFETs. Typical DC performance of the MESFETs with finger length of 0.8 μm and finger width of 100 μm were an I_{DSS} of 200 mA/mm, transconductance g_m of 125 mS/mm and source-drain breakdown voltage of $> 15\text{V}$.

The MPA MMIC demonstrated a power of 25 dBm at 1 dB compression, and a gain of more than 25 dB across the frequency band. The specified return loss of 9.5 dB for S 11 and S 22 was only achieved at midband but not yet for the complete 1 GHz bandwidth. Power added efficiency of the MPA MMIC under the mentioned bias conditions is 21 %. Typical RF power density of the used DIOM MESFET at 6 GHz is 400 - 450 mW/mm.

High Power Amplifier (HPA)

The HPA consisting of two stages was designed using the large-signal design tools of MSCs foundry service. In the meantime own large-signal CAD tools are operational.

The first stage is based on a 3 μm - MESFET driving a pair of 4 μm - devices (Fig. 1e). In both cases, the unit finger width was 200 μm . To minimize distributed effects and improve thermal resistance, a central via hole is used for the second stage MESFET. All matching circuits were realized with microstrip transmission lines. The most critical part of the circuit was the output matching network, transferring the low-value FET impedance to 50 Ω .

The HPA MMIC was designed to provide 3 W output power and a gain of at least 9 dB at a drain bias of 9.75 V and an operating current below 1400 mA. Typical DC performance of the selected 0.8 μm DIOM MESFETs were an I_{dss} of 220 - 240 mA/mm, transconductance of 105 - 110 mS/mm and source-drain breakdown voltage $>18\text{V}$.

In Fig. 6 we show the output power of different HP DIOM FETs versus gatewidth at 1 dB gain compression and 5.5 GHz. The bias conditions were $V_{\text{ds}} = 10\text{V}$ and $I_{\text{op}} = 110\text{ mA/mm}$. The duty cycle of the pulse measurement was 10%. In both cases (curve A,B), the high power density was maintained with increasing gatewidth. For the first group of devices (curve A), we measured 480 mW/mm power at a gatewidth of 1 mm and 430 mW/mm at a gatewidth of 5 mm. The second set of devices (curve B) showed $P_{-1\text{dB}} = 640\text{ mW/mm}$ for $w = 1\text{mm}$ and 520 mW/mm for $w = 5\text{mm}$. The difference between the two wafers is that one has a single (curve A) and the other a double implanted channel profile (curve B), both optimised with a physical MESFET program.

The measurements of the HPA MMIC showed an output power of 2.8 W for the MESFETs of curve A and 3.6 W for the MESFETs of type B at 1 dB gain compression. In both cases the small signal gain was about 16 dB. The power added efficiency of the better HPA MMIC showed the excellent value of 31%.

5. X-Band GaAs T/R Module MMICs

The object of a recently finished study was the realization of a T/R module prototype for applications in the lower X-Band with 10% bandwidth. The GaAs microwave circuits developed included the following components:

- A two-stage LNA consisting of two MMIC chips based on 0.5 μm -MESFETs. Typical performance of the MMIC was a NF of 3.0 dB and gain of 9.0 dB.
- A 4-bit attenuator realized with four MMIC chips. Each of the attenuator MMICs used three MESFETs as voltage-variable resistors (15) in a pi configuration (see Fig. 7). Four different chips were necessary with the following states 2/3 dB, 2/4 dB, 2/6 dB, and 2/10 dB, i.e. the insertion loss at "on-state" is 2 dB and at "off-state" is 3, 4, 6 or 10 dB. The complete 4-bit MIC showed an insertion loss of $< 8\text{dB}$, return loss $> 15\text{ dB}$ and maximum attenuation range of 22 dB at 9 GHz. The advantages of this attenuator are the low-loss broadband behaviour and the compact chip size of the subfunction MMICs.
- A 4-bit switched line phase shifter was fabricated using eight equal SPDT FET switch MMICs (Fig. 8). We used four FETs in a series-shunt configuration, so that complementary voltages will set the SPDT switch in one of its two states. For the complete 4-bit MMIC we achieved an insertion loss of 9 - 10 dB, a return loss $> 12\text{dB}$, and a worst case phase variation of $\pm 7^\circ$. Again the broadband response and compact MMIC structures are the attractive factors of the device.
- In this case, the high power amplifier based on three driver FETs and one power FET stage with 2.5 W was realized as a MIC by MSC.
- The control and power conditioning circuits of the T/R module were realized with Si CMOS circuits in special custom design.

The complete receiver module showed a gain of 32 dB. The RF output power of the transmitter was 2.5 W, and the NF of the receiver was 5.5 dB.

Based on these results and the experience with the C-Band MMIC components, a new generation of broadband X-Band MMICs is in development or planned to start. This includes an LNA with a simulated NF $< 2.5\text{ dB}$ designed with very low noise 0.3 μm MESFETs, and a 6-bit VGA using S₀G FET.

A technology study on enhanced DIOM power MESFETs is also in progress. The up to now achieved power densities of more than 500 mW/mm at 1 dB gain compression are encouraging results.

6. Conclusions

A set of C-Band T/R module MMICs was realized as laboratory samples using the high-yield, high-uniform selfaligned DIOM production technique. Due to this technique, the samples showed already very accurate results although preliminary FET models have been used. These experience together with improved FET models, derived by on-wafer RF measurements, are the basis for the currently started development of MMICs for COBRA.

A remarkable result was the achieved RF output power of 3.6 W at 1 dB gain compression for a HPA MMIC terminated with 50 Ω . This corresponds to a power added efficiency of 31%.

The exclusively use of the selfaligned DIOM technique allows higher integration levels in future including the combination of small signal and power circuits.

The experience will be used to develop broadband PAR systems in X-Band. Besides, these GaAs MMICs are of interest for future applications like MIDS (Multifunctional Information Distribution System), NIS (NATO Identification System), and synthetic aperture radar for satellite systems.

References

- (1) E.Pettenpaul, J.Huber, H.Weidlich,
European patent no. 81100732.7 (1981), US patent no. 4.377.030 (1983)
- (2) E.Pettenpaul, W.Heidenreich, J.Huber, W.Flossmann,
"A High-Temperature Sensor Based on Monolithic GaAs Hall IC",
GaAs IC Symp. Digest (1985), pp. 169-172
- (3) E.Pettenpaul
"State-of-The Art OF MMIC Technology And Design In West Germany",
IEEE MTT-Symp. Digest (1987), pp. 763-766
- (4) N.Yokoyama, T.Mimura, M.Fukuta, and H.Ishikowa,
"A Selfaligned Source/Drain Planar Device for Ultrahigh-Speed GaAs MESFET VLSI's",
ISSCC Symp.Digest (1981), pp. 218-219
- (5) K.Yamasaki, K.Asai, T.Mizutani, and K.Kurumada,
"Selfaligned Implantation for N-Layer Technology (SAINT) for High-Speed GaAs IC's",
Electron.Letters 18 (1982), pp. 119-121
- (6) E.Pettenpaul, H.Kapusta, A.Weisgerber, H.Mampe, J.Luginsland, I.Wolff,
"CAD Models of Lumped Elements on GaAs up to 18 GHz",
IEEE Trans MTT-36 (1988), pp. 294-304
- (7) E.Pettenpaul, F.Ponse, O.Berger, H.Kapusta,
"Device-Physics Model and Equivalent-Circuit Model for GaAs MESFETs",
Siemens Res.& Dev.Reports 16 (1987), pp. 210-218
- (8) G.Dambrine, A.Cappy, F.Holidore and E.Playez,
"A new Method for Determining the FET Small-Signal Equivalent Circuit",
IEEE Trans MTT-36 (1988), pp. 1151-1159
- (9) G.Ghione, C.Naldi, E.Pettenpaul, F.Ponse,
"Physical and Equivalent-Circuit Models for GaAs MESFETs",
ESPRIT Technical Week (1988) Digest
- (10) Y.C.Hwang, Y.K.Chen, R.J.Naster,
"A Microwave Phase and Gain Controller with Segmented Dual Gate MESFETs in
GaAs MMICs",
IEEE MTT Symp-Digest (1984), pp. 1-5
- (11) R.J.Naster and Y.C.Hwang,
"An L-Band Variable-Gain Amplifier GaAs MMIC with Precise Binary Step Control",
GaAs IC Symp. Digest (1987), pp. 235-238
- (12) K.H. Snow, J.J. Komiak, D.A.Bates,
"Wideband Variable Gain Amplifiers in GaAs MMIC",
IEEE MTT Symp. Digest (1988), pp. 183-187
- (13) C.Andricos, I.J.Bahl, and E.L.Griffin,
"C-Band 6-Bit GaAs Monolithic Phase Shifter",
IEEE Trans. ED-32 (1985), pp. 2760-2765
- (14) A.W.Jacomb-Hood, J.A.Windyka, M.S.Booth, K.H.Snow, S.B.Adams,
"C-Band Phase and Gain Control MMIC",
GaAs IC Symp. Digest (1988), pp. 257-260
- (15) G.S.Barto, K.E.Jones, G.C.Herrik, and E.W.Strid,
"Surface-Mounted GaAs Active Splitter and Attenuator MMICs Used in a 1-10 GHz
Leveling Loop",
IEEE Trans. ED-33 (1986), pp. 2100-2106

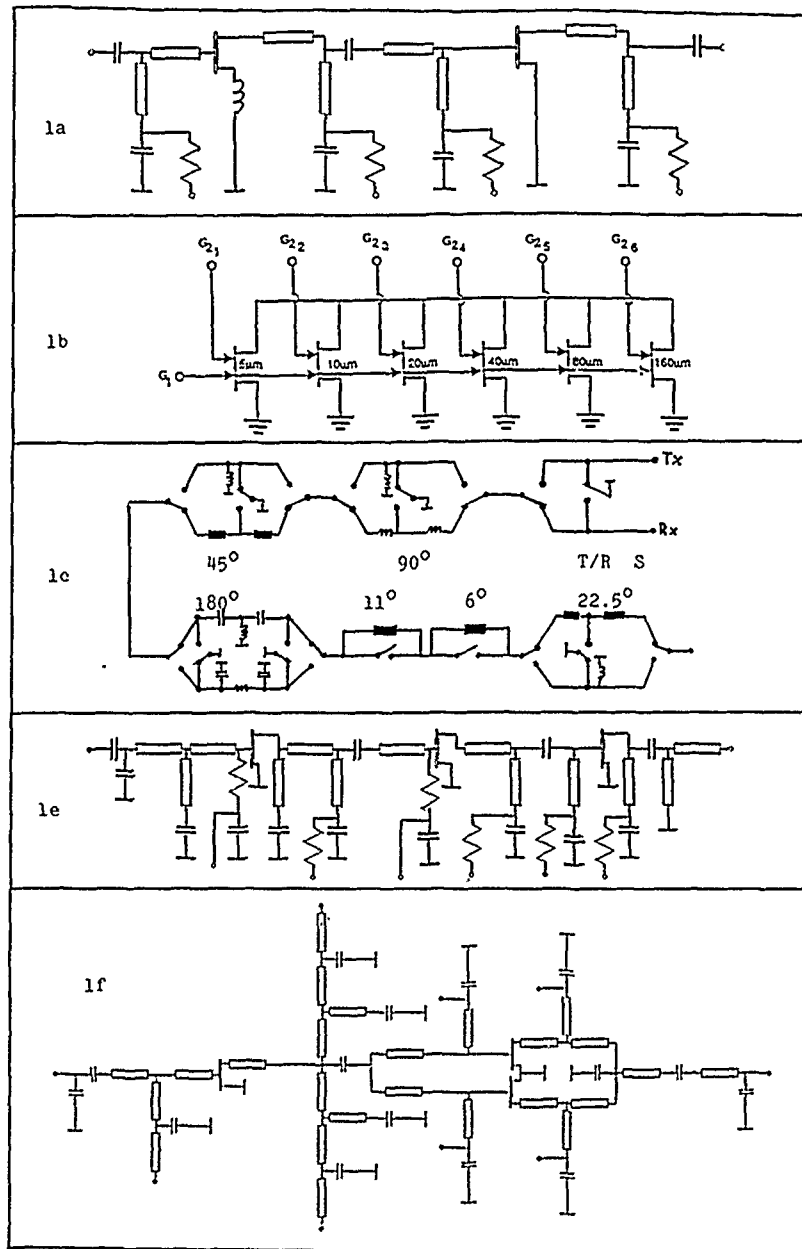


Fig.1 : Schematic Circuit Diagram of the C-Band
T/R Module MMICs: LNA (1a), VGA (1b), PHS (1c),
MPA (1e), HPA (1f)

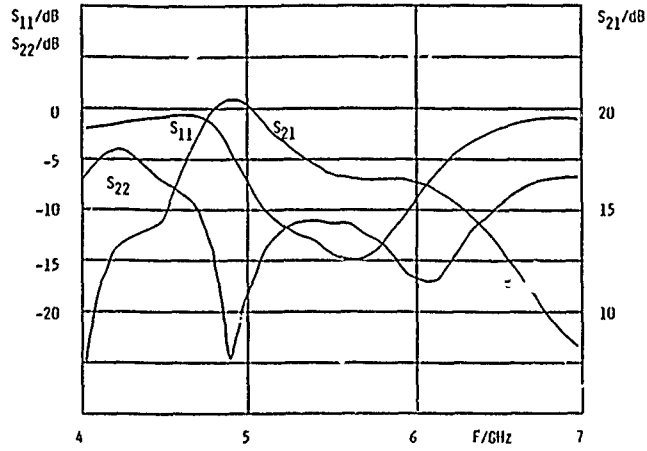


Fig.2 : Low Noise Amplifier MMIC Performance

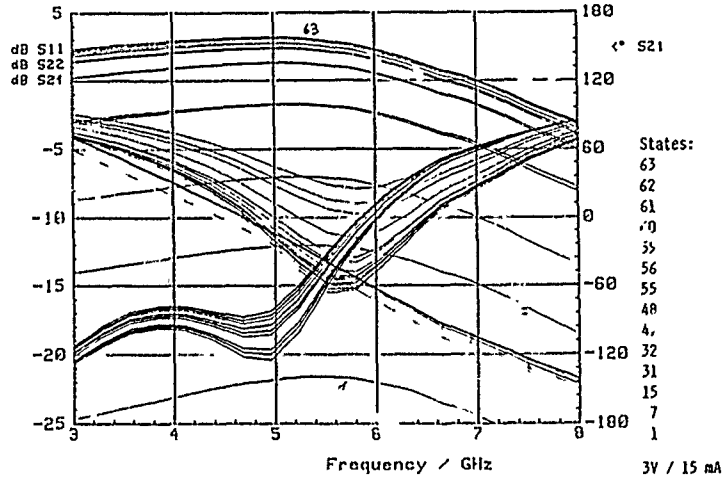


Fig.3 : 6-bit Variable Gain Amplifier MMIC Performance

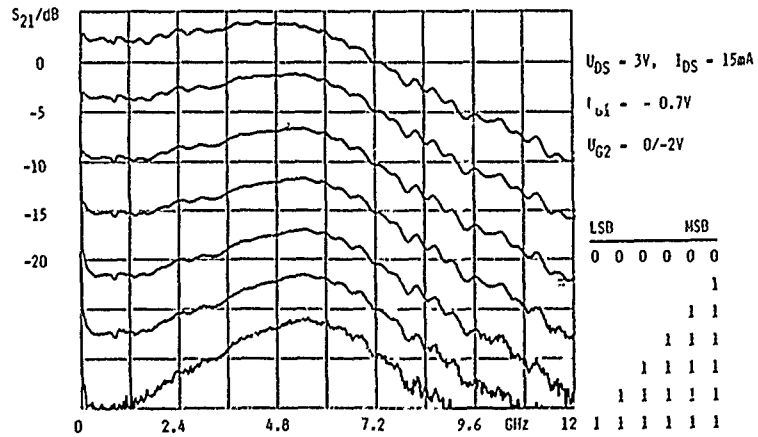


Fig.4 : 6-bit VGA Gain in the most important States

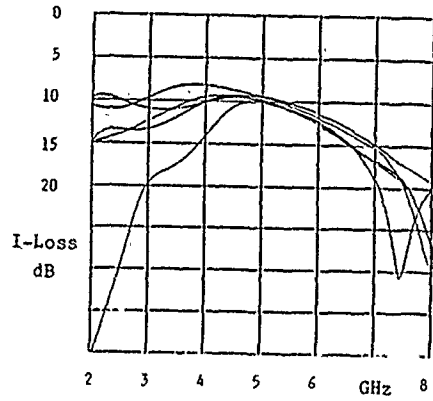


Fig.5: 6-bit Phase Shifter MMIC, Insertion loss

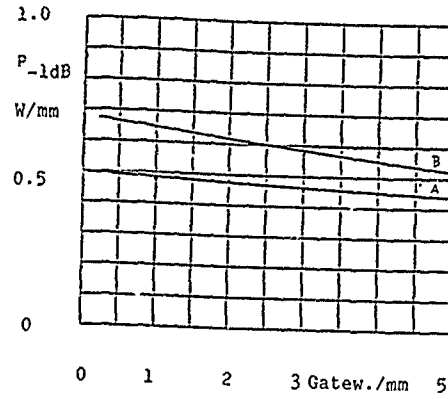


Fig.6: RF Output Power at 6 GHz, DIOM Power MESFET

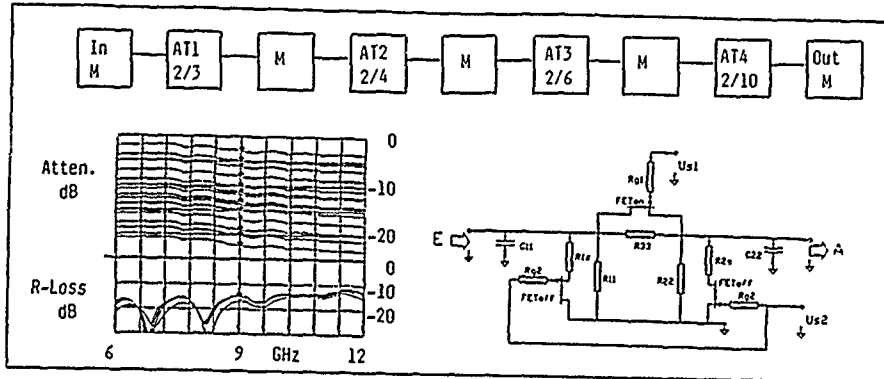


Fig.7: 4-bit X-Band Attenuator Circuit Diagram, Circuit of the Subcomponent MMICs, and Performance

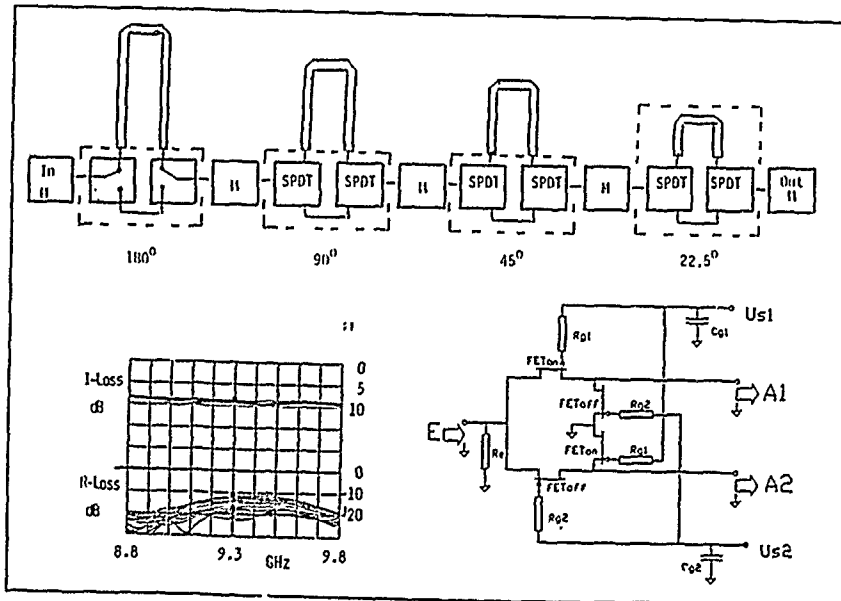


Fig.8: 4-bit X-Band Phase Shifter, Circuit Diagram, Circuit of the SPDT MMICs, and Performance

Discussion

Paper n° 8

Question : Mr. P. BRIERE (Thomson-CSF)

- What are the MMIC chip size of the C band module ?
- Do you use a different gate to drain spacing (than gate to source) in order to increase breakdown voltages ?

Answer : Dr. PETTENPAUL

- Chip size is of course different for the 5 MMICs. The smallest device is the VGA with about 1,5 mm² and the largest MMIC is the phase shifter with about 9 mm²; the power circuits are between. First design is not optimised with respect to chip size.
- This was not necessary because the most sensitive device, the high power amplifier, howed a breakdown voltage of more than 18 V.

PERFORMANCES OF MMIC X-BAND POWER AMPLIFIERS OBTAINED IN FOUNDRY

by

Gilles Apercé
Electronique Serge Dassault
55, Quai Marcel Dassault
92214 Saint-Cloud
France

ABSTRACT

Two class A X-Band power MMICs chips designed at ESD for phased array applications are described. Both have been consistently manufactured in just one foundry pass. The former has been processed by "M/A - COM" in 1987 and the latter by "TEXAS INSTRUMENTS" in 1989.

A 10 GHz pulsed output power of 30 dBm saturated with 29 dB associated gain and 13% power added efficiency was achieved for the first power amplifier (M/A-COM foundry). The accurate small signal modeling of active and passive elements was the key to obtain these very good performances in the first design iteration.

A 18% power added efficiency with 29 dBm output power at 1 dB compression gain and 24 dB associated gain in CW was obtained for the second amplifier (T.I. foundry).

CW performance over 9-11 GHz was accurately predicted using a large signal FET model (developed with our non-linear characterization tools) and a harmonic balance analysis. Massive DC and RF measurements were performed on the wafers.

Good chips were then sorted out with the help of our database. We obtained 58% DC + RF yield.

INTRODUCTION

In our effort to reduce size and cost of transmit/receive modules used in airborne phased array radar applications, Monolithic Microwave Integrated Circuits (MMICs) have become a primary focus of many development programs.

The design of a Monolithic Microwave Integrated Circuit usually takes multiple foundry iterations that make this process long and expensive. A good knowledge of the constituting elements helps to reduce the time and cost of designs.

A special effort in the modeling of passive elements and in the small and large signal characterization of field effect transistors was the key to obtain very good performance for a X-band GaAs miniaturized monolithic power amplifier after the first foundry pass.

High yield (and low cost) is of major concern in the mass production of monolithic integrated circuits. In order to obtain a high manufacturing yield, a process tolerant design approach combining sensitivity and statistical analysis has been performed.

This paper presents the efforts and results in designing and testing X-Band power amplifiers.

CIRCUIT DESIGN

Our aim was to obtain at least 25 dB gain over a frequency band of 10% with a 1W output power at 1 dB compression gain in pulsed mode.

- Passive Elements [1]

Spiral inductors were the most important and required a very careful modeling. The computational method used and developed by Ph. Dueme at ESD is completely independent of the technology of the foundry. The model is based on the computation of linear and mutual inductances, including the effect of the image spiral due to the ground plane, and the computation of parasitic ground plane, and inter-turns capacitances. The accuracy of the model depends strongly on the way the repartition of these capacitances is taken into account along the spirals. The straight forward calculation allows optimization on geometric parameters. The accuracy of the model helps to obtain a compact circuit, by predicting the effect of parasitic coupling parameters.

The model was verified with very accurate measurements on wafer obtained with a test bench including cascade Microtech RF probes associated with a HP 8510 network analyser calibrated on wafer with TRL method [2].

Figure 1 shows a comparison between the simulation and the measurement of a 1 nH spiral inductor.

- FET'S modeling

- The small signal FET model achieved with our own tools was based on the work of Lille University [3] and completed with the model provided by the foundry.

- The effective large signal output impedance had been estimated using the well known technique of combining a DC load line with the small signal output capacitance for the first ESD design (M/A—COM foundry).
- The same method plus our own non-linear characterization tools based on pulsed I-V curves measurement has been used to obtain a large signal model for the second ESD design (T.I. foundry).
- Amplifiers modeling
 - Amplifiers consist of three stages of single Gate FET
 - First Amplifier
 - The first, second and third stages have 700, 1400 and 2800 μm gate peripheries respectively, with a gate length of 1 μm .
 - The design is very compact (total area of 3 mm^2) (Figure 2).
 - Second Amplifier
 - The first, second and third stages have 600, 1200 and 2400 μm gate peripheries respectively, with a gate length of 0.5 μm .
 - Total area 5.5 mm^2 (Figure 3).

With results of first amplifier, sensitive and statistical analysis, we identified the circuit parameters that have dominant effects on amplifier performances.

We improved the RF Yield for the second amplifier with this process tolerant design approach.

Figure 4 shows sensitive analyses on G_m critical parameters.

For the two amplifiers, the large signal output circuit was designed first and treated as a fixed termination for designing the interstage and input networks. Optimisation of the interstage network for gain flatness and input circuit for return loss was completed using "Super-Compact" CAD software.

Large signal analysis in class A of the CW performance for the second ESD Design was accomplished using harmonic balance simulators "Libra" and "Microwave Harmonica".

Figures 5 and 6 show the drain load cycle for the two last stages obtained with "Microwave Harmonica" and non-linear models based on Y.Tajima [4]. Results demonstrate that when the output FET is at 1 dB of compression, the second stage is still in linear region.

AMPLIFIERS PERFORMANCES

- First Amplifier (M/A—COM founder) [5]
 - We measured 30 dBm saturated (Figure 7) with 29 dB associated gain and 13% power added efficiency on 10% bandwidth. These measurements were obtained under pulsed drain operation at 1 microsec pulse length and 5% duty factor.
 - We also designed on the same wafer a two stages amplifier. A comparison between simulation, pulsed measurement and CW measurement shows an excellent agreement. The gain dispersion is due to effect in "on wafer" measurement (Figure 8).
- Second Amplifier (T.I. founder)
 - The measured output characteristics shown in Figures 9, 10, 11 indicated a power added efficiency of 18% with an output power at 1 dB compression gain of 29 dBm in CW mode across the 9–11 GHz frequency range. Those results have been obtained with the same biasing conditions on each amplifier stage.
 - Those conditions correspond to a 23.6 dB small signal gain. A greater gain can be obtained with different gate biasing voltages on each stage but it's more convenient to use uniform biasing voltages for the integration aspect.
 - The difference between the simulated and measured gain is due to FET model, too optimistic for transconductance G_M (influence of temperature).
 - Up to now, measurements in pulsed mode haven't been performed but one can expect better results than in CW mode.
 - DC measurements had been made by T.I. on wafers. We obtained a 78.8% total DC yield.
 - RF measurements were performed on the wafers with lower biasing voltages in order to avoid thermal dissipation problems. Figure 12 shows the DBS21 histogram provided by our measurement Data Base. We obtained a total yield DC+RF of 58% with a gain of 27.5 dB \pm 1 dB.
 - Good chips were sorted out and samples were measured with the full bias voltage.

CONCLUSION

We have demonstrated that one foundry pass design of GaAs X-Band power amplifier is feasible. This was achieved by accurate linear and non-linear, passive and active circuits characterizations.

Our efforts in designing and testing power amplifiers in high volume have been presented.

ACKNOWLEDGEMENTS

I would like to thank M.J.Villard, M.Cambon, H.Bobot, Ph.Dueme and P.Fages from ESD. I would also like to thank M/A-COM and TI foundry teams, M.Fache and Pl. Ouvrard for their support.

M.J.Villard, working on the non-linear characterization tools at ESD.

M.Cambon, working on our measurement data base.

Ph.Dueme, working on passive elements model (spiral inductor model).

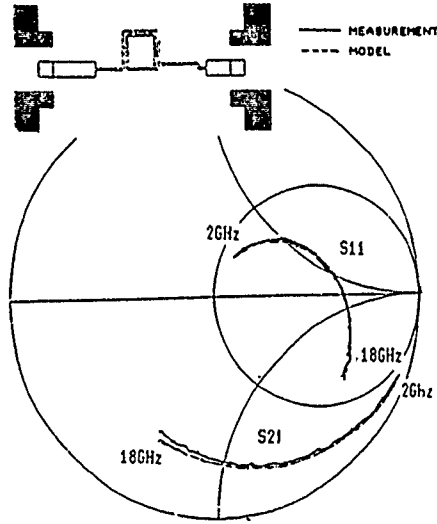
H.Robot and P.Fages, working on wafer measurements.

BIBLIOGRAPHY

- [1] Dueme, Ph. *Méthodologie de conception des circuits monolithiques hyperfréquence sur Arséniure de Gallium*. L'Onde
Apercé, G. Electrique, vol.96 No.2, Mars—Avril 1989.
- [2] Ouvrard, Pl. *La mesure des circuits monolithiques hyperfréquences en liaison avec la conception*. Journée Nationale
Fages, P. Microondes, Nice, juin 1987.
- [3] Dambrine, G. *A New Method for Determining the FET Small-Signal Equivalent Circuit*. IEEE Transactions on
Cappy, A. Microwave Theory and Techniques, vol.36, No.7, July 1988.
Heliodore, F.
Playez, E.
- [4] Tajima, Y. *Design of Broad-Band Power GaAs FET Amplifiers*. IEEE Transactions on Microwave Theory and
Miller, P. Techniques, vol. MTT-32, No.3, March 1984.
- [5] Apercé, G. *Réalisation rapide d'un amplificateur monolithique de puissance en bande X à l'aide de modélisations
Dueme, Ph. précises*. Journées Nationales Microondes, Nice, Juin 1987.

The Design of the First Amplifier presented was supported by French administration under DRET contract.

FIG. 1 COMPARISON BETWEEN MEASUREMENTS AND SIMULATION OF 1nH SPIRAL INDUCTOR .



PHOTOGRAPHS OF MMICS AMPLIFIERS

FIG. 2 M/A-COM FOUNDRY

FIG. 3 TEXAS INSTRUMENTS FOUNDRY

FIG. 7 OUTPUT POWER VERSUS INPUT POWER AT 10GHZ
(FIRST AMPLIFIER , M/A-COM FOUNDRY)

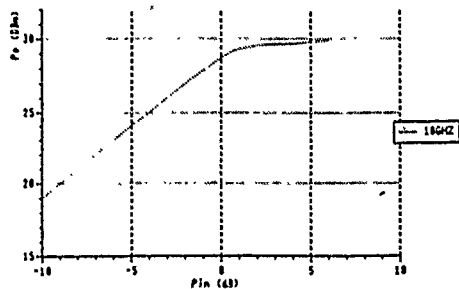


FIG. 8 TWO STAGES AMPLIFIER
COMPARISON SIMULATION-MEASUREMENTS

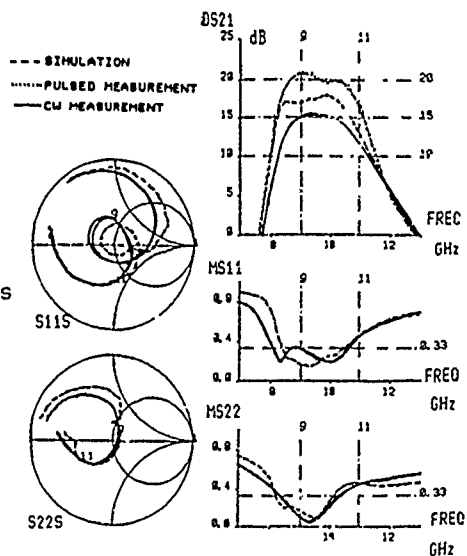


FIG. 12 HISTOGRAM
DBS21 AT 10GHZ ON 107 AMPLIFIERS
ON WAFER MEASUREMENTS AT LOWER BIASING CONDITIONS

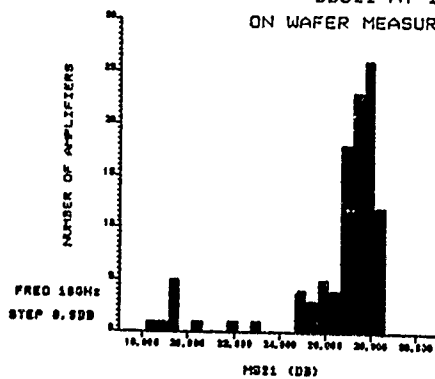


FIG. 9 OUTPUT POWER VERSUS INPUT POWER
(SECOND AMPLIFIER, T. I. FOUNDRY)

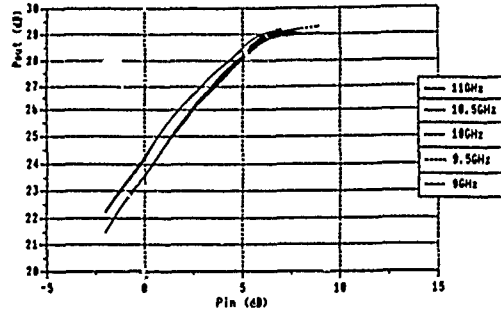


FIG. 10 OUTPUT POWER AT 1DB COMPRESSION GAIN
VERSUS FREQUENCY (SECOND AMPLIFIER, T. I. FOUNDRY)

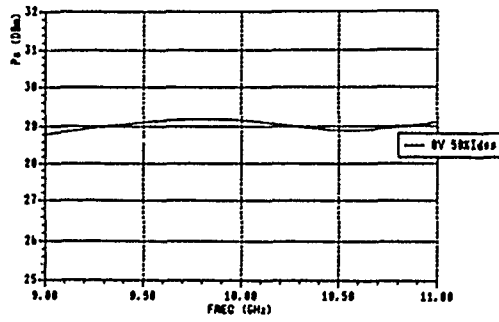
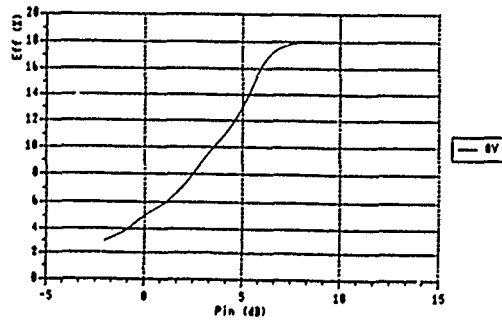


FIG. 11 POWER ADDED EFFICIENCY VERSUS INPUT POWER
(SECOND AMPLIFIER, T. I. FOUNDRY)



MILLIMETER-WAVE MONOLITHIC INTEGRATED RECEIVER CIRCUITS

Lorenz-Peter Schmidt, Bernd Adelseck
 TELEFUNKEN SYSTEMTECHNIK, D-7900 Ulm, FRG
 Alexander Colquhoun, Telefunken electronic, D-7100 Heilbronn, FRG
 Heinrich Dämbkes, Daimler Benz Research Center, D-7900 Ulm, FRG

ABSTRACT

Recent advances in the development of millimeter-wave semiconductor devices and monolithic integrated circuits are reported. Based on a compatible process, allowing for integration of Schottky diodes and MESFETs on one chip, receiver circuits have been developed for the 35, 50-60, and 94 GHz frequency ranges. Also, the present status of work on broadband mixers and dielectric resonator oscillators will be presented. Further, single and dual gate HEMTs with excellent noise figures have been developed forming a very promising basis for mm-wave low-noise amplification.

INTRODUCTION

Concepts for future millimeter-wave airborne radar sensors, e.g. for helicopters and missiles, increasingly rely on phased array configurations. This calls - even more than at microwave frequencies - for consequent utilization of monolithic integrated components and supercomponents, since the antenna element spacing decreases with increasing frequency.

On the other hand, an increasing threat for aircrafts, arising from millimeter-wave radar guided missiles, will have to be taken into account. Therefore, the frequency range of airborne radar warning receivers and ESM/ECM systems will have to be extended to the millimeter waves. Severe weight and volume restrictions will call for compact highly integrated and reliable millimeter-wave converters.

This paper reports on recent advances in design, technology and development of millimeter-wave semiconductor devices and monolithic integrated circuits, potentially suitable for use in phased array radar, radar warning receiver and LPI communications systems. The work to be described is being performed at TELEFUNKEN SYSTEMTECHNIK, Ulm in cooperation with TELEFUNKEN electronic, Heilbronn, and the Daimler Benz Research Institute, Ulm.

During the last years, a compatible process has been developed, allowing for integration of very low noise Schottky diodes and MESFETs on one chip. Using this technology, balanced mixers and IF amplifiers have been integrated on a single chip for operating frequencies around 35 GHz, 50 GHz and 60 GHz. A 94 GHz version currently is processed. In a modified circuit configuration, broadband mixers with approximately 10 GHz inherent bandwidth, suitable for RWR application, are under development.

Also, first results on millimeter-wave dielectric resonator oscillators for the 30 GHz frequency range will be presented.

Recently developed single and dual gate HEMT devices and subsequent circuit simulations demonstrate excellent noise figures and are currently used for the design of mm-wave low noise amplifiers.

The circuits under work will allow for rigorous integration of millimeter-wave receivers in the 18-100 GHz frequency range.

M³C TECHNOLOGY

For the monolithic integration of both planar Schottky mixer diodes and GaAs MESFET's, a novel technology has been developed and used for the fabrication of receiver circuits (2/, 4/). The technology differs from most other MMIC technologies, as it incorporates an n+ buried layer to reduce the series resistance of the Schottky mixer diodes. For the present work IF frequencies of up to 5 GHz are envisaged and the integration with further stages, such as the local oscillator, should be possible. For this reason, recessed gate MESFET's with electron-beam lithography of the gate structures were included. All the lithographic processes apart from that for the gate metallization are carried out using standard contact lithography. A schematic cross section of the completed active devices is shown in Fig. 1.

The buried n+ zones are formed by selective implantation of Si+ and Si++ into the semi-insulating substrate using SiO₂ as a mask. The sheet resistance of the buried layer was optimized by varying the implantation parameters and the subsequent rapid thermal anneal (RTA).

After suitable surface preparation, the active n layer ($d = 0.2 \mu\text{m}$, $n = 3.5 \times 10^{17} \text{cm}^{-3}$) and a further n+ layer ($d = 0.1 \mu\text{m}$, $n = 2 \times 10^{18} \text{cm}^{-3}$) are deposited by MOCVD. This active layer is used for both the MESFET devices and the mixer diodes so that the carrier concentration of the material for the Schottky diodes is higher than that usually used for this application. In the areas between the active devices these epitaxial layers are subsequently made highly resistive by selective boron implantation. AuGe ohmic contacts are fabricated using a suitable lift-off procedure and RTA alloying. The Schottky contacts for the MESFET gates and the Schottky diode fingers are defined by electron lithography. A single layer PMMA resist process is applied. The exposure conditions are optimized to give undercut resist profiles suitable for lift-off processing. The gate structures are aligned to the source and drain contacts using alignment marks fabricated with the AuGe metallization. After wet chemical recess etching, the contacts are formed by evaporation of Ti Pt Au and lift-off. All the devices are passivated by a plasma deposited Si₃N₄ layer. This material is also used as an insulator for the MIM overlay capacitors.

The technology also includes the fabrication of both air bridges for low-capacitance crossovers and via holes for low-inductance ground connection.

DIODES AND MESFETS

A wide variety of diode and transistor configurations has been fabricated to get optimum devices for receiver applications. A diode with 3 fingers each $0.3 \times 4 \mu\text{m}^2$ is shown in Fig. 2. The measured values $C_j = 11 \text{ fF}$ and $R_s = 6.1 \Omega$ result in an $f_T = 2370 \text{ GHz}$.

The fabricated MESFETs have gate lengths between 0.3 and 1.0 μm and different gatewidths in π - and multi finger configuration to satisfy the different requirements of the different parts of the receiver circuit. The short gatelength transistors are used for an integrated LO, consisting of a dielectric resonator stabilized FET oscillator and a buffer amplifier in the 24 - 30 GHz frequency range.

Together with the Schottky mixer diodes, varactor diodes are under development to realize varactor diode doubler circuits.

S-parameter measurements of the short gatelength transistors showed an extrapolated $f_{\text{max}} = 70 \text{ GHz}$ and a $\text{MAG} = 7 \text{ dB}$ at 30 GHz. The transistors with longer gatelengths (0.75 μm) were used for the design of an integrated low noise IF amplifier with 2 stages for an IF bandwidth from 4 to 5 GHz. Device noise figures of 0.8 dB at 4.5 GHz with an associated gain of 11 dB have been measured.

MILLIMETER WAVE MIXER AND RECEIVER CIRCUITS

The technology and the devices described have formed the basis for the development of millimeter wave balanced mixers and mixer /IF amplifier chips. The work started with a 35 GHz balanced mixer, integrated with a 0.5 - 1.0 GHz IF amplifier (1), and was followed by several mixer /IF amplifier configurations for signal and LO frequencies in the 50 - 60 GHz frequency range and an IF near 4 GHz (2-4). Fig. 3 shows complete 60 GHz receiver chip on a 150 μm GaAs substrate.

LO and signal frequencies are fed to the diodes through a branchline coupler which has been designed using in house software with improved models of the MSL-Tee junction and coupling between the lines of the coupler (6). An improved bandwidth of 15 % was achieved by adding 4 open ended stubs to the coupler. As the coupler has a 90° phase difference between its two output ports, a line length of a quarter of a wavelength was added to one port to get a phase difference of 180° at the center frequency of the mixer. The RF-short between the diodes is realized by a radial stub.

Two side coupled DC stops allow DC bias of the diodes through two bandstop filters for optimum performance. For self bias operation the two bias pads are connected to ground. The IF-output is also realized as a bandstop filter with a radial stub to reject LO and signal.

Fig. 4 shows the measured conversion loss and noise figure of a 60 GHz mixer chip versus LO power in self bias operation. A DSB-noise figure of $N_F = 3.3$ dB combined with 6 dB conversion loss was achieved. The LO-power was $P_{LO} = 6.5$ dBm at 55.4 GHz. IF was 4.1 GHz in this case.

The two stage IF amplifier employs two $0.75 \mu\text{m}$ MESFET's. The first stage is optimized for lowest noise figure and the second stage for highest gain. The noise and gain performance are shown in Fig. 5. The measured minimum noise figure was 1.7 dB with an associated gain of 20.6 dB at 4 GHz.

The layout of a 94 GHz balanced mixer on $100 \mu\text{m}$ GaAs developed recently is shown in Fig. 6. As best values a conversion loss of 7.5 dB with an associated noise figure of 4.0 dB (DSB) in self bias operation has been measured. The associated LO power consumption was 5 dBm (Fig. 7). Presently, the 94 GHz balanced mixer is being integrated with a 0.5 - 2 GHz IF amplifier on a chip.

Recent experiments with Lange couplers have proven that wide-band balanced mixers can be realized by replacing the branchline couplers in the mixers (Fig. 3, Fig. 6) by Lange couplers. Bandwidths in the order of 10 GHz at mm-wave frequencies are expected, making these devices ideally suitable for RWR applications.

DIELECTRIC RESONATOR OSCILLATORS

The present concept for LO supply of our mm-wave mixers is based on the $0.3 \mu\text{m}$ MESFETs described above and on M³IC process compatible varactor diodes for frequency multiplication. A fundamental frequency is generated by a dielectric resonator stabilized MESFET oscillator (DRO) and amplified and decoupled by a MESFET buffer amplifier and then doubled or tripled to the desired LO frequency by a varactor multiplier (Fig. 8).

Experiments with hybrid integrated DRO's with MESFETs from the M³IC process and circuit configurations easily transferable to monolithic designs, very promising results have been obtained in the 20 - 30 GHz frequency range (/9/). The layout of the circuit is shown in Fig. 9. A common source topology with series feedback was employed. The dielectric resonator is coupled to the gate line of the MESFET and the output port is at the drain side. This type of DRO exhibits a superior frequency stability and pulling and a low phase noise due to the isolation between the frequency determining element and the output. As indicated in Fig. 9, the output frequency of the oscillator is easily adjusted over a wide range (20 - 26 GHz) by placing the dielectric resonator at corresponding positions along the gate line. The output power is 12 ± 1 dBm over the specified frequency range, and the phase noise is better than -80 dBc/Hz at 10 KHz from carrier frequency (Fig. 10). Presently, a monolithic version of this oscillator is processed.

LOW NOISE HETEROSTRUCTURE DEVICES AND CIRCUITS

During the last few years, heterostructure field effect transistors (HEMT) have demonstrated their excellent noise properties up to the 100 GHz frequency range. After optimization of discrete devices the HEMT technology is now being developed towards fabrication of monolithic integrated circuits- mainly low noise microwave and mm-wave amplifiers.

Our research activities towards low noise HEMTs have concentrated on the following features (/10/):

- high mobility and high velocity of the electrons
- highest sheet electron density in the channel
- good confinement of the carriers in the channel
- high transconductance g_m to output conductance g_d ratio g_m/g_d
- low parasitic capacitances with high c_{gs} to c_{gd} ratio.

Consequent improvements in layer design and recent advances in electron-beam lithography have led to HEMT devices with outstanding performance. For example standard AlGaAs/GaAs HEMTs from our labs show a cut-off frequency of 60 GHz for a gate length of $0.9 \mu\text{m}$. For shorter gates ($0.3 \mu\text{m}$) the cut-off frequency f_{max} increases to 120 GHz (Fig. 11). These devices exhibit very low noise figures of 0.55 dB at 12 GHz and 0.7 dB at 18 GHz (/11/).

The best noise figures ever reported for GaAs based HEMTs have been achieved by us using $0.25 \mu\text{m}$ gates and very high carrier concentrations in the channel resulting in 0.45 dB of noise figure at 18 GHz at 300 K (Fig. 12), (/12/). These devices are very promising candidates for mm-wave low noise amplification. Presently, low noise amplifiers are under

design in the 30 and 60 GHz frequency range. Also, a 2 - 18 GHz travelling wave amplifier is processed on the basis of dual gate HEMTs in a cascode configuration (Fig. 13): The predicted performance is plotted in Fig. 14.

Pseudomorphic HEMTs on GaAs and on InP are currently studied in the research labs and have already demonstrated even better performance than conventional HEMTs. These devices probably will be the work horses of the next generation M³ICs.

Further, heterojunction bipolar transistors (HBTs) are currently developed for mm-wave power amplifier and low phase noise oscillator applications.

CONCLUSION

The results presented in this paper demonstrate that high performance semiconductor devices and mm-wave monolithic integrated circuits (M³ICs) are available for system applications up to 100 GHz. Within a few years, nearly all circuit functions of mm-wave sensor front-ends might be covered by available M³IC technology, opening new perspectives for highly integrated, highly reliable millimeterwave systems.

ACKNOWLEDGEMENT

The authors would like to thank the German "Ministerium für Verteidigung" and the "Ministerium für Forschung und Technologie" für financial support.

REFERENCES

- /1/ Adelseck, B.; Colquhoun, A.; Menzel, W.; Schmegner, K.E.: A 35 GHz Monolithic Receiver, MM 88 Proceedings, London, pp. 505-510.
- /2/ Colquhoun, A. et al.: A fully integrated 60 GHz receiver, GaAs-IC-Symp. Digest, 1989, pp. 185-188.
- /3/ Adelseck, B. et al.: A monolithic 60 GHz diode mixer in FET compatible technology, MMIC-S-Digest, 1989, pp. 91-94.
- /4/ Adelseck, B. et al.: A monolithic 60 GHz diode mixer and IF amplifier in compatible technology, IEEE-Trans. on MTT, vol. 37, Dec 89, pp. 2142-2147.
- /5/ Pucel, R.A. et al.: Signal and noise properties of Gallium Arsenide Microwave Field Effect Transistors, Advances in Electronics and Electron Physics, Vol. 38, pp. 195-265 (Academic Press, NY, 1975).
- /6/ Menzel, W.; Wolff, I.: A method for calculating the frequency dependent properties of microstrip discontinuities, IEEE-Trans. on MTT, vol. 25, Feb. 77, pp. 107-112.
- /7/ Giannini, F.; Sorrentino, R.; Urba, J.: Planar circuit analysis of microstrip radial stub, IEEE-Trans. on MTT, vol. 32, Dec. 84, pp. 1652-1655.
- /8/ Held, D.N.; Kerr, A.R.: Conversion loss and noise of microwave and millimeter wave mixers, IEEE Trans. on MTT, vol. 26, Feb. 78, pp. 49-61.
- /9/ Dieudonné, J.M.: A simple broadband MESFET DRO design for mm-wave applications. Proc. GaAs 90, Rome, 1990.
- /10/ Dämpkes, H.: Heterostructure devices for GHz communication. Proc. MIOP, Sindelfingen 1990.
- /11/ Narozny, P. et al.: "On wafer noise parameters of AlGaAs/GaAs HFETs for X-Band low noise MMICs", to be published
- /12/ Narozny, P. et al.: "Extremely low noise GaAs HFET", submitted for publication

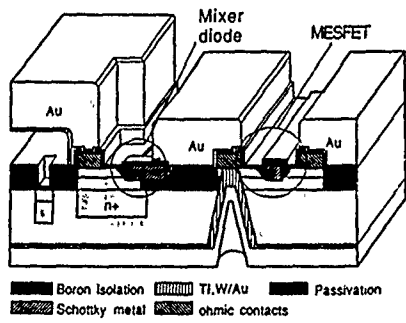


Fig. 1: A schematic cross section of the active devices.

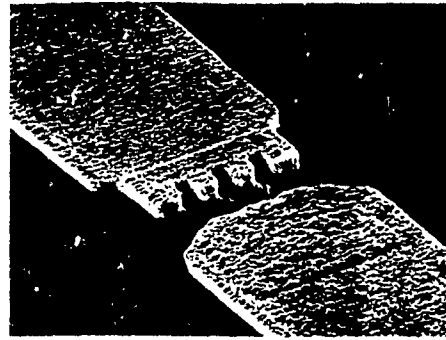


Fig. 2: A three-finger Schottky diode

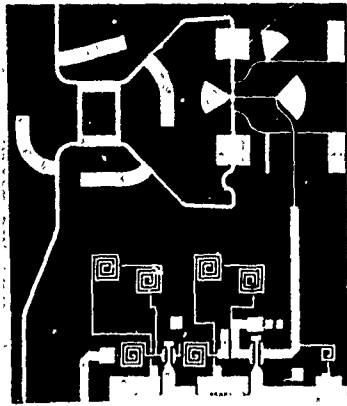


Fig. 3: A 60 GHz receiver chip (Chip size 4 x 4.5 mm)

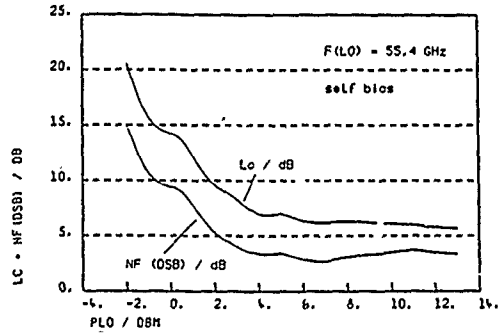


Fig. 4: Conversion loss and noise figure of the 60 GHz mixer

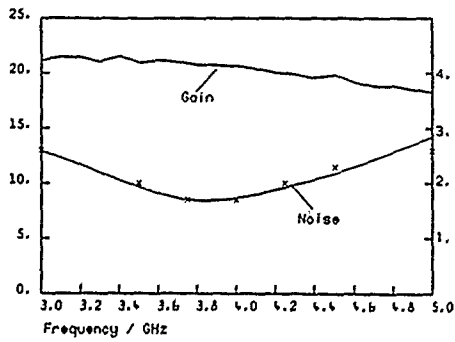


Fig. 5: Noise figure and associated gain of the IF amplifier

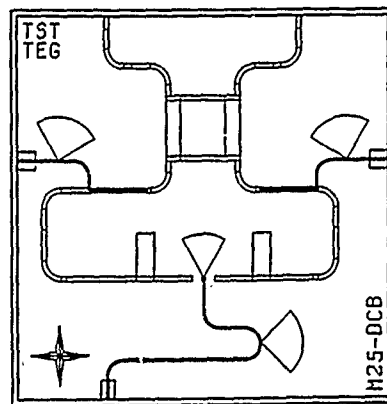


Fig. 6: Layout of a 94 GHz balanced mixer (Chip size 2 x 2 mm)

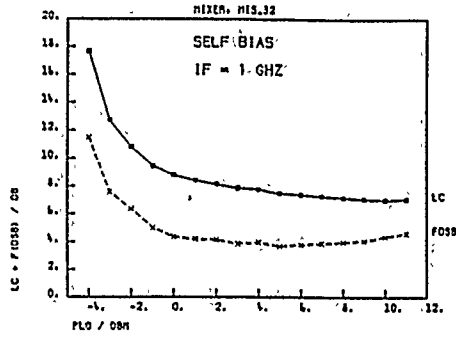


Fig. 7: Conversion loss and noise figure versus LO power of a 94 GHz balanced mixer without DC-stop

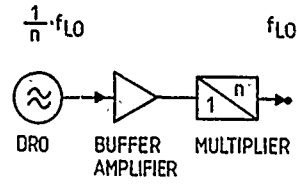


Fig. 8: LO power generation

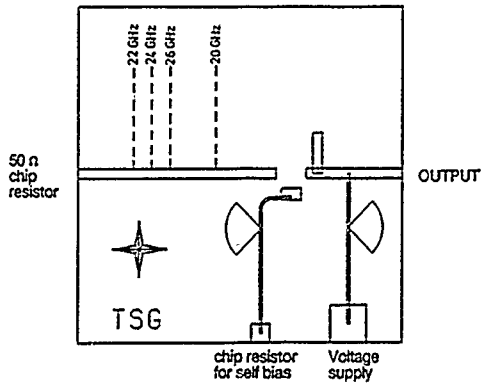


Fig. 9: Layout of a dielectric resonator stabilized MESFET Oscillator (DRO)

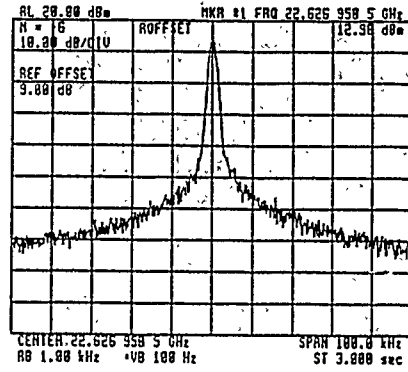


Fig. 10: DRO output spectrum at 22.6 GHz

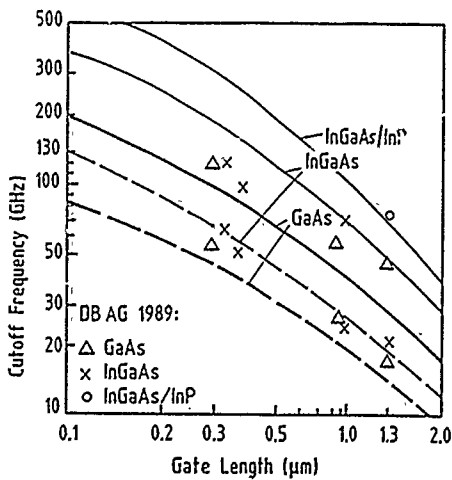


Fig. 11: Current gain cut-off frequency f_T and power gain cut-off frequency f_{max} versus gate length for HEMTs based on different materials. Dashed line: f_T , solid line f_{max} for the best published data. Experimental data are from Daimler-Benz Research Center, Ulm.

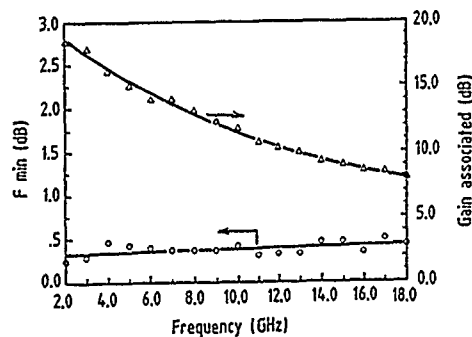


Fig. 12: Noise figure and associated gain of a 0.25 x 90 μm HEMT

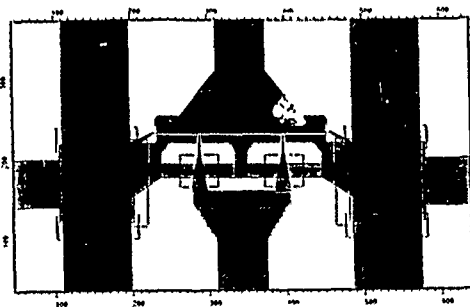


Fig. 13: Layout of a dual gate HEMT in a Cascode configuration

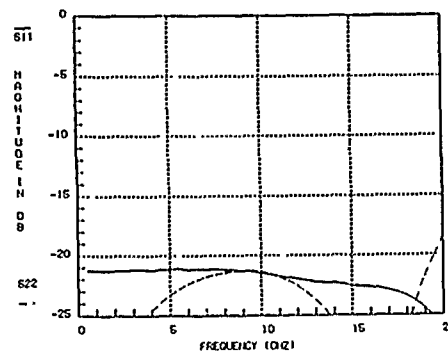
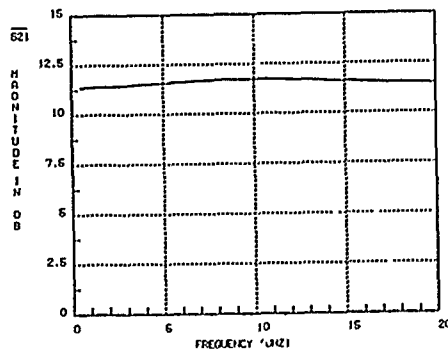


Fig. 14: Simulated performance of a 2 - 18 GHz travelling wave amplifier

Discussion

Paper n° 10

Question : Mr. R.J.P. DOUVILLE (CRC, OTTAWA, OBSERVER)

- Where do you feel the commercial softwares begin to fail with frequency ?
- Does this include Linmic and EM Sim ?

Answer : Dr. Peter SCHMIDT

•We have made reference measurements in the range 30-40 GHz and have found significant deviations between measurements results and results of commercially available software. So, at least the mm-wave frequency range 30-100 GHz causes some problems for these programs.

•At the time of our measurements campagne, yes. Meanwhile, improvements are being installed and we are exchanging informations with some software to support these improvements.

Question : J.K. COLDWELL (SIEMENS PLESNEY RADAR)

Please indicate timescale for availability of GaAs devices in required quantity and affordable prices to produce mm-wave phased array radar antenna.

Answer : Dr. Peter SCHMIDT

For simple configurations like passive reflect arrays and far frequencies in the lower mm-wave range, e.g. 35 GHz, I expect a 4-5 years period until monolithic modules are available in sufficient quantity and quality.

BROADBAND COUPLING STRUCTURES FOR MICROWAVE ARITHMETIC CIRCUITS AND PHASED ARRAYS

by
Joseph A. Mosko
Naval Weapons Center
China Lake, California 93555-6001

INTRODUCTION

There are new opportunities emerging that will provide improved system performance or even coverage where at present it is not affordable in the general area of passive and active airborne microwave sensors. Avionics, radar warning receivers, and antiradiation homing applications are examples. As multiple sensors and ever wider bandwidth systems are developed for future applications, it becomes more and more important to provide broader coverage, faster processors, and smaller and more compact systems, which also need to be more integrable onto various platforms.

Experience in the microwave component area and in broadband, compact radiators has identified several opportunities for better solving certain design problems that exist today, as well as for proposing a new structure of promise. Altogether, there are four specific designs discussed--some in complete detail, and others in outline, with all pertinent references listed. Also there is an example of a wideband, high-quality system shown that indicates what is achievable when the "whole thing was put together."

ELECTROMAGNETIC INTRADERMAL COUPLER FOR MICROWAVE NETWORK INTERCONNECTIONS

Introduction

There are many requirements for interconnecting densely packed microwave circuits that are placed side by side to form a microwave system. Examples are receivers, transmitters, and signal processing equipments. It is not always possible to bring the various transmission lines to the edges of the circuits that must be connected. Figure 1 shows a large conformal array as an example. The system could be constructed using precision multilayer printed circuit technology to form the array elements, control circuitry, microwave beam former, and signal distribution levels as suggested in Figure 2. The various circuits located behind the radiator elements are to be designed in conventional stripline, with their groundplanes serving as shields between adjacent networks. Obvious feed throughs interconnecting one level to another are shown in Figure 3. This technique has some drawbacks. Nonstandard operations are required to form a wide-band, high-fidelity microwave path around right angle bends, which also tend to scatter energy at such right angle junctions.

A better methodology is proposed here for the first time. This methodology has the advantage of flexibility, can be constructed by planar circuit fabrication techniques, and preserves isolation from one circuit level to the next, including that of direct current (DC). It is based on the rigorous synthesis and design of coupled transmission lines and has no inherent limitations on the bandwidth of operation. The following description of operation is based on the more commonly understood properties of 3 dB quadrature couplers--not on the equally correct, but less commonly understood, scattering matrix representation of this complex microwave junction.

After the description of the idea, detailed design equations will be presented that can lead to arbitrary bandwidth electromagnetic intradermal couplers (EICs).

Tandem Connected Quadrature Couplers

Countless power amplifiers and combiners use tandem connected quadrature couplers (Figure 4). It is well known that amplifiers located between couplers contribute to the overall gain of the system, while amplifier imperfections (impedance mismatch and gain unbalance) tend to end up in the two termination loads and, on the whole, have a minor impact on the overall gain (References 1 and 2). Figure 5 shows more precisely the response of two arbitrary but common impedance quadrature couplers in tandem (References 3 and 4). We note that when the coupler is matched in impedance to the system, perfect directivity is preserved (zero output at "isolated" port 4) and all the power is transferred to port 3.

If the signal flow is symmetrically intercepted at any point between the two couplers of Figure 5, then by symmetry, the output signals of Figure 5 emerge on the input side of the first hybrid, as indicated in Figure 6. Now we observe that unless the coupler is precisely -3 dB (i.e., $\alpha = \pi/4$), some of the coupler output power will be reflected back into the input port as represented by the $\cos 2\alpha$ voltage reflection coefficient.

One of the simplest examples of the -3 dB coupler is the single quarter wavelength hybrid (References 5 and 6). If, for example, we design the coupler for optimum operation over a 1.5:1 bandwidth, then the coupled lines have a normalized, even mode impedance of 2.45838; and an odd mode impedance of $1/2.45838$ ohms. This leads to a coupling variation with frequency as follows: at the band edges ($f=1.$, and $f=1.5$), coupling is the lowest, or -3.12 dB (or $\alpha = 44.29$ degrees); at the midband frequency, coupling is the highest, or -2.90 dB (or $\alpha = 45.72$ degrees). When such a design is used in the shorted or open output port configuration, as in Figure 6, the return loss is as plotted in Figure 7. Note that the worst-case return loss is -32 dB at the input of the coupler system for the 1.5:1 bandwidth of interest. Of course, as the frequency is moved further and further from the passband, more and more of the signal is reflected at the input port and is determined by the $\cos 2\alpha$ value.

The above discussion is completely general, except for the assumption of a common system impedance. The couplers can be realized in any suitable form of coupling. The next section will consider a particularly advantageous form of coupled striplines for the proposed EICs.

Slit-Coupled Electromagnetic Intradermal Couplers

Figure 8 shows an end view of slit-coupled striplines (Reference 7), a more general case of the universally used, broadside-coupled striplines (Reference 8). It features a slit in the central ground plane by which the coupling between the two striplines can be controlled: no slit, no coupling. If there is a large slit in respect to the stripwidths, then coupling can be very tight. It also depends on the "s" dimension. Figure 9 shows the conceptual design of the EIC. The aperture in the center ground plane, B, serves to couple energy in the stripline circuit between planes A and B to the otherwise isolated circuit between ground planes B and C.

Coupled line synthesis is based on an exact conformal mapping solution (Reference 7) and is given in Equations 1 through 8, where ϵ_r is the relative dielectric constant of the stripline material.

$$\sqrt{\epsilon_r} Z_{oc} = 188.3652 \frac{K'(k_e)}{K(k_e)} \quad (1)$$

$$\sqrt{\epsilon_r} Z_{oo} = 188.3652 \frac{K'(k_o)}{K(k_o)} \quad (2)$$

$$k = k_0, \text{ the modulus} \quad (3)$$

$$a = \frac{s}{b} K, \text{ a parameter} \quad (4)$$

$$\beta = \text{sn}^{-1}(k_e/k_0, k), \text{ a parameter} \quad (5)$$

$$\alpha = \text{sn}^{-1} \left[\frac{1}{k} \frac{\sqrt{Z(a)}}{\sqrt{Z(a) \text{sn}^2 a + \text{sna} \cdot \text{cna} \cdot \text{dna}}}, k \right], \text{ a parameter} \quad (6)$$

$$\frac{w}{b} = \frac{1}{\pi} \log \frac{\Theta(\alpha + a)}{\Theta(\alpha - a)}, \text{ normalized strip width} \quad (7)$$

$$\frac{ss}{b} = \frac{1}{\pi} \log \frac{H(\beta + a)}{H(\beta - a)}, \text{ normalized slit width} \quad (8)$$

where

Θ = Jacobian theta function

H = Jacobian eta function

Z = Jacobian zeta function

sn, cn, and dn = Jacobian elliptic functions

$$K = \int_0^1 \frac{dt}{\sqrt{(1-t^2)(1-k^2 t^2)}} = \text{complete elliptic integral of the first kind, with } k \text{ as the modulus}$$

K' = complete elliptic integral of the first kind with complementary modulus $k' (= \sqrt{1-k^2})$

$$\text{sn}^{-1}(\xi, k) = \int_0^\xi \frac{dt}{\sqrt{(1-t^2)(1-k^2 t^2)}} = F(\xi, k) = \text{incomplete elliptic integral of the first kind}$$

and we note

$$\Theta_1(u) = \Theta(K + u)$$

If we were to design the previously mentioned 1.5:1 bandwidth coupler in one of today's popular stripline media (woven fiberglass in Teflon, $\epsilon_r = 2.17$), we would find that

$$\begin{aligned} s &= 0.25 \text{ mm (0.010 inch)} \\ w &= 1.19 \text{ mm (0.0466 inch)} \\ ss &= 3.44 \text{ mm (0.1355 inch)} \\ b &= 2.82 \text{ mm (0.111 inch)} \end{aligned}$$

In comparison, a conventional broadside coupled stripline (Reference 8) pair in the same material would be

$$\begin{aligned} s &= 0.25 \text{ mm (0.010 inch)} \\ b &= 2.66 \text{ mm (0.105 inch)} \\ w &= 1.18 \text{ mm (0.0464 inch)} \end{aligned}$$

(and, effectively, $ss = \text{infinity}$)

While we recognize that the above dimensions and tolerances thereof may represent a challenge in manufacturing, it is in no way the only means of achieving the performance and bandwidth so far stated. For example, it may be more desirable to design the -3 dB coupler as a tandem connection of two -8.34 dB couplers, thus relieving stringent tolerances on the s dimension in a particular design. This simply means that there would be two nearby coupled lines per side of the center ground plane, with their corresponding pair of coupling apertures. The corresponding dimensions then become (again, $\epsilon_r = 2.17$)

$$\begin{aligned} s &= 1.02 \text{ mm (0.040 inch)} \\ w &= 2.14 \text{ mm (0.084 inch)} \\ ss &= 3.68 \text{ mm (0.145 inch)} \\ b &= 3.63 \text{ mm (0.143 inch)} \end{aligned}$$

The frequency response of this tandem connected -8.34 dB pair of couplers does not exactly match the single -3.01 dB coupler design mentioned above. The coupling varies from band edge at -3.164 dB to mid band at -2.86 dB (with the hybrid coupling angle varying 25.50 ± 0.50 degrees). The mismatch at the input to the coupler pair is plotted in Figure 10, together with that of the -3 dB coupler of Figure 7 for comparison. For most practical applications, the performance difference is negligible, while the ease of construction and accompanying reduction of tolerance are much appreciated.

Just as multiple section couplers are always utilized for extended bandwidth operation, a system of tandem connected, multi-section coupled lines, with the appropriate control apertures, can also be employed. The design is always straightforward and based on an exact conformal mapping solution for the coupling geometries.

UNCOUPLED COUPLER FOR STRIPLINE LINE CROSSINGS

We find that in some microwave applications utilizing broadband couplers, we occasionally need to cross two lines, at different elevations, preferably with little or no coupling between them. This may be possible, depending on the bandwidth of operation of the system.

If it is essentially a single frequency of interest, then we need to design a symmetric one-half wavelength coupler very similar to the more common one-quarter wavelength coupler. This is possible because there is no coupling at such a frequency, regardless of how much coupling there might have been at the lower frequency when the device is electrically half the length, or $\lambda/4$, long.

When an extended bandwidth operation is required (say 10 to 20 GHz), we must design a coupler basically made up of two halves of DuHamel Magic-Ts (References 9 and 10) and arranged back to back. DuHamel Magic-Ts owe their nominal coupling level to the severity of junction impedance mismatch, where the tightly coupled and uncoupled lines meet. With little or no impedance mismatch, there similarly will be little or no coupling for any frequencies above some cutoff value. Thus by arranging two back-to-back Chebyshev impedance transformers, superb even- and odd-mode impedance match is achieved, as with DuHamel couplers, which leads to arbitrarily low coupling between two line crossings. It is a high-pass filter structure. The lower the low frequency of operation, the longer the device must be for a given level of performance.

Figure 11 shows the topological view of such a stripline coupler for operation above 12 GHz and a coupling level less than -30 dB. For example, two striplines, separated by a 0.020-inch height within a stripline circuit having a 0.100 inch ground plane spacing, $\epsilon_r = 2.17$ and, at a 50 ohm characteristic impedance, can be crossed with coupling levels versus crossover lengths, as given in Table 1. Note that the length is normalized to the wavelength in the material at the lowest frequency of interest. We should also note that whenever we design for a maximum coupling of -50 dB or less, we should also recall that experimental high quality couplers often have directivities of only 20 to 40 dB because of construction, measurement, and material limitations or tolerances. Moreover, if the even-mode and odd-mode phase velocities are not precisely equal, then the isolated port of the uncoupled coupler can be (and usually is) of higher power than the so-called coupled port in the high pass portion of the frequency range for which the device was designed. (This can lead to *negative* directivity for this coupler in the passband!) Indeed, the author has used this type of device in making relative measurements of permittivity of stripline materials within a lot, simply because it can be so sensitive. For example, coupler material samples behaved differently when cut from the base material in the "long" versus "narrow" orientation from random fiber type Teflon/fiberglass substrate (Reference 11).

TABLE 1. Maximum Coupling Levels of Uncoupled Coupler in Passband Versus Length.

Coupler characteristic	Design example number					
	1	2	3	4	5	6
Length (wavelength at band-edge)	0.8	1.0	1.2	1.5	2.0	3.0
Max. coupling (above band-edge frequency), dB	-23.5	-28.7	-34.4	-42.6	-56.2	-83.5

COMPACT, TIGHTLY COUPLED STRIPLINES IN HIGH DIELECTRIC MATERIALS

It is of considerable interest to us now to design our microwave circuits in high dielectric materials (for manufacturing considerations) or to simply shrink the physical size of circuits. Broadband (i.e., decade bandwidth and greater) microwave networks, including precision -3 dB couplers, are almost always realized in three-layer stripline form--preferably homogeneous, isotropic dielectrics almost like Teflon. Furthermore, most practicing designers have found that Cohn's virtually exact (Reference 8) or other approximate (Reference 12) design equations for various coupled lines are very adequate for almost all designs, which is quite fortunate. On the other hand, when the material's $\epsilon_r = 6$ (instead of 2.2 as before), many design constraints are no longer met. Moreover, if we desire to design broadband structures at $\epsilon_r = 13$, such as for GaAs technology, almost all common design procedures fail. (Currently, commercially available microwave computer aided design (CAD) software, including TRANSCAD, TOUCHSTONE, etc., similarly fails.) Therefore, exact conformal mapping based procedures or carefully derived numerical solutions to synthesis and design questions must be used.

Broadside coupled lines can be designed on the basis of the exact solution (Reference 7) based on ratios of elliptic integrals, etc. (some equations have been called out previously):

$$\sqrt{\epsilon_r} Z_{oe} = 120 \cdot 3652 \frac{K'(k_e)}{K(k_e)} \quad (1)$$

$$\sqrt{\epsilon_r} Z_{00} = 188.3652 \frac{K'(k_0)}{K(k_0)} \quad (2)$$

$$k = k_0, \text{ the modulus} \quad (3)$$

$$a = \text{sn}^{-1}(k_e/k_0, k), \text{ a parameter} \quad (9)$$

$$\alpha = \text{sn}^{-1} \left[\frac{1}{k} \frac{\sqrt{Z(a)}}{\sqrt{Z(a) \text{sn}^2 a + \text{sn} a \cdot \text{cna} \cdot \text{dna}}}, k \right], \text{ a parameter} \quad (6)$$

$$\frac{w}{b} = \frac{1}{\pi} \log \frac{\Theta(\alpha + a)}{\Theta(\alpha - a)}, \text{ normalized strip width} \quad (7)$$

$$\frac{s}{b} = \frac{a}{K}, \text{ normalized strip spacing} \quad (10)$$

A general observation might be as follows. As we go from soft substrate materials with $\epsilon_r \approx 2.2$ to harder materials with $\epsilon_r \approx 10$, all critical dimensions tend to shrink; line widths and line spacing become significantly smaller. Table 2 shows the broadside coupled line dimensions for constant coupling at a 50 ohm characteristic impedance as the dielectric material varies. Note that the s/b ratio at $\epsilon_r = 13$ is approximately half that at $\epsilon_r = 2.2$, while the w/b ratio changes by an order of magnitude. So if we currently have trouble controlling tolerances with $\epsilon_r = 2.2$ soft materials, then new innovations are welcomed for higher dielectric material applications.

TABLE 2. Broadside Coupled -6 dB Coupler Dimensions for Various Values
($Z_0 = 50$ ohms; $Z_{0e}/Z_0 = 1.6667$).

Design parameter	Design number								
	1	2	3	4	5	6	7	8	9
ϵ_r	2.17	3.	4.	5.	6.	7.	9.	11.	13.
s/b	0.2565	0.2384	0.2198	0.2036	0.1893	0.1765	0.1543	0.1360	0.1204
w/b	0.6317	0.4837	0.3719	0.2968	0.2420	0.2018	0.1447	0.1072	0.0814

At this point, it may be worthwhile to call our attention to a little known reference for conveniently and accurately calculating the ratio of complete elliptic integrals K/K' versus k , the modulus (Reference 13). Hilberg provides us with extremely simple expressions for this purpose, which gives better accuracy more directly than any known tables.

As long as closed form, exact design equations are available as in Equations 1 through 10, they are always preferred over numerical procedures. For Shelton coupled line pairs (Reference 12) where very good (especially for $\epsilon_r < 3$) though not *exact* solutions exist, the practical approach is to design the coupled lines by integral equation solution (References 14 and 15). These numerical algorithms are flexible, quick, and, when compared to the above mentioned rigorous solutions, can and do yield accuracies to arbitrary precision. They also allow us to consider the coupling between multiple strips other than a pair of strips, as previously discussed. A particularly interesting system of coupled strips--four within a pair of groundplanes--has important applications to the feeding of phased array elements such as multimode four arm spirals or dual circularly polarized broadband radiators, the topic of the next section.

ORTHOGONAL QUAD-MODE IMPEDANCE TRANSFORMERS WITH PHASED ARRAY APPLICATIONS

Multimode radiators have different radiation impedances (Reference 16) for the various radiation modes of excitation. When such radiators are connected to a feed network of given characteristic impedance (typically 50 ohms), an uncommon impedance transformer is best suited for this application (References 17 and 18). In recent years, several important opportunities for application of this technology have developed. Examples are the dual circularly polarized avionics antennas (References 19 and 20) and precision direction finding systems (Reference 18).

Figure 12 shows the tightly coupled four stripline feed near the spiral feed point (Reference 18). Typical dimensions there are 0.178 mm (0.007 inch) strip width; 0.152 mm (0.006 inch) to 0.254 mm (0.010 inch) strip separations; and strip offsets varying from completely overlapped to separated by a strip width or more.

While sufficient design detail is given elsewhere (Reference 18), it can be readily visualized that the four strip coupled line system of Figure 12 can support and carry a total of four completely independent, and analytically orthogonal, modes of excitation. It therefore can support all possible modes of radiation of a multifilament spiral or other phased array radiator. Because transverse electromagnetic (TEM) modes propagate on the coupled quad-strip system, there are no fundamental limitations of frequency of operation. Furthermore, it is possible and very practical (Reference 18) to etch such a multimode impedance transformer very much like a common planar wideband stripline circuit. This device matches the various radiation impedances to the network characteristic impedance. All is precisely possible because of all the necessary degrees of freedom in the design of the four coupled strip: any stripwidth(s) can be chosen; and any strip separation(s) can be chosen for a given dielectric material and multimode radiator. For example, typical radiation impedances for a dual mode spiral radiator are 94 and 133 ohms. A transformer with practical dimensions can match these radiation impedances to a 50 ohm receiver/transmitter system. Another example is that of the dual CP (circularly polarized) radiator (References 19 and 20). There the optimum impedance is approximately 130 ohms for both modes of interest and, again, a practical design solution may be found.

While it is beyond the scope of this paper to present detailed design-procedures (which are available elsewhere), some experimental results are available and will be presented.

RECOMMENDATIONS

While microwave design specialists develop and extent various CAD procedures, newer coupling structures must be addressed and made available to the design community. Also, it should be recognized that as we turn to new materials and integration concepts, some popular design approaches of the past will not be accurate enough.

There are common problems that some microwave designers and antenna engineers face. It is advantageous that these problems be solved together rather than separately in their individual domains. For example, Figure 13 shows samples of measured radiation patterns of a 50:1 bandwidth multimode radiator and arithmetic feed network. The patterns cover a 40 dB variation of power versus azimuth angle measured while the linearly polarized source was spinning to show the axial ratio of the wideband CP antenna. Considering tolerances and construction and material limitations, it would be difficult, if not impossible, to optimize the feed network and radiator separately and then join them into a working system.

SUMMARY AND CONCLUSIONS

Four specific coupling structures were introduced or were described in detail. Each has important applications now and in future systems. For example, "smart skins" with integrated microwave circuitry for processing and radiation may make use of a novel coupling aperture. Various rigorous design equations are available for high-performance coupler designs, be they on common soft (low ϵ_r s) or the newer monolithic microwave integrated circuit (MMIC) capable (high ϵ_r s) materials. Numerical solutions are ideally suited to CAD/CAM (computer aided manufacturing) practices and could be extended to promising newer devices involving multi-element coupled transmission lines.

REFERENCES

1. Engelbrecht, R. S., and K. Kurokawa. "A Wideband Low Noise L-Band Balanced Transistor Amplifier," *Proceedings of IEEE*, Vol. 53, No. 3 (March 1965), pp. 237-247.
2. Kurokawa, K. "Design Theory of Balanced Transistor Amplifiers," *Bell System Technical J.*, October 1965, pp. 1675-1698.
3. Monteath, G. D. "Coupled Transmission Lines as Symmetrical Directional Couplers," *Proceedings of IEE*, Part B, Vol. 102, No. 3 (May 1955), pp. 383-392.
4. Shelton, J. P., and J. A. Mosko. "Synthesis and Design of Wide-Band Equal-Ripple TEM Directional Couplers and Fixed Phase Shifters," *IEEE Trans. on Microwave Theory and Techniques*, Vol. MTT-14, No. 10 (October 1966), pp. 452-473.
5. Jones, E. M. T., and J. T. Bolljahn. "Coupled Strip-Transmission-Line Filters and Directional Couplers," *IRE Trans. on Microwave Theory and Techniques*, Vol. MTT-4, No. 2 (April 1956), pp. 75-81.
6. Matthaei, G. L., L. Young, and E. M. T. Jones. *Microwave Filters, Impedance Matching Networks, and Coupling Structures*, Norwood, Mass., Artech House, 1980.
7. Yamamoto, S., T. Azakami, and K. Itakura. "Slit-Coupled Strip Transmission Lines," *IEEE Trans. on Microwave Theory and Techniques*, Vol. MTT-14, No. 11 (November 1966), pp. 542-553.
8. Cohn, S. B. "Characteristic Impedances of Broadside-Coupled Strip Transmission Lines," *IRE Trans. on Microwave Theory and Techniques*, Vol. MTT-8, No. 6 (November 1960), pp. 633-637.
9. DuHamel, R. H., and M. E. Armstrong. "A Wideband Monopulse Antenna Utilizing the Tapered-Line Magic-T," *15th Annual Symposium on USAF Antenna Research and Development*, Allerton Park, U. of Ill., September 1965.
10. *Parallel Coupled Lines and Directional Couplers*, Young, L. (ed.). Dedham, Mass., Artech House, 1972, pp. 206-233.
11. Mosko, J. A. "Progress, Problems, and Material-Related Considerations in Broadband Coupler Design," 1981 MIC Workshop, Brainerd, Minn., 28-30 September 1981.
12. Shelton, J. P. "Impedances of Offset Parallel Coupled Strip Transmission Lines," *IEEE Trans. on Microwave Theory and Techniques*, Vol. MTT-14, No. 5 (May 1966), p. 249. (Note that log is ln or log_e.)
13. Hilberg, W. "From Approximations to Exact Relations for Characteristic Impedances," *IEEE Transactions MTT*, Vol. 17, No. 5 (May 1969), pp. 259-265.
14. Kammler, D. W. "Calculation of Characteristic Admittances and Coupling Coefficients for Strip Transmission Lines," *IEEE Trans. on Microwave Theory and Techniques*, Vol. MTT-16, No. 11 (November 1968), pp. 925-937.
15. Chestnut, P. C. "On Determining the Capacitances of Shielded Multi-conductor Transmission Lines," *IEEE Trans. on Microwave Theory and Techniques*, Vol. MTT-17, No. 11 (October 1969), pp. 734-745.

16. Deschamps, G. A. "Impedance Properties of Complementary Multi-terminal Planar Structures," *IRE Trans. on Antennas and Propagation*, Vol. AP-7 Special Supplement (December 1959), pp. S371-S378.
17. Corzine, R. G., and J. A. Mosko. "Direction Finding Antenna Interface." U.S. Pat. 4 609 888. Filed 2 October 1980; issued 2 September 1986.
18. Corzine, R. G., and J. A. Mosko. *Four-Arm Spiral Antennas*, Norwood, Mass., Artech House, 1989.
19. DuHamel, R. H. "Dual Polarized Sinuous Antenna." U.S. Pat. 4 658 262. Filed 19 February 1983; issued 14 April 1987.
20. Chu, T-T., and H. G. Oltman. "The Sinuous Antenna," *Microwave Systems News*, June 1988, pp. 40-48.

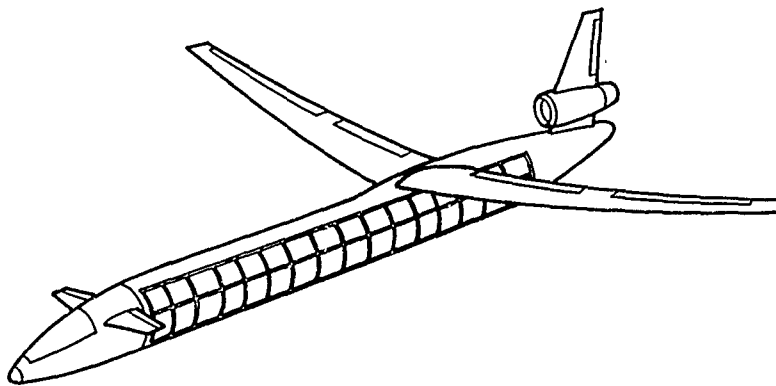


FIGURE 1. Large Conformal Array.

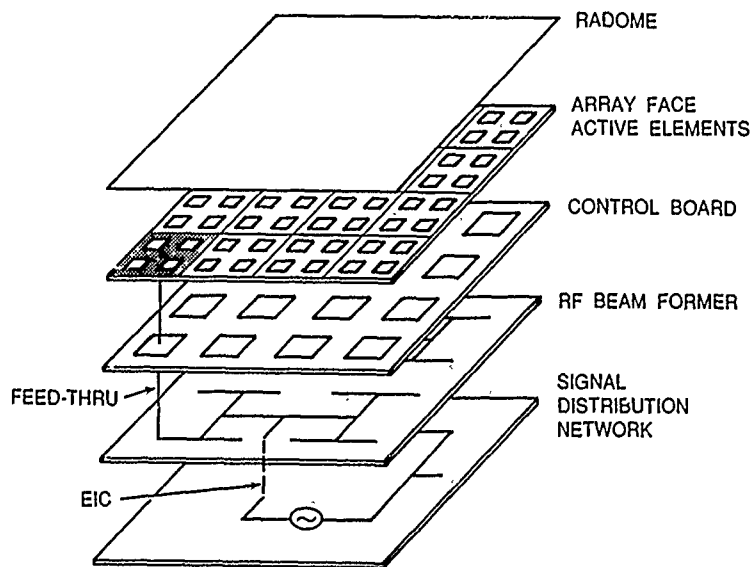


FIGURE 2. A Multilayer Circuit Construction With Interconnects.

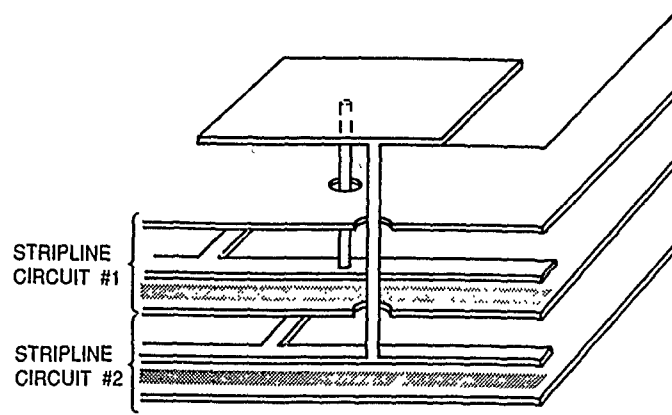
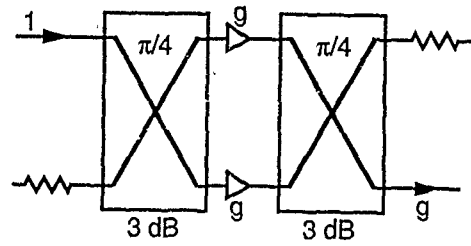


FIGURE 3. Possible Circuit Feed-Throughs.



Where:

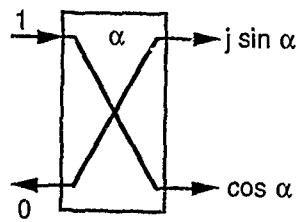


FIGURE 4. Tandem Connected 3 dB Couplers.

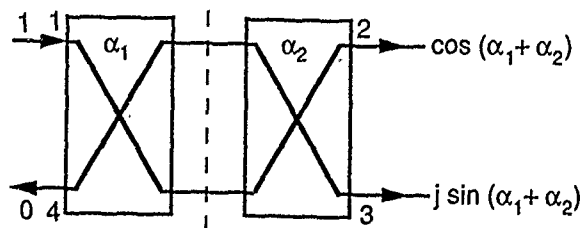


FIGURE 5. Arbitrary Common Impedance Quadrature Couplers in Tandem.

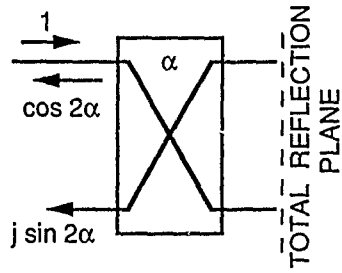


FIGURE 6. Quadrature Coupler With Identical Complete Reflections at Output Ports.

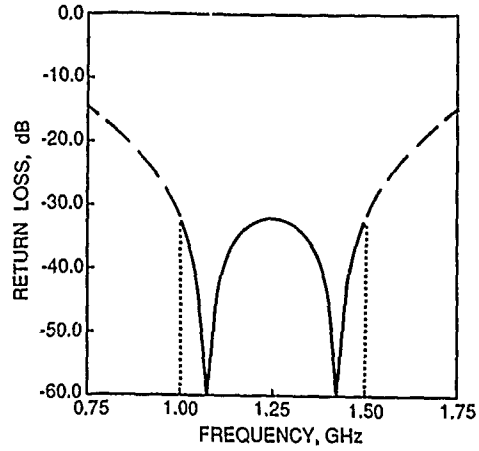


FIGURE 7. Theoretical Return Loss Versus Frequency of Perfectly Mismatched -3 dB Quadrature Hybrid.

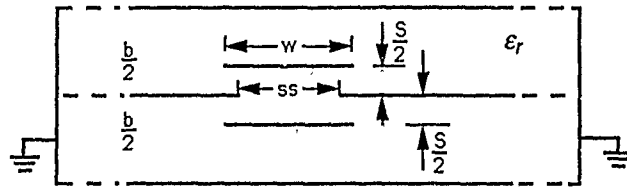


FIGURE 8. End View of Two Slit-Coupled Strip Transmission Lines.

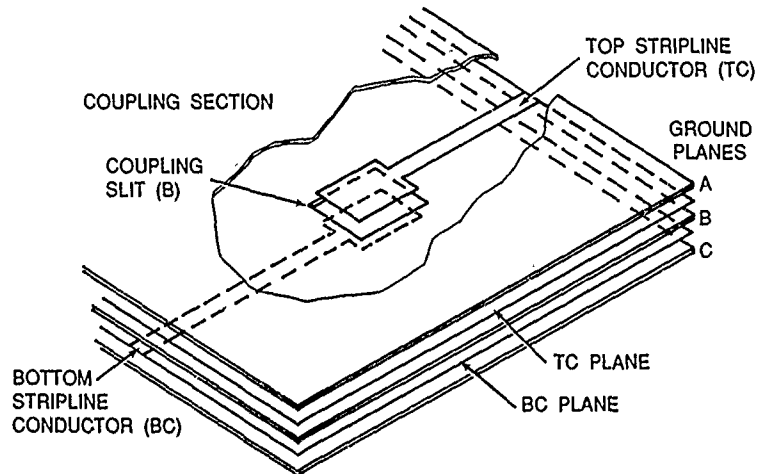


FIGURE 9. Proposed Electromagnetic Intradermal Coupler.

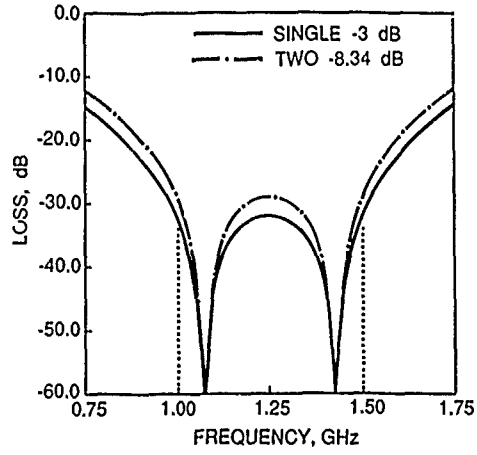


FIGURE 10. Theoretical Return Loss of Perfectly Mismatched Quadrature Couplers.

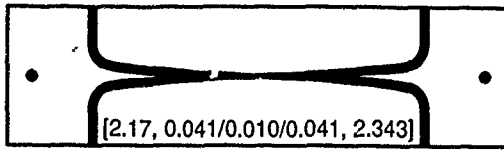


FIGURE 11. Uncoupled Coupler; 12 GHz High Pass.

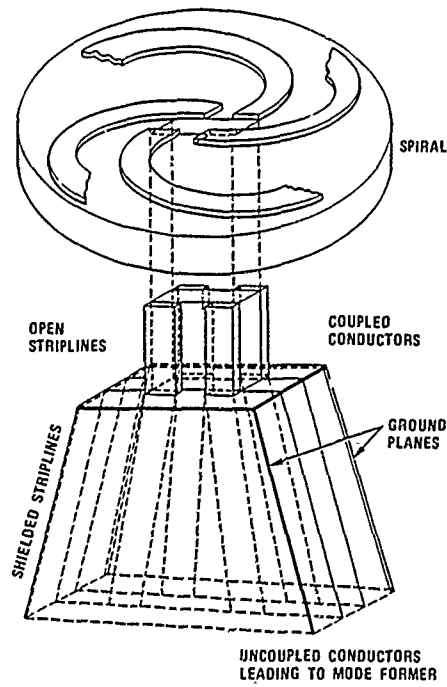


FIGURE 12. Coupled 4-Strip Impedance Transducer With Radiator.

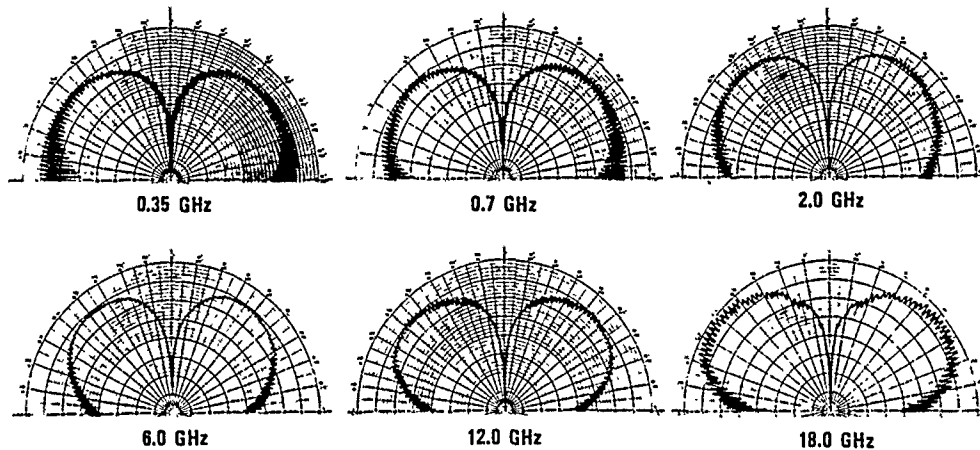


FIGURE 13. Measured Difference Mode Radiation Patterns of Broadband Spiral Monopulse System.

Discussion

Paper n° 11

Question : JOHN P. HURREL (unregistered)
At what frequency must stripline losses be included into your coupled line equations for wideband applications.

Answer : J.A. MOSKO

- the design equations, based on rigorous conformal mapping solutions, assume perfect, zero thickness conductors, as well as lossless dielectric materials. The losses are usually tolerable if we select low loss materials and rolled copper (not electro-deposited or "rough" copper).
- it would be nice if we could use air dielectrics, such as with suspended substrates. However, we do not know of any practical way to construct broadband -3db quadrature couplers over 1-20GHz in such a median
- just as there are charge singularities at edges of striplines (or current singularities), there will similarly be high currents at the edges of the aper-

ture which controls the coupling from the circuit to the other circuit. Again, rolled copper (smooth, non-granular) has the lowest losses and is the preferred approach.

- the I²R losses of the proposed approach should be as low, or lower, than the "obvious" approach using small pins penetrating groundplanes in order to connect one circuit with another.

Question : Mr. R.J.P. DOUVILLE (CRC, OTTAWA, OBSERVER)

Have you tried to apply you aperture coupling equations to aperture coupled patch antennas ?

Answer : MOSKO

- no, I almost never work with radiators which have such low bandwidth capability as patch antennas
- I believe that aperture coupling is possible to excite patches or extract power from patches when suitably implemented.

LOGARITHMIC AMPLIFICATION FOR PASSIVE AIRBORNE DIRECTION FINDING IN THE 1990s

by

Richard Smith Hughes
Analog Circuit Design Consultant
Code 35205
U.S. Naval Weapons Center
China Lake, Calif. 93555-6001

SUMMARY

Logarithmic amplifiers (log amps) are an indispensable component in most airborne passive direction finding (DF) sensors, including both antiradiation missiles (ARMs) and radar warning receivers (RWRs) on aircraft. The modern early warning (EW) threat necessitates covering increased instantaneous radio frequency (RF) bandwidths and processing increasing pulse densities, coupled with needs for lower power dissipation, smaller size, and lower cost. Because of these constraints, the log amp designer is often at a loss. Successive detection log intermediate frequency (IF) amps (SDLAs) have the excellent pulse characteristics needed for high duty cycle pulse processing but are limited in instantaneous bandwidth and have generally poor unit-to-unit tracking, large power consumption, and high cost. Detector/log video amps (DLVAs) can offer exceptional unit-to-unit tracking and wide instantaneous bandwidth, but have degraded pulse characteristics (limiting the pulse density that can be processed). Both log amp techniques are fairly expensive and power hungry (power dissipation varies from several hundreds of milliwatts to watts, depending on the design).

The log amps of the 1970s through mid 1980s will not meet the stringent requirements of the 1990s. And at this time, there is no single logging technique that satisfies all requirements. However, log IF/RF amps should decrease their tracking errors and increase their instantaneous bandwidth; DLVAs should improve their pulse fidelity; and both should decrease in size, power dissipation, and cost--all of which will require new circuit topologies and circuit elements (heterojunction bipolar transistor (HBT), metal-epitaxy-semiconductor field-effect transistor (MESFET), complementary bipolar silicon, etc.).

This report will present an historical perspective of the why's and how's of modern log amps, with emphasis on their application-specific strong and weak points. New circuit elements and topologies will be presented that may well determine where the log amps of the 1990s are headed.

LIST OF SYMBOLS

ARM	antiradiation missile
A_v	voltage gain
D	a log amp figure of merit, W/dB
DF	direction finding
I	log amp input intensity
I_{Bias}	full wave detector bias current
IDR	log amp instantaneous dynamic range
I_L	log output current
$(I_L/I_{Bias})(min)$	normalized minimum full wave detector current, $V_{in} = 0$
K	boltzmann's constant
K_1, K_2	log amp constants
LS	logarithmic slope, V/dB
N	number of log stages (full wave detectors)
P_m (dBm)	maximum log amp input for logarithmic action

P_t (dBm)	minimum log amp input for logarithmic action
PTAT (A _v)	proportional to absolute temperature current source for voltage gain stabilization
PTAT (os)	proportional to absolute temperature current source for full wave detector stabilization
q	electron charge
R _{os}	full wave detector bias resistor
RWR	radar warning receiver
T	absolute temperature in degrees kelvin
T _{ss}	tangential sensitivity
V _T	KT/q
Δ	angle of arrival difference voltage
ε(dB)	logarithmic error

INTRODUCTION

Log amps are used in most aircraft RWR and ARM DFs. The principal reason for log amps in monopulse DF systems is the elimination of the absolute received power level in the angle of arrival process.

Figure 1 illustrates a basic monopulse DF (References 1 and 2). Two antennas have their axes tilted and provide a gain pattern as a function of angle (θ) (Reference 3). Consider a signal in the position shown in Figure 1. In this figure, the antenna patterns are highly simplified, and the antenna gains are normalized. The input signal to the two receivers (mixing, if used, is omitted for simplicity) is a function of transmitted power and frequency as well as a function of the antenna gain, $G(\theta)$. Assume that the two antennas are physically close together such that the signal at the faces of the two are equal. Letting I represent this signal, then

$$e_{\eta_A} = G_A(\theta)I \quad (1)$$

and

$$e_{\eta_B} = G_B(\theta)I \quad (2)$$

where $G_A(\theta)$ and $G_B(\theta)$ are the antenna gains as a function of angle (θ). Obviously, these two signals are a function of both $G(\theta)$ and the signal at the antennas' face, I . I can change from microvolts (μV) to volts (V) in a short time span (depending on range, frequency, antenna lobe pattern, etc.), and automatic gain control (AGC) has been used to normalize this widely varying input dynamic range (Reference 4). The use of log amps removes the need for the AGC amplifiers (and associated circuitry) and also makes use of the unique properties of logarithmic arithmetic.

The general transfer function for a log amp may be given as

$$e_{out} = K_1 \log K_2 e_{in} \quad (3)$$

where K_1 and K_2 are constants associated with the log amp. Substituting Equations 1 and 2 into Equation 3 and assuming K_1 and K_2 are equal for the two logs, the outputs of the two log amps in Figure 1 may now be given as

$$e_{out_A} = K_1 \log K_2 I G_A(\theta) \quad (4)$$

$$e_{out_B} = K_1 \log K_2 I_{G_B}(\theta) \quad (5)$$

Taking the difference of the two signals

$$\Delta \equiv e_{out_A} - e_{out_B} \quad (6)$$

or

$$\Delta = K_1 \log K_2 I_{G_A}(\theta) - K_1 \log K_2 I_{G_B}(\theta) \quad (7)$$

or, since $\log A - \log B = \log A/B$, Equation 7 may be given as

$$\Delta = K_1 \log [K_2 I_{G_A}(\theta)] / [K_2 I_{G_B}(\theta)] \quad (8)$$

or

$$\Delta = K_1 \log [G_A(\theta)] / [G_B(\theta)] \quad (9)$$

The result given in Equation 9 is most important as the resultant signal, Δ , represents the angle of arrival, both in terms of magnitude and sign, independent of the signal input intensity. This angle-of-arrival signal, Δ , is valid each time the signal is present; thus only one pulse (monopulse) is needed to determine the angle of arrival. The accuracy of Δ is dependent on the quality of the log amp, a subject many EW companies have been addressing for the past 25 years.

The various basic log amps, with their strong and weak points, will be presented momentarily; however, it is of benefit to review the real world log amp transfer function delineated in Figure 2.

The ideal log output may be given as

$$e_L = LS P_{in}(\text{dBm}) - LS P_o(\text{dBm}) \quad (10)$$

where

- LS = logarithmic slope (V/dB)
- $P_o(\text{dBm})$ = input power (for least mean square curve fit) for $e_L = 0V$
- $\epsilon(\text{dB})$ = error, in dB, of actual log response to ideal

It should be pointed out that the constants in Equation 10 are, within limits, design dependent. The log amp designer tries to ensure that LS, $P_o(\text{dBm})$, and $\epsilon(\text{dB})$ are insensitive to temperature, input frequency, time, etc., which is not a mundane task. Log amp characteristics may well determine the accuracy of a given DF system.

There is no one log amp technique (log IF/RF, DLVA, or true log IF/RF) that is suitable for all applications. Which log technique should be used is application specific and may well have an impact on the system architecture.

There are three basic types of log amps as illustrated in Figure 3. The DLVA performs the logging function after detection (Figure 3a). The input bandwidth is only limited by the detector; however the detector does limit the input dynamic range. Log IF/RF amps utilize gain preceding the

detector(s) as illustrated in Figure 3b. The IF/RF bandwidth is limited by the interstage gain amplifiers. However, a much larger input dynamic range is obtainable than with DLVA.

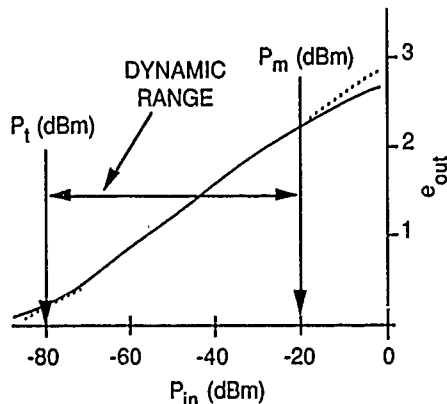
System requirements should dictate which log amp type is best suited; however, a basic understanding of log amp characteristics and comparisons is necessary for a system determined choice. To aid in your decision, several log amp related specifications are presented with a basic DLVA/log IR/RF comparison.

SYSTEM REQUIREMENTS

INPUT DYNAMIC RANGE

The output of a log amp is generally linear until the logarithmic threshold, P_t (dBm), is reached. The logarithmic response extends to P_m (dBm), the maximum input for logarithmic action. The input dynamic range is

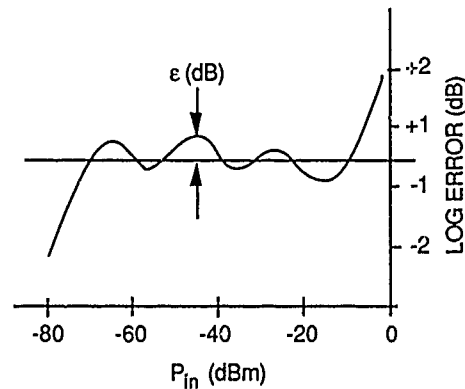
$$\text{input dynamic range} = |P_m \text{ (dBm)} - P_t \text{ (dBm)}|$$



DLVA 40 to 50 dB (can be extended with special designs)
log IF/RF >70 dB

LOGARITHMIC CONFORMITY (LOGARITHMIC ERROR)

The logarithmic conformity is the error, referred to the input (in dB), from a linear regression curve fit.



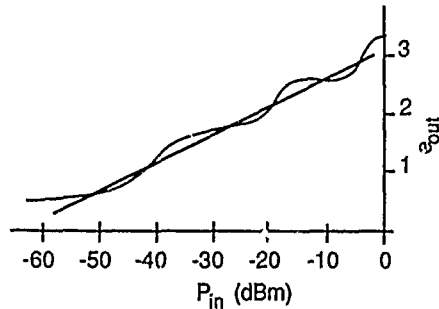
DLVA ± 0.3 to ± 1 dB, depending on design; quite temperature- and input-frequency-independent
log IF/RF ± 0.5 to ± 3 dB, depending on design; sensitive to temperature and input frequency

MATCHING

DLVA ± 0.3 to ± 1 dB, depending on design; less sensitive to temperature and frequency
log IF/RF ± 1 to ± 3 dB, depending on design; sensitive to temperature and frequency

LOGARITHMIC SLOPE

The logarithmic slope (LS) is the change in output voltage, Δe_{out} , divided by the change in input power, ΔP_{in} (dBm), for the linear regression (best straight line) curve fit.

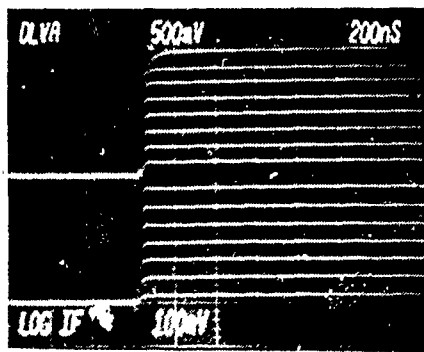


DLVA	easily selectable, 75 mV/dB typical; insensitive to temperature and frequency
log IF/RF	usually fixed by design; 25 mV/dB typical; sensitive to temperature and frequency

Note: Care must be taken for any post-log direct current (DC) level shifts. A 50-mV DC shift represents a 2-dB error for a log amp with a 25-mV/dB log slope.

RISE TIME

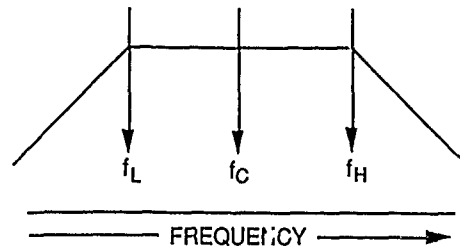
Classical rise time (10 to 90%) is not valid for log amps; however, it is easy to measure and is an effective method for comparison purposes.



DLVA	30 to 50 nsec; can be input power level dependent
log IF/RF	10 to 50 nsec; well designed log IF/RF amps offer distinct advantages in pulse response

INPUT FREQUENCY AND BANDWIDTH

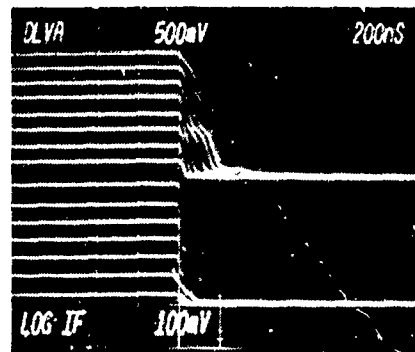
Due to logarithmic action, the 3-dB frequency responses are specified by 3 log slopes below the average value. Care must be taken by the system engineer to ensure that unwanted frequencies are filtered out.



DLVA	inherently broadband; $f_H > 25$ GHz, $f_L < 100$ MHz and bandwidths in excess of 10 GHz
log IF/RF	$f_H < 2$ GHz, $f_L < 100$ MHz; bandwidths limited to approximately 1 GHz

RECOVERY TIME

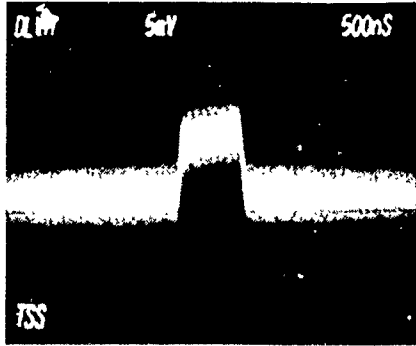
How long does it take for the log amp output to drop to within 1 dB of the baseline when the signal is removed? (This is the log amp recovery time.) Individual system requirements determine if the 1-dB measurement is sufficient.



DLVA	200 to 500 nsec or longer, depending on design
log IF/RF	<100 nsec for well-designed amps; log IF/RF amps offer distinct advantages for recovery time

TANGENTIAL SENSITIVITY

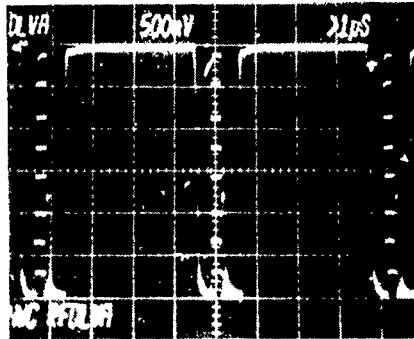
Tangential sensitivity, T_{SS} , for log amps has the same definition as for linear amps (provided that the T_{SS} value is below the logarithmic threshold; P_r (dBm), which is usually the case). T_{SS} is that input power necessary to give an output signal-to-noise ratio of 8 dB.



DLVA -40 to -50 dBm, depending on design; can be increased by the addition of pre-detector amplification
 log IF/RF -60 to -85 dBm, depending on design

MAXIMUM DUTY CYCLE/PULSE DENSITY/CONTINUOUS WAVE (CW)

Does your system require CW operation? Does your system require pulse processing of a narrow pulse following a long one? Can your system "shut down" for short periods for DC normalization? These requirements are related and may well determine which log technique to use.



DLVA "true" DC-coupled amps can handle CW but are more expensive and less accurate (over temperature) than pseudo-DC coupling (utilizing a DC restore loop); pseudo-DC coupled amps can handle large pulse densities, however, the DC nulling loop must be periodically updated
 log IF/RF can easily handle CW and large pulse densities; log IF/RF amps offer distinct advantages for pulse density/CW

POWER SUPPLY REQUIREMENTS

Power supply requirements generally necessitate both positive and negative voltages (± 5 to ± 15 V). The supply current depends on the design, with power dissipation ranging from several hundred milliwatts to several watts. A useful figure of merit relates power dissipation and instantaneous dynamic range (this figure of merit is quite useful when considering channelized receivers utilizing log amps)

$$D \equiv \frac{P}{IDR} \text{ W/dB} \quad (11)$$

COST

The cost of log amps also depends heavily on the design requirements, with costs ranging from \$300.00 for alternating current (AC) coupled DLVA to \$3,000.00 for a wide bandwidth log IF/RF amp. DLVAs tend to cost less than log IF/RF amps, especially as the bandwidth and center frequency are increased.

GENERAL DLVA AND LOG IF/RF COMPARISON

DLVA

The DLVA has an inherently wide input frequency range, limited by the detector and not the logging elements. Logarithmic conformity is excellent over wide bandwidths, and tightly matched units (within ± 0.5 dB) are fairly easily obtainable (References 5 and 6). Pulse fidelity, rise time, and recovery time are overshadowed by log IF/RF amps. Excellent strides to improve pulse fidelity, cost, power drain, and size are being obtained by Anadyne, Inc. (Reference 7); however, much remains to be done to obtain a truly integrated DLVA chip. Depending on design requirements, the DLVA is less expensive (much less so if pseudo-DC coupling is sufficient) than log IF/RF amps.

LOG IF/RF

Log IF/RF amps have an inherent capability for larger instantaneous dynamic range and superior pulse characteristics than their DLVA counterparts. However, their bandwidths are much lower, and their logarithmic conformity with temperature and frequency and unit-to-unit matching are worse than their DLVA counterpart. Also, a well designed DLVA will be less expensive and dissipate less power. Log IF/RF amps inherently provide limited IF/RF for phase processing, a fact that must be kept in mind.

LOGARITHMIC AMPLIFICATION FOR THE 1990s

Modern airborne DF systems (and channelized receivers) will require the processing of ever increasing pulse densities, with better accuracy, lower power consumption, smaller size, and at a lower cost than units presently available. To achieve these goals the "log amp on a chip" must become a reality. The log amp designers of the 1990s will have to utilize modern semiconductor materials (field-effect transistors (FETs), HBTs, silicon bipolar monolithic microwave integrated circuits (MMICs), complementary bipolar, etc.) to reduce size (and cost) and to increase frequency response. Clever circuit design and new log amp topologies will be necessary to reduce power drain and to ensure logarithmic responses independent of temperature and frequency.

SEMICONDUCTOR TECHNOLOGY

Galium arsenide (GaAs) monolithic technology is currently redefining log IF/RF state-of-the-art performance. Smith describes a GaAs FET monolithic 0.5- to 4-GHz "true" log RF amp (Reference 8). The bandwidth obtained is spectacular; however, the power drain is in excess of 5 W ($D = 72$ mW/dB). Oki and others describe the use of heterojunction bipolar transistors (HBTs) in a 1- to 3-GHz "true" log RF amp (Reference 9). The instantaneous dynamic range for the Oki log IF/RF is smaller than that reported by Smith (50 dB). However, the power drain is only 1.1 W ($D = 22$ mW/dB). Yu and others describe a 0.4- to 1.6-GHz successive detection log IF/RF using high-electron mobility transistor (HEMT) technology for the linear amps and planar tunnel diodes for detectors (References 10 and 11). A 70-dB instantaneous dynamic range is reported with a power drain of 5.4 W ($D = 77$ mW/dB). Gorman and others describe a SDLA using HBT monolithic technology (Reference 12). The bandwidth is 0.5 to 1.5 GHz, with an impressive power drain of 0.4 W ($D = 6.66$ mW/dB).

New silicon bipolar technologies are emerging that will increase the bandwidth of log IFs (and DLVAs). Dielectrically isolated and complementary bipolar processes yield f_T s in excess of 2 GHz for PNP as well as NPN transistors. Both processes are available in application specific integrated circuit format, which will open new opportunities for log amp designers. Plessey Semiconductor has advertised a successive detection log IF utilizing an oxide isolated bipolar process that, using three custom integrated circuits, achieves a bandwidth in excess of 300 MHz and a dynamic range of 63 dB (References 13 and 14). The power dissipation is 1.4 W ($D = 22.2$ mW/dB). The log

slope for this circuit is frequency sensitive. However the limited IF output phase is quite input power insensitive (a useful feature if a combination amplitude/phase monopulse can be utilized). Some of the semiconductor technologies that will be utilized in the 1990s are listed in Table 1.

TABLE 1. Log Amp Semiconductor Technology Comparison.

Technology	Dynamic range, dB	Log type	Bandwidth, GHz	Dissipation, W	D, W/dB	Ref. no.
GaAs FET	70	True log IF/RF	0.5-4	5.0	0.072	8
IIBT	50	True log IF/RF ^a	1-3	1.1	0.022	9
HBT	60	SDLA	0.5-1.5	0.4	0.0066	12
HEMT	85	SDLA	2-6	5.75	0.068	10, 11
Silicon bipolar (oxide isolation)	63	SDLA	0.06-0.8	1.4	0.022	13, 14
Silicon bipolar	45	DLVA	Very wide, detector dependent	0.45	0.01	7
ASIC bipolar/dual channel (lateral PNP)	40	DLVA	0.3-1.2	1.1 total (2 log amps)	0.014	5, 6

^aTrue log IR/RF amps inherently require more power than SDLAs.

HBT technology offers excellent opportunities for log IF/RF amps for frequencies up to 2 to 3 GHz. They have a low D(W/dB) factor and, being bipolar, many existing bipolar designs can be implemented. Wide bandwidths may require HEMTs or other power hungry technologies and the ever present DLVA may continue to be the best approach to pursue (especially in light of modern complementary bipolar application specific integrated circuits (ASIC) technologies).

NEW TOPOLOGIES

Modern complementary bipolar integrated circuit technology offers the circuit designer first class NPNs (with f_T in excess of 5 GHz) and PNPs (with f_T in excess of 3.5 GHz), which should increase the frequency while maintaining the DC accuracy offered by silicon monolithic integrated circuit design practices.

Figure 4 illustrates a unique log amp configuration utilizing the high frequency capability of complementary bipolars and the accuracy of well matched linear integrated transistors (Reference 15). (This configuration is credited to Barrie Gilbert, of Gilbert multiplier fame, a Division Fellow at Analog Devices, Norwood, Mass.) Transistors Q_1 and Q_2 and proportional to absolute temperature (PTAT) current source PTAT (A_V) constitute a temperature independent voltage gain. Transistors Q_3 and Q_4 , with resistors R_{OS} and PTAT current sources PTAT(os), provide the bias voltage for the full wave detector $Q_5 - Q_8$. A complete circuit analysis is beyond the scope of this paper. However a comprehensive report is in process and, when published, may be requested.

Figure 5 summarizes the log cell transfer function where

- A_V = low level voltage gain for Q_1 and Q_2 (a design parameter)
- V_T = KT/q
- K = boltzmann's constant
- q = electron charge
- T = temperature in degrees Kelvin
- I_{Bias} = full wave detector bias current (Figure 4)(a design parameter)

$$\begin{aligned} (I_L/I_{\text{Bias}}) (\text{min}) &= \text{minimum log current for } V_{\text{in}} = 0 \text{ (a design parameter)} \\ K_L &= [2 / (I_L/I_{\text{Bias}}) (\text{min})] - 1 \end{aligned}$$

Figure 6 is a possible implementation of a log amp using the basic log cell. The constant current source $N(I_L/I_{\text{Bias}}) (\text{min})$ ensures that I_L is zero for $V_{\text{in}} = 0$. The log current compensation current source compensates for the lateral shift in the log output current with temperature. An alternate method to account for this shift is to vary the gain as a function of temperature of the X1 amp according to the following formula:

$$\text{X1 gain} = 1 + 0.00325 (T_2 - T_1) \quad (11)$$

Figure 7 illustrates the log output current as a function of input voltage without compensation (Figure 7b), with X1 gain compensation (Figure 7c), and with log current compensation (Figure 7d). The log slope is temperature insensitive (43.5 $\mu\text{A}/\text{dB}$) and the logarithmic error, $\epsilon(\text{dB})$, is less than ± 0.3 dB. The instantaneous input dynamic range is 60 dB (-75 to -15 dB) for ± 1.0 -dB error.

A single log stage (Figure 4) was analyzed using SPICE models for the ATT ALA201/202 UHF linear array (Reference 16). The 10-dB amp (Q1 - Q4 in Figure 4) frequency response was greater than 700 MHz and the full wave detector (Q5 - Q8) frequency response was greater than 400 MHz. This log technique should yield excellent results from DC to several hundreds of MHz using modern complementary bipolar ASIC and well designed PTAT current sources, etc.

CONCLUSIONS

To obtain the characteristics needed for the 1990s, new technologies/topologies will be necessary. Clever circuit designers will provide the topologies and may well drive the solid state technologies that will be used. The HBT offers excellent characteristics for integrated log amps for frequencies up to approximately 3 GHz. Complementary bipolar ASIC linear arrays should provide the components for logs from DC to 400 to 500 MHz.

The EW system engineer will still be faced with choosing the best log technique. However, once the decision is made, log accuracy should be better and lower in both cost and size than available today.

REFERENCES

1. Hughes, R. S. *Logarithmic Amplification*. Dedham, Mass., Artech House, 1986.
2. Lipsky, S. E. "Log Amps Improve Wideband Directionfinding," in *Microwaves*, May 1973, pp. 42-53.
3. Cohen, W., and C. M. Steinmetz. "Amplitude and Phase Sensing Monopulse System Parameters," in *Microwave J.*, October 1959 (pp. 27-33) and November 1959 (pp. 33-38).
4. Hughes, R. S. *Analog Automatic Control Loops in Radar and EW*. Dedham, Mass., Artech House, 1988.
5. -----, "RF Detector Logarithmic Video Amplifier," in *Microwave J.*, August 1989, pp. 137-48.
6. -----, U.S. Naval Weapons Center, China Lake, Calif. *Matched Detector Logarithmic Video Amplifiers Using Linear Application Specific Integrated Circuits*, August 1989 (NWC TP 7016).
7. Anadyne, Inc., Santa Cruz, Calif. *Application Notes for the Anadyne, Inc. L-17C1*, August 1989.

8. Smith, M. A. "A GaAs Monolithic True Logarithmic Amplifier for 0.5 to 4 GHz Applications," in proceedings of 1988 IEEE Microwave and Millimeter-Wave Monolithic Circuits Symposium, pp. 37-40.
9. Oki, A. K., and others. "High-Performance GaAs Heterojunction Bipolar Transistor Logarithmic IF Amplifiers," in proceedings of 1988 IEEE Microwave and Millimeter-Wave Monolithic Circuits Symposium, pp. 41-45.
10. Yu, W. M., and others. "Low-Power GaAs DLVA's Cut Delays Through Ku-Band," in *Microwaves & RF*, July 1989, pp. 137-38.
11. Menlo Industries, Inc., Fremont, Calif. *Log Amp Catalogue*, 1989.
12. Gorman, G. M., and others. "A GaAs HBT Monolithic Logarithmic IF (0.5 to 1.5 GHz) Amplifier with 60 dB Dynamic Range and 400 mW Power Consumption," in 1989 IEE *MTT-S Digest*, pp. 537-40.
13. Tran-Nguyen, D. "An Eight Stage Log Amplifier," in *RF Design*, November 1986, pp. 84-89.
14. Plessey Semiconductors, Cheney Manor, Swindon, U.K. *SL2521 B 1.3 GHz Dual Wideband Logarithmic Amplifier*, October 1986.
15. Analog Devices, Norwood, Mass. "DC Coupled Demodulating 120 MHz Logarithmic Amplifier (AD 640) data sheet" (1989).
16. ATT Microelectronics, Allentown, Penn. *ALA200 Family Design Manual*, 1988.

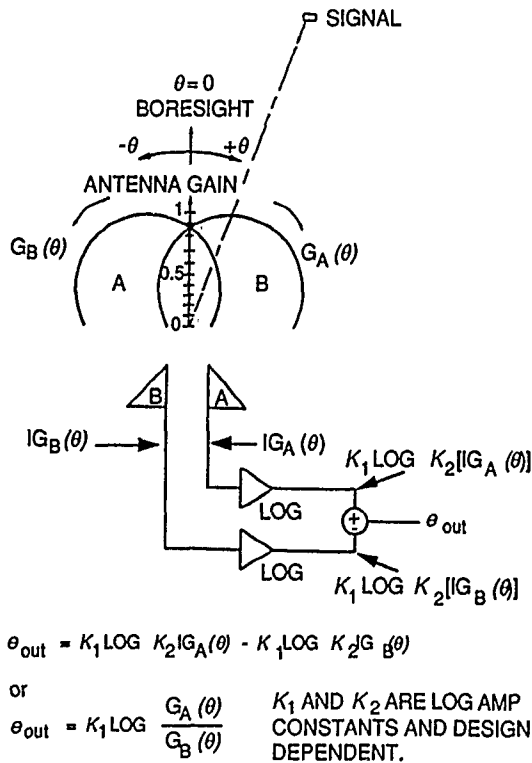


FIGURE 1. Basic Monopulse Direction Finder.

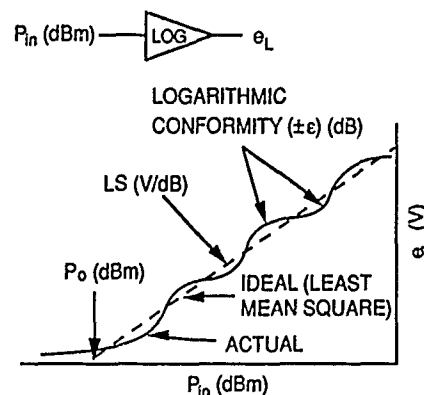
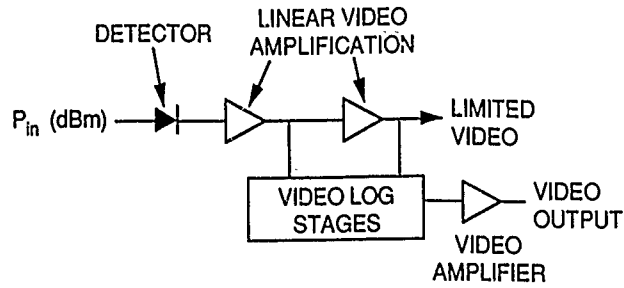
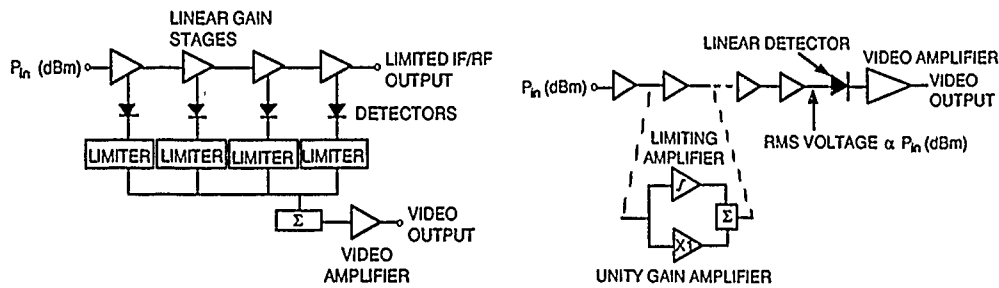


FIGURE 2. Practical Logarithmic Transfer Function.



(a) Detector log video amp (DLVA).



(1) Successive detection (SDLA).

(2) "True" log IF/RF.

(b) Log IF/RF amps.

FIGURE 3. Basic Log Amp Types.

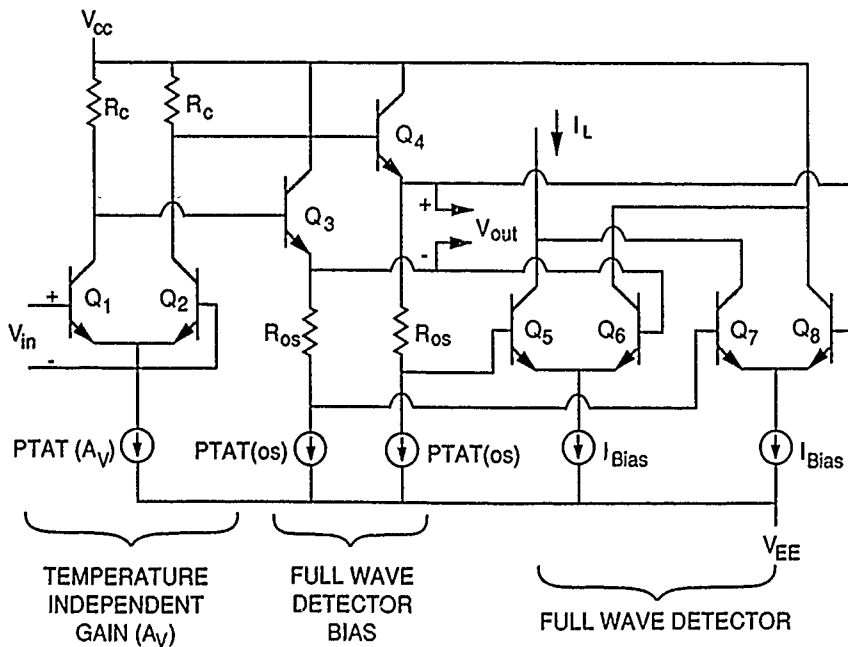


FIGURE 4. Basic Log Cell.

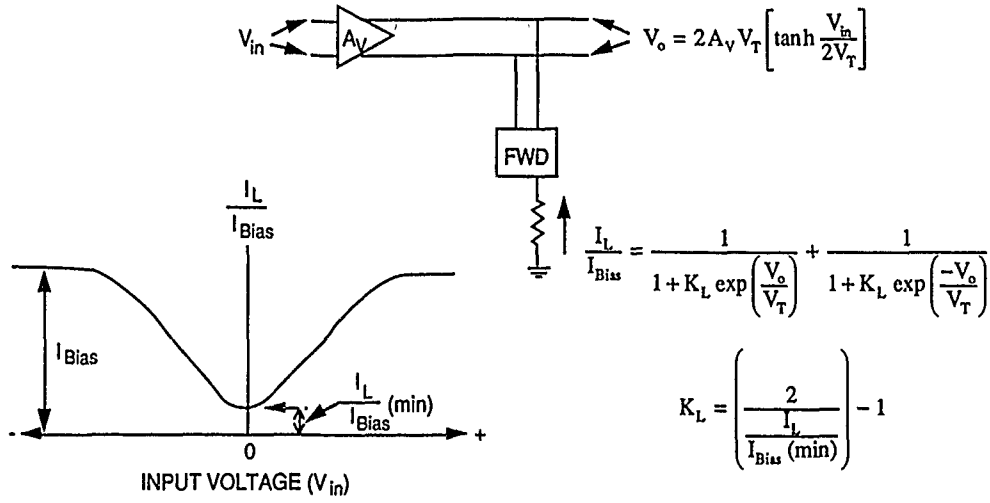


FIGURE 5. Temperature Insensitive DC Coupled Log Cell Characteristics.

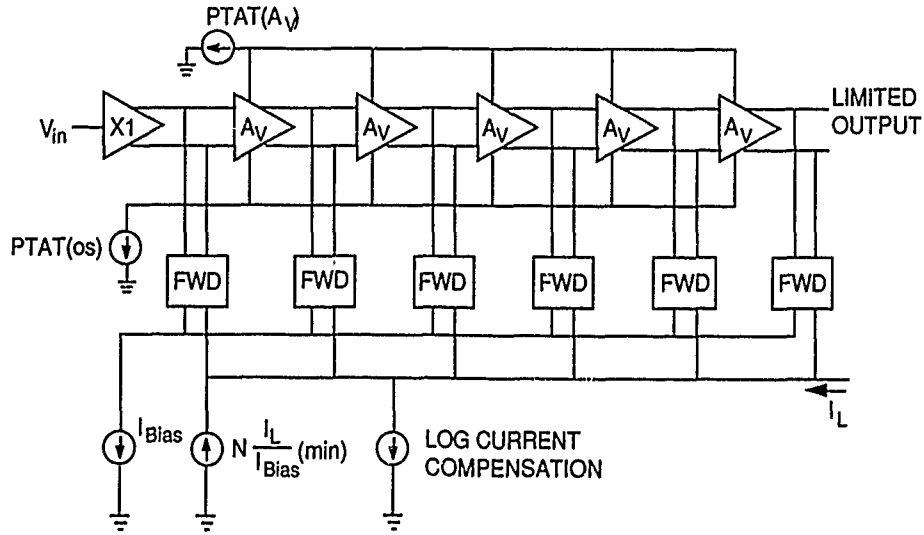
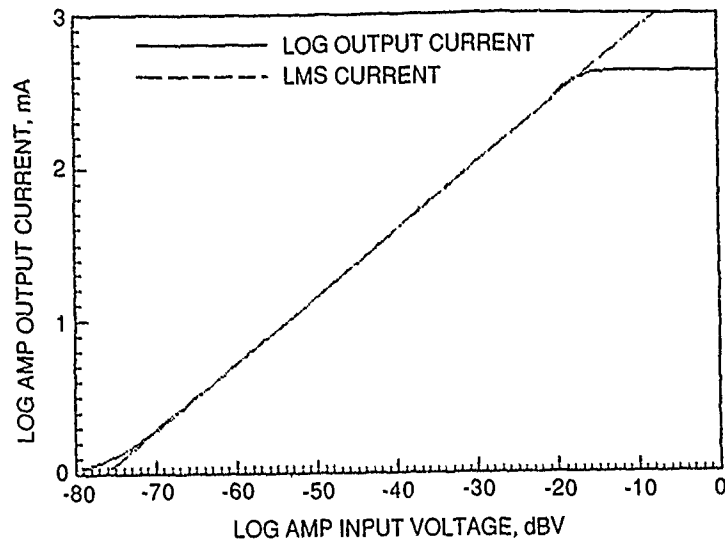
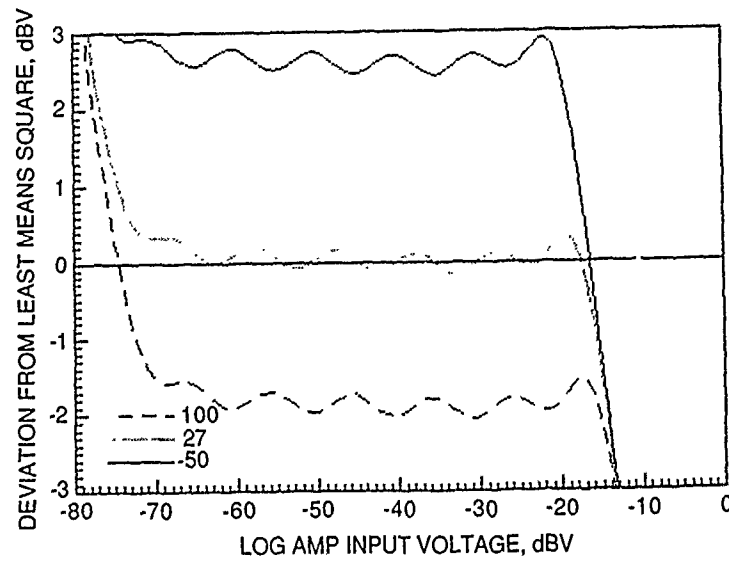


FIGURE 6. Six Stage (N=6) Full Wave Detector Log Amplifier.

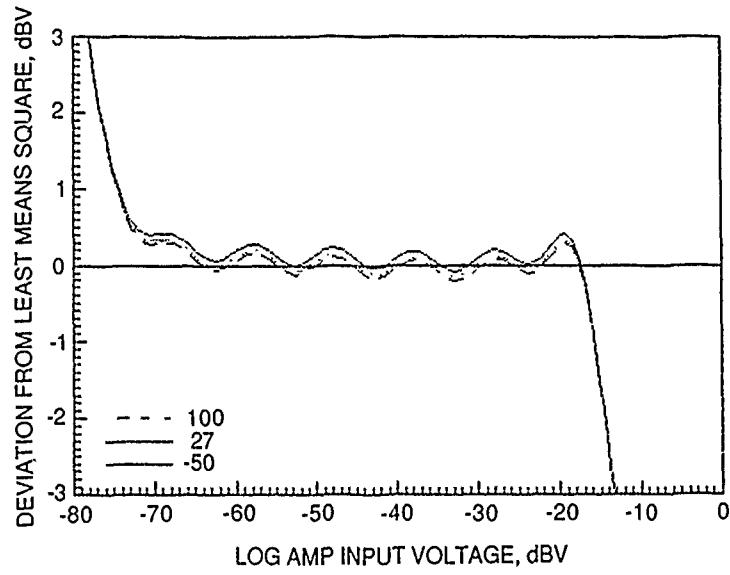


(a) Log output current and LMS deviation versus input voltage.
 $T = 27^{\circ}\text{C}$; $P_o(\text{dBm}) = -76.42$; $LS = 43.5 \mu\text{A/dB}$.

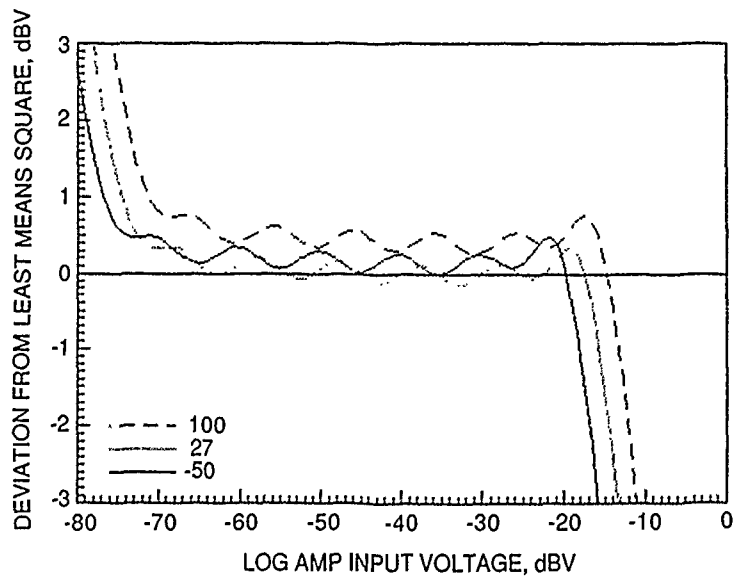


(b) Deviation from least mean square versus input voltage.
 No log temperature compensation.

FIGURE 7. Six Stage Log Characteristics. ($I_{\text{Bias}} = 500 \mu\text{A}$,
 $A_V = 10 \text{ dB}$, $(I_L/I_{\text{Bias}})_{\text{min}} = 0.1$.)



(c) Deviation from least mean square versus input voltage.
X1 gain compensation ($\text{Gain} = 1 + 0.00325(T_2 - 27^\circ\text{C})$).



(d) Deviation from least mean square versus input voltage.
Log current compensation.

FIGURE 7. (Contd.)

Discussion

Paper n° 12

Question : Ing. F. LABBROZI (Registro Aeronautico Italiano, Observer)

Could you speak about input noise problems and linearity ?

Answer : HUGHES

Normally logarithmic action does not occur until the wanted signal to noise ratio is obtained : linear amplification for small (threshold) signals, logarithmic amplification thereafter. Thus

classical signal sensitivity theory is quite valid. References 1 and 4 in my paper contain an extensive bibliography on signal sensitivity.

Linearity (or logarithmic conformity) depends on the logarithmic elements (differential amplifiers for DLVA and detectors for log IF amplifiers) and on the gain preceding each log element. Reference 1 covers this in detail, however in general if each log element operates over a 10 dB dynamic range one can expect a linearity within ± 0.3 dB or so. This increases to ± 0.5 dB for 12 dB per stage and ± 1 dB for 15dB per stage.

T/R MODULES FOR PHASED-ARRAY ANTENNAS

Colette FEIGNET *
 Yves MANCUSO *
 J. Claude RESNEAU **

* THOMSON-CSF/RCM - 178 Bd Gabriel Péri 92240 MALAKOFF FRANCE

** THOMSON-CSF/SDC - 18 avenue du Maréchal Juin 92363 MEUDON LA FORET FRANCE

SUMMARY

The concept of phased-array radar is critically dependant on the availability of compact, reliable and low power-consuming T/R modules. The purpose of the following presentation is to give an overview on two major programs actually at development stage within the THOMSON Group and on three major development axis (electrical concept optimization, packaging and size reduction).

We conclude saying that our achievements have proven the technical feasibility of the concept and enlighting three major improvement axis, based on reliability, power added efficiency and RF tests optimization.

I - INTRODUCTION

The concept of advanced phased-array radars which is based on the combination of a large number of active elements is critically dependant on the availability of compact and minimized weight, low consumption and high reliability microwave T/R modules. The main guideline for designing any T/R module to be part of such system is to achieve the best possible trade-off between performances, reliability and manufacturing cost.

Two major active phased-array programs are currently at development stage within THOMSON-CSF Group, being respectively in C-Band for counter-battery radars and in X-Band for ground-based and airborne radars.

In the course of the engineering efforts implemented to elaborate and refine the design of the required spread of T/R modules, adapted integrated microwave technologies have been successfully developed, such as MMHIC (Miniature Hybrid Microwave Integrated Circuit) or MMIC (Monolithic Microwave Integrated Circuits). A great emphasis was simultaneously put on packaging design and test optimization.

The purpose of the following presentation is to give an overview on the various achievements to date and the current stages of both C- and X-Band programs at THOMSON-CSF.

II - DEVELOPMENT AXIS

II.1 Electrical concept

We compared analog and digital options for monolithic phase-shifters and attenuators, which were designed from system requirements for radar T/R module applications. The complete functions - including the associated Silicon driving circuits - were evaluated according to the following criteria : RF bandwidth, phase and amplitude accuracy, total semi-conductor (GaAs and Si) areas and costs, power consumption. The block diagrams of a T/R module are given in figure 1 for both analog and digital phase shift options, which were both considered and assessed as part of T/R module studies. In the analog case each channel of the module is equipped with a phase-shifter and a variable gain amplifier, because of the no-reciprocity of these microwave functions. In the digital case, the phase-shifter is common to the two channels. The Silicon driving circuits ensure the interface between the informations given by the control steering unit and the microwave circuits.

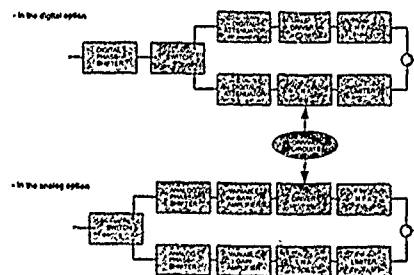


FIGURE 1 : T/R MODULE BLOC DIAGRAM

We shall proceed in the next few pages with the detailed comparison between the above two options in the particular case of an X-Band T/R module.

II.1.1. MMIC

The following MMICs were fabricated using THOMSON standard GaAs process.

X-Band 0-360° analog phase-shifter

The analog phase-shifter covers the full 0-360° range by modulating and combining the amplitude of four orthogonal vectors (figure 2). At the circuit input, a 0-180° splitter provides two opposite signals which are split into two ways with high-pass or low-pass 45° phase shifting cells. The amplitude of each vector is then controlled by a dual-gate FET, used as a variable attenuator. The four vectors are finally combined with a lumped elements combiner. A constant module turning vector can be obtained with an appropriate choice of the second gate control voltages.

Insertion losses are lower than 10 dB and both input and output VSWR are lower than 1.5 over a 20 % bandwidth. The voltage control law (figure 2) has to be stored in a digital memory. In order to minimize the size of this memory, we process by using only 8 points by arch, and the remaining values are obtained by linear interpolation. By using such method the maximum errors are 0.8 dB for the amplitude and 6° for the phase.

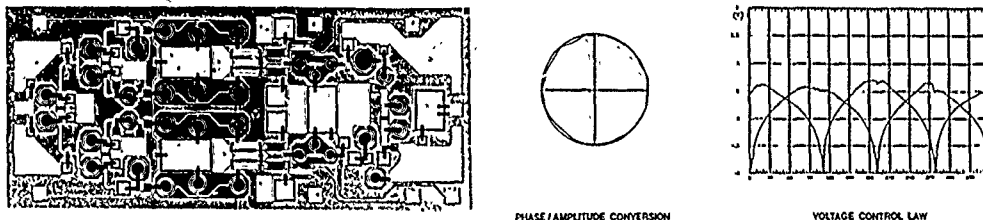


FIGURE 2 : ANALOG PHASE-SHIFTER

X-Band gain control amplifier

This circuit is a four stages amplifier (figure 3), including two dual-gate FETs in order to obtain a 40 dB dynamic range. The second gate termination impedance has been optimized to reduce the insertion phase variation while controlling the amplitude of the output signal. The maximum gain is about 25 dB in X-Band.



FIGURE 3 : GAIN CONTROL AMPLIFIER

X-Band 5 bits digital phase-shifter

The 180°, 90° and 45° are classical switched phase shifting cells. The 22,5° and 11,25° are based on the loaded line principle, but using lumped elements (figure 4). Insertion losses are about 10 dB ; for all the phase states over a 20 % bandwidth, we obtain a 2 to 3 dB amplitude variation.

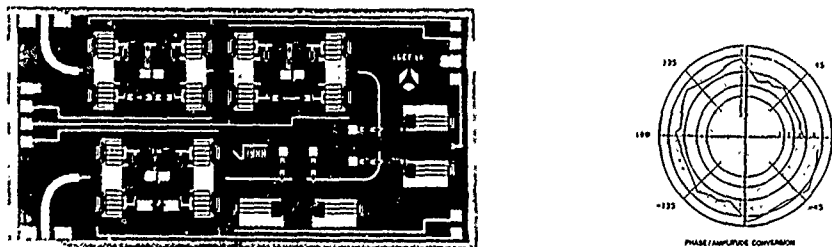


FIGURE 4 : DIGITAL PHASE-SHIFTER

X-Band digital variable gain amplifier

This circuit is a one-stage amplifier using a segmented dual-gate FET. In order to provide a 30 dB dynamic range with a 5 bits quantification, five second-gate segments and a total first gate periphery of 1 200 μm are needed (figure 5). Resistive input and output matchings lead to a 3 dB maximum gain in a wide frequency range.

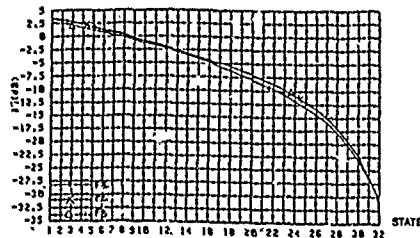
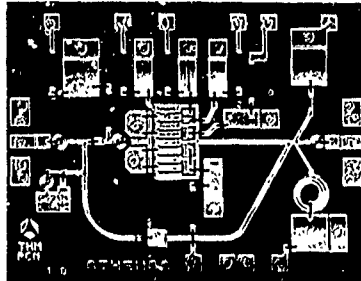


FIGURE 5 : DIGITAL VARIABLE GAIN AMPLIFIER

II.1.2. On-Silicon driving circuits

The driving circuits of a T/R module have to ensure the interface between the informations given by the control steering unit and the microwave functions. Gate and drain power supplies, through bias modulators, are common for the two options. The differences lie in the control of the phase-shifters and attenuators. In the digital case a simple CHOS gate array can be used to switch the voltages of the different bits. In the analog case, not only digital-analog converters are necessary, but also a calculation interface and a memory, in order to correct the control law dispersions between phase-shifters (and also the important temperature variation).

II.1.3. Two options comparison

The two options were compared in term of performances, power consumption and total implanted semi-conductors cost. The table below (figure 6) shows that the required phase and amplitude accuracy as well as the frequency bandwidth (more than 20 %) are obtained in both cases. We take note of the good behaviour of the digital phase-shifter with the temperature change. The last table gives for a complete T/R module the total semi-conductor areas and associated cost related to Silicon and Gallium Arsenide expected mass production costs. This analysis has shown that the cost of the Silicon circuits is as crucial as that MMIC and that the digital option becomes cheaper than the analog one from 1.5 \$ per Silicon square millimeter.

	DIGITAL OPTION		ANALOG OPTION	
	PHASE SHIFTER + ATTENUATOR			
EFFICIENCY (NUMBER OF CHIPS)	1	1	1	1
FREQUENCY BANDWIDTH	0C	0C	0C	0C
BASE ELEMENTS	FET DRIVER	DUAL GATE FET	DUAL GATE FET	DUAL GATE FET
DRIVE GATE PERIPHERY	0.6 mm	4.6 mm	5.4 mm	3.0 mm
BASE AREA	0 mm ²	30 mm ²	28.8 mm ²	36.8 mm ²
MICROWAVE LOSSES	+0.01	+2.01	+0.01	+10.01
AM/FM	46.2 3 10 0.05	46.2 3 10 0.05	46.2 3 10 0.05	46.2 3 10 0.05
TEMPERATURE BEHAVIOUR	46.2 3 10 0.05	46.2 3 10 0.05	46.2 3 10 0.05	46.2 3 10 0.05

MODULE SEMICONDUCTEUR AREAS	DIGITAL OPTION	ANALOG OPTION
GAAS	45 mm ²	37.5 mm ²
SI	59 mm ²	111 mm ²

	DIGITAL OPTION	ANALOG OPTION
MMIC (PHASE SHIFTER + ATTENUATOR)	0.8 W	6.7 W
DRIVING CIRCUITS	2.2 W	2.8 W
TOTAL CONSUMPTION	3.0 W	5.5 W

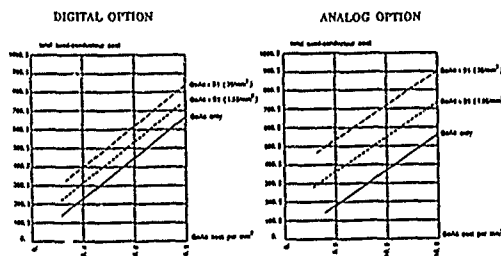


FIGURE 6 : TWO OPTIONS COMPARISON

II.2 Microwave technologies

The first T/R module was manufactured at THOMSON-CSF in 1981, using the HMIC (Hybrid Microwave Integrated Circuits) technology (figure 7).

The size was 15 mm x 100 mm and we measured 0.5 W output power and 5 dB noise figure over a 5 % bandwidth.

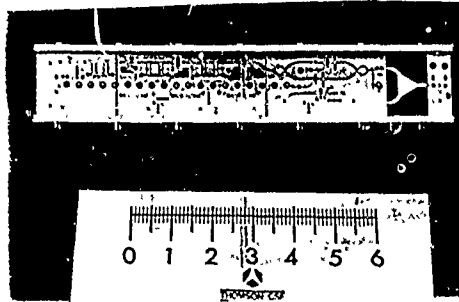


FIGURE 7 : HMIC T/R MODULE

The standard HMIC consists in ceramic substrates on which are etched conductive lines by using thick-film or thin-film techniques. Several manual processing steps are needed like wire bonding and active or passive components soldering. They represent failure-prone steps in the manufacturing cycle and a potential variability factor in the microwave performances, the overall effect being a yield reduction and, as a consequence, a cost increase.

In view of above, THOMSON decided to develop within the Group a semi-integrated technology, in order to avoid the costly insertion of the passive components.

The feature of the MIMIC process consists in prefabricating on an alumina or silica substrate, and as a continuous sequence of operations, a large number of miniature circuits including all the passive elements, only the active components having to be inserted. Five mask sets are necessary to fabricate RLC elements like resistors, spiral inductors, interdigital or MIM capacitors. Connections use via-holes and air-bridges. A first example is shown in figure 8 : an X-Band two-stages 200 mW amplifier, with a size of 6 mm x 4 mm. Figure 9 gives another example : the transmit channel of an X-Band T/R module.

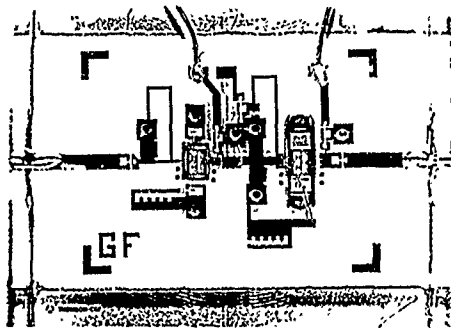


FIGURE 8 : X-BAND MEDIUM POWER AMPLIFIER

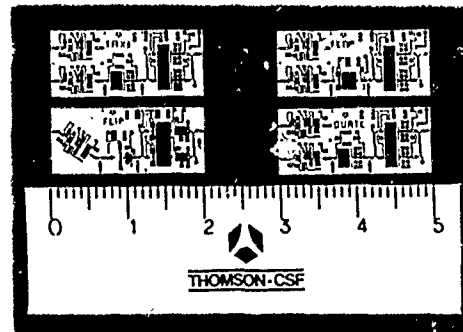


FIGURE 9 : T/R MODULE TRANSMIT CHANNEL

Based on this semi-integrated technology we designed in 1987 a module with a reduced size of 15 mm x 50 mm (figure 10).

The peak power reaches 2.5 W over all the expected frequency range. The circulator (8 mm x 8 mm), which has been developed to be used with only one magnet, provides 0.3 dB losses and more than 25 dB isolation from 8 GHz to 12 GHz.

The noise figure of the complete receive channel is less than 3 dB, including circulator and limiter losses.

The reflection-type phase-shifter consists in three Lange couplers, with PIN diodes for the 180° and 90° bits, and hyperabrupt GaAs varactor diodes for the analog 0-90° phase shift.

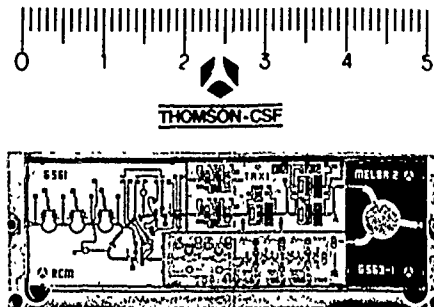


FIGURE 10 : MIMIC T/R MODULE

MIMIC technology is particularly suited for high power circuits using discrete FETs and is compatible with MMIC integration for other active functions. We presented in 1987 a 16 W pulsed X-Band solid state transmitter using this technology.

The most significant cost reduction will be achieved for mass production with the MMICs advent. All the matching circuits are fabricated on the same substrate as the active devices. An important effort is made to minimize the total area and to optimize the design for not being sensitive to process dependant parameters thereby reducing the cost of each chip.

The THOMSON-CSF standard GaAs processes (low-noise and power processes) include overlay capacitors, spiral inductors, implanted and metallic resistors. Air-bridges are used to interconnect elements, and via holes to link them to the ground through the 100 μ m thick substrate. S-parameters measurements are provided by an on-wafer measurement set-up including an automatic prober, RF CASCADE probe heads, DC probe cards, a network analyser and automatic power supplies controlled by a computer.

II.2 Packaging

The main technological issues for T/R module packaging design are weight, cost, isolation, thermal resistivity, hermeticity and compaction of the interconnections. The design has also to be compliant with L, S, C and X-Band T/R modules specifications.

A ceramic package has been designed to solve the above requirements.

The MMIC are either brazed or glue attached to an alumina (or metallic) carrier. These carriers are brazed and automatically bonded to the connection lines etched on the alumina main substrate.

The microwave trough-wall access were designed for 50 Ω impedance and the process was refined to obtain a good reproducibility of the glass sealing of the alumina frame with regard of thickness, configuration, adherence and dielectric constant.

Investigations have been carried out in parallel in order to define material to be used for the fabrication of the heatsink, main requirements being the following :

- high thermal capability,
- low weight (in particular for airborne applications),
- good match with alumina expansion factor.

III - APPLICATION PROGRAMS

III.1. C-Band program

III.1.1. Program overview

Named COBRA (COunter Battery RADar), the program which is presented below is the first industrial project based on a multi-national cooperation and aiming at large scale production of T/R modules. This program is divided in two phases :

- A development phase for which contract was formally awarded and signed in the course of February 1990 involving the EUROART consortium with following membership :

- . GENERAL ELECTRIC
- . SIEMENS
- . THOMSON-CSF
- . THORN-EMI

During this development phase, THOMSON will be in charge of :

- . system engineering
- . simulation
- . signal processing
- . radar processing
- . T/R modules
- . MMIC

This phase which is including three radars prototypes to be manufactured shall be completed by the end of 1994. The implication for THOMSON Group is materialized in fabricating a few thousands of T/R-modules within the next 3 years.

- A production phase which is presently scheduled for 1996. Beside any estimate of worldwide market prospects, we may expect about 60 radars to be built to cope with the european needs only as of today. At production stage THOMSON's scope is to cover part of T/R modules and MMIC fabrication.

III.1.2. C-Band T/R module specifications

The main characteristics in a 10 % RF bandwidth are the following :

Electrical :

- Transmit :
 - . output power : 4 to 6 W peak
 - . duty cycle : 10 %
 - . phase shifter quantification : 4 bits
- Receive :
 - . noise figure : 4 dB
 - . gain : 21 dB
 - . gain control : 6 bits, linear in amplitude
 - . phase-shifter quantification : 4 bits
- Consumption :
 - . 3,2 W average
 - . 27 W peak

Mechanical :

- Size : 82 x 27 x 4,5 mm³
- Weight : 35 g

III.1.3. C-Band T/R module design

As shown in the photograph given figure 11 this module includes 7 MMICs :

- a 4 bits phase-shifter including the T/R switch (6.5 mm²),
- a 6 bits variable gain amplifier (1.6 mm²),
- two low-noise amplifiers (2 mm² each-figure 12),
- a driver amplifier (4.5 mm²),
- two 3 W high power amplifiers mounted in a balanced configuration (12.5 mm² each-figure 13).

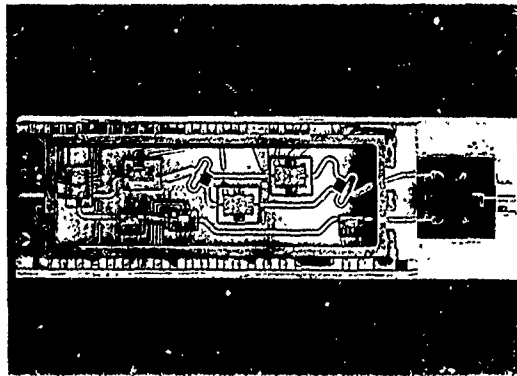


FIGURE 11 : C-BAND T/R MODULE

Each MMIC is reported in a carrier, to be RF tested and burned-in before being assembled in a ceramic package as described here above. The module is RF tested before and after electrical sealing. Final tests are performed after the assembly in a package including 4 T/R modules and the associated driving circuits.

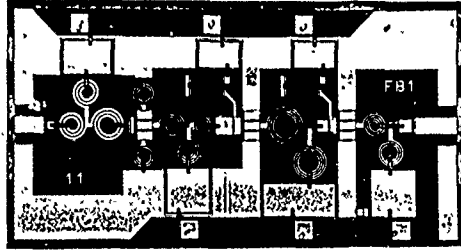


FIGURE 12 : C-BAND LNA

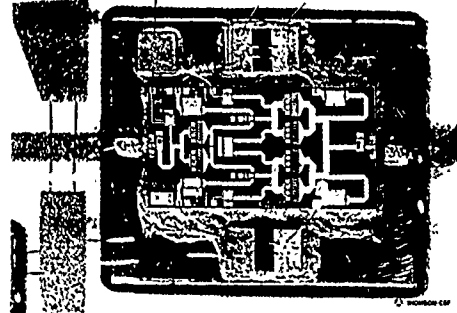


FIGURE 13 : C-BAND HPA

III.1.4. C-Band T/R modules measurements

The main results are as follows :

- the CW output power reaches 4 W to 5 W over all the expected frequency range, as shown in figure 14.
- the receive channel has a 35 dB gain with an associated noise figure which is comprised between 3 and 4 dB for all the attenuation states (figure 15), including the circulator and limiter losses.
- the attenuation dynamic is greater than 20 dB.

The 4 bits phase-shifter presents 6 dB insertion losses and a relative phase-shift of $\pm 10^\circ$ (figure 16).

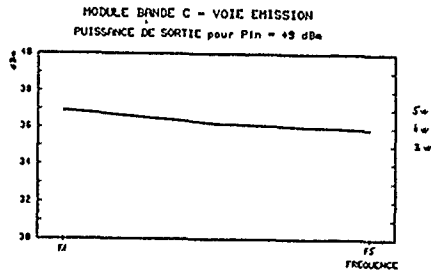


FIGURE 14 : C-BAND T/R MODULE OUTPUT POWER

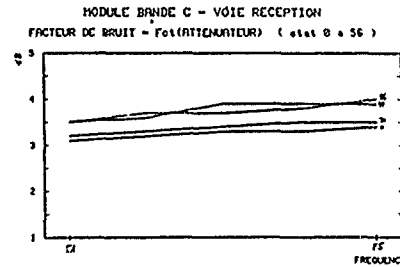


FIGURE 15 : C-BAND T/R MODULE NOISE FIGURE

4 BIT PHASE SHIFTER

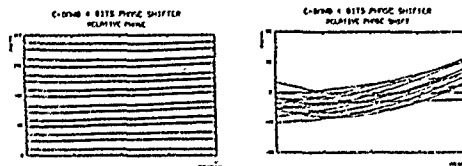


FIGURE 16 : C-BAND MMIC PHASE-SHIFTER

III.2. X-Band Program

III.2.1. Program overview

In order to optimize the non-recurrent engineering costs and to reduce the mass production costs, the Group decided to develop a common X-Band T/R module for airborne and ground-based radars applications.

The main milestones of the program are the following :

- the design and breadboarding of a dozen T/R modules,
- the manufacturing of a breadboard representing a part of an X-Band active phased-array, including about 100 T/R modules,
- the qualification of the T/R module technology.

This program will be concluded by the complete definition of two phased-array antenna prototypes, being respectively for airborne and ground-based radars applications.

III.2.2. X-Band T/R module specifications

The expected specifications in order to satisfy the antenna requirements are listed below :

- CW output power : about 2 W
- noise figure : less than 5 dB
- gain control : 5 bits over the 30 dB dynamic range
- phase-shifter : 5 bits quantification

III.2.3. X-Band T/R module design

This module (figure 17) uses MMIC for all sub-circuits except for the high power amplifier which is made using two FETs. The circuits are reported on metallic or ceramic carriers. The compaction of the interconnections together with cost reduction leads also to the use of a ceramic package. The driving circuits, shared between two active microwave modules, are manufactured on a multilayer thick-film alumina. They include the following functions : a microcontroller, digital and analog interfaces and bias modulators for the FETs in order to reduce the power consumption.

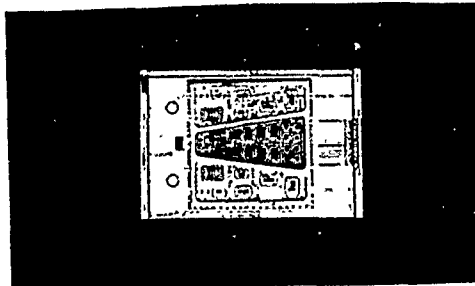


FIGURE 17 : X-BAND T/R MODULE

III.2.4. X-Band MMIC measurements

The results for the digital phase-shifter and attenuators have been given in paragraph II.1.

The MMIC low-noise amplifier provides 20 dB gain with a 3.5 dB associated noise figure

The high-power amplifier is made of two THOMSON power FETs between Lange couplers. At 1 dB compression, we obtain 33 dBm (2 W) with a 30 % power added efficiency (figure 23) ; in pulsed modes we obtain up to 1 dB additional output power.

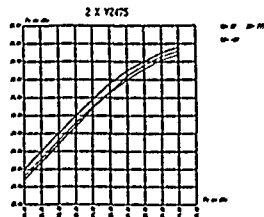


FIGURE 18 : X-BAND HPA

IV - IMPROVEMENT AXIS

IV.1. Reliability

No need to say that a key point in favour of active phased-array antennas is definitely the built-up potential for significant improvement from the reliability standpoint. Such progress margin for the whole system reliability is originating from the large number of modules acting in parallel and contributing to the overall performances via simultaneous combined effects. The increased reliability is actually tied-up with the applicability of the so-called "smooth degradation concept" to the system.

Reliability consideration should be input at design stage and treated as part of specifications or essential criteria in lieu of being accepted de facto as a measurement tool of engineering and fabrication achievements. A major target for designers is to carry-out detailed appraisals of reliability aspects for each individual technological step within the fabrication process. Such long term investigation requires to follow the path of extensive data collection regarding degradation phenomena and associated activation energy in order to reach the stage of establishing realistic and accurate enough simulation models to be in a position to optimize the design of the circuits on both performances and reliability aspects.

The multiplicity of connections being a weak point for any circuits and contributing to reducing the level of reliability, the future research and development axis should include the feasibility study of increasingly integrating. In addition to above technical considerations any gain in terms of integration is a further step towards cost effectiveness

IV.2 Power added efficiency

The need to reduce the dissipated power and the cooling requirements for phased-array antennas puts a tremendous premium on achieving significantly higher power-added efficiency. As a consequence we investigate class-B operation, often in a push-pull configuration, with the following potential advantages compared to class-A :

- higher power-added efficiency (until 40-45 % in X-Band),
- negligible power dissipation at no RF power,
- under backoff, the efficiency of a class-B amplifier does not degrade as rapidly as that of a class-A amplifier.

IV.3. RF tests optimization

The MMIC test flow chart which is currently followed includes, both on-wafer DC and RF test and on-carrier RF test. Such heavy step by step testing induces high expenses both in terms of time and budget which represent a significant portion of the final semi-conductor estimated cost. In addition to itemized testing of individual components, a full scheme of measurements is implemented prior to acceptance of any module, again contributing to load the overall fabrication cost.

Our efforts are directed towards classifying and defining the number and the extent of necessary and sufficient tests required to ensure a high quality fabrication standard at competitive cost.

V - CONCLUSION

We have presently reached a reasonably advanced stage of the pure engineering phase of the T/R module projects which are currently in course of implementation within the THOMSON Group. A significant number of preliminary tests including at full scale have been successfully carried-out. Our achievements have proven the technical feasibility of the concept as such and shall be used from now or as a basis for the forthcoming development phases.

We would like to conclude saying that in order to guarantee the commercial viability of such projects and to make the industrialisation of the T/R modules fabrication a reality within the next few years, three priority axis of work are directly enlightened from the brief presentation purpose of our paper of today :

- performances : with the improvement of the total power-added efficiency as a main goal,
- Reliability : through the development of accurate modelling tools to be in a position to design-to-reliability and to real-time assess the smooth deterioration process and the remaining life duration expectancy of any T/R module-based system,
- Cost : each among the three main components of the final overall cost of such systems (semi-conductors, technologies for assembly and packaging, large scale fabrication and testing) being highly critical, all of them shall equally be given due consideration at each step of the development phases.

MMIC IMPACT ON AIRBORNE AVIONIC SYSTEMS

Edward J. Jones & William J. Bocchi, Jr.

Rome Air Development Center/RBES
Griffiss AFB NY 13441-5700

Abstract

The latest advances in Monolithic Microwave Integrated Circuit (MMIC) technology and its impact on airborne avionic systems, along with a unique technique for designing reliability into MMIC devices, is described in this paper. Current MMIC transmit/receive (T/R) module performance is presented along with current hybrid module results for comparison. For example, typical RMS phase error for a 10 GHz T/R MMIC module is about one half of a hybrid module, which can increase antenna performance by 5dB. RADC's pioneering work in developing and applying finite element analysis (FEA) techniques to MMIC T/R modules to determine temperature and stress levels within microscopic regions of these devices is also shown. For the first time, the ability to assess the reliability of new MMIC designs using this analytical tool makes it possible to avoid time consuming and costly after-the-fact test and redesign of a given device/module.

1.0 Introduction

Airborne active avionic systems are required to perform very sophisticated and precise functions without overburdening the operating crew and the performance of the platforms to which they are attached. Future systems will also have to cope with much higher threat diversity and threat densities. This will require more efficient and effective control of both radiated and received energies. Along with requirements for higher system performance, a higher level of operational availability is required to support the longer missions and higher maintainability requirements of future systems and platforms. To achieve the required level of availability without simultaneously increasing costs, reliability of system components and systems themselves must increase. Satisfying all of the above requirements will be difficult and can only be achieved by higher levels of system integration, uses of new system architectures, uses of better manufacturing controls and methods, and the application of new component technologies.

Active aperture phased array is the antenna architecture being developed to fill the above requirements for airborne radar and ECM systems. This type of antenna architecture has three major advantages over conventional dish antennas: 1) the speed and agility of an electronically steered radiated and received beam, 2) multiple beam capability and 3) the use of highly reliable solid-state amplifier modules. Therefore, these types of arrays have the capability of increasing system performance and functional flexibility, and be highly reliable, thereby significantly increasing system availability. The two most important requirements of any radar or ECM system/antenna are the requirements for electronic performance and low cost. To date, few active phased arrays have been demonstrated due to high cost.

The key component in any active aperture phased array antenna is the transmit/receive (T/R) module. The classical T/R module contains a power amplifier for transmitter gain and power output, a low-noise amplifier for receiver gain, a bidirectional phase shifter for phase control, and a digital controller. Four key problems normally associated with solid-state modules of this type are: 1) high cost, 2) low reliability, 3) less than octave bandwidths, and 4) large size and weight. Since many hundreds or even thousands of T/R modules would be used in any one system, it is obvious that a low cost, highly reliable module component technology is required for a system to be affordable and available.

Monolithic Microwave Integrated Circuit (MMIC) technology is the technology being developed to meet the above requirements for low cost, highly reliable module components, wide bandwidth, small size and weight, and is described in the following section along with a unique technique for designing reliability into MMIC devices.

2.0 MMIC T/R Module Technology and Its Impact on Airborne Avionics

MMIC technology is an approach wherein all of the active and passive components of a circuit and its required interconnections are formed on a single semiconductor material; e.g., gallium arsenide (GaAs). MMIC technology appears to be ideal to fulfill the above T/R module requirements because of the inherent low cost, improved reliability and reproducibility, small size and weight, circuit design flexibility, and broadband performance associated with an integrated circuit process.

Low cost, improved reliability and reproducibility are derived from two areas: 1) inherent low cost involved with production of integrated circuits due to the lack of manual handling and assembly, and 2) lack of a large number of wire bonds. Wire bonds have always been a serious problem for reliability and reproducibility of any microwave circuit. The elimination of a large number of wire bonds also eliminates undesired parasitics and circuit discontinuities which limit broadband performance of conventional hybrid solid-state circuits. Small size and weight are intrinsic properties of the MMIC approach.

The key components and major challenge for the MMIC T/R module designer is the power/driver amplifier and the low-noise amplifier. A large effort has been under way for several years aimed at fulfilling the MMIC amplifier requirements. The two MMIC amplifier concepts that have been receiving the most attention over the past few years are the distributed or traveling wave amplifier and the conventional feedback amplifier. A survey of the latest results show that distributed power amplifiers have the capability of producing a watt or less in power with about 5dB of gain and an efficiency of about 15% over an octave bandwidth. The distributed low-noise amplifiers have the capability of producing about 10dB of gain with about a 5 to 7dB noise figure over an octave bandwidth. In comparison, the conventional feedback type power/driver amplifiers have the capability of producing up to 5 watts of power with anywhere between 5 to 30dB of gain with an efficiency of about 25% over a 20% bandwidth. The conventional feedback type low-noise amplifiers have the capability of producing up to 25dB of gain with as low as a 2.5dB noise figure.

A number of design issues are associated with selecting the components for a T/R module for a given phased array. For the radar T/R module case, the primary transmitter/amplifier issue is to obtain nearly uniform gain and power output over the required bandwidth with very low power ripple and phase error. A second major issue is prime power consumption since the transmit power amplifier in the module is the major source of power consumption in an array. The primary receiver amplifier issue is to obtain nearly uniform gain and noise figure over the required bandwidth with very low phase error. MMIC T/R module results to date are very promising and are presented in Table 1. Table 1 also contains the current hybrid module results for comparison.

Table 1
State-of-the-Art T/R Module Results

	MMIC T/R Module Results				Receive	
	Power (W)	Gain (dB)	Efficiency (%)	Gain (dB)	Noise Figure (dB)	Phase Error (RMS Deg)
L-Band	2.5	31	20	32	3.5	4.0
S-Band	10.0	30	25	25	4.0	4.0
C-Band	8.0	30	24	25	4.0	3.5
X-Band	2.5	30	25	20	4.0	4.5
Hybrid T/R Module Results						
S-Band	20.0	16	20	20	3.0	10.0
X-Band	1.5	30	15	10	4.0	8.0

Typical radar systems employ an RF amplification chain driving a dish or corporate feed passive phased array. The RF signal (RF excitation) from the STALO is amplified through a chain which consists of three stages of amplification: a predriver, a driver, and a high-power amplifier. A traveling wave tube (TWT), a klystron tube or a high-power, solid-state amplifier would be used for the high-power amplifier. These systems typically have a radiant to prime power efficiency of 10 to 15%. This low efficiency is primarily due to two reasons: 1) high RF power losses in the transmit beam-forming network of the corporate feed system which can be as high as 5 to 8dB, and 2) the power required for the transmitter environmental control and cooling system within the corporate feed network.

In comparison, an active phased array employing MMIC transmit/receive modules has a radiant to prime power efficiency of 20 to 25%. Therefore, for a given radiated power the active phased array will use less prime power. This translates to a lower rate of prime power consumption for a given mission, which would allow more time on station for an airborne system. Also, by having the T/R modules very close to the antenna, the detection ability of the system increases due to the fact that the module's high gain, low-noise amplifier is introduced into the system's receiver chain well before the high loss incurred in the beam-forming network; thereby, increasing the ability to see low observable targets. Another performance advantage that an active phased array has over a dish system is the ability to electronically steer the radiated beam thus giving the operator the ability to look longer in high threat areas and thus the ability to integrate small targets out of clutter.

An analysis was performed using typical T/R module results to determine the impact of module errors on antenna performance. An "ideal" antenna was defined for this analysis as a large array with half wavelength element spacing, 60dB Taylor weighting and with T/R modules employing 6-bit phase shifters; resulting in a 60dB one-way sidelobe antenna pattern. The results of introducing T/R module errors and failures into the antenna is shown in Table 2. The net result of this analysis is that the errors introduced by module errors and failures have a profound impact on system performance. Therefore, MMIC technology should have a major impact on systems in the future since it is now being shown that this technology can produce T/R modules with less errors or tighter tolerances and are more reliable than in the past.

Table 2
Summary of T/R Module Error Effects on Peak Antenna Sidelobe Level
for Large Array

Module Errors	Increase From "Ideal" Level (dB)
1dB Amplitude, 5 Deg Phase	
No Module Failures	+10
1% Module Failures	+13
5% Module Failures	+18
2dB Amplitude, 10 Deg Phase	
No Module Failures	+14
1% Module Failures	+16
5% Module Failures	+20

3.0 Applying Finite Element Analysis Techniques

Finite element analysis (FEA) is a computer simulation technique that can predict material response or behavior of a modeled device. MMIC devices such as power and driver amplifiers generate large amounts of heat in extremely small regions in the gallium arsenide circuit. Furthermore, this concentrated heat generation varies rapidly with time during the on/off pulsing operation of the amplifier. FEA makes it possible to predict the thermal response of a MMIC device. Even more significant, FEA can also predict the material stresses due to thermal gradients within dissimilar materials layered together. Knowing the material stresses, and using appropriate material failure theories, an assessment of reliability due to mechanical and structural failure mechanisms can be made. The ability to assess the reliability of new designs using this analytical tool makes it possible to avoid time consuming and costly after-the-fact test and redesign.

Analytical modeling of MMIC devices presents unique issues that must be dealt with. The fundamental modeling problem is the small feature size of the region of interest (a few micrometers in size) but with a much larger region between the heat sources and the final heat sink. The solution is to use a succession of finite element models plus the use of thermal symmetry to reduce model size. Finite element thermal analyses of a C-band transmit/receive radar module under life test at RADC have been documented in Reference 3. Reference 3 describes thermal modeling techniques, 2-dimensional vs. 3-dimensional thermal analyses, and transient thermal simulations, and is available from either author of this paper. The following topics, not included in Reference 3, will be discussed: 1) Finite Element Model Structural Boundary Conditions; 2) Material Stresses; 3) Failure Theories.

When modeling only a portion of an integrated circuit to determine material stresses due to a varying temperature distribution throughout the entire chip and all substrate layers, it is necessary to simulate the structural effects of the missing material along all boundaries of the model. Figure 1 shows the temperature distribution in a gallium arsenide chip with three transistor cells. The heavy dark lines show lines of thermal symmetry; that is, equal temperatures at equal distances from the line. It can be shown that physical displacements perpendicular to these lines are equal to zero. Figure 2 shows the nodal displacements in a plane that passes through the center of the two closely spaced FET cells (line A-A in Figure 1). Notice that the displacements are primarily in the Y-direction and that displacements perpendicular to the plane are essentially zero. This validates the use of adiabatic lines of thermal symmetry as boundaries of a structural model providing zero displacement boundary conditions are specified at all nodes of the boundary in directions perpendicular to the symmetry plane.

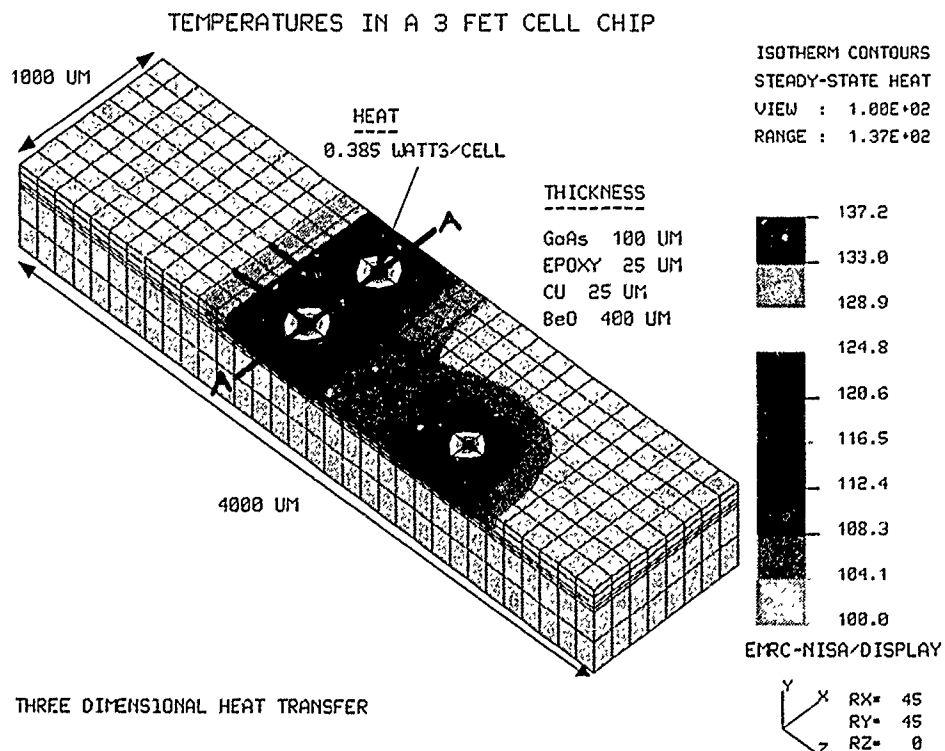
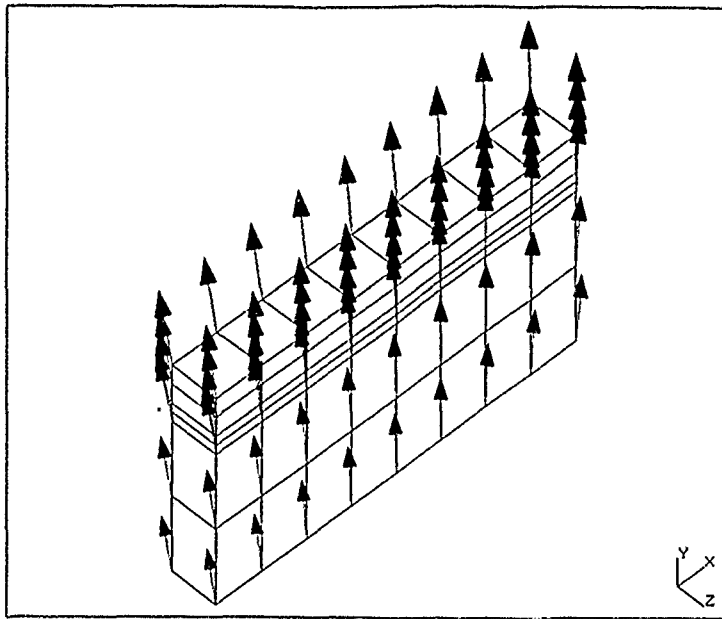


Figure 1

DISPLACEMENTS AT A PLANE THRU TWO FET CELLS

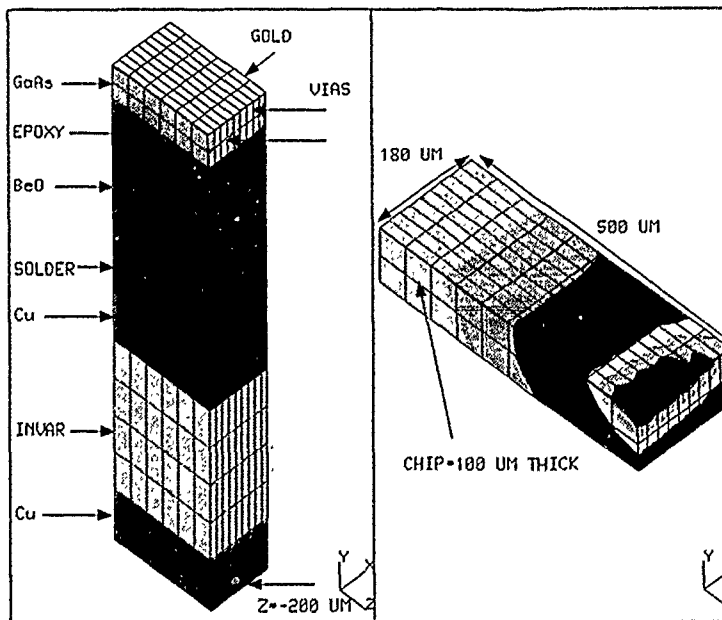


DISPLT. - VECTORS
 MAX. DEF = 3.08E+00
 NODE NUMBER = 1524
 SCALE = 1.0
 (MAPPED SCALING)

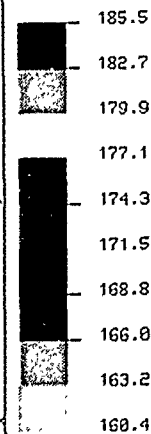
3-D THERMAL STRESS

Figure 2

THERMAL MODEL WITH GOLD AND GaAs TEMPERATURES



ISOTHERM CONTOURS
 STEADY-STATE HEAT
 VIEW : 1.60E+02
 RANGE : 1.85E+02



EMRC-NISA/DISPLAY

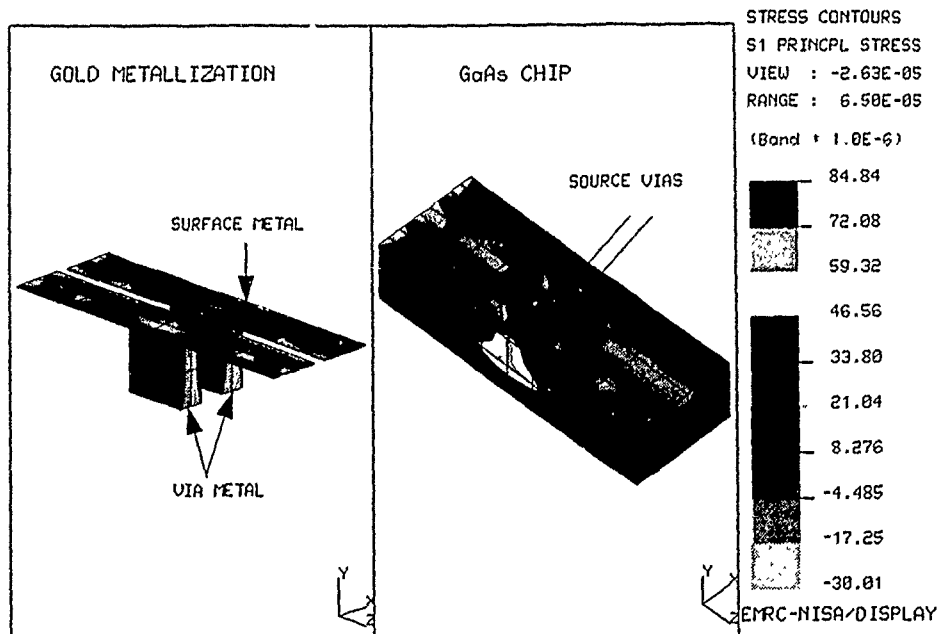
3-D HEAT TRANSFER 1/4 FET CELL WITH SOURCE AND DRAIN METAL

Figure 3

Figure 3 shows the thermal model and the output temperatures in the chip and gold surface metal. These temperatures are available in a thermal results file and are read into the stress analysis data file. Thus every node point has a specified temperature. With the proper boundary conditions specified as discussed above, and the specification of each material's modulus of elasticity and coefficient of thermal expansion, material stresses can then be computed. Figure 4 shows the principal stresses in the surface metal and the chip. The stress values are in units of newtons per square micrometer. There are 12 stresses that are computed: three normal stresses in the x, y, and z directions, three shear stresses in the xy, yz, and xz planes, three principal stresses, and three "equivalent" stresses (maximum shear, Von Mises, and octahedral shear). Figure 4 shows only one of the 12 possible stresses that are computed. Which stresses are the ones of concern? Principal stresses are the maximum and minimum normal stresses acting in directions usually different from the model's global x, y, and z directions. One of the three principal stresses, along with the maximum shear stress, represent the largest stresses at a point in the material. The Von Mises and octahedral shear stresses are equivalent stresses that allow a comparison to be made with the maximum normal tensile stress that causes a failure of the material in question during a uniaxial tensile test.

For noncyclic loadings, the maximum principal normal stress for brittle materials and the maximum Von Mises stress for ductile materials, should be below the material's yield point in tension. The maximum shear stress should be less than one half of the tensile yield point. For cyclic loadings, these stress values should be below the material's endurance limit or fatigue limit. The endurance limit is usually somewhere between one quarter and one half of a material's ultimate tensile strength. If one is willing to accept failure at some specified number of stress cycles, then stress versus number of cycles to failure (S-N) material data must be used. This data usually shows considerable scatter and is highly influenced by many factors. The data is usually available only for zero mean stress with completely reversed bending or shear loadings. There are several techniques to modify this data to account for nonzero average stress situations. For materials that are stressed beyond the elastic limit, but below the ultimate strength, the number of load cycles is determined using material data that relates strain, instead of stress, with number of load reversals. A current contractual effort sponsored by RADC is conducting research in the area of stress analysis and theories of failure for materials used in electronic and microelectronic applications.

PRINCIPAL STRESSES IN SURFACE METAL AND CHIP



3-D THERMAL STRESS 1/4 FET CELL

Figure 4

A final point concerning thermal stress analysis of dissimilar materials bonded together should be made. Figure 5 is a stress contour plot that shows node point stresses on the viewing planes (newtons/square micrometer). These node point stresses are averaged using the element stresses for every element that shares the node point. When dissimilar materials share a node point, because the coefficients of thermal expansion are different, each material experiences a different stress at the node location. It is very important not to rely on averaged results but to examine the element stresses at the shared nodes between dissimilar materials. For example, at node 1642, a selected shared node point between gold and gallium arsenide elements, the averaged principal stress was 8,540 lbs. per square inch (PSI) while the unaveraged principal stress was 12,035 PSI for the gallium arsenide element. This high stress result, incidentally, would indicate a 100 percent probability of failure in the chip since the material's yield point in tension is only 6,100 PSI. This model, however, had a very high arbitrary value of heat sink temperature specified at 100°C with a maximum temperature of 185.5°C in the chip (see Figure 3). Room temperature of 20°C was specified as the zero stress state. Lower heat sink temperatures will lower all material stresses. The key point,

however, is to always check the unaveraged element stresses for those elements that share nodes with elements of a different material. This data will be in the printed output results file and will not be in the contour plots that use averaged stresses.

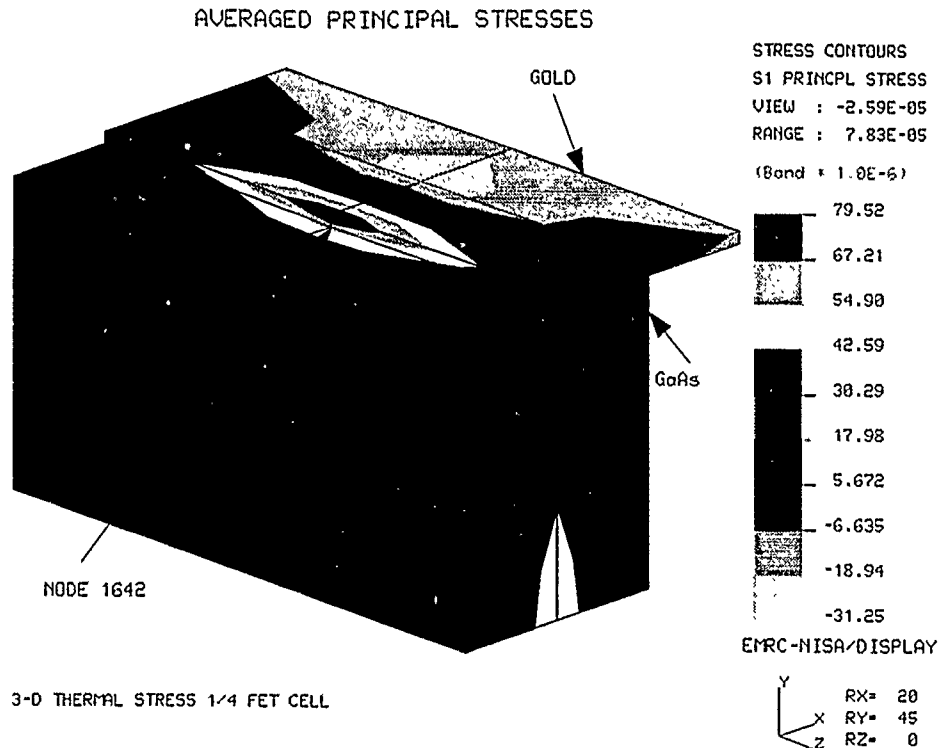


Figure 5

4.0 Conclusions

MMIC circuits have been under development for the past few years and are starting to find their way into microwave systems. However, significant work still needs to be accomplished before MMIC chips are placed into an operational military system. To date, the MMIC world has concerned itself primarily with the technical aspects of producing the chips; i.e., designing for microwave performance. However, two items that will determine the future of MMIC is total cost of a finished unit and the reliability of the unit. Total cost of a finished unit can be broken down into four major areas: 1) chip design, 2) fabrication, 3) assembly/packaging, and 4) testing in all phases of fabrication. At the present time, about two thirds of the total cost of a unit is due to assembly and testing. The above major cost drivers and the reliability aspect are being addressed with RADC leading the way in developing final acceptance testing techniques and reliability analysis techniques. RADC pioneered the development of large signal pulse measurement techniques and T/R module test station technology (1, 2) and now Hewlett Packard and Wiltron have introduced pulse network analyzers as products in the past year. RADC has also pioneered the development and application of finite element analysis techniques to MMIC circuit analysis so that now it is possible to determine temperature and stress levels within microscopic regions of a given device. The ability to assess the reliability of new designs using this analytical tool makes it possible to avoid time consuming and costly after-the-fact test and redesign of a given device/module.

It is apparent that MMIC technology will have a profound impact on radar systems in the near future. This impact will be from an economic point of view by making active phased arrays less costly and by increasing system performance and availability. In conclusion, it is obvious that MMICs are starting to become available for system use, but a lot of effort still needs to be accomplished before they are used in military systems, such as airborne radar systems.

References

1. E. J. Jones, "T/R Module Evaluation Test System", Automatic RF Techniques Group (IEEE) Fall 82 Conference, Boulder, Colorado, November, 1982, UNCLASSIFIED.
2. E. J. Jones, "The Requirements for a General Purpose Automatic Pulse Measuring System", Automatic RF Techniques Group (IEEE) Fall 83 Conference, Albuquerque, New Mexico, November, 1983, UNCLASSIFIED.
3. W. J. Bocchi, "Finite Element Modeling and Thermal Simulations of Transistor Integrated Circuits", RADC-TR-89-176, October, 1989, UNCLASSIFIED.

Discussion

Paper n° 15

Question : Mr. R.J.P. DOUVILLE (CRC, OTTAWA, OBSERVER)

- Are 1% failure in array modules totally random or did you consider "worst case" from point of view of specific failures ?
- See any need for self-check / diagnostics in modules ?

Answer : Mr JONES

- totally random for the data shown here
- yes, we are working on self-check techniques for both the module and the array

Question : JOHN P. HURREL (unregistered)

How is the finite element model applied to the interfacial region between different materials and what physical parameters are needed to specify the reliability of those interfacial regions ?

Answer : Mr BOCCHI

The analysis at the boundary is somewhat simplistic. It assumes a perfect bond and that the material properties for each material at the bond are the same as for the bulk material. This is probably not true. If we knew the true properties of the material at the bond, we could model the bond with a separate layer of elements. Physical testing might provide insight on the strength of the bond layer.

FIBRES OPTIQUES SPECIALES ET CAPTEURS POUR L'AERONAUTIQUE SPECIAL OPTICAL FIBRES AND SENSORS FOR AERONAUTICS

Jean-Pierre LE PESANT and Marc TURPIN

THOMSON-CSF Laboratoire Central de Recherches

Domaine de Corbeville 91404 ORSAY CEDEX FRANCE

RESUME

Les principales motivations pour l'utilisation des fibres optiques à bord des avions pour les communications, le contrôle de la navigation et celui des moteurs, sont l'immunité aux interférences électromagnétiques et à la foudre, le faible poids, le faible diamètre et le haut degré de flexibilité de mise en forme des données à transmettre. Après une courte présentation des technologies actuelles de fabrication des fibres optiques, nous discuterons quelques unes des applications maintenant accessibles aux fibres optiques pour les communications de bord, l'acquisition des paramètres physiques et des données de navigation et pour la transmission de puissance électrique vers des capteurs. Nous donnerons des valeurs typiques des caractéristiques rendues accessibles par l'évolution des technologies.

SUMMARY

The primary motivations for using fibre optics for onboard communications, flight and engine control in aircrafts, are immunity from electromagnetic interferences and lightnings, lighter weight, smaller size and a high degree of data formatting flexibility. After a short presentation of the present status of the optical fibres fabrication technologies, we shall discuss some of the applications currently accessible for optical fibres in terms of in-flight communications, navigation and physical data collection and optical power transmission. We shall give typical values of the characteristics made achievable by the evolution of the technologies.

I INTRODUCTION

Aboard modern aircrafts, flight information and data processing are becoming increasingly more complex. They involve large data rates, sophisticated and cumbersome communication networks and processing units, and will need a progressive trend toward sensor fusion for the sake of redundancy, required by security reasons. In the same time, new composite materials are used for the fabrication of the aircraft body, with lower metal proportions, and the disadvantage of lowering the galvanic protection of the data links. This has triggered an active research and development effort for the implementation of large-band-width, small size and small weight data links, characterized by a low sensitivity to electromagnetic interferences and counter-measures.

Single mode optical fibres are capable of bringing an answer to these requirements and some authors have introduced the "fly by light" concept for the new generations of aircrafts [1-3]. This paper will restrict itself to the case of

silica glass optical fibres, drawn from synthetic fused silica, which have a small diameter, high tensile strength, extremely high bandwidth, and provide light weight cables immune to inductive interferences and not subject to ground loop problems.

II OPTICAL FIBRE FABRICATION TECHNOLOGY

There are three basic types of optical fibres: multimode step-index, multimode graded-index, and single-mode step-index. The latter ones have a small core diameter (5 to 10 μm) which supports only one mode of light and leads to the ultimate in high bandwidth because there is no intermodal pulse broadening. Furthermore, in certain cases, the material dispersion and the waveguide dispersion can be made of opposite signs and of similar magnitude, thus canceling each other out, over a narrow wavelength region, and yielding a zero-dispersion waveguide.

Many types of fabrication technologies [4-5] have been investigated so far by various authors, and among them we may cite:

- the Double Crucible Method (Fig.1), in which the fibre is continuously drawn from the molten pure silica and doped silica;

- the Vapour Axial Deposition Method (Fig.2), in which the starting materials are first aggregated from a flame reaction, to form a composite rod, called "preform", to be subsequently drawn through an oven;

- the Modified Chemical Vapour Deposition (MCVD) Method (Fig.3), in which the preform is fabricated by deposition of layers of controlled composition inside a synthetic silica tube which is subsequently collapsed to form a solid rod. The preform is then drawn through an oven as above.

Across the section of the fibre, going inwards, one distinguishes the outside silica envelope, the optical cladding, and the optical core, in which most of the light travels. This structure is common to all optical fibres and is obtained with all the fabrication methods. The index profile obtained across the fibre is either of graded index or of step index.

The MCVD preform fabrication method has the advantage of allowing a very flexible and very precise control of the composition of the layers, the purity of which is very well defined, in a manner very similar to the one achieved in the microelectronics industry: the raw materials are high purity liquids which are vapourized before entering the reaction zone where the heat-activated chemical reaction and deposition take place in a closed envelope, the silica tube itself, which acts as an efficient protection against external contamination.

Typical drawing furnace temperatures are of the order of 2000 °C. A diameter reduction from a preform made by MCVD to the optical fibre is typically 100, so that one can draw 10 km of 0.125 mm diameter fibre from a 1 meter long, 12.5 mm diameter preform, and 40 km from a 25 mm diameter one !

TYPICAL CHARACTERISTICS OF OPTICAL FIBRES

As we said above, the optical fibres considered here are small diameter (0.1 to 0.3 mm) silica fibres, the cross section of which is homothetic of the initial preform rod (typical diameter 10 to 20 mm). Their light guiding properties arise from their built-in index of refraction profile. Typical characteristics of interest for the applications discussed here, for communication links and for sensors, are as follows:

Bandwidth : 1 to 20 GHz

Attenuation : 0.2 to 10 dB / km
Weight : 65 grams per kilometer (with coating)

Outside diameter : 0.125 mm (bare fibre)
0.250 mm (coated fibre)

Mechanical strength : 1 to 4 GPa

PROTECTION AGAINST ENVIRONMENT AND STATIC FATIGUE. (HERMETIC COATING)

Optical fibres have a very good intrinsic mechanical strength against traction, but are characterized by a brittle behaviour when they are bare. To account for that fact, they are usually jacketed with a polymer coating, in-line with the drawing process. Epoxy-acrylate is widely used for that purpose.

However, when the fibre is submitted to peculiar packaging conditions (e.g. small diameter spools) or adverse environmental conditions (e.g. moisture, aggressive chemicals), this jacket does not provide a sufficient enough protection. It is then necessary to apply a primary hermetic coating before the jacketing (Fig.4).

The purpose of that hermetic coating is to protect the fibre against two hazards of particular concern: hydrogen, which reduces the transmission capability of the glass fibre, and glass flaws, which may reduce the mechanical reliability of the fibre.

Sealing against hydrogen.

The diffusion of molecular hydrogen into a glass fibre may lead to a drastic increase of the signal loss and to a degradation of the performances of the communications system. This hydrogen can be generated naturally in the fibre environment as a result of corrosion of metals such as steel, which is used for cable sheathing. These losses are more pronounced at 1550 nm, which means that one has to be careful not to test the system only at a lower wavelength (e.g. 1310 nm) where it may be efficient, but also at the operational wavelength.

The best way to avoid this problem is to apply on the bare fibre, within the fabrication process, a hermetic coating to the fibre, which prevents molecular hydrogen from diffusing into the core of the fibre where the optical transmission takes place. This coating is a primary layer, subsequently followed in the same process by a secondary layer (e.g. epoxy acrylate for mild temperatures applications).

Stabilisation of glass flaws.

The processed silica glass obtained by drawing an optical fibre from fused silica has indeed a high mechanical strength: it is in fact

stronger than steel of an equivalent size. However, just like for any other processed material, flaws may degrade that strength. These glass flaws increase in size and depth under the aggression of moisture. Hence, the second function of the hermetic layer is to prevent any intrusion of water into the flaws, across the outer surface of the fibre. This prevents the flaws from growing, maintains the initial strength of the fibre and improves the life time of the system.

III FIBRE OPTIC COMMUNICATION LINKS FOR AIRCRAFTS

An increasing need for higher data rates is emerging in the aircraft communication networks, due to the large number of sensors and actuators and to the coming demand for high definition display interconnection. As an example, high definition display interconnections, required for a flexible enough presentation of the flight information on a few cockpit displays, will need at least 1.3 Gbits/s. This will necessitate the use of semiconductor lasers (to allow an amplitude modulation at suitable frequencies) and single mode fibres (to avoid the modal noise and its effect on speckles between connectors under vibration conditions).

To summarize the state of the art, one can say that the communication components do exist at an advanced stage: 10 Gbits/s data rates have been demonstrated at the laboratory stage and 16 Gbits/s seem feasible. However, the digital transmission of data is still awaiting further developments of appropriate electronic components for these very high rates.

At the practical application level, 20 Mbits/s links, comprising an LED (800 nm), a multimode 100/140 fibre, and a PIN photodiode detector, have been demonstrated in flight (e.g. AMD Rafale) for computer and flight control communications (except displays).

Future developments :

Optical links with a band width of 2 to 16 GHz will be of paramount importance for microwave signals coming from radar antennas and from other microwave sensors used for counter-measures. In March 1990, the CNET in France has reported [6] a fibre optic link in the bandwidth 3.7 - 4.2 GHz, 11 km long, between a reception antenna and an exploitation station, for satellite video communications. Better lasers are still to be fabricated, with less noise and an improved bandwidth linearity.

Wavelength multiplexing will bring the flexibility of multiplexing data of either an identical nature, or of a completely different

one (e.g. analogic and digital), and the direct optical demultiplexing techniques with passive components (gratings). Practical applications will involve the development of efficient multiple wavelength sources with well defined spectra (e.g. 16 wavelengths separated by 4 nm from each other).

Network standardization in terms of component and system compatibility will also bring significant progresses for performance and cost.

IV FIBRE OPTIC SENSORS

1) NAVIGATION SENSORS :

Gyroscopes

Fibre optic gyroscopes [7-9] are based on the Sagnac effect which can be observed by means of the propagation of light waves in two opposite directions in the same optical fibre coil (Fig.5). The effect produces a phase difference between the two light waves, which is a function of the variation of orientation of the rotation vector with respect to the normal to the coil. Typical sensitivities are in the range of 300 to 600 degrees per second and the typical drift does not exceed 1 to 2 degrees per hour. The detection has been demonstrated to be very insensitive to magnetic fields and external disturbances such like vibrations.

Current developments have been extensively described in the literature (see references given in [7-9]). Practical implementation use integrated optics for the Y coupler and the modulator and allow very compact and ruggedized designs.

Note: Laser gyroscopes have been investigated and implemented for roughly 10 years and are used for guidance systems for airplanes and rockets. The precision is currently 5/1000 degrees per hour. However, spurious effects arise from back-scattering on the cavity mirrors, causing interferences of the two cavity laser modes which lead to a "blind zone" centered on the zero reorientation values. This disables the detection by the gyroscope of small and medium values of rotation. This effect is usually counteracted by maintaining the cavity under continuous rotation by means of sophisticated and costly precision mechanisms which are not necessary in the case of fiber optic gyroscope.

Accelerometers

Present designs of accelerometers imply the use of transducers to transform the acceleration variable into a measurable parameter. Typical examples use the

compliance of deformable structures such like cylinders, tubes, or membranes, associated with a load, either to modify an optical path at the end of the fibre [10], or to stress the fibre itself. In this case a differential phase delay is induced and an interferometric device is required for readings. Other Sensors are based on the variation of the coupling efficiency between two optical fibres leading to an intensity measurement. One can note that no intrinsic types of optical fibre sensor for acceleration have been reported today. Current designs are mainly used for measuring vibrations (Fig.6).

Typical required values are respectively a range of 1 to 10g with an accuracy of 0.5g for acceleration, and 1 to 10g with an accuracy of 1 mg for vibrations.

2) DISPLACEMENT SENSORS :

Among the mesurands outlined by aircraft manufacturers, mechanical displacements receive a large attention in terms of optical fibre sensor studies, because of the complexity of classical systems when a large number of transducers is required (more than one hundred aboard an aircraft) for measurement of angular and linear displacements.

The main approach in this area is based on the classical Gray-code, adapted to optics in disc or linear elements. Following a predetermined binary function of transmittance (transparent=1, opaque=0) and a sufficient number of optical channels (number of bits), the position of the moving part is determined.

Several solutions concerning the optical channels have been proposed. The simplest one is the use of one optical fibre per bit, but this approach leads to a large number of fibres (keeping in mind the multiplexed sensor network aspect) (Fig.7). By using smarter techniques, the optical leads can be reduced to one or two optical fibres. For example, the channel multiplexing can be made in time domain (pulsed light source and differential time delays) or spectral domain (continuous broadband light source and dispersive device)[15].

3) AIRCRAFT MONITORING

Pressure sensors

Fibre optic pressure sensors described in the literature currently implement single mode optical fibres, jacketed with a specific pressure sensitive coating which serves as a transducer for stressing the fibre. The pressure effect induces a phase shift of the light travelling in the fibre. The most classical means to measure

such a phase shift with a high accuracy are the interferometric arrangements (for example, all fibre Mach-Zehnder interferometer), for which one fibre acts as the sensor and a second fibre is used as a reference. Another approach consists of using birefringent fibres, and measuring a differential phase shift. This last method is of great practical interest, because the problem of stabilization of reference fibre (reference arm of the interferometer) is canceled.

Conversely, the intrinsic pressure sensitivity of a single mode optical fibres can be obtained by a specific design of the internal structure of that fibre. As an example, let us consider the case of side hole fibres. In this case, after fabrication of the preform, part of the outside silica material is removed mechanically to form large grooves, the preform is then sealed inside a silica tube and put on the drawing tower. Under appropriate conditions of drawing process, the fibre exhibits large holes (Fig.8) across its section and all along its length. These holes not only stress the fibre to make it birefringent, but also transform an outside isotropic pressure into an anisotropic stress on the optical core. This stress is a function of the pressure and can be calibrated so as to allow its measurement.

Thomson-CSF has developed and patented a polarimetric pressure sensor which utilises a birefringent polarisation preserving pressure sensitive fibre which takes advantage of such a side hole fibre (Fig.9). The detection scheme uses the pressure sensitive phase difference between two orthogonal light waves travelling in the fibre, which are brought to interfere at the processing unit, far from the detection area if necessary. Typical sensitivities are presently of the order of two fringes (12 radians) per 10^5 Pa, per meter of fibre, and are being improved.

Temperature sensors

All optical fibres are sensitive to temperature and this is often considered as a draw back for many applications, although it can be compensated for, if necessary, in some cases (e.g. for pressure measurements). However, when the temperature itself is the parameter of interest, the fibre can be engineered to have an enhanced sensitivity to temperature. As an example, let us consider the case where part of the outside silica material of the preform has been mechanically removed (Fig.10) and replaced by another silica material of a different thermal coefficient of expansion. After being drawn, the fibre will exhibit internal stresses which induce in it a

birefringence with a temperature behaviour. Here again, a phase difference arises between two orthogonal light waves travelling in the fibre, yielding the way to optical detection of the temperature variation. At Thomson-CSF, we have demonstrated, using a polarimetric method [11] that several temperature intrinsic sensors can be hooked together along the same optical path lead with the same light source but operated as independent sensors, and read in a multiplex scheme.

Typical sensitivities are of the order of 1 fringe (6 radians) per degree Celsius and per meter of fibre.

Polarimetric schemes

The polarimetric concept is based on the birefringence properties of specific fibres. High birefringence fibres can be used in two different ways which can be implemented in polarimetric sensor networks.

Starting from a broadband polarized light source, insensitive optical fibre leads are obtained by launching light in one of the eigen modes of the fibre. The high birefringence allows to conserve the input linear state of polarization over a long length of fibre (typically several hundred meters). The polarimeter, which is the sensing part of the network, is obtained with the same fibre when both eigen modes are excited. As a consequence of the birefringence, a differential propagation of both eigen modes is appearing, yielding a phase delay which can be measured. The transfer of light from one axis to the other is obtained by a controlled local relative rotation of the eigen axes of the fibre (i.e. splice, twist, stress...), and the amount of coupled light is related to the relative axes rotation. The end of the sensor network, is defined (still on the same fibre) by a 45° coupling point, which allows to use the remaining long length section of fibre as an output insensitive lead. This arrangement provides a well defined remote sensing element localised on an optical fibre. By using specific fibres, intrinsic sensors are defined for remote measurement of pressure, temperature or other parameters of interest like deformations and stresses.

As shown on figure 9, a sensor serial network can be realised by making several coupling points on the same fibre. Each length of fibre separated by such coupling points is one sensor. In order to separate the sensors in terms of cross-talk, the distance between two coupling points (sensor length) has to be longer than the coherence length of the light travelling in the fibre. By this way, each wave train emitted by the light source is divided into decorrelated wave trains at the network output. The multiplex scheme is obtained by a

coherence effect. An interferometric device is used to compensate the corresponding optical path differences (phase delays), providing mesurand informations from the different sensors.

Liquid-level and flow sensors

Liquid-level sensors are required for the control and the monitoring of fuel distribution into tanks. A large number of sensors is based on the optics refraction laws. Light from an LED emitter is launched into an input optical fibre and is totally reflected inside an internal reflection prism device, before returning to the detector through the output fibre. According to the refraction laws, light is totally reflected only when the prism is in the air. If a liquid is present, the refractive index is modified and light refracts into the fluid (Fig.10). This type of sensor works as a simple optical switch. By using the more sophisticated Optical Time Domain Reflectometry (OTDR), a serial network of such sensors can be implemented, giving an attractive solution for the oil-leak detection which is strongly required with a large number of sensors and a high spatial resolution for a precise location of leaks. Flow sensors generally use microbend loss sensors. The flow velocity information is given by output intensity modulation coming from an optical fibre attached to a vibrating piece placed in a calibrated turbulent zone [12].

Engine monitoring.

The engine environment has very adverse operating conditions in terms of measurement, mainly due to very large ranges of temperature, pressure and vibrations. As a typical example, depending on the location, temperature varies from -40 to 1900°C, pressure from 3 to 5000 kPa, and vibration from 1 to 10 kHz! Because of an obvious need for corrosion-resistant materials, small size solid-state probes distributed in a large number of sensors are required. Optical fibre sensors appear to be one of the best solutions.

V COMPOSITE STRUCTURE SENSORS

The increasing use of light-weight, low radar signature carbon-fibre reinforced composites is urging the need for continuous, long term monitoring of the structures for the detection of in-use behaviour and material fatigue. We give here several examples of applications of optical fibres inserted in composite materials, but it must be kept in mind that the diameters of the carbon fibres

and of the optical fibres themselves are rather different (respectively 10 μm and 100 μm) and that the inclusion and implementation of the latter ones in composites is not straightforward, and at least induces some mechanical disturbance, although the chemical compatibility is judged rather good.

Stress and strain sensors

The composite materials described above are very attractive because of their ease of molding into complex shapes, and their strength-to-weight ratio which can be significantly higher than that obtainable from any metals, although they have an inherent anisotropy and compressibilities which are very much dependent on orientation. These materials are usually very flexible and can sustain dynamic strain levels of 1% without noticeable deterioration, which is not the case of most mechanical strain-measuring devices. Silica glass optical fibres have mechanical characteristics very comparable to the ones of carbon fibres and can withstand the same large dynamic strains in a reversible manner.

Furthermore, the fabrication of these molded airframe structures involves pressing them together and curing the bonding agent of the fibres at temperatures ranging from 150 to 400 °C. For sections which are thicker than others, it is crucial to ensure that the thermal treatment has been completed throughout the bulk of the structure. For that purpose, the use of optical fibres is envisaged for the monitoring of in-process temperature and strain profiles.

Delamination sensors

During their life time, the composite structures may be subject to fatigue or accidents that are caused either by ageing or by impact damages (e.g. tools dropped during ground maintenance, or in-flight collisions with birds etc...). These may cause delaminations that are usually only visible underneath the point of impact, on areas which are in most instances enclosed within the airframe structure. The presence of optical fibres in the composite may allow the detection of such hidden delamination areas and help preventing subsequent failure of the airframe.

Smart structures

In the concept of "smart structure" configurations, the sensors play an active role to monitor stress loads and damages that occur in that structure, due for example to ice loading of the wings or hostile weaponry. Then, the sensor data collection and analysis must be organized to report to the flight control computer, in real time, how close to 100% mission capability the aircraft is actually

performing, and consequently warn the pilot against modified limiting values (e.g. lower maximum value of the acceptable acceleration limit).

At least two lightwave sensing principles can be envisaged: microbending detection and phase difference sensing.

In the first case, one measures the intensity attenuation due to the bending caused in a multimode fibre by the strain; in the second case, it is the phase difference variation, between two orthogonal wave polarizations that is measured, and it requires the use of a single mode, polarization maintaining fibre.

McDonnell-Douglas Corp. plans flight testing on an F-15 Eagle fighter aircraft in 1991 to monitor the composite-made leading edge of the plane's outer wing. According to Herbert Smith [13], among the multimode fibres evaluated for microbending sensing, a special type produced by Corning Glass Works seems to be appropriate. The fibre optic strain sensor system would replace the conventional strain gauges and accelerometer units that are presently used to monitor the aerodynamic loads. If proven successful, the new system would have the advantage of providing real time data availability and processing, instead of after-the-mission results of the traditional units.

Smart skins

The "smart skin" concept concerns the outer surface of the aircraft, or "skin", that contains embedded electronic warfare devices, such as radars and antennas, as well as navigational devices such as position sensors.

When the smart skin is made of polymer composites, the inclusion of optical fibres into it can also serve the purpose of detection of the environmental conditions, such like temperature or pressure, and of localization of the occurrence of hazards such like ice loading or laser beam impacts. The sensor network of the smart skin can measure the variations of the vibration frequencies of the airframe due to ice-loading or to the loosening of the struts. Preliminary investigations on a model airplane have been conducted in the laboratory and in flight [13] at the Virginia Polytechnic Institute (USA).

For the case of laser beam impact, preliminary investigations, using single mode fibres, have been conducted in the gigahertz bandwidth, for the detection and separation of the compressional wave (total phase) due to the formation of a plasma near the specimen surface, and the shear pulse (differential phase) caused by the impact of the laser pulse on that surface.

VI POWER-BY-LIGHT

Optical fibres offer also the additional advantage of allowing the transportation of energy in the form of optical power, without external interferences or counter-measures, from an optical power source to a classical or semi-classical sensor or actuator where that power is transformed into electrical power by a photovoltaic cell. The signal obtained from the detector can then be converted back into an optical signal which is carried back to the central processing unit via an optical link which is also interference-immune (Fig.11).

At OFC'90 [14] a novel high efficiency AlGaAs/GaAs photovoltaic cell has been reported, which was associated to fibre optic couplers and combined with high power, matched wavelength (814 nm), semiconductor lasers and low loss optical fibre cables. The generated electrical power (4 V, 0.25 A) represents a significant advance in power-by-light applications. A uniform illumination of 7.15 W/cm² yields power conversion efficiencies in the 54-59% range.

VII CONCLUSION

The fabrication and implementation of high quality and high reliability single mode fibres is opening the way to an increasing variety of applications for aircrafts, ranging from large bandwidth, high data rates, communications, to sensor networks for flight control and monitoring.

For communications, optical fibres allow 1 to 10 Gbits/s for flight information exchange and high definition cockpit displays. This may go up to 15 gbits/s in the future.

In the field of navigation sensors, fibre optic gyroscopes have been extensively studied and their specific advantages are now being assessed in flight. Accelerometers are now drawing attention for the ranges 1 to 10 g for accelerations and vibrations.

Other fibre optic sensors are studied for aircraft monitoring, to measure temperature, pressure, liquid levels and flows. They have the specific advantages of allowing interference-free remote sensing with light-weight sensor networks compatible with adverse environments such as aggressive chemicals and medium-high temperatures.

The new light-weight carbon-fibre reinforced composites do also bring specific opportunities to use the optical fibres for structure monitoring ("smart structures") during and after their fabrication process, and for detection on the outer surface of the aircraft ("smart skin").

We think that these promising applications

are a strong motivation for active research in the field of special optical fibres and sensors for aeronautics, with the strong support of the existing fibre optic technological back-ground.

VII REFERENCES

- [1] J.R.TODD, "Toward Fly-by-Light Aircraft", Proc. Soc. Photo-Opt. Instrum. Eng.989, 38 (1988).
- [2] W.L.GLOMB,Jr., "Fiber Optic Circuits for Aircraft Engine Controls", Proc. Soc. Photo-Opt. Instrum. Eng. 840,122 (1987).
- [3] F.J.LEONBERGER, W.L.GLOMB,Jr., and J.R.DUNPHY, "Fly by light: fiber optics for aircraft communication, control and sensing", Tech.Dig.Opt.Fib.Comm.Conf.OFC'90, WA4, p.48, San Francisco, USA (1990).
- [4] J.C.DALY "Fiber Optics", CRC Press,Inc. Boca Raton,Florida,USA
- [5] J.E.MIDWINTER "Optical Fibers for Transmission", John Wiley & Sons Edit. (1979).
- [6] Electronique Actualités 23 March 1990 p.16 (1990)
- [7] H.C.LEFEVRE "Fiber Optic Gyroscopes", in "Optical Fiber Sensors", Vol.2, p.381, Artech House Inc.(1989).
- [8] H.C.LEFEVRE,S.VATOUX,M.PAPUCHON and C.PUECH, "Integrated optics:a practical solution for the fiber-optic gyroscope", SPIE proceedings Vol.719 (1986)
- [9] H.C.LEFEVRE, "Evolution of the fiber optic gyroscope", OFS'90, p124, Springer proc.24, edit H.J.ARDITTY and all.
- [10] A.S.GERGES, T.P.NEWSON and D.A.JACKSON, Optics Lett.14 N°20 (1989)
- [11]M.TURPIN,D.ROJAS,C.PUECH,"Nouveaux concepts de capteurs repartis "tout fibre", congrès mesucora, Paris,1988
- [12] K.KYUMA "Physical and Chemical Sensors for Process Control",in "Optical Fiber Sensors" Vol.2, p.653, Artech House Inc.(1989).
- [13] J.KREIDL, Lightwave July 1989
- [14]J.M.BERAK,W.L.GLOMB,Jr.,A.J.SHUSK US Tech. Dig. Opt. Fib.Comm. Conf. OFC'90 WM34, San Francisco, USA (1990)
- [15] B.CULSHAW, "Applications of fiber optic sensors in the aerospace and marine industries", in "optical fiber sensors", Vol.2, p.701, Artech House Inc.(1989).

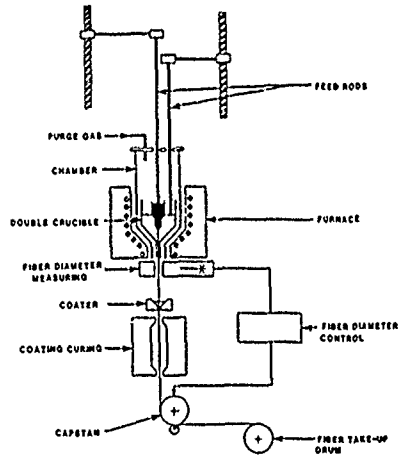


Fig.1 Double Crucible Fabrication Method (from ref.4)

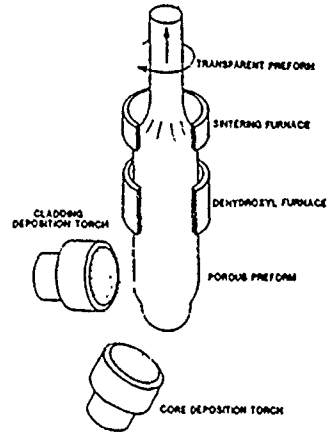


Fig.2 Outside Vapour Deposition Method (from ref.4)

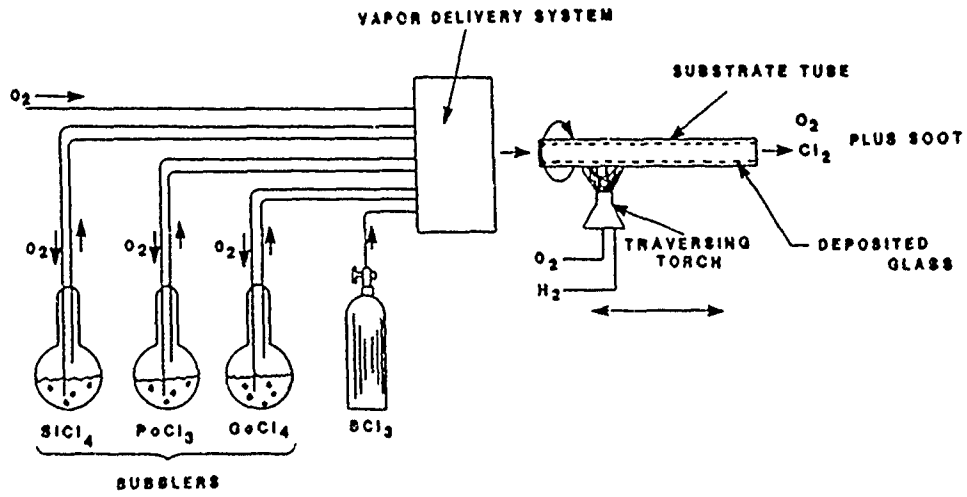


Fig.3 Modified Chemical Vapor Deposition Method (from ref.4)

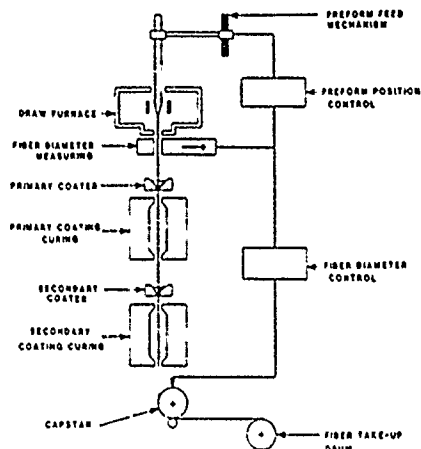


Fig.4 Fibre Drawing Apparatus (from ref.3)

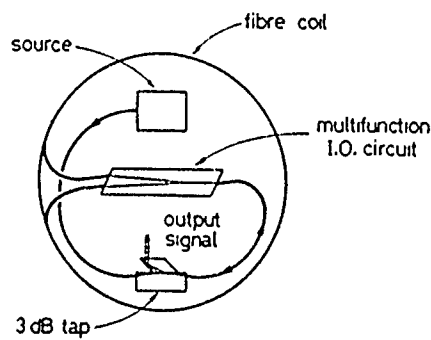


Fig.5 Fibre Optic Gyroscope (Thomson-CSF design)

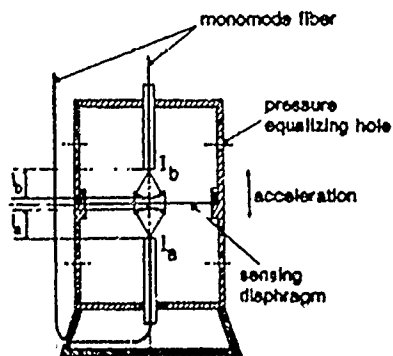


Fig.6 Fibre Optic Accelerometer (from ref.10)

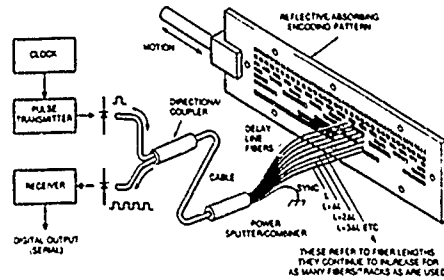


Fig.7 Linear Displacement Sensor (from ref.3)

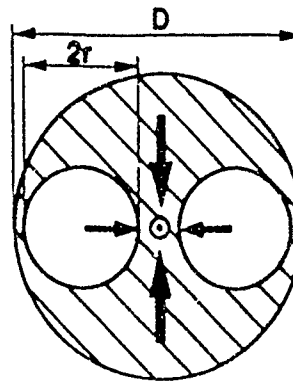


Fig.8 Side Hole Fibre for Pressure Measurements

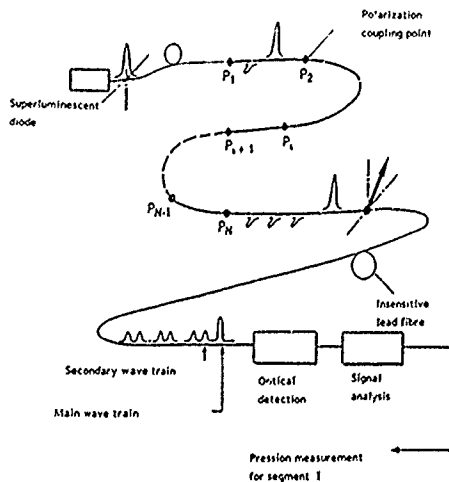


Fig.9 Polarimetric Pressure Sensor System (Thomson-CSF design)

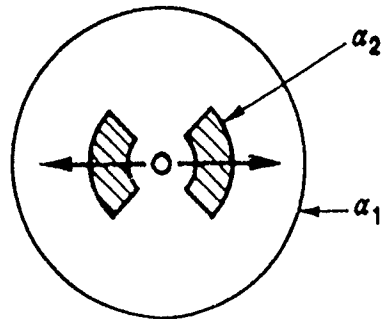


Fig.10 Temperature Sensitive Optical Fibre

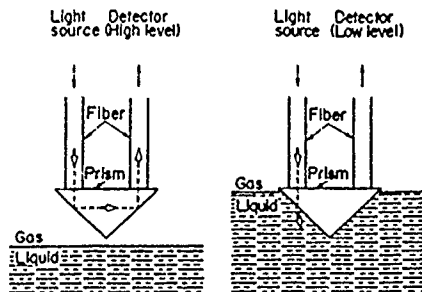


Fig.11 Liquid Level Sensor (from ref.12)

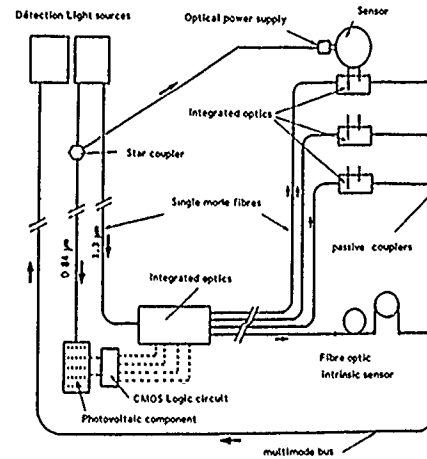


Fig.12 Power by Light System (Thomson-CSF design)

Discussion

Paper n° 16

Question : M. JACKSON (THORN EMI - UK - Observer)

- As several of the sensors described utilise the polarization purity of orthogonal modes in the fibre, are special precautions needed to maintain the purity when the fibre is coiled around a former to form a gyroscope, for example ?
- What is the sensitivity of the laser gyroscope and the drift rate ? Could it be used to measure rates of a few degrees per second ?

Answer : Dr. LE PESANT

- Yes, special precautions have to be used to maintain the quality of the polarization preserving fiber and it is an important characteristics of the process. Polarization separation can be of the order of 30 dB and special winding conditions are applied.

- Present sensitivities range from 200 to 500 degrees/hour and are going up toward 1000 degrees/hour. Yes, a few degrees per second are possible. The maximal drift is about 0.1 degree/hour.

Question : Dr. T. WEIL (Thomson Technologies Conseils, Technical Evaluator)

- Concerning the multiplexed temperature sensor, do you need to use the same fibre all the way long for all the sensors or are there ways to couple birefringent fibre while avoiding to mix the polarizations?

Answer : Dr. LE PESANT

- The temperature sensors can be on the same fiber. The number of them depends on the desired signal to noise ratio and signal processing precision. Up to 50 sensors can be envisaged. For more sensors, one can use additional linear networks.

THE USE OF OPTICAL METHODS
FOR MICROWAVE SIGNAL DISTRIBUTION
AND CONTROL

Ian McMillan
Marconi Space Systems Ltd
Anchorage Road,
Portsmouth,
United Kingdom.

ABSTRACT

It has now become practical to distribute radio frequency signals with GHz frequencies along optical fibres and to use optical power splitters and filters as one might use their microwave equivalents.

Lower mass designs are therefore possible and the low transmission loss of optical fibre means that loss due to distances of up to fifty metres, as might be encountered in an aircraft or spacecraft, may be ignored.

The inherent wide bandwidth and stable phase characteristics of optical components as well as their possible parallel channel capability can also be readily exploited.

As an example of the use of such techniques a signal distribution system has been designed which when coupled with a novel very high speed data transmission method has been used to control a ground demonstrator of a spaceborne phased array synthetic aperture radar.

Such a radar requires the low mass and high quality distribution of 5GHz signal to around 500 individual transmit-receive modules as well as the collection and summation of the dual polarisation receive signals and the high speed control of the array.

Since spacecraft antenna of this size, 20 metres by 2 metres, have to be folded for satellite launch additional constraints exist from those common on ground radars.

The design choices available for such a requirement are discussed and the practical realisation of such an all optical distribution system is presented together with the resultant measured performance.

With power, mass and cost at a premium in most future designs such methods have to be considered in the concept stages of new systems.

Introduction.

Spaceborne radars of either the real or the synthetic aperture (SAR) type require significant aperture dimensions, currently in the 10 metre size and in the near future up to 20 metres[1]. Such structures require to be folded so that they may be efficiently transported to their final position by the launch vehicle. The use of distributed transmitters and receivers (TR) in such radars, mounted closely behind the relevant radiators, requires the distribution

of microwave radio frequency and control signals and the collection and summation of multiple received channels (In the case where reception is in two polarisations) and diagnostic telemetry. The number of TR modules will be large from 300 to 2000 units.

The use of coaxial distribution suffers from the disadvantages of high mass and limited flexibility across bending joints and alternative use of direct radiation methods is complex for two way communication. The advent of the ability to generate and receive high radio frequency signals of 0.1 to 10 GHz and simply pass them by optical fibre, optical splitter and optical wavelength multiplexer of low mass has provided a new solution to the distribution problem in such spaceborne radars.

The need for Europe to provide a higher performing and more cost effective successor to its current Remote Sensing spaceborne radar, the Active Microwave Instrument of ERS-1, has led to design work into an advanced successor and a ground based demonstrator of the necessary techniques and system concepts. This demonstrator consists of a subset of a full 20 by 2 metre phased array transmitting at 5.3 GHz with distributed TR modules driven by a multi-mode synthetic aperture control system. The distribution system between the central part and the array modules is wholly by optical fibre methods at 5 GHz for transmission and 300 MHz for the dual polarisation receive signals.

Distribution System Requirements.

Such a distribution system requires to be able to control reliably 512 TR modules such that the failure of one module or its distribution link does not affect the others. The distribution is therefore by a star method and is arranged in a random manner so that even mechanical fibre failures do not produce failures in adjacent area of the radiating array.

Forward path requirements.

The forward path of such a system is required to pass three types of signal, which can be time multiplexed. During transmission a linear frequency modulated (lfm) 5.3 GHz pulse with a bandwidth of up to 40 MHz must be distributed. During the reception period a 5.0 GHz local oscillator signal must be passed.

For control, in the interpulse period, a 10 microsecond long 10 MBaud digital signal is amplitude modulated on to a 5.0 GHz carrier and distributed. The control signal synchronises a local TR module control which among other tasks controls the scan-while-receive antenna beam phasing.

Possible methods for forward path.

A single channel with a bandwidth of 400MHz centred

transmission taking place at a different frequency with frequency conversion within the module. Such a system would have other advantages since any displacement of the TR module orthogonal to the array surface is compensated since the total space path length before the TR module and after it is constant. This system has been described by Shaw and Dybdal [2]

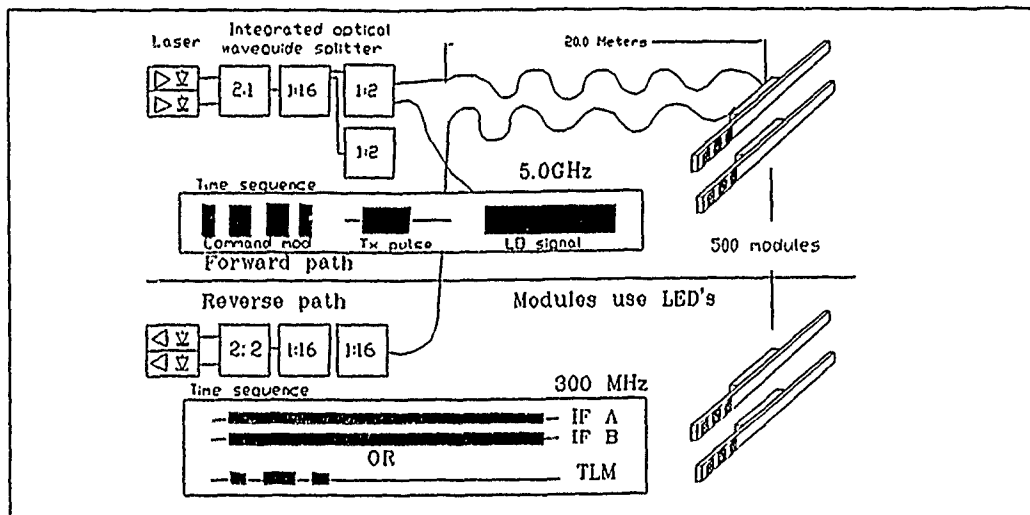


Figure 1 System Arrangement

on 5.125GHz would be adequate due to the time multiplexed method of transmission.

Simple Coaxial.

Naturally one would think of a flexible coaxial cable system for this purpose since a waveguide system would be likely to be heavier and certainly inflexible. Probably to make the system secure against failure the system would require multiple cables driven by a power splitter. Power splitting 500 ways and phase stable distribution by flexible coaxial cable to individual TR modules will readily provide a significant mass problem. The torque required to fold antenna segments in a spaceborne array must be held to the minimum since the damping characteristics of the mechanical hinge system must work under very difficult thermal conditions which are difficult to accurately predict. Too fast an action produced a significant mechanical impulse when the deployment stops with severe effects to the strength requirements and the spacecraft dynamics and too weak a force can prevent deployment and complete mission failure.

Free Space Distribution.

An alternative method would be to transmit directly by free space from a position behind the array to individual antenna on each TR module. The

Optical Space Distribution.

An optical carrier may be used to carry the 5GHz signal as an amplitude modulation. This may then be collected and photodetected to give a 5GHz signal for each TR module in a similar way to the rf space fed method. It has the advantage of non-interference with the final transmission from the front of the array but has significant disadvantages in the power of the optical source required to illuminate the rear of the array.

Guided Optical Distribution.

By using a semiconductor laser and amplitude modulating its output which is subsequently power split with an optical splitter a set of parallel fibre optic cables may be used to guide the signal to each TR module where it may be photodetected and returned to an rf signal at 5GHz.

Selected method.

Forward path realisation.

In the current demonstrator a directly modulated semiconductor laser at 1300nm is employed to provide the source which is then split successively by a 2 and then a 16 way optical splitter to give 32 channels of output. The initial split by two hybrid allows a flight system to have a cold redundant laser in the unused

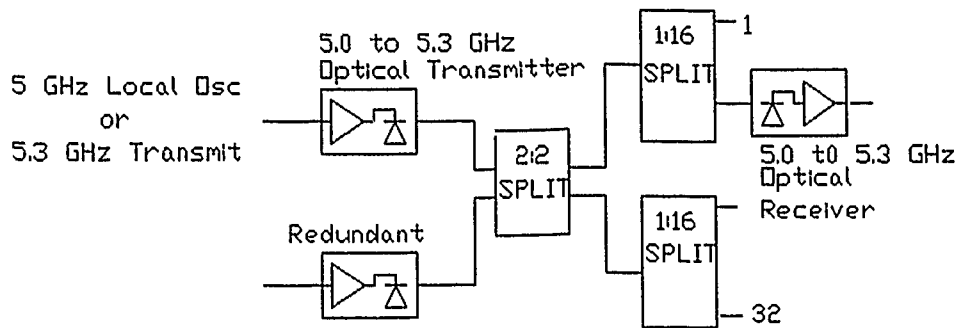


Figure 2 Forward Path System

port. A fibre which may be up to 30 metres long, passes the channel to the remote TR module where it is detected by a pin diode photodetector, amplified and passed to the rest of the module. The transmission fibre, with mechanical protection, is 0.8 grams per metre and may be readily attached to the structure. The link margins of such a system allows one laser diode to drive 32 channels with sufficient margin to allow for space radiation damage and gain changes in the components. The phase stability (which is of considerable importance in SAR systems) of fibre components is superior to comparable coaxial systems and joining of fibres in a flight system would be by fusion joints. It should be noted that a comparable coaxial system would have a rf loss of around 14 dB whilst the optical transmission loss is negligible. The optical system has however a significant loss in the conversion of electrical to optical power. In a system of many TR modules the important component for energy is the TR module photodetector and amplifier. Currently the energy required for the amplifier is around 200mW per tr. The Forward Path arrangement is shown in figure 2.

The performance measurement on the forward channel show the following performance:

Forward Link Performance.	
For a subsystem driving 32 TR modules at a separation of 20 metres.	
4.98 to 5.33 GHz Channel	
Input power	0dBm
Output Power	0dbm in each of 32 channels
Signal to noise ratio	-115.5 dBHz ⁻¹
Terminal return loss	21dB.

Return path requirements.

The return path has two requirements which are non-simultaneous. The first requirement is to pass two channels each of which have a bandwidth of 50 MHz centred on 300 MHz, these are the intermediate frequency (if) returns of the dual polarisation receiver.

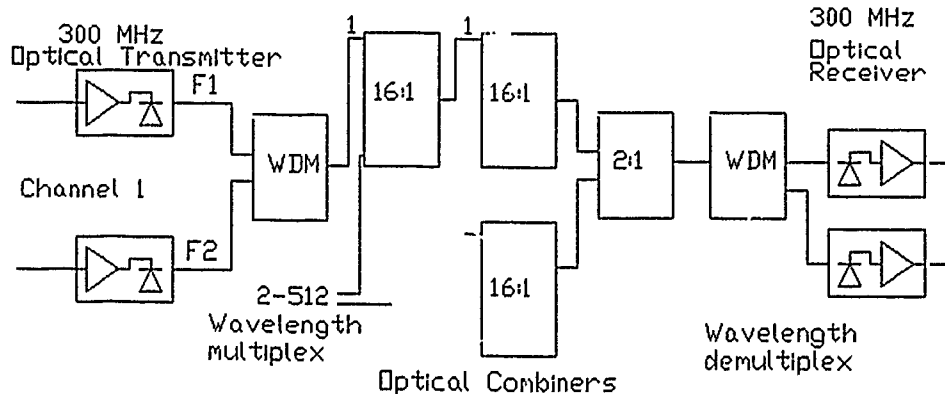


Figure 3 Return Path System

For each of these polarisation signals it is necessary to sum all the 512 return signals. The second requirement is to provide an output from one TR module telemetry signal which is a baseband signal of 20 Kbaud. The data rate has been chosen to compensate for the lower total energy to keep the link design simple.

Possible methods for return path.

Simple coaxial.

Since two simultaneous channels are required a simple coaxial system is not adequate. The if signals are both centred at 300 MHz so a upconversion on one channel and a set of filters to separate the channels is required in each TR module. Combination

Selected method.

Return path realisation.

The return path generator within the tr module consists of two similar sources directly modulated by either a 300 MHz if signal or a baseband ifm signal. The sources for the two polarisations have different optical wavelengths one being at 800nm and the other at 1300nm. The source power required is low so a light emitting diode is used. In the future semiconductor led's of the MESA surface emitting type which have a much lower current and increased modulation efficiency will be used. The two light signals are combined within the TR module by a optical

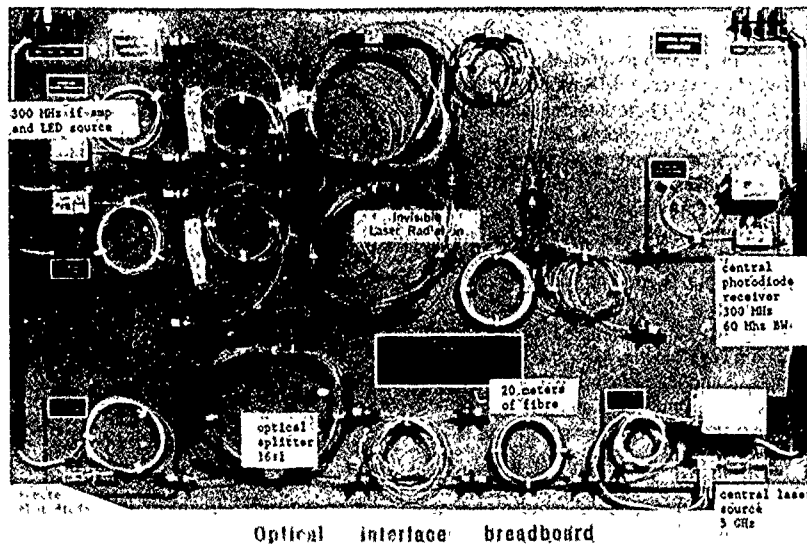


Figure 4 Photograph of demonstrator

of the signals requires a complex intermediate frequency combiner of the 500 TR module outputs and then frequency separation and downconversion. Clearly this is complex and suffers from more mass penalties than the corresponding forward path method.

Free Space path method.

For both rf and optical methods the generation of the separate carriers and the transmission method introduces many complexities so this method is discarded.

Guided Optical path method.

A guide optical path method allows two optical carriers with octave wavelength separation to be passed down the same simple fibre. The source may be a light emitting diode with low power which is amplitude modulated. Many hundreds of fibres may be readily combined in an optical method and the resultant non-coherent illumination hereby summed. Photodetection at a central source then provides the resultant if channel.

wavelength division multiplexer and the resultant signal passed by a 20 meter fibre to an initial 16:1 integrate optical combiner. Its output passes to a further 16:1 combiner which drives a 2:2 combiner. The outputs of the combiner drive dual redundant wavelength division multiplexors and avalanche pin diode photodetectors and amplifiers.

The requirement for a higher bias voltage for an avalanche diode is not so much of an embarrassment

Return Link Performance.

270 to 330 MHz Channel
Input Power -20dBm.
Output Power -36dBm.
combining circuit of 512 to 1
Output noise -150 dBHz⁻¹

Digital PRBS Encoded telemetry channel
at 20KbitSec⁻¹
Bit error rate 1 times 10⁻⁷

in the central control module as they would be in a TR module.
The Return path arrangement is shown in figure 3.

Hardware realisation.

A demonstrator system has been built and tested which has allowed all the link budgets of the forward and return path system to be measured under realistic conditions. The planar layout of this equipment is shown in figure 4.

Conclusion.

This optical distribution system which has been designed and built as part of a larger Advanced Sar demonstrator program for the European Space Agency has demonstrated the considerable advantages of an optical solution for distribution and summation of dual polarisation high stability microwave signals from many

hundreds of TR modules distributed across a folding structure in a low mass environment.

References.

- [1] I. McMillan, "Trade-offs in a Space Based Surveillance Radar", AGARD Symp. High Resolution Air and Spaceborne Radar, The Hague, May 1989.
- [2] Shaw and Dybal, "A Space-fed Local Oscillator for Spaceborne Phased Arrays", IEEE MTT-S Digest 1988.

Acknowledgements.

The author wishes to acknowledge the valiant work of C.R. Pescod and his colleagues at Marconi Research Centre who built the demonstrator and for our colleagues at the European Space Agency who have encouraged the work.

Discussion

Paper n° 17

Question : M. JACKSON (THORN EMI - UK - Observer)

What is the dynamic range of the optical system in the TR modular array receiving path ?

Answer : Mr. Mc MILLAN

The total dynamic range of the return path in the described configuration has been established as 39 dB compared with the instantaneous dynamic range requirement of 30 dB.

It would be possible to increase this further but extension to, say, 60 dB would require other modulation techniques.

Question : Mr. AL JELALIAN (Raytheon, Author)

Can laser diode power to the antenna be increased by array diode concerts ?

Answer : Mr. Mc MILLAN

Yes, we currently use single diodes of 1 mW power to ensure long life and high reliability. Single diodes up to 8 mW can also be used and adjacent arrays of diodes can be used for higher power.

LASER OBSTACLE AND CABLE UPDATE SENSOR

1 May 1990

C.K. Bullock, R.T. Hintz, and W. Tanaka
Targeting and Fire Control Division
Naval Weapons Center
China Lake, California 93555-6001

SUMMARY

The "REAL NIGHT" foreign weapon evaluation (FWE) program was evaluating an integrated night attack avionics suite for an A-6E aircraft. The most recent addition to this avionics suite is a CO₂ laser terrain following/obstacle avoidance (TF/OA) sensor. This paper describes the requirement for this type of sensor, the characteristics of the system, and some preliminary test results gathered during A-6 flights at the Naval Air Test Center (NATC) at Patuxent River, Maryland.

1.0 INTRODUCTION

Future air-to-ground attack missions face an ever increasing arsenal of ground-to-air weapons. If piloted attack is to remain an option, it must counter this defense system by staying outside of its lethal envelope. This requires expensive (but not as costly as aircraft) stand-off weapons that are hard to target, or it requires dropping weapons from extremely high altitudes resulting in greatly reduced accuracy. A most promising tactic is to fly fast and low. This can be accomplished during daylight hours, but systems must be developed to allow this at night and under poor visibility conditions. Night navigation at low altitudes has been addressed in a series of United Kingdom (U.K.) and United States (U.S.) programs. Head-up displays (HUD), forward-looking infrared (FLIR) sensors, and night vision goggles (NVG) have been integrated into capable night navigation systems. Such a system was tested in fiscal year (FY) 1987 on the REAL NIGHT platform at NATC, Patuxent River, Maryland and other U.S. locations. However, one problem with these night navigation systems is the lack of depth perception when using a FLIR. The addition of a covert terrain-following (TF), obstacle avoidance (OA) laser radar is required to address this deficiency. Current microwave radars will not provide the covertness required, and cannot detect small obstacles and cables.

The Royal Aerospace Establishment (RAE), Bedford, U.K., has developed a carbon dioxide CO₂ laser radar for terrain avoidance (TA) and is currently collecting data with this system. As a parallel effort the RAE, Farnborough, U.K., put together an air-to-ground simulator capability to determine acceptable rangefinder ranges, HUD symbology, and assess the benefits of a laser radar under poor visibility. The data from these efforts was shared with U.S. representatives and has led to a pair of FWE programs. Under an FWE program starting in FY 1986, the RAE simulator has been restored and upgraded for the Navy Terrain Avoidance by Laser (NATAL) trials. In the second FWE program, the U.S. Navy is evaluating a Laser Obstacle and Cable Update System (LOCUS) from the General Electric Company (GEC) Avionics. The sensor hardware was developed at the GEC Avionics, Borehamwood, U.K. facility, and the processor and software were developed and assembled at Rochester, U.K.

2.0 NATAL

The NATAL trials had two purposes. First, the Naval Air Systems Command (NAVAIR), Washington, D.C., wanted to familiarize a cross-section of U.S. pilots with the problems of flying at low altitudes at night and introduce them to some of the technology available to permit operation in this regime. The second purpose was to evaluate the usefulness of a TA laser radar. The Naval Weapons Center (NAVWPNCEN) was given the responsibility of supporting RAE, Farnborough, in developing the format for the NATAL trials and then wrote the final report (see reference 1). RAE put together the simulator, picked the flight routes, and conducted the tests. NAVWPNCEN performed the final analysis of the data and wrote the final report.

In the following sections the NATAL simulator facility and the NATAL trials are described. Pilots' evaluations and analyses of the data from the test trials are presented. Suggestions are made for improvements on the simulator and the conduct of any future trials.

2.1 NATAL SIMULATOR

The simulator is a research facility which RAE, Flight Systems Division, Farnborough, has put together for studying the operation of cockpit mission systems by the pilot of a fixed-wing, single-seat military aircraft during the crucial phases of ground attack missions. Figure 1 shows the facility layout. It consists of a simulated cockpit, a control room, a number of special computers, a terrain board, and a camera carriage. The portion of this facility that has been funded by the U.S. Navy is the Beta computer and software used to model CO₂ laser TA systems.

The pilot is provided with the essential visual conditions encountered when flying at low level and high speed, and is expected to fly over hilly terrain that contains vertical obstacles. The full color external scene is projected by a single window television system having a 30- x 40-degree field of view (FOV), fixed in the forward direction. Flight, weapon aiming, and steering information are superimposed (as on a HUD) using an optical combiner. Both are collimated to optical infinity and, together with the conventional cockpit instruments and a moving map display, give a simulation of daytime conditions.

For the NATAL test runs, the simulator is set up to simulate night-flying conditions. Current night-flying equipment is simulated in the cockpit. A fixed-forward infrared camera supplies an aligned unmagnified image on a television raster HUD. The pilot uses this high-quality, but restricted, view ahead in conjunction with a set of NVG, which increase the external FOV to the full 30 x 40 degrees. This enables him to look out and around. The cockpit is illuminated with blue-green light, which is complementary to the red-sensitive goggles, enabling the pilot to peer beneath the goggles to look into the cockpit and read his instruments. The simulator is enclosed within a light-tight box to ensure that the cockpit has the proper lighting for use of the NVG. The external scene video signals are manipulated to create a monochromatic sensor HUD image, occupying a 20- x 20-degree FOV.

The cockpit is fixed and the feel of the controls is simulated by a hydraulic loading system. The cockpit layout (Figure 2) is based loosely on the Harrier GR5, but it is simplified and contains a central collimated head-down display. The aircraft performance and control characteristics also resemble the GR5 during wing-borne flight. Infrared video cameras are put in

the cockpit where they enable pilot's movements to be monitored and recorded unobtrusively.

The external scenic image is obtained from a color television camera that is driven over a brightly illuminated 2000:1 scale model by a multichannel gantry mechanism (Figure 3). The effective flying area can be extended by controlling the camera motion so this is reflected at the model edges, as though the aircraft path continued into the contiguous terrain seen in the vertical mirrors surrounding the model. At present a 25-fold increase provides flight over a 95- x 36-km area. During the short transitions at the model boundaries, the inappropriate camera image is suppressed, leaving the pilot with the visual sensation of encountering sudden, dense cloud. It is also possible to control the degradation of the camera image to simulate the obscuration effects of low clouds and fog.

The U.S. Navy investment now provides a simulation of a CO₂ laser TA system. This acts like a range-finding laser radar, which can penetrate smoke or fog, to examine the vertical profile of the hills ahead of the aircraft. It then computes the instantaneous climb or dive command to achieve a safe ground-hugging path and displays this on the HUD.

To induce the pilot to fly a low, ground-hugging and preplanned route, a dense array of radar-directed antiaircraft missile and gun defenses are simulated. The pilot receives audio warning when tracked by a missile or gun radar, while the head-down display shows him the tactical situation as interpreted by the aircraft radar warning receiver. The only countermeasure he is allowed to employ to avoid the defenses is to fly low enough to cause the ground radar to break lock through terrain obscuration or cluttering effects. He is told not to maneuver off the planned course to avoid these defenses.

Figure 4 shows the main functions of the units which make up the facility. There are five interconnected minicomputers with attached floating-point processors, together with the cockpit, control room, and visual flight attachment. The Gamma computer calculates the behavior of the aircraft and can be considered as the hub of the facility. The control room contains a large equipment rack, acts as an experiment control station, and holds most of the video system.

2.2 RESULTS

A statistical analysis of the simulator data (152 flights by 16 pilots) showed there was a significant interaction between the visibility and the TA laser. This interaction was seen in the mean height data shown in Figure 5. When the visibility was poor, the pilots flew significantly lower when the TA laser was on. The significant interaction demonstrates that in poor visibility conditions the TA laser can help the pilot fly lower, while in good visibility conditions, little difference was seen.

3.0 LOCUS MODELING

The usefulness of the TA laser for the detection of cables and obstacles will now be demonstrated by the modeling of the LOCUS system. It is the purpose of this section to lay out the equations that predict the detection ranges for cables for the LOCUS system. There is one paper on this subject (reference 2), which will be drawn on heavily. Also measurement papers

(references 3 and 4', on the reflection coefficients of cables and wires were utilized.

3.1 SIGNAL-TO-NOISE EQUATION

The LOCUS is basically a monostatic, heterodyne system, operating with a 15 MHz offset between the local oscillator and the transmitter lasers. Thus, the power signal-to-noise is given by:

$$S/N = \frac{\eta P_s}{h \nu B} \quad (1)$$

where $\eta = \eta_m \eta_q \eta_s \eta_t$

P_s = signal power returned to receiver

h = Planck's constant

ν = optical frequency

B = intermediate frequency bandwidth

η_m = mixing efficiency

η_q = quantum efficiency of detector

η_s = speckle factor

η_t = turbulence factor

3.1.1 Signal Power

The power returned from the cable to the detector in the receiver is given by the standard radar equation (reference 5). It is partitioned below to indicate the contribution of each of the effects (power per unit area at range R) (antenna gain of transmitter) (normalized laser radar cross-section) (range effect on reflected power) (area of receiver) (transmission efficiency of optics and the atmosphere).

$$P_s = \left(\frac{P_t}{4\pi R^2} \right) \cdot \left(\frac{4\pi}{\pi \left(\frac{\theta}{2} \right)^2} \right) \cdot \left(\frac{\sigma}{4\pi} \right) \cdot \left(\frac{1}{R^2} \right) \cdot A_r \cdot (\tau_o e^{-2\delta R})$$

This reduces to:

$$P_s = \frac{P_t \tau_o A e^{-2\delta R}}{\pi^2 R^4 \theta_d^2 \sigma} \quad (2)$$

where P_t = peak transmitter power

τ_o = optical efficiency

A_r = area of receiver

δ = extinction coefficient of atmosphere

R = range to target

θ_d = divergence angle of transmitter

σ = laser radar cross-section

3.1.2 Laser Radar Cross-Section

A useful model for the laser radar cross-section (LRCS) for power line cables is presented in reference 2. It is assumed that the electric field is optimally directed horizontally along the length of the cables. This simple model is based on the helical structure of power cables and the surface roughness of the cables. The LRCS of a cable is given by:

$$\sigma = \begin{cases} \sigma_s & -\alpha \leq \theta \leq \alpha \\ \sigma_d & \text{elsewhere} \end{cases} \quad (3)$$

where σ_s and σ_d are the specular and diffuse backscatter LRCS respectively, and θ is the incidence angle of the radiation with the cable. The cable pitch angle, α , is given by

$$\tan \alpha = \frac{\pi D}{P} \quad (4)$$

where D = diameter of cable

P = the helical period.

Now the average specular LRCS is given by:

$$\sigma_s = \frac{5\pi a P M F}{2 \cos \alpha} \quad (5)$$

where M = number of surface strands illuminated

F = depends on the strand curvature and wavelength (reference (2) given value of 0.05 at 10.6 μ m)

a = strand radius.

An estimate of the number of exposed strands which are illuminated is given by:

$$M = \frac{\theta_d R \sin \alpha \delta}{2a} \quad (6)$$

where δ = packing efficiency of the strands (data in reference (2) shows this to be about 0.83).

The combining of equations (4) through (6) gives the average specular LRCS as

$$\sigma_s = \frac{5 \pi^2 F \delta}{4} D \theta_p R \quad (7)$$

The average diffuse LRCS is given by

$$\sigma_d = 4 A k^4 s^2 t^2 \beta^2 \cos^4 \theta e^{-k^2 t^2 \sin^2 \theta} \quad (8)$$

where $A =$ illuminated area $= D R \theta_d / \cos \theta$

$k =$ wavenumber $= 2\pi/\lambda$

$\lambda =$ wavelength

$s =$ standard deviation of the surface heights

$t =$ correlation length that defines how fast a surface with a given s varies with distance

$\beta =$ scattering matrix element ($\beta = 1$ for horizontal transmit/horizontal receive).

Factoring in the above definitions into equation 8, gives

$$\sigma_d = (4k^4 s^2 t^2 \cos^3 \theta e^{-k^2 t^2 \sin^2 \theta}) D \theta_d R \quad (9)$$

3.1.3 Signal-to-Noise (S/N) Equation

Combining equations 1, 2, 7, and 9 gives the average S/N for the cables as:

$$\frac{S}{N} = \frac{\eta P_t \tau_o A_r D e^{-2\delta R}}{h \nu B \pi^2 R^3 \theta_d} \begin{cases} \frac{S \pi^2 F \delta}{4} & -\alpha \leq \theta \leq \alpha \\ 4k^4 s^2 t^2 \cos^3 \theta e^{-2k^2 t^2 \sin^2 \theta} & \text{elsewhere} \end{cases} \quad (10)$$

3.2 DETECTION RANGES

Using the parameters for the LOCUS system and the cables given in Tables 1 and 2, it is now possible to determine the detection ranges for the cables

versus angle. Substituting in the numerical values for the parameters, equation (10) becomes

$$\frac{S}{N} = (3.16 \times 10^{13}) \left(\frac{D e^{-2\delta R}}{R^3} \right) \begin{cases} .512 & -\alpha \leq \theta \leq \alpha \\ .031 \cos^3 \theta e^{-.352 \sin^2 \theta} & \text{elsewhere} \end{cases} \quad (11)$$

It is of interest to take the ratio of the S/N for the diffuse and specular returns. This gives

$$\frac{S/N}{S/N} = 16.5$$

or a 12dB difference at $\theta = 0$.

In the GEC Avionics data package on the LOCUS system, there was a curve showing the performance against a 10 mm cable (See Figure 6). This curve shows that for $\theta = 10$ degrees and $\delta = 0.4/\text{km}$, there is a detection range of 1.65 km. If these parameters are substituted into Equation (11), assuming a specular return (e.g., $\alpha > 10$ degrees), the $S/N = 9.63$. This is a little low, but for the remainder of this paper a signal-to-noise ratio of 10 or 10dB shall be assumed to be consistent with the GEC Avionics prediction.

Figures 7 and 8 show sample solutions for equation 11 assuming $S/N = 10$ for two cable sizes, 10 and 40 mm. In Figure 7, the detection range is plotted against the extinction coefficient for both spectral and diffuse returns at normal incidence. In Figure 8, a pitch angle of 20 degrees is assumed, and the detection range is then plotted versus the angle off of normal to the cable. This shows that the detection range drops considerably once the pitch angle of the cable is exceeded.

Equation (11) can be used to calculate ranges for other cable sizes or pitch angles, or atmospheric conditions. The equation will vary for bare wires, and a separate paper will be written for them. The parameters used in Table 2 are for slightly rough cables at $10.6 \mu\text{m}$.

4.0 LOCUS HARDWARE

The LOCUS hardware was installed on the A-6E REAL NIGHT aircraft and test data obtained on two flights. This section describes the hardware and provides a sampling of the limited data obtained for this sensor. The scenario for this application is shown in Figure 9, and involves low and fast operation of an attack aircraft in unfamiliar areas containing hazardous obstacles along the intended flight path.

4.1 SYSTEM SPECIFICATIONS

The approach uses a pulsed coherent CO_2 laser system with the characteristics shown in Table 3. A block diagram for the hardware is given in Figure 10. It addresses the critical interface with the pilot's HUD, where objects must be inserted on a new real-time basis to be effective. This information processing and display requires a high speed computer capability (200 MIPS) which is the most significant innovation in this work. The system scans out an unusual scan pattern (Figure 11), and utilizes a 0.35 mrad beam

overlay to maintain a high probability of detection for objects as small as one-half inch cables. The scan coverage is limited, and the range performance should be increased to at least 3 km, but this does still provide a valuable test vehicle for evaluating this approach. The LOCUS coverage relative to the FLIR display on the HUD is shown in Figure 12. Obstacle detections are stored in three-dimensional inertial frames, and the returns gathered from consecutive scans are painted onto the display providing a build-up of the image. The system requires one-fifth of a second to cover an entire frame (10,000 pulse per frame) and produces five frames of information per second.

The LOCUS sensor is shown in Figure 13, and its installation in the pod is depicted in Figure 14. The pod includes environmental control units (ECUs), signal processors, and recorders for the LOCUS sensor.

4.2 TEST RESULTS

The limited testing of this system involved runs against towers and cables. Figures 15 and 16 show samples from these runs with detections of towers at 2.4 km and cables at 1.8 km. The figures show the scan pattern with the line of data extracted being highlighted. It then provides a profile view of the scene with the obstacle highlighted. In the case of cables, the imagery shown is taken from the navigational FLIR (NAVFLIR) on the HUD just as the cables pass out to the field of regard (FOR) of the FLIR (since the FLIR could not image the cables at the 1.8 km that LOCUS detected them).

4.3 FUTURE TESTING

The evaluation of laser TF/OA for Navy attack aircraft is planned for the Morning After (MA) demonstration aircraft. The MA is a proposed Nunn Amendment program involving the U.S. and several NATO countries.

5.0 CONCLUSION

The CO₂ laser radar has again demonstrated its ability to detect even extremely small (but potentially disastrous) obstacles at useful tactical ranges. All three services are currently investigating this laser radar application for manned and unmanned aircraft. Future tests of LOCUS type hardware will provide considerable insight into the robustness of this approach.

References

1. Savage, S.F. and Bullock, C.K., "Laser Terrain Avoidance Simulator Trials", NAVWPNCEN Technical Publication 6940, September 1988.
2. Al-Khatib, H.H., "Laser and Millimeter-Wave Backscatter of Transmission Cables", Proceedings of the International Society of Optical Engineering, Vol. 300, R.C. Harney, editor, 25-26 August 1981, San Diego, California, pp. 212-229.
3. Hayes, C.L., and Brandewie, R.A., "Reflection Coefficients for Wires and Cables at 10.6 μm ", Applied Optics, Vol. 17, No. 7, July 1973, pp. 1564-1569.
4. Savan, M., "Retroreflectance of Wires and Cables at 10.6, 1.5, and 1.06 Micrometers", White paper from Center for Night Vision Electro-Optics, Fort Belvoir, Virginia, 19 pages.
5. Barton, D.K., "Radar System Analysis", Artech House, Inc., Dedham, MA, 1979, pp. 110-111.

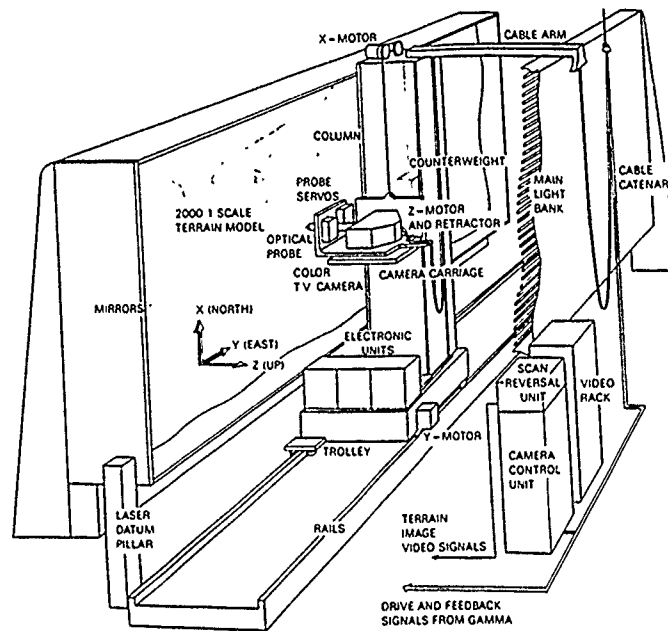


FIGURE 3. VISUAL FLIGHT ATTACHMENT SCHEMATIC.

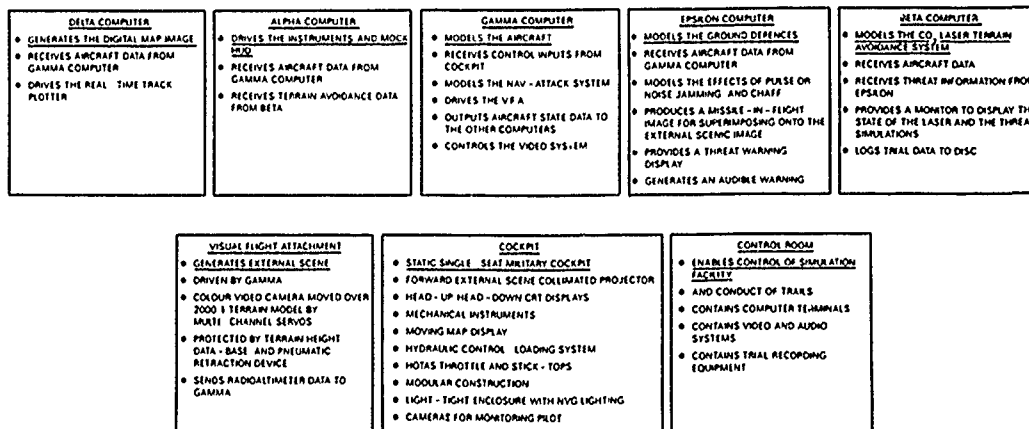


FIGURE 4. The Functional Units of the Air-to-Ground Simulation Facility.

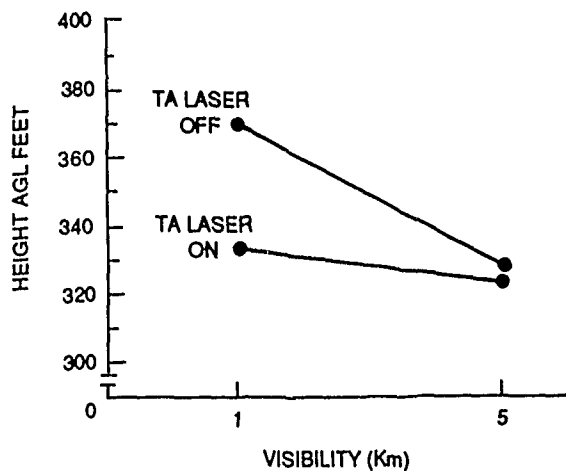


FIGURE 5. INTERACTION BETWEEN TA LASER AND VISIBILITY.

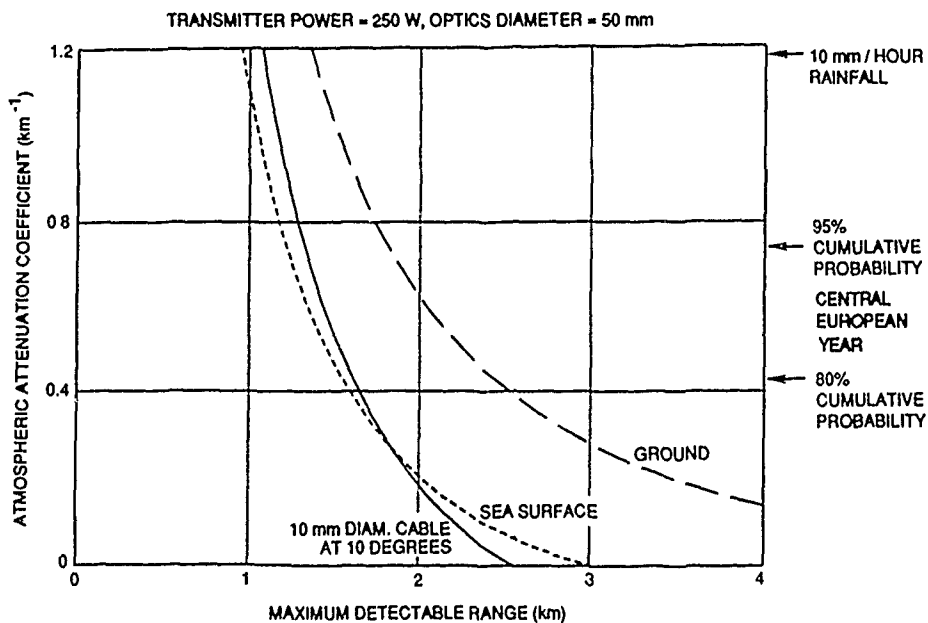


FIGURE 6. LOCUS DETECTION RANGE VERSUS ATTENUATION COEFFICIENT.

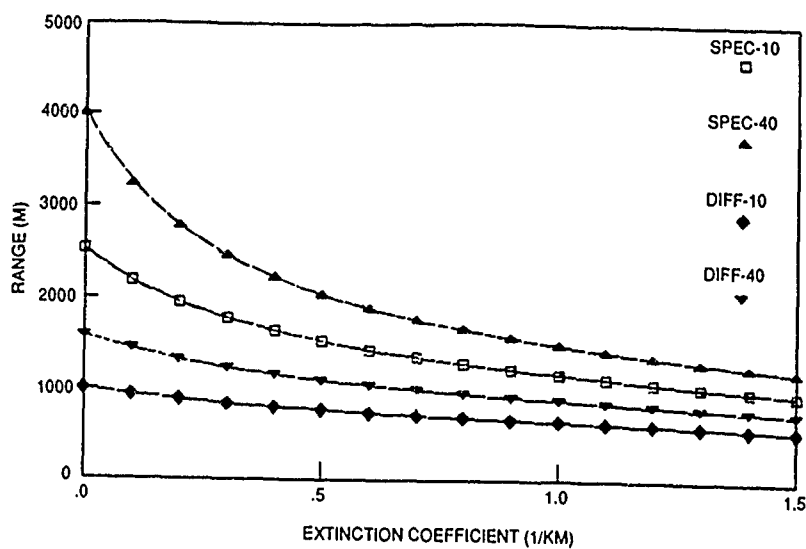


FIGURE 7. DETECTION RANGE EXTINCTION COEFFICIENT.
 Note: SPEC-10 means spectral return from 10mm cable.
 DIFF-10 means diffuse return from 10mm cable.

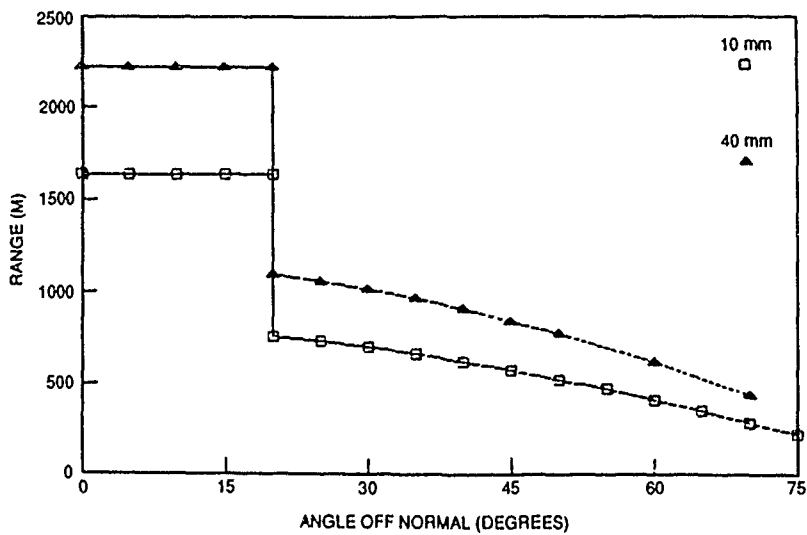
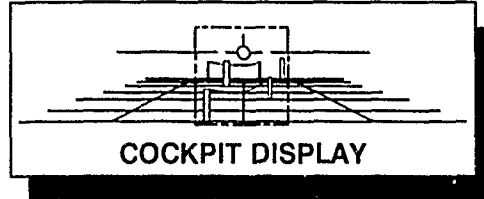


FIGURE 8. DETECTION RANGE VERSUS ANGLE.
 Note: Pitch angle = 20 degrees, $\delta = .4/\text{km}$.



COCKPIT DISPLAY

**LASER OBSTACLE AND
CABLE WARNING SENSOR
(LOCWS)
FOR
PROJECT REAL NIGHT**

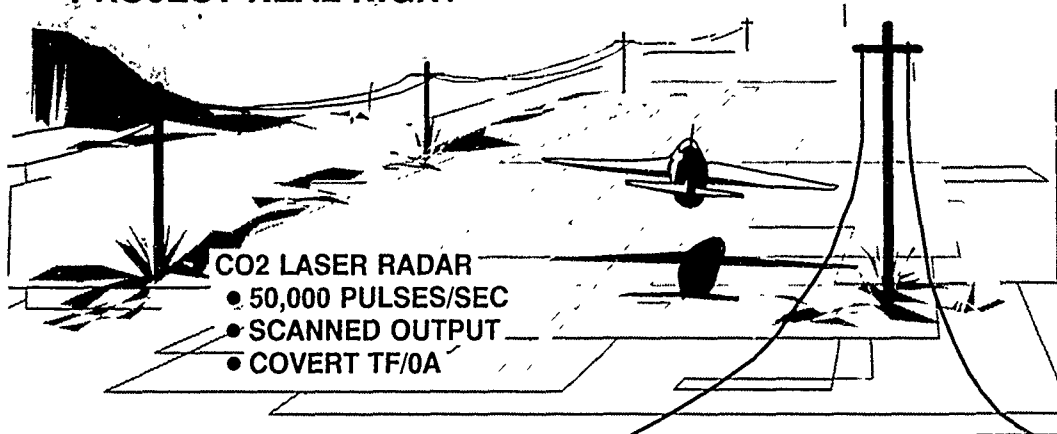


FIGURE 9. LOCUS FOR PROJECT REAL NIGHT.

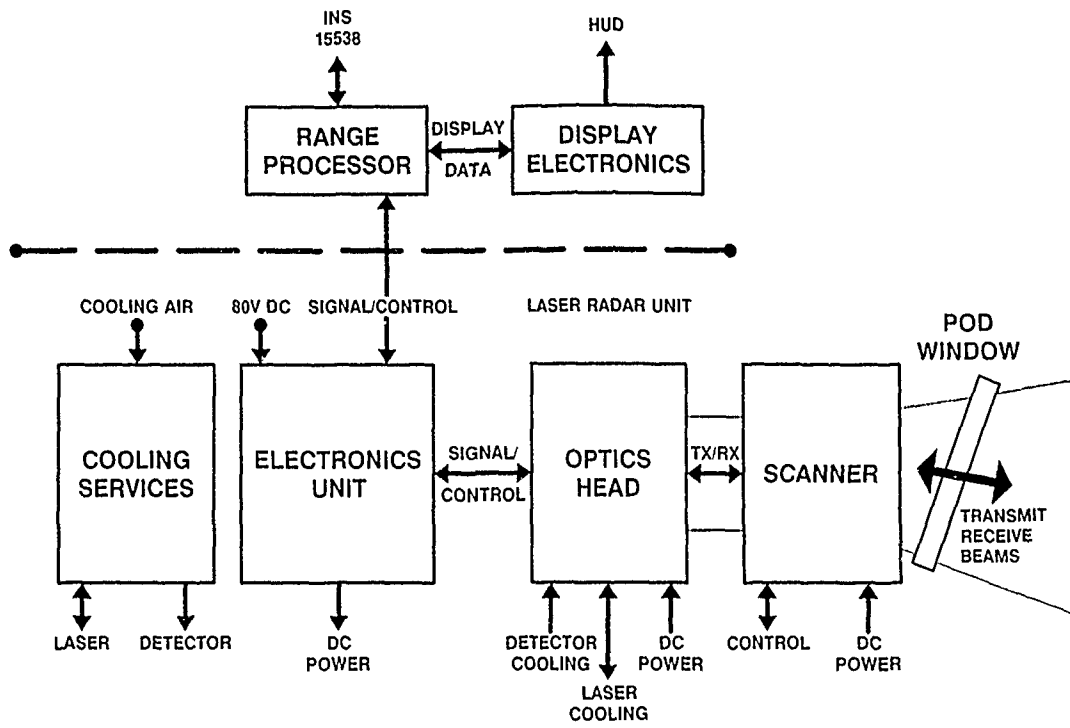


FIGURE 10. LOCUS BLOCK DIAGRAM

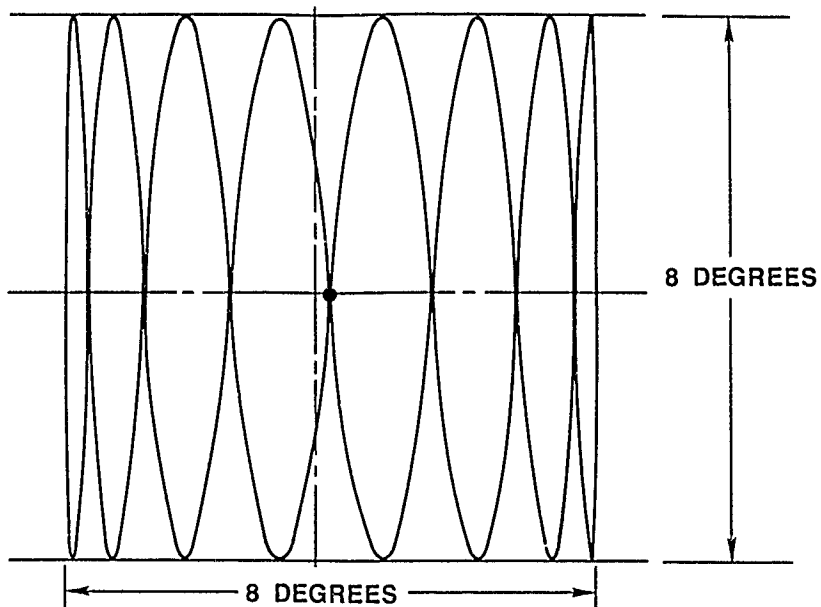


FIGURE 11. LOCUS SCAN PATTERN.

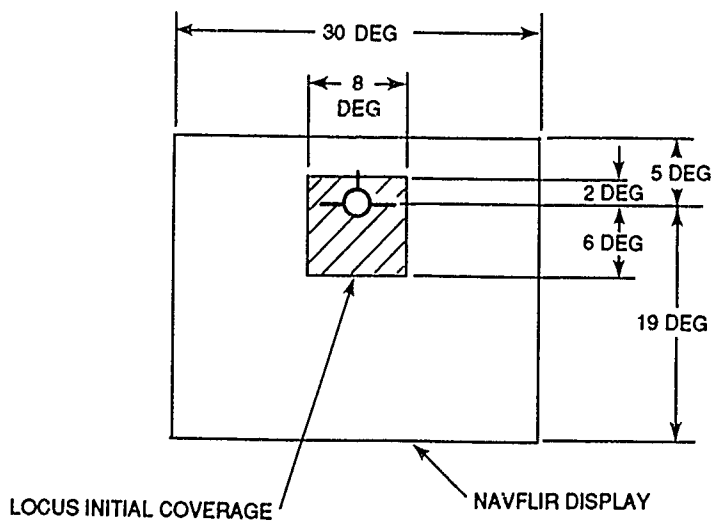


FIGURE 12. LOCUS COVERAGE RELATIVE TO NAVFLIR DISPLAY ON HUD.

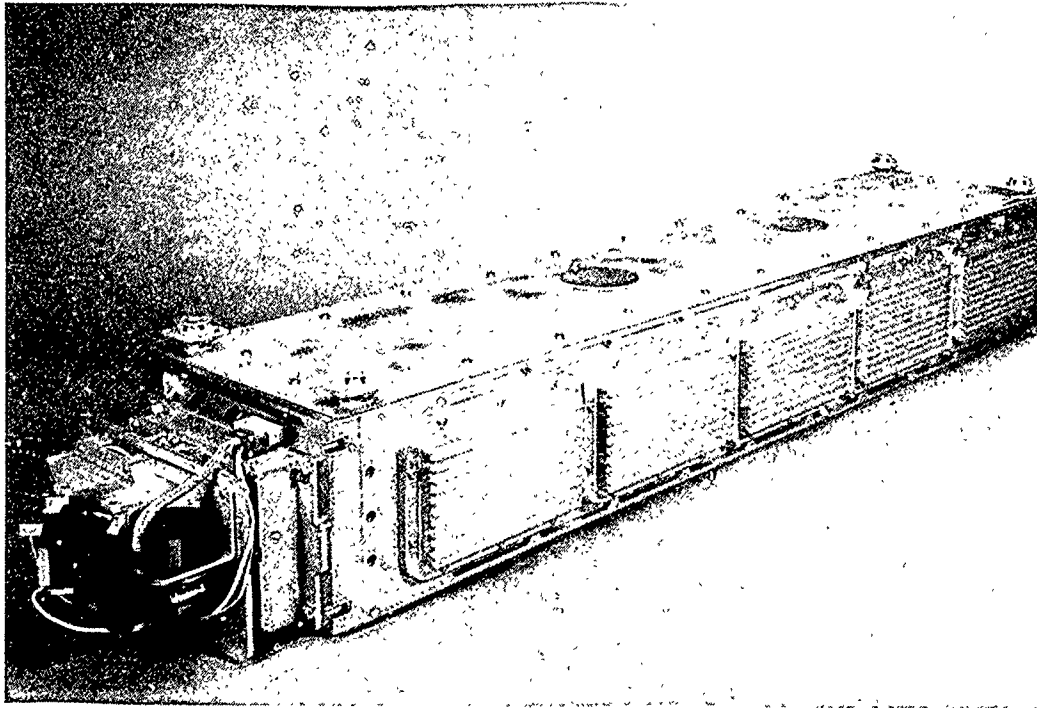


FIGURE 13. LOCUS SENSOR

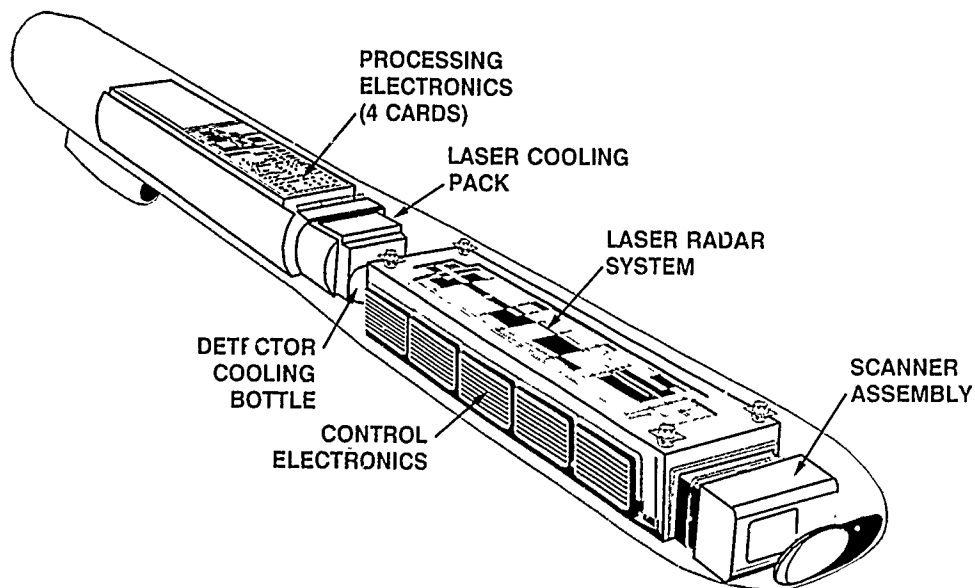


FIGURE 14. LOCUS DEMONSTRATION SYSTEM

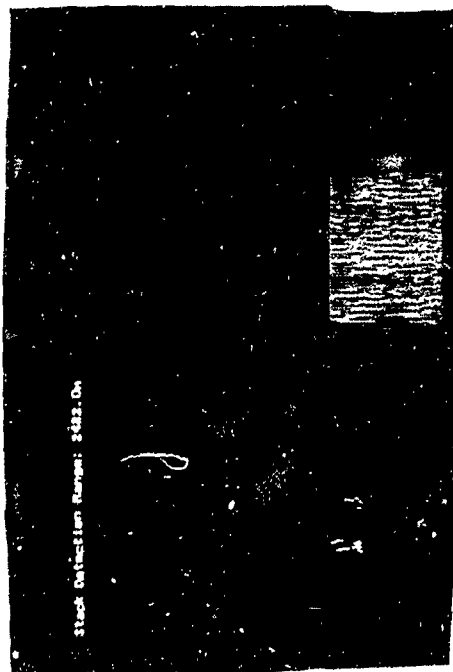
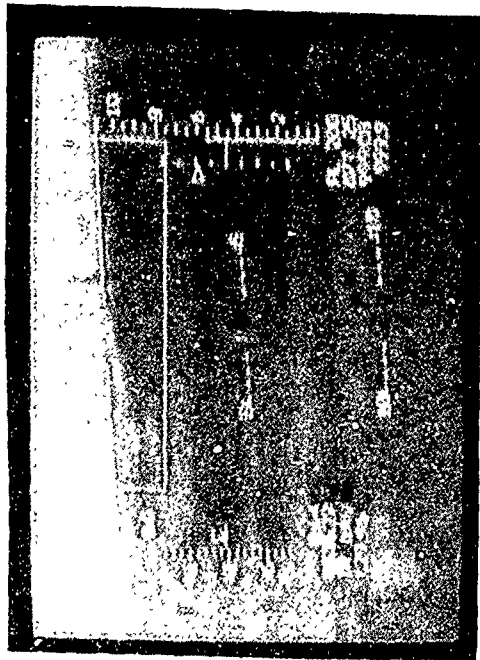


FIGURE 15. LOCUS (TWIN TOWERS AT 2.4 Km).

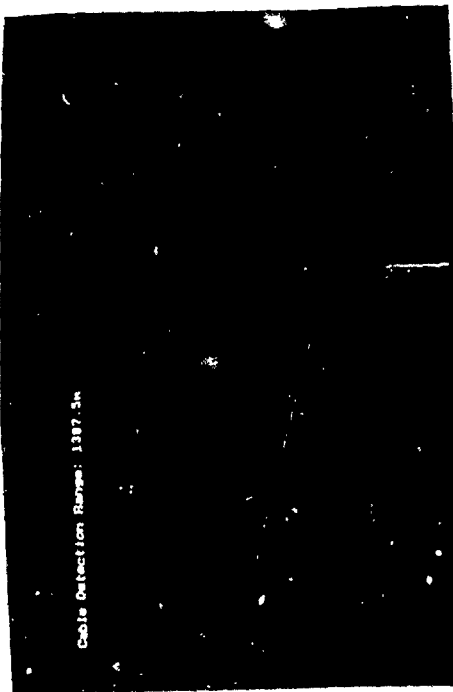
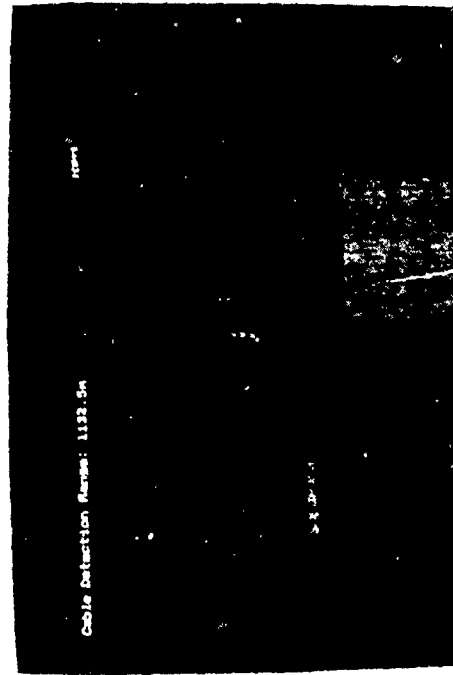
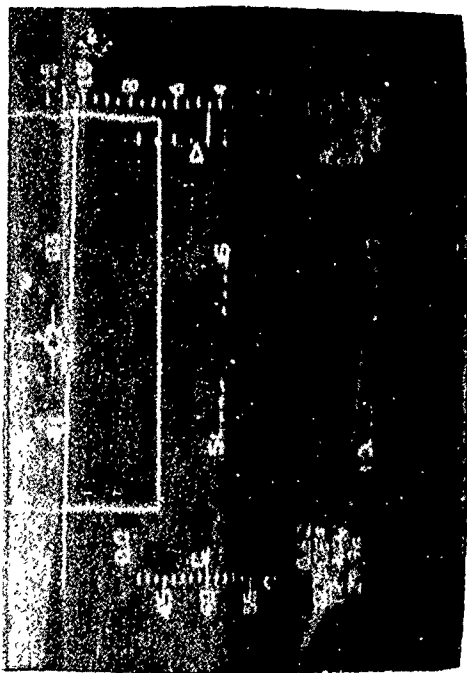


FIGURE 16. LOCUS (WIRES AT 1.8 Km)

TABLE 1. PARAMETERS FOR THE LOCUS SYSTEM.

SYMBOL - PARAMETER	VALUE
P_t - Peak transmitter power (W)	250
λ - Wavelength (μm)	10.59
B - Intermediate frequency bandwidth (MHz)	6
η - Efficiency factor	.10
τ_o - Optical efficiency	.35
A - Area of receiver (m^2)	.00196
δ - Extinction coefficient (1/km)	--
R - Range (m)	300 - 3100
θ_d - Divergence of transmitter (mrad)	0.5

TABLE 2. CABLE PARAMETERS USED IN CALCULATIONS
(SEE FOOTNOTE 3).

SYMBOL - PARAMETER	VALUE
F - Form and wavelength dependent factor	.05
δ - Packing efficiency of strands	.83
s - Standard deviation of surface heights (μm)	.25
t - Correlation length of surface (μm)	1.00

TABLE 3. LOCUS PARAMETERS.

Operating Wavelength	10.6 Microns
Pulse Repetition Frequency	50 KHz
Transmitted Peak Power	250 Watts
Receiver Diameter	50 mm
Beam Divergence	0.5 mrad
Optical Efficiency	0.35
Pulse FWHM	100 ns
Beam Overlap Separation	0.35 mrad
Pixels per Frame	10.000
Frame Rate	5 per Second
Elevation Scan	+2 to -6 Degrees
Azimuth Scan	+4 to -4 Degrees
Volume (Sensor Package)	2.3 cu.ft.
Weight	140 lbs.
Power Consumption	950 Watts

Discussion

Paper n° 19

Question : Dr. L. P. SCHMIDT (Telefunken Systemtechnik - F.R.G., Author)

For the specified cable detection range capability of 1800 m, what is the cable diameter and how does the range degrade under fog or battle-field dust conditions ?

Answer : Mr. TANAKA

The detected cables were on the order of several centimeters in diameter. Smaller cables give different range performance. But wire reflectivity is a complex issue, more data needs to be collected. In fact, weathered cables actually can enhance sensor performance, since it yields a more diffuse return (less angular sensitivity).

Question : Mr. B. MORBIEU - Sextant Avionique, Observer

I understood that you had one shot per pixel. Does it not affect a lot the probability of detection ?

Answer : Mr. TANAKA

Yes, the sensor detected a single pulse per pixel. However, due to the scan pattern which intercepts the obstacles many times and over many frames, a lower probability of detection (less than 50 %) can be tolerated and still present images sufficient to detect and recognize the obstacles. Don't forget that the display is cumulative and thus compensates for this lower probability of detection.

INFRARED LASER RADAR SYSTEMS

A. V. Jelalian
 D. R. Bates
 RAYTHEON COMPANY
 528 Boston Post Road
 Sudbury, Massachusetts 01776
 U.S.A.

SUMMARY

Infrared laser radars constitute a direct extension of conventional radar techniques to very short wavelengths. Whether they are called lidar (light detection and ranging) or ladar (laser detection and ranging), they operate on the same basic principles as microwave radars. Because they operate at much shorter wavelengths, ladars are capable of higher accuracy and more precise resolution than microwave radars. On the other hand, ladars are subject to the vagaries of the atmosphere and are thus generally restricted to shorter ranges than microwave radar. Rather than supplanting microwave radar, ladar opens up new applications that exploit the great shift in wavelength. Ladar applications include:

- Tactical imaging systems
- Missile guidance
- Aircraft guidance
- Clear air turbulence and severe storms sensors
- Fire control and line-of-sight command systems

Carbon dioxide lasers operate at wavelengths between 9 and 11.5 microns spanning much of the 8-12 micron atmospheric "window." They are very efficient coherent light sources with typical "wall plug" efficiencies of the order of 5-10 percent. These characteristics coupled with the recent emergence of rugged, compact CO₂ laser packages has greatly stimulated the development of versatile and diverse ladar systems.

The paper will discuss atmospheric attenuation throughout the electromagnetic spectrum and assess the impact that weather has on system selection, with a view toward complementary use of active radar and active and passive optical systems.

CO₂ laser radar field test results will be presented to indicate the performance potential for moving target detection and range detection and imaging of targets. Simultaneous measurements from a common aperture active and passive system test will also be presented, and complementary uses of a combined system capability to perform automatic target detection will be assessed.

1. INTRODUCTION

Modern laser radar systems combine the capability of radar and optical systems to allow simultaneous measurement of range, reflectivity, velocity, temperature, azimuth and elevation angle. These six dimensions of target information can be utilized in fire control system applications to allow target acquisition, tracking, classification and imaging. The modulation capabilities of microwave radar systems can be applied to laser transmitters to allow accurate target measurement and time/frequency gating of atmospheric or terrain background clutter. The optical resolution associated with laser systems results in very small angular beamwidth to allow imaging, aimpoint assessment, and target tracking.

Microwave radar systems typically have angular beamwidths that inhibit tracking ground targets in multipath or high clutter conditions. The need for low altitude flight, for aircraft survivability purposes, results in a requirement for detection and avoidance of obstacles and power transmission lines, along with the ability to perform terrain following. In these low altitude conditions the detectability of microwave transmissions, low microwave off-axis wire cross sections, coupled with atmosphere and terrain clutter cross section results in the consideration of laser radar systems.

Combining the six-dimensional measurement capability and the optical resolution of the laser radar systems allows substantial clutter rejection, very low probability of beam intercept, and substantially increases the potential for autonomous operation.

2. MICROWAVE SYSTEM

If all-weather radar system operation is desired, a wavelength of 1 centimeter or longer is typically chosen. However, these systems must deal with the limitations due to multipath, countermeasures, and angular resolution noted below:

- multipath - results in inaccurate elevation tracking
- countermeasures - results in target range information being denied by a stand-off jammer, or vehicle presence detected

angular resolution - results in limited target classification, separation, identification and aimpoint selection.

Because of these and other reasons, systems are developed which, although they are not all weather, provide a significant adverse weather capability. Presently, millimeter and infrared systems are being considered for this role. Operation in the millimeter waveband will allow target detection under more adverse weather conditions of advection fogs and battlefield obscurants than infrared systems. However, multipath (1,2,3,4) problems such as those which occur over snow-covered terrain, runways, water surfaces and smooth roads may prevent accurate target elevation tracking for ground-to-ground and low altitude air-to-ground conditions where accurate target tracking (<1 mrad) is required, while rain backscatter can provide an atmospheric clutter problem. Because snow-covered terrain can statistically occur for periods of time longer than poor visibility conditions, and aimpoint selection is required for some weapon systems, optical portions of the electromagnetic spectrum are considered for these radar-type applications.

The basic multipath effect is caused by a transmission of microwave energy to a target shown in Figure 1, at a low elevation angle. The microwave radar beamwidth, θ_B , is sufficiently wide that some of the energy from the antenna system illuminates the terrain or water in addition to the target. As a result, some of the reflected energy from the ocean or background is reflected to the target and subsequently returned to the microwave radar system. In such a reflection pattern, the receiver sum signal is caused to increase and decrease, depending upon the phase of that reflected energy.

Additionally and more importantly, the energy reflected from the surface is scattered back directly to the microwave radar system, causing the difference channel of the tracking system to have an error signal prevalent in it caused by the signal return from the ocean or the terrain. To the degree that the signal returned from the lower path is within the view of the receiver main beam or side lobes of the microwave antenna, it provides an error source. This error source causes the microwave antenna system to have significant errors in the elevation track, dependent upon the surface backscatter effect. Correspondingly, to the degree that the surface reflection factor is symmetrical about the microwave receiver, this effect is less prevalent in the azimuth channel. As a result, one can configure a laser system search field which is broader in elevation than it is in azimuth. The use of lasers and the corresponding wavelength associated with them results in a very much narrower beamwidth. As a result, more of the electromagnetic energy propagated from the laser can be directed to the target and subsequently the multipath errors are significantly eased.

Having introduced the subject of the beamwidth of a laser transmitter, it should be noted that the beamwidths typically used in the microwave field are referenced to the 3-dB beamwidth. However, beamwidths conventionally utilized in optics usually refer to the beamwidth to the $\frac{1}{e}$ or $\frac{1}{e^2}$ or full width half maximum point.

Techniques utilized in the development of laser radar systems involve the same electromagnetic radiation theories utilized in the microwave portion of the spectrum, and as a result significant similarities exist. Figure 2 illustrates the electromagnetic spectrum labeled in terms of the letter nomenclature for microwave systems having typical wavelengths in terms of centimeters; whereas the optical spectrum is denoted in terms of micrometers (μm) and is characterized by regions of the electromagnetic spectrum where atmospheric windows exist, allowing propagation to occur. Lasers exist that operate in each of these windows. Table 1 illustrates attenuation as a function of wavelength for both the laser and microwave wavebands.

In the visible waveband where the ruby laser operates ($0.69 \mu\text{m}$) the atmospheric "seeing" conditions have a very dramatic effect upon the amount of attenuation per kilometer that the laser beam encounters. Visibility on a clear day is 15 km, with corresponding one-way attenuation of 1 dB/km. Introduction of haze into the atmosphere reduces the visibility to 3 km and increases the attenuation to 5 dB/km. Moving to the $1.06 \mu\text{m}$ wavelength (the wavelength associated with a YAG laser), it may be observed that the above conditions produce less attenuation than they did in the visible region; further movement to the mid-infrared ($3-5 \mu\text{m}$) and the far-infrared at $10.6 \mu\text{m}$ decreases the haze attenuation to 1 dB/km. The predominant attenuation mechanism in that far-infrared region is absorption by H_2O . The left column under the $10.6\text{-}\mu\text{m}$ wavelength addresses the problems of humidity in sub-arctic, mid-latitude, and tropical environments, and data for atmospheric attenuation under tropical environments result in a factor of 3 dB/km. Correspondingly, a chief concern is system operation in fog and rain.⁽⁶⁻⁸⁾ The column under $\lambda = 10.6 \mu\text{m}$ illustrates that a radiation fog having visibility of 0.5 km would have attenuation of 3 dB/km. These figures may be contrasted with those commonly found in microwave radar textbooks⁽⁹⁻¹⁰⁾ for attenuation at microwave wavelengths from 1 cm to 0.3 cm. These last three columns indicate the ability of longer wavelength electromagnetic systems to penetrate fog with less attenuation.

Rainfall attenuation may be observed to be essentially the same from the 0.3-cm band through the infrared portion of the spectrum. Operation at longer wavelengths is seen to be significantly less affected by atmospheric propagation and typically results in all-weather system operation.

3. LASER RADAR SYSTEMS THEORY

3.1 Beamwidth

In reviewing the ability of laser systems to operate in radar-type system applications, one should compare the lasers' potential to provide the standard ranging, angle tracking and velocity measurement capability normally required of microwave systems. The diffraction-limited beamwidth (θ) of the transmitting source, operating at a wavelength (λ) with a transmitting aperture diameter (D) is expressed by Equation (1) to be approximately

$$\theta = C \lambda / D \quad (1)$$

where C is a constant

One may see from Table 2 that beamwidths of laser systems are orders of magnitude smaller than those of microwave radar systems. For applications where increased angular precision and aperture size limitations exist, the laser offers significant potential.

3.2 Doppler Shift

Correspondingly, the ability of a radar system to sense target velocities by use of the Doppler principle may be expressed by Equation (2):

$$F_D = \frac{2v \cos \phi}{\lambda} \quad (2)$$

where V = relative target velocity
 λ = transmission wavelength
 ϕ = angle between relative velocity vectors

Because of the shorter operating wavelengths associated with lasers, the Doppler-shifted frequency from a target is significantly increased, and as a result there are more cycles of Doppler shift for each foot per second of target motion as shown in Table 3. As a result of the lasers' increased accentuation of the Doppler shift, target velocities may be instantaneously measured more accurately.

3.3 Receiver Detection Techniques

In Figure 3, diagrams are shown for incoherent and coherent detection receivers. The incoherent detection receiver at optical wavelengths is similar to a video radiometer receiver (i.e., an envelope detector at microwave wavelengths). However, the signal-to-noise ratio (SNR) equation has additional terms besides the signal power (P_{sig}) called the optical background (P_{bk}) which is caused by undesired signals such as sunlight, cloud reflections, flares, etc. The received signal competes with these external and other internal noise sources at the receiver. The received optical power, after suitable filtering, is applied to the optical detector; square-law detection then occurs, producing a video bandwidth electrical signal.

The coherent detection receiver is similar to the incoherent, except, a portion of the laser signal is coupled to the optical detector via beamsplitters. As a result, the optical detector has the local oscillator power (P_{LO}) at frequency (f_0) in addition to the received signal power (P_{bk}).

Additionally, the receiver has a dark current noise thermal receiver noise, $1/f$ noise and generation recombination noise.

Having discussed the noise mechanizations, let us now turn to the SNR expressions.

The SNR equation for incoherent detection may be expressed as:

$$SNR = \frac{n P_{sig}^2}{h f \{2B (P_{sig} + P_{bk})\} + K_1 P_{dk} + K_2 P_{th}} \quad (3)$$

The SNR equation for coherent detection may be expressed as:

$$SNR = \frac{n P_{sig} P_{LO}}{h f \{B (P_{LO} + P_{sig} + P_{bk})\} + K_3 P_{dk} + K_4 P_{th}} \quad (4)$$

where:

SNR = electrical signal power/electrical noise power
 n = quantum efficiency
 h = Planck's constant (6.6×10^{-34} joule-second)
 f = transmission frequency
 B = electronic bandwidth
 P_{sig} = received signal power

P_{bk} = background power
 P_{dk} = equivalent dark current power = $\frac{AB}{(D^*)^2}$
 P_{th} = equivalent receiver thermal noise = $\frac{4KTBN_F}{R}$
 P_{LO} = reference local oscillator power
 K_1 = $\frac{\rho_i}{q}$
 K_2 = $\frac{1}{\rho_i q}$
 K = Boltzmann's Constant
 T = receiver temperature (290°K)
 N_F = receiver noise figure
 R = resistance

where: A = detector area (cm²)
 ρ_i = the detector current responsivity
 q = the electron charge (1.6×10^{-19} coulombs)
 D^* = specific detectivity ($\frac{\text{cm} - \text{Hz}^{1/2}}{\text{W}}$)

The SNR for the incoherent system has the received signal power squared in its numerator and has a summation of noise terms associated with the return signal, the background signal, the dark current, and the thermal noise of the receiver in the denominator. The returned signal power and the background power are included as noise sources in the detection process because of the random photon arrival rate. In the coherent detection system, the local oscillator power is an additional source of noise (compared to the incoherent system) and the numerator is related to the product of the received signal power and the local oscillator power. The local oscillator power is very important in the detection process; here, it may be increased so that it overwhelms all of the other noise sources. As a result, the local oscillator power in the denominator cancels out the local oscillator power in the numerator; the SNR is directly proportional to the received signal power, rather than to the received signal power squared (as with the incoherent system). Additionally, because the local oscillator power becomes the predominant noise source, the coherent detection system typically is background-immune.

For coherent detection where the local oscillator power is increased to provide shot-noise-limited operation of the receiver, the SNR expression for coherent detection can be reduced to:

$$\text{SNR} = \frac{i_{sig}^2}{i_N^2} = \frac{\eta P_{sig}}{h\nu B} \quad (5)$$

Comparing the SNR for a coherent system to the SNR for an incoherent system with the following typical parameters at 10.6 microns,

η = 0.5
 $h\nu$ = 1.9×10^{-20} joules
 D^* = 2×10^{10} cm $\sqrt{\text{Hz}/\text{watt}}$
 \sqrt{A} = 0.03 cm
 ρ = 4 amperes/watt
 R = 1000 ohms

yields the S/N ratio for a coherent receiver which is 30 dB more sensitive than the incoherent detection systems. Recent detector sensitivity improvements would reduce this to approximately 25 dB.

Figure 4 illustrates the reference transmitter power versus SNR relationship for coherent and incoherent detection laser radar systems utilizing a typical 100-ns pulse width. It may be observed that as the SNR requirement increases, the transmitter power of the coherent system increases linearly and that of the incoherent system increases as the square root. In the limit, incoherent detection systems approach the sensitivity of coherent systems for very large SNR's. For a typical SNR requirement of 100 (20 dB), the coherent system is seen to have a 30-dB increased sensitivity over that of an incoherent system.

3.4 Measurement Accuracy

Coherent detection laser radar receivers are typically Gaussian noise limited and, as a result, RMS measurement errors may be characterized by those utilized in microwave radar systems.

Due to the short wavelength operation of laser radars, Doppler shifts are extremely large compared to microwave systems. This results in IF signals in the receiver allowing short measurement time intervals, thereby permitting simultaneous range, velocity and

angle measurement. This inherent capability of laser radar systems to provide five-dimensional target data R, V, I, angle-angle with optical resolution capability has resulted in laser radar systems being evaluated for precision fire control and autonomous missile guidance applications.

The one sigma range (σ_R) and velocity (σ_V) measurement accuracy for pulse, frequency-modulated, and amplitude-modulated waveforms may be shown to be:

$$\text{Pulse: } \sigma_R = \frac{K C \tau}{2 \sqrt{S/N}} \quad (6)$$

$$\text{FM: } \sigma_R = \frac{C}{2 \frac{dF}{dT}} \sigma_F \quad (7)$$

$$\sigma_F = \frac{3}{\pi T \sqrt{2 S/N}}$$

$$\text{AM: } \sigma_R = \frac{C}{4 \pi F_{AM} M \sqrt{S/N}} \quad (8)$$

$$\text{Velocity: } \sigma_V = \frac{\lambda}{2} \sigma_F \text{ where } \tau = \frac{1}{B} \quad (9)$$

where:

- τ = pulse width
- C = speed of light
- $\frac{dF}{dT}$ = chirp characteristics
- σ_F = one sigma estimate of frequency
- σ_V = one sigma estimate of velocity
- F_{AM} = AM modulating frequency
- M = modulation index
- T = measurement time

The pulse and frequency-modulated waveforms have a velocity measurement accuracy capability as a function of receiver processor bandwidth as shown in Figure 5. Here it may be observed that there is a tradeoff required for pulse systems to simultaneously measure range and velocity, i.e., good range accuracy - poor velocity accuracy.

This trade is not required for FM systems as the slope of the measurement accuracy plots are in the same direction, and chirp characteristics may be chosen to result in good simultaneous range and velocity measurement accuracy.

The curves are plotted for: $S/N = 50$ for the FM system, 100 for the pulse systems, and assumes the signals are at an intermediate frequency within the receiver such that the processing bandwidth is the inverse of the pulse width. The FM chirp characteristic utilized is 10^{12} Hertz per second.

3.5 Search Field

Typical figures of merit for microwave radar search systems involve the power aperture area product. The larger this ratio, the more capability a radar system has to scan a large field in a given time. As shown below the figure of merit for a laser radar system is not identical to that of a microwave system.

The steradian search field (Ω) may be represented by

$$\Omega = \frac{F.T. \theta^2}{T.O.T.} \quad (10)$$

where:

- F.T. = frame time
- θ = circular aperture beamwidth
- T.O.T. = time on target

Evaluating the search field for radar and laser systems we may represent the S/N expression respectively as

RADAR

$$S/N = \frac{P_R}{KT B N_F} \quad (11)$$

COHERENT LASER RADAR

$$S/N = \frac{n P_R}{h \nu B} \quad (12)$$

- P_R = Received signal power
- K = Boltzmann's Constant
- T = Temperature
- B = Bandwidth
- N_F = Receiver Noise Figure

$$\begin{aligned} \eta &= \text{Detector Quantum Efficiency} \\ h &= \text{Planck's Constant} \\ \nu &= \frac{c}{\lambda} = \text{Frequency} \end{aligned}$$

assuming the system bandwidth is matched to the time on target, i.e., $B = \frac{1}{T.O.T.}$

Results in the steradian search field becoming

$$\Omega_R = \frac{F.T. P_T \sigma_D \eta_{SYS}^2}{16 S/N K T N_{FR}^4} \quad (13)$$

$$\Omega_L = \frac{F.T. P_T \sigma_D \lambda \eta_{SYS} \eta_{DET}}{16 S/N h c R} \quad (14)$$

if we let the detector quantum efficiency be equivalent to:

$$\eta_{DET} = \frac{1}{N_F} \quad (15)$$

and assume that the frame time, cross section, system efficiency, S/N requirement, and range are the same for both radar and laser systems, for example only, the search field equations may be parametrically expressed as:

$$\Omega_R = K_1 P_T D^2 \quad (16)$$

$$\Omega_L = K_2 P_T D_2 \lambda \quad (17)$$

and results in the conclusion that the coherent laser radar system search field figure of merit ($P_T D^2 \lambda$) is wavelength dependent, i.e., for similar power aperture area products, the longer wavelength systems have greater scan field capability. In this example the laser footprints were assumed contiguous. Increased search field capability may be obtained by utilizing multiple transmitter and receiver beams or by spacing the laser footprints in a noncontiguous manner, consistent with target size and detection requirements.

4. LASER RADAR FIELD TEST RESULTS

Raytheon 10.6-micron laser radar systems employing coherent detection receivers have been utilized in field and flight test experimentation since 1968. A generic laser radar block diagram is shown in Figure 6.

In this configuration the laser is modulated to provide information content to the transmitted signal which is coupled through the interferometer, optics, and scanner to illuminate the scan field of interest. The received signal is then coupled, via reciprocity through the interferometer, to the receiver detector where it is mixed with a sample of the laser signal in the form of a local oscillator.

The receiver output is processed by the signal processor to extract target information and then processed by the data processor where all information is compiled to provide target position, range, velocity, and an image. Figure 7 illustrates a 1968 ground signal returned from a 5-watt coherent 10.6-micron airborne system (McManus, Chabot, Goldstein). Figure 7A and Figure 7B illustrate this Doppler-shifted signal along with an aerial camera photograph with the laser boresighted to the center of the frame. Figure 7C illustrates the Doppler-shifted signal of a pedestrian walking at a crosswalk, as observed in the aerial camera photograph to the left. In the next sequence, the laser footprint passes over the pedestrian and one observes the aircraft ground speed in pictures 7D and 7E. Early success of these experimental systems encouraged further technology development. However, laser devices were too large, weighing as much as 450 pounds. Subsequently, Raytheon developed an air-cooled 5-watt laser weighing 7.5 pounds including power supplies and cooling. The coherent 5-watt laser was configured into the scanning laser radar shown in Figure 8. This system was designed, fabricated and flight tested under USAF and DARPA sponsorship in 1975. A conceptual diagram of the system is shown in Figure 8. Here the 0.5-milliradian beam was propagated to the terrain via a Palmer scan. The beam advances in a contiguous manner across the terrain (via aircraft flight velocity) to yield a coherent Doppler spectrum in the receiver.

The backscattered Doppler-shifted target signal was then processed in a surface acoustic wave signal processor, recorded on tape, and subsequently played back on the

ground through a CRT display. The system was configured for a remotely piloted vehicle (RPV) application with the tape recorder simulating the data link. Thresholding of the Doppler-processed signal intensity resulted in gray scale rendition on a photographed CRT. Figure 9 illustrates a strip made in such a manner. The CO₂ laser radar map, made at a 50-degree depression angle, is shown as the central image in Figure 9. Surrounding this picture are 70-millimeter aerial camera photographs from a vertically oriented camera. One may readily observe that optical quality photographic images may be made with CO₂ laser radars, and also that speckle effects may be reduced by suitable processing.

Having demonstrated optical resolution capability, let us now evaluate the MTI radar aspects of this system. Figure 10 illustrates a 70-mm aerial camera scene of a forested area at Fort Devens, Massachusetts. There is a tank suitably noted in Figure 10A traveling on a road. A return signal from the forest or road is Doppler shifted relative to the aircraft velocity and appears at a frequency $f_0 + f_D$ while a return signal from the moving tank appears at a frequency $f_0 + f_D + f_{\text{target}}$ and, as such, appears in a different Doppler filter. The surface acoustic wave delay line processor is programmed to give an MTI cue, in real time, when a Doppler return greater than 5 knots is indicated in adjacent pixels. Figure 10B illustrates this moving target flag which occurs at full intensity, or one gray shade, on the display. Additionally, it may be noted that several target clutter intensity spots cause false alarm indications which are distributed through the scene. Altering the target detection algorithms to require a "N detections out of M trials" detection approach results in Figure 10C and a significant false alarm reduction. One may also note what appears to be a second target in this scene which was not observed in the photograph. A clutter patch of the duration and continuity of motion, required to pass the MTI target detection requirements, tends to rule out a false target detection.

Forward-looking ground-based systems⁽¹¹⁾ have been configured to demonstrate target acquisition and imaging capabilities. Figure 11 illustrates MTI detection and imaging over a 6° x 5° raster scan field of a moving tank, obtained by a Raytheon-developed system. These measurements were funded by U.S. Army, Navy and Air Force contracts. Figure 11 shows photographs of a visual picture of an M-48 tank and CO₂ laser radar image of the same vehicle. Tank targets tended to have a significant diffuse component as noted by the number of consecutive returns. This may be contrasted to that of a helicopter noted in Figure 12, where specularities contributed to the image. Helicopter blade rotation caused the Doppler return to be outside the bandwidth of the imaging filter so that the blades were not imaged.

Figure 13 illustrates an amplitude-modulated CW laser received signal from a stationary target which has been processed to illustrate range measurement characteristics.⁽¹²⁾ Here color is utilized to portray range measurement. In this image the range ambiguity of the 8-MHz amplitude-modulated (AM) tone is seen as horizontal bands over the display. The color scale bar under the picture indicates that returns at longer ranges are color shaded red, while shorter ranges are white and blue respectively. Red color highlights the tank turret and gun barrel. Figure 14 illustrates how edge extraction techniques implemented in the computer can be utilized to identify internal features of another vehicle. Here the windshield, bumpers, truck side body, air conditioner and other areas are highlighted.

Simultaneous measurement programs with passive IR systems have been conducted. One of these results indicates the diurnal washout of a tanker truck located at a range of 4 km along with that of a CO₂ laser range image of the same vehicle. Figure 15 also illustrates the ability of the system to measure wires at distances of 2800 meters.

In 1984 Raytheon proposed the use of these laser radar principles to the USAF Armament Division, Eglin AFB, Florida, for the purpose of autonomous guidance for tactical stand-off weapons. The resultant contract was termed the Tactical Ladar Seeker (TLS) Program. The TLS program consisted of two phases. Phase one was a system design study and Phase two was a captive flight demonstration of the selected approach.

Phase one activities included system simulation studies related to AGM-130, powered glide bombs. A typical system scenario consisted of a 25-nmi mission, wherein aircraft position and inertial transfer alignments occurred. The targets selected were:

- Mobile SAM sites
- Bridges
- Buildings
- Runways
- Buried Targets

System range requirements were determined to be approximately 1 km and necessitated simultaneous active and passive operations at 10.6 microns and 8-12 microns respectively. This hardware was designed and supplied to the USAF by Raytheon for a captive flight demonstration. The purpose of the captive flight test was to demonstrate:

- Autonomous, real time, target detection and classification
- Autonomous aimpoint selection

Figure 16 illustrates the seeker hardware mounted in the nose section of a C-45 aircraft along with photographs of the bridges and tactical target scenes.

Figure 17 illustrates simultaneous active/passive airborne bridge and ship imagery while Figure 18 illustrates MTI target detection of cars and trucks on a highway along with passive imaging of the same scene. In Figure 19 active/passive imagery of an airport scene may be observed. Here aircraft parked in front of the hangar area have different characteristics in the two scenes. The range image illustrated two parked aircraft while the passive scene suggests three. This is due to a thermal shadow caused by a recently departed aircraft.

A video TV camera was boresighted to the Raytheon sensor and a computer graphics generator was utilized to indicate target detection via a box generated on the detected target. Real-time classification of the target resulted in the suitable detection box being color shaded red. Figure 20 illustrates the bridge detection box located over several pier structures. Subsequent computer processing resulted in the computer selection of a bridge pier aimpoint. Similar detection, classification and aimpoint selection occurred for mobile targets.

5. FIRE CONTROL LASER RADAR ADJUNCTS

Laser radar systems can operate as adjuncts to microwave radar or passive IR systems. In this role limited data rate laser radars can be utilized to scan the region containing the potential target. Here the target angular position, range, and velocity may be determined more accurately and potentially improve the false target reporting of the primary sensor. The following evaluates a 10.6-micron and a 1.06-micron laser radar configuration for this role. Initial concerns associated with flight worthiness of coherent systems were eliminated with the successful flight test of a pulse Doppler laser radar in 1972.

Figure 21 illustrates a block diagram of the airborne pulse Doppler radar developed for NASA in 1970. Here a master oscillator power amplifier transmitter configuration is utilized to increase the coherent master oscillator power. Utilization of a polarization controlled optical modulator allows pulse waveform selection. The energy contained within a pulse train is then propagated to the target, reradiated and subsequently collected by the coaxial telescope and subsequently processed by a signal processor to provide range, velocity and angle information. The unit was mounted to either look forward or through the side of a Convair 990 NASA aircraft in 1972.

Figure 22 illustrates the NASA 990 pod configuration to direct the beam forward of the aircraft. Table 4 illustrates some of the hardware specifications, while Figure 23 illustrates an A-scope display of a Raytheon airborne pulse Doppler CO₂ laser radar, having 10 kW of peak power. Here one may see, in the lower part of the figure, an A-scope display, where the X-axis is seen to have a range capability of 0-16 nmi. At approximately 13 nmi an 8-dB S/N ratio may be seen on this A-scope, thereby illustrating that coherent CO₂ systems can be configured to operate in realistic environments and have sufficient coherence to perform long range measurement. In order to demonstrate the capability of systems such as these for fire control applications, calculations were performed using parameters described in Table 5. Range performance as a function of atmospheric conditions is portrayed in Figure 24 for one-square-meter cross section target. Even in haze conditions the system has greater than a 10-km capability, while in 4 mm/hr of rainfall the performance calculation indicates greater than 5-km capability.

A similar set of calculations were conducted⁽¹³⁾ for a 100-millijoule, 1.06-micron laser having an incoherent receiver, having the performance parameters shown in Figure 25. Ranges in excess of 10 km may be realized from this system in clear weather. This may be observed on Figure 26 which shows the probability of detection vs. S/N ratio as a function of range with a neodymium laser. Under the conditions of clear visibility a 50 percent probability of detection may be observed in excess of 7 nmi for the neodymium laser with silicon avalanche detector, and approximately 4 nmi for a silicon detector. In the advent of haze, the YAG system range performance (Figure 27) is reduced to less than 3 km.

In summary, over the past two decades laser radar systems have undergone substantial development. Today these systems are mature, reliable and effective in addressing program needs and have successfully demonstrated real-time target detection, classification and aimpoint selection, and modern day fire control system designers (shown in Figure 28) will need to review the electromagnetic spectrum from the world of active/passive radar and optics.

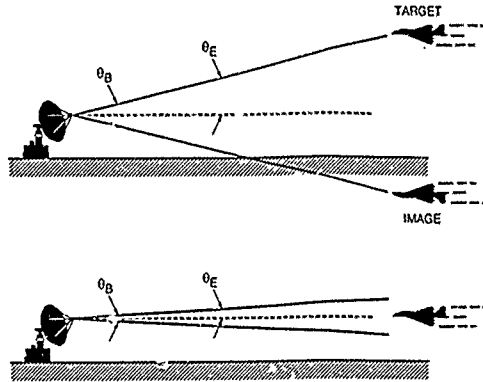


Figure 1. Multipath Errors

EOA 989

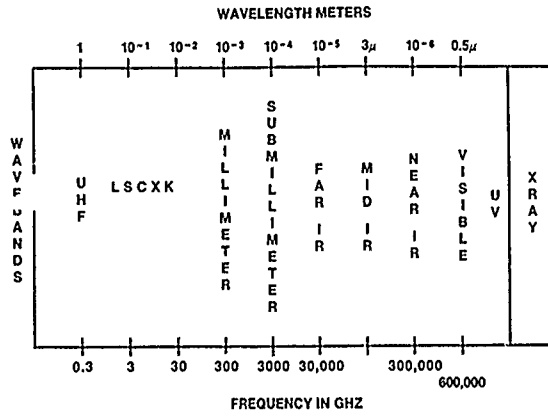


Figure 2. Frequency Spectrum-UHF Through X-Ray Bands

EOA-1262

Table 1. Atmospheric Propagation

dB/km	λ 0.7 μ m	λ 1.06 μ m	λ = 3.8 μ m	λ = 10.6 μ m	0.3 cm	λ 1 cm	λ 3 cm
0.2	EXTREMELY CLEAR	EXTREMELY CLEAR	CLEAR (V = 23 km)	SUB ARCTIC WINTER			12.5 mm/h
0.6	STANDARD CLEAR (V = 25 km)	STANDARD CLEAR		CLEAR		2.5 mm/h	FOG (V = 100 ft)
0.8		CLEAR				FOG (V = 100 ft)	50 mm/h
1.0	CLEAR (V = 15 km)		HAZE SUB ARCTIC SUMMER		ADVECTION FC (V = 10 ft)		
2	LIGHT HAZE (V = 5 km)		HAZE (V = 3 km)	MID LATITUDE SUMMER	RAIN 2.5 mm/h		
3	MEDIUM HAZE (V = 5 km)	HAZE (V = 3 km)		TROPICAL	RADIATION FOG (V = 0.5 km) RAIN 4 mm/h	RAIN 4 mm/h	12.5 mm/h
5	HAZE (V = 3 km)				SNOW 0.2 mm/h		25 mm/h

V = VISIBILITY

GOODWIN
HENSCH
CHU

McCLATCHEY

BARTON
SKOLNIK

EOA 9872

Table 2. Beamwidth

Transmitter	Wavelength (Centimeters)	Aperture (Centimeters)	Beamwidth
Radar	3	30	100 mrad
Millimeter	0.3	30	10 mrad
CO ₂ Laser	10 ⁻³	10	100 μrad
YAG Laser	10 ⁻⁴	10	10 μrad
Ruby Laser	0.7 x 10 ⁻⁴	10	7 μrad

Table 3. Doppler Shift

Transmitter	Wavelength (Centimeters)	Frequency (Gigahertz)	Doppler Shift Ft/Sec (Hertz)
Radar	1	30	57
Radar (Millimeter)	0.3	90	171
CO ₂ Laser	10 ⁻³	30,000	57,000
YAG Laser	10 ⁻⁴	300,000	570,000
Ruby Laser	0.7 x 10 ⁻⁴	430,000	724,000

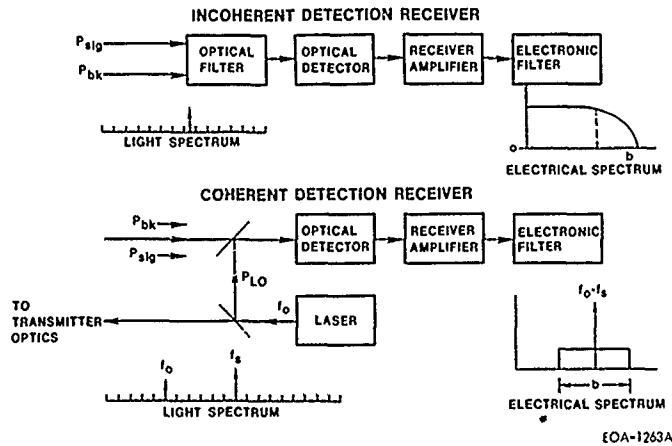


Figure 3. Incoherent and Coherent Detection Receivers

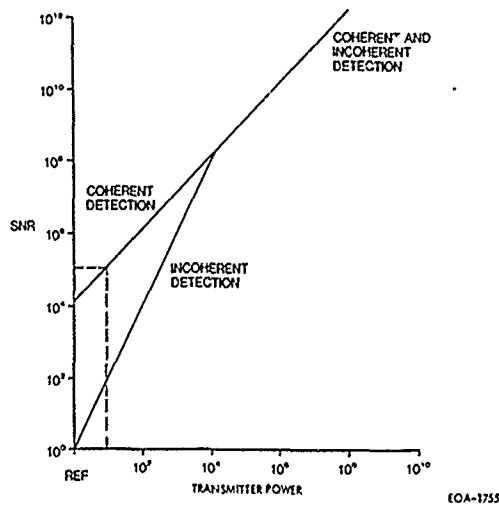
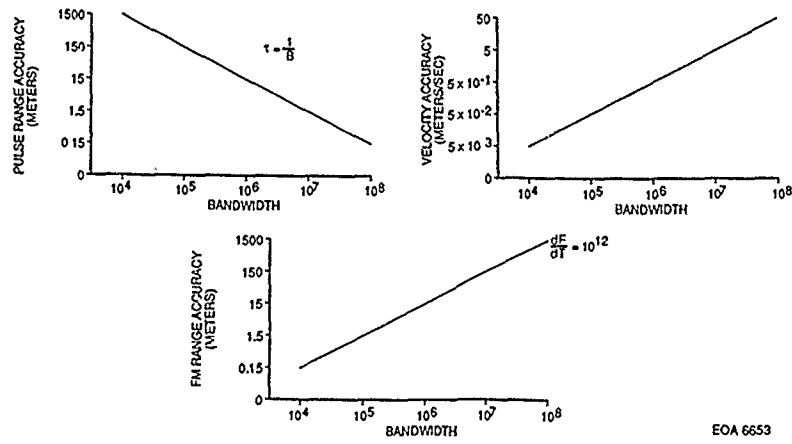
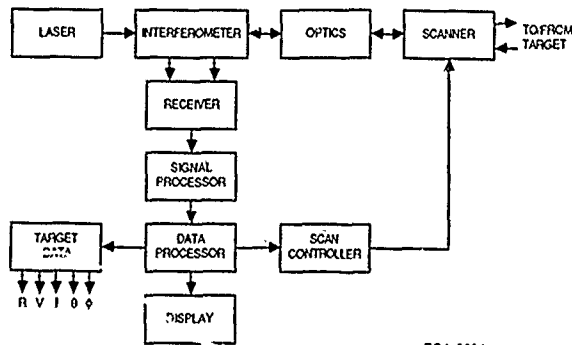


Figure 4. Transmitter Power vs SNR



EOA 6653

Figure 5. Range/Velocity Accuracy vs Bandwidth



EOA-6604

Figure 6. Typical Laser Radar Block Diagram

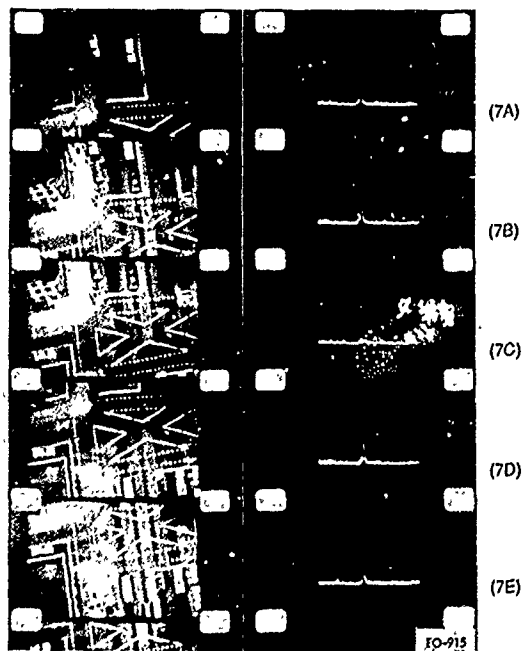
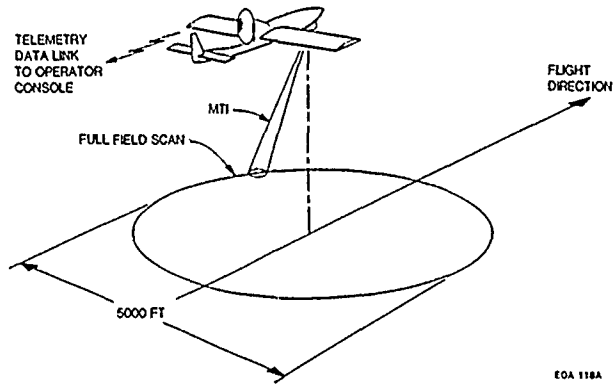
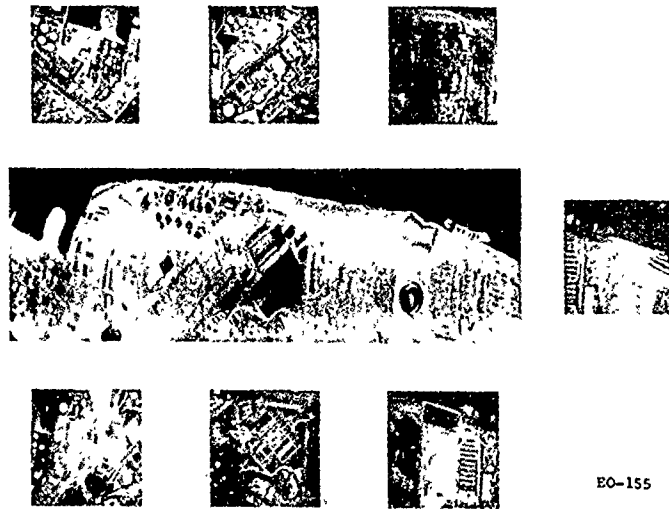


Figure 7. CO₂ Laser Doppler AMTI of a Person Walking Across an Intersection (McManus, Chabot, Goldstein)



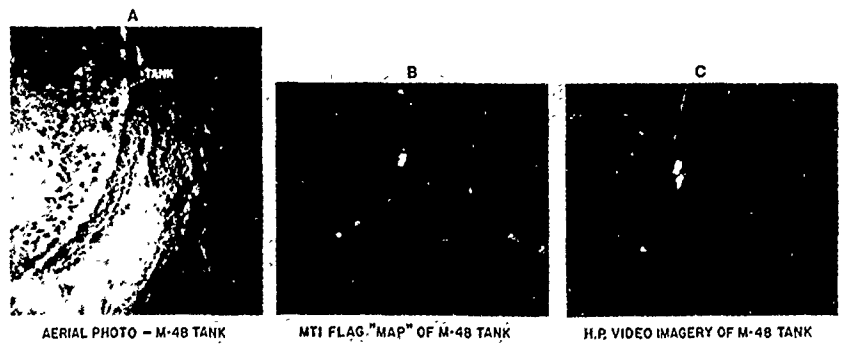
EOA 118A

Figure 8. RPV Palmer Scan Geometry



EO-155

Figure 9. Coherent CO₂ Imagery



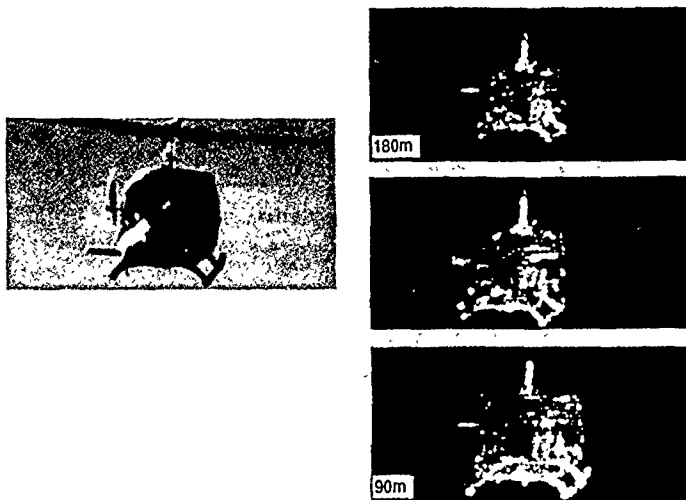
EO-32

Figure 10. MTI Deception of M-48 Tank at Altitude of 1000 Feet



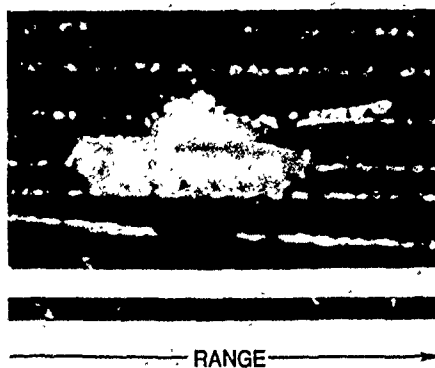
RANGE	250 m	
VELOCITY	10 MPH	
S/N	~ 25 dB	
BW	100 kHz	
VIDEO PROC	LOGARITHMIC	EO-473A

Figure 11. M-48 Tank Approaching



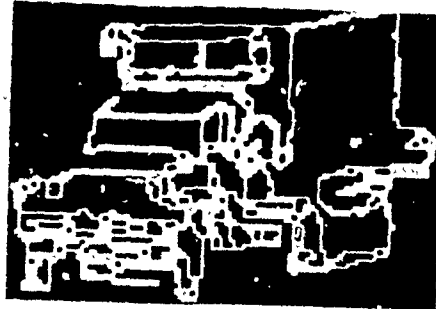
EO-477

Figure 12. UH-1 Helicopter



EO-2622

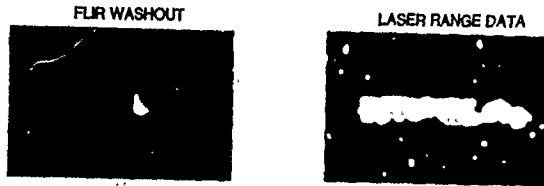
Figure 13. Laser Radar Range Image



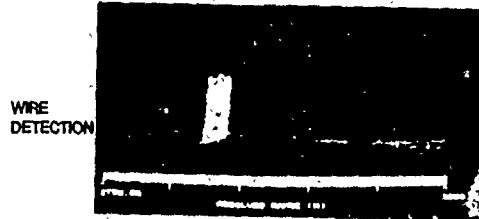
STATIONARY TARGET
INDICATION (STD)

EO-2696

Figure 14. Range Image Edge Extinction



SIMULTANEOUS ACTIVE AND PASSIVE DATA (TANKER TRUCK)

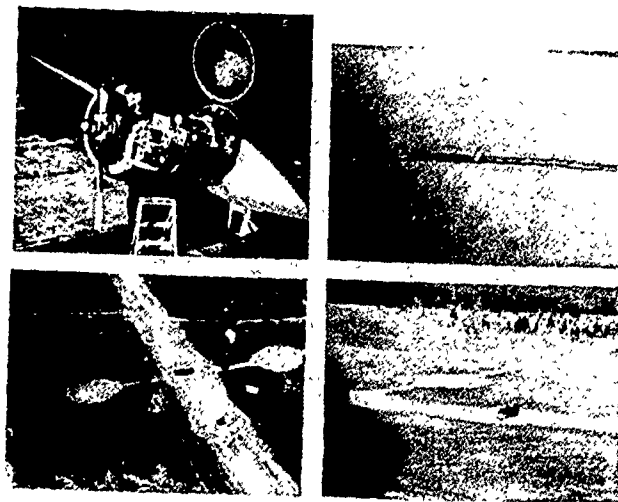


WIRE
DETECTION

ABSOLUTE RANGE DATA:
2760 — 2800 m

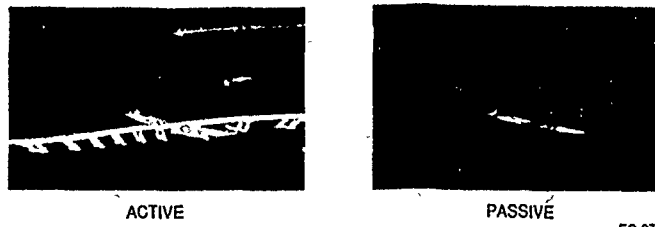
EO-2700

Figure 15. CO₂ Laser Radar Capabilities



EO-2701

Figure 16. Flight Tests



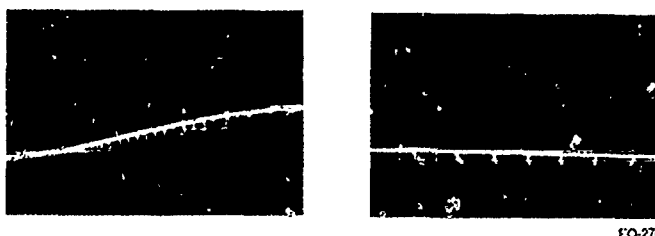
ACTIVE PASSIVE EO-2702
 Figure 17. Active/Passive Bridge Images



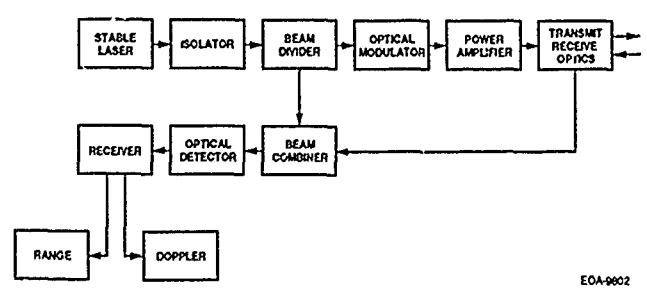
ACTIVE PASSIVE EO-2703
 Figure 18. Active/Passive Images - MTI Detection



ACTIVE PASSIVE EO 2704
 Figure 19. Active/Passive Images - Hangar Complex



EO-2705
 Figure 20. Bridge Detection and Aimpoint Selection



EOA-9002
 Figure 21. Block Diagram of Airborne Pulse Doppler Laser Radar

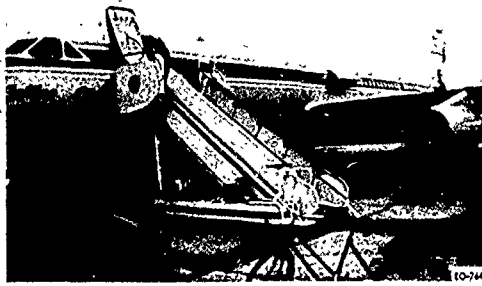


Figure 22. NASA Convair 990 Aircraft in Which Pulse Doppler Laser Radar was Mounted

Table 4. Raytheon Pulse Doppler Laser Radar

<u>System Parameters</u>	
Operating Wavelength	10.6 μm
Pulse Width	Variable 1-10 seconds Selectable Pulses of 2 μs , 4 μs , 8 μs
Repetition Rate	200 pps
Optics Size	12" Cassegrain
Output Polarization	Circular or Vertical
Display	Range-Velocity
Recording Single Range Cell	Amplitude-Velocity
Recording System	Analog or Digital

(Compliments: Raytheon Company, Sudbury, MA; and NASA Marshall Space Flight Center, Huntsville, AL)

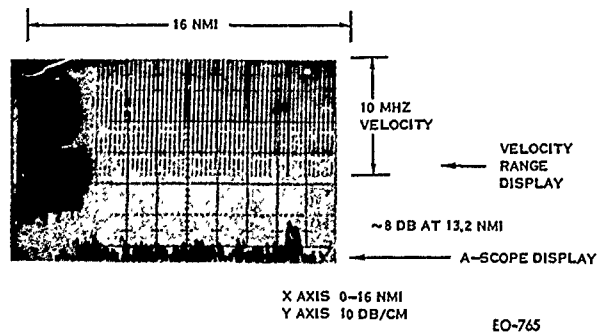


Figure 23. Pulse Doppler Laser Radar Return

Table 5. CO₂ Laser System Parameters

Transmitter Peak Power	10 kW
Optics Diameter	10 cm
Transmitter/Receiver Beamwidth	0.1 mrad
Pulse Width	1.0 to 10 μs Nominal 4 μs
Detector Quantum Efficiency	0.5
Detector Temperature	77° K
System Losses	20 dB
S/N	20 dB
Target Cross Section	1.0 m ²
Detection Technique	Coherent
Operating Wavelength	10.6 μ
Repetition Rate	Handover Volume Dependent

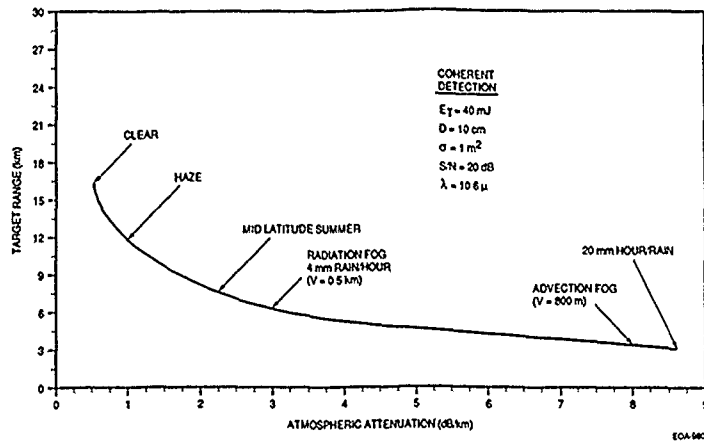


Figure 24. Pulse Doppler Laser Radar Performance Calculations

LASER:

WAVELENGTH	1.06 μm
PULSE ENERGY	100 mJ
PULSE LENGTH	0.02 μs
BEAM DIVERGENCE	0.4 mrad
CROSS SECTION	1 m ²
S/N	22 dB
RANGE ^(B) , CLEAR (VISIBILITY ~15 nm)	5.7 nmi (10.4 km)
RANGE ^(B) , HAZE (VISIBILITY ~2 nm)	2.5 nmi (4.6 km)

NOTES: (A) WITH QUADRANT SILICON AVALANCHE PHOTODIODE DETECTOR

(B) AGAINST A 1 m²(σ) TARGET FOR INITIAL DETECTION, DETECTION PROBABILITY = 95% PER SCAN

EOA-9604

Figure 25. YAG(A) Laser System Parameters

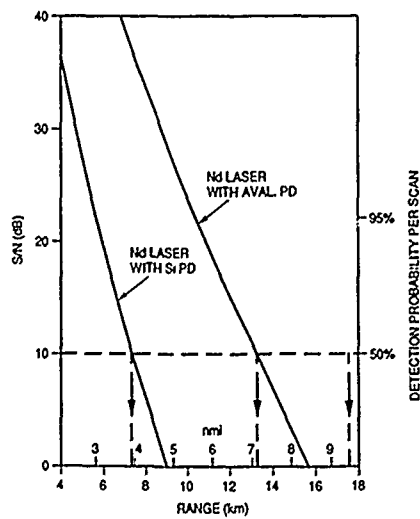
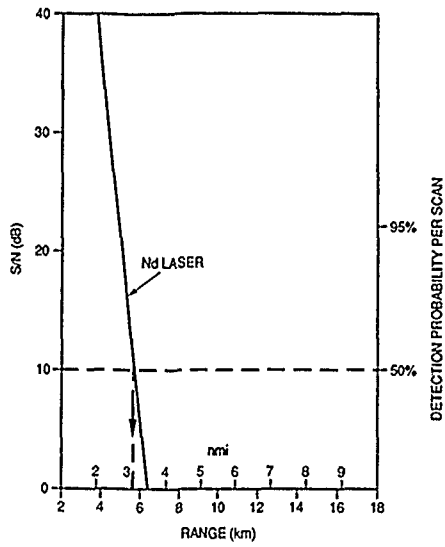


Figure 26. Sensitivity of ND/YAG Laser System in Clear Weather (Visibility 30 km)



EOA 9879

Figure 27. Sensitivity of ND/YAG Laser System Visibility ~ 4 km (Haze)



Figure 28. Laser Radars

REFERENCES

- (1) Barton, D.K.: Low Angle Radar Tracking, Proc. IEEE Vol. 62 No. 6 June 1974.
- (2) Cornwell, P.E.: Raytheon Company, Wayland, MA, Multipath Measurements at 140 GHz Report No. PEC 79:71.
- (3) Wallace, Bruch: 140 GHz Multipath Measurement Over Varied Ground Clutter, EASCON 79
- (4) Hayes, Dallas T.: et al.: Millimeter Wave Propagation Measurements Over Sayon, EASCON 79.
- (5) McClatchey, R.; Selby, J.; AFCRL, Bedford, MA, Environmental Research Paper No. 419, 12 October 1968, AFCRL-72-0611.
- (6) Goodwin, F.; and Nussmeier, T.: IEEE J. Quantum Electron, Vol. QE-4, No. 10, October 1968, p. 616.
- (7) Rensch and Long; Appl Opt, Vol. 9, No. 7, July 1970, pp. 1563-1573.
- (8) Chu, T.S.: Bell System Technical Journal, May/June 1968, pp. 723-759.
- (9) Barton, D.K.: Radar System Analysis, Artech House, Dedham, MA, 1976.
- (10) Skolnik, M.I.: Introduction to Radar Systems, McGraw-Hill, NY, 1962.
- (11) Jelalian A.; Keene, W.; Kawachi, D.; Sonnenschein, C.; Freedman, N.: Raytheon Company, Sudbury, MA, Low Probability of Intercept Multifunctional Tactical Sensors, Volume 2, Phase II, March 1980, AFWAL-TR-80-1006.
- (12) Osche, G.R.; Young, D.S.; Wilson, W.J.: Raytheon Company, Sudbury, MA, IR STARTLE Technology Demonstrator System, 19 August 1986, DAAK70-80-C-0192.
- (13) Jelalian, A.; Kawachi, D.; and Miller, C.: "Radar Electronic Counter-Counter-measures," Electro 1976, Boston, MA, 1976.

REPORT DOCUMENTATION PAGE									
1. Recipient's Reference	2. Originator's Reference	3. Further Reference	4. Security Classification of Document						
	AGARD-CP-482	ISBN 92-835-0584-0	UNCLASSIFIED						
5. Originator	Advisory Group for Aerospace Research and Development North Atlantic Treaty Organization 7 rue Ancelle, 92200 Neuilly sur Seine, France								
6. Title	ADVANCES IN COMPONENTS FOR ACTIVE AND PASSIVE AIRBORNE SENSORS								
7. Presented at	the Avionics Panel Specialists' Meeting held in Bath, F 9-10 May 1990.								
8. Author(s)/Editor(s)	Various		9. Date September 1990						
10. Author's/Editor's Address	Various		11. Pages 202						
12. Distribution Statement	This document is distributed in accordance with AGARD policies and regulations, which are outlined on the Outside Back Covers of all AGARD publications.								
13. Keywords/Descriptors	<table border="0"> <tr> <td>Airborne sensors</td> <td>Millimeter wave radar</td> </tr> <tr> <td>Avionics</td> <td>Optical modulators</td> </tr> <tr> <td>Microwave monolithic ICS</td> <td>Phased array radar</td> </tr> </table>			Airborne sensors	Millimeter wave radar	Avionics	Optical modulators	Microwave monolithic ICS	Phased array radar
Airborne sensors	Millimeter wave radar								
Avionics	Optical modulators								
Microwave monolithic ICS	Phased array radar								
14. Abstract	<p> A The survivability of aircraft and their capability of carrying out different missions rely on numerous sensor systems such as radars, altimeters, radionavigation, measure and countermeasure equipments. It is very important that the most advanced semiconductor technologies be used in those systems as early as possible because avionic equipment performance is limited by the available components. This specialists' meeting focused on emerging semiconductor component and sensor technologies. </p> <p style="text-align: right; margin-top: 20px;"> <i>NEWS FURNISHED - RPH</i> </p>								

<p>AGARD Conference Proceedings No.482 Advisory Group for Aerospace Research and Development, NATO ADVANCES IN COMPONENTS FOR ACTIVE AND PASSIVE AIRBORNE SENSORS Published September 1990 202 pages</p> <p>The survivability of aircraft and their capability of carrying out different missions rely on numerous sensor systems such as radars, altimeters, radionavigation, measure and countermeasure equipments. It is very important that the most advanced semiconductor technologies be used in those systems as early as possible because avionic equipment performance is limited by the available components. This specialists' meeting focused on</p> <p>P.T.O.</p>	<p>AGARD-CP-482</p> <p>Airborne sensors Avionics Microwave monolithic ICS Millimeter wave radar Optical modulators Phased array radar</p>	<p>AGARD Conference Proceedings No.482 Advisory Group for Aerospace Research and Development, NATO ADVANCES IN COMPONENTS FOR ACTIVE AND PASSIVE AIRBORNE SENSORS Published September 1990 202 pages</p> <p>The survivability of aircraft and their capability of carrying out different missions rely on numerous sensor systems such as radars, altimeters, radionavigation, measure and countermeasure equipments. It is very important that the most advanced semiconductor technologies be used in those systems as early as possible because avionic equipment performance is limited by the available components. This specialists' meeting focused on</p> <p>P.T.O.</p>	<p>AGARD-CP-482</p> <p>Airborne sensors Avionics Microwave monolithic ICS Millimeter wave radar Optical modulators Phased array radar</p>
<p>AGARD Conference Proceedings No.482 Advisory Group for Aerospace Research and Development, NATO ADVANCES IN COMPONENTS FOR ACTIVE AND PASSIVE AIRBORNE SENSORS Published September 1990 202 pages</p> <p>The survivability of aircraft and their capability of carrying out different missions rely on numerous sensor systems such as radars, altimeters, radionavigation, measure and countermeasure equipments. It is very important that the most advanced semiconductor technologies be used in those systems as early as possible because avionic equipment performance is limited by the available components. This specialists' meeting focused on</p> <p>P.T.O.</p>	<p>AGARD-CP-482</p> <p>Airborne sensors Avionics Microwave monolithic ICS Millimeter wave radar Optical modulators Phased array radar</p>	<p>AGARD Conference Proceedings No.482 Advisory Group for Aerospace Research and Development, NATO ADVANCES IN COMPONENTS FOR ACTIVE AND PASSIVE AIRBORNE SENSORS Published September 1990 202 pages</p> <p>The survivability of aircraft and their capability of carrying out different missions rely on numerous sensor systems such as radars, altimeters, radionavigation, measure and countermeasure equipments. It is very important that the most advanced semiconductor technologies be used in those systems as early as possible because avionic equipment performance is limited by the available components. This specialists' meeting focused on</p> <p>P.T.O.</p>	<p>AGARD-CP-482</p> <p>Airborne sensors Avionics Microwave monolithic ICS Millimeter wave radar Optical modulators Phased array radar</p>

<p>emerging semiconductor component and sensor technologies. Papers presented at the Avionics Panel Specialists' Meeting held in Bath, England, 9—10 May 1990.</p> <p>ISBN 92-835-0584-0</p>	<p>emerging semiconductor component and sensor technologies. Papers presented at the Avionics Panel Specialists' Meeting held in Bath, England, 9—10 May 1990.</p> <p>ISBN 92-835-0584-0</p>
<p>emerging semiconductor component and sensor technologies. Papers presented at the Avionics Panel Specialists' Meeting held in Bath, England, 9—10 May 1990.</p> <p>ISBN 92-835-0584-0</p>	<p>emerging semiconductor component and sensor technologies. Papers presented at the Avionics Panel Specialists' Meeting held in Bath, England, 9—10 May 1990.</p> <p>ISBN 92-835-0584-0</p>

END